NUMERICAL SIMULATION OF PORE-SCALE HETEROGENEITY AND ITS EFFECTS ON ELASTIC, ELECTRICAL AND TRANSPORT PROPERTIES

A DISSERTATION

SUBMITTED TO THE DEPARTMENT OF GEOPHYSICS

AND THE COMMITTEE ON GRADUATE STUDIES

OF STANFORD UNIVERSITY

IN PARTIAL FULFILLMENT OF THE REQUIREMENTS

FOR THE DEGREE OF

DOCTOR OF PHILOSOPHY

Ratnanabha Sain

November 2010

Abstract

"Asato mā sad gamaya
Tamaso mā jyotir gamaya"
(Sanskrit) meaning:
From ignorance, lead me to truth;
From darkness, lead me to light;

This dissertation describes numerical experiments quantifying the influence of pore-scale heterogeneities and their evolution on macroscopic elastic, electrical and transport properties of porous media. We design, implement and test a computational recipe to *construct* granular packs and consolidated microstructures replicating geological processes and to *estimate* the link between process-to-property trends. This computational recipe includes five *constructors*: a Granular Dynamics (GD) simulation, an Event Driven Molecular Dynamics (EDMD) simulation and three computational diagenetic schemes; and four property *estimators* based on GD for elastic, finite-elements (FE) for elastic and electrical conductivity, and Lattice-Boltzmann method (LBM) for flow property simulations.

Our implementation of GD simulation is capable of constructing realistic, frictional, jammed sphere packs under isotropic and uniaxial stress states. The link between microstructural properties in these packs, like porosity and coordination number (average number of contacts per grain), and stress states (due to compaction) is *non-unique* and depends on assemblage process and inter-granular friction. Stable jammed packs having similar internal stress and coordination number (CN) can exist at a range of porosities (38-42%) based on how fast they are assembled or compressed. Similarly, lower inter-grain friction during assemblage creates packs with higher coordination number and lower porosity at the same stress. Further, the heterogeneities in coordination number, spatial arrangement of contacts, the contact forces and internal stresses evolve with compaction non-linearly. These pore-scale heterogeneities impact effective elastic moduli, calculated by using infinitesimal perturbation method. Simulated stress-strain relationships and pressure-dependent elastic moduli for random granular packs show excellent match with laboratory experiments, unlike theoretical models based on Effective Medium Theory (EMT).

We elaborately discuss the reasons why Effective Medium Theory (EMT) fails to correctly predict pressure-dependent elastic moduli, stress-strain relationships and stress-ratios (in uniaxial compaction) of granular packs or unconsolidated sediments. We specifically show that the *unrealistic assumption of homogeneity* in disordered packs and subsequent use of continuum elasticity-based homogeneous strain theory creates non-physical packs, which is why EMT fails. In the absence of a rigorous theory which can quantitatively account for heterogeneity in random granular packs, we propose *relaxation corrections* to amend EMT elastic moduli predictions. These pressure-dependent and compaction-dependent (isotropic or uniaxial) correction factors are rigorously estimated using GD simulation without non-physical approximations. Further, these correction factors heuristically represent the pressure-dependent heterogeneity and are also applicable for amending predictions of theoretical cementation models, which are conventionally used for granular packs. For predicting stress-ratios in uniaxial compaction scenario, we show the

inappropriateness of linear elasticity-based equations, which use elastic constants only and do not account for dissipative losses like grain sliding.

We further implement and test a computational recipe to construct consolidated microstructures based on different geological scenarios, like sorting, compaction, cementation types and cement materials. Our diagenetic trends of elastic, electrical and transport properties show excellent match with laboratory experiments on core plugs. This shows the feasibility of implementing a full-scale computational-rock-physics-based laboratory to construct and estimate properties based on geological processes. However, the elastic property estimator (FE simulation) shows limitations of finite resolution while computing elastic properties of unconsolidated sediments and fluid-saturated microstructures.

Acknowledgement

My PhD would not have "*P*iled-*h*igher-and-*D*eeper" (© JC) without the inspiration, support and benevolence of several people. This work was financially supported by Stanford Rock Physics and Borehole Geophysics (SRB) project and its affiliates, for which I am truly indebted. I acknowledge my qualifying exam committee—Gary Mavko, Tapan Mukerji, Greg Beroza and Wei Cai—for finding my research proposal worthy of consideration, and my reading committee—Gary, Tapan, Jack Dvorkin and Mark Zoback—for accepting this work as *fully adequate in scope and quality* for PhD.

I owe a lot of gratitude to my adviser, Gary Mavko. I have truly cherished countless discussions with him: technical, professional and personal. Throughout my 5+ years at Stanford, I have wondered the depths of his scientific insight, knowledge,

and ideas. He has helped me *see* physics on his yellow notepads and through his amazing illustrations, specially the one with rubber balls and Hawaiian sand. Thanks for accepting me as your student, inspiring my thoughts to bloom, teaching me how to present my talks, and allowing my weird schedule! Truly, I have not met a *professor* with a better sense of humor and (stunning) photographic skills.

Thanks to my co-adviser, Tapan Mukerji, for introducing me to diverse subjects including this dissertation subject. Ever since my first acquaintance with Stanford, he has guided and advised me regarding scientific research, courses (he possibly knows *all* Stanford courses), simulations, books, market investments and lately (sea)food. Contrary to my fears, his transition from the small cubicle in Mitchell basement to 3X-sized room in Green basement only increased the length of our discussions! Often, these discussions extended to our walks from Main Quad to Stanford Avenue.

The bulk of what we do at SRB is inspired by Amos Nur—our father figure. His work and ideas carry the vision of understanding physics in uncertain conditions. Thanks Amos! Thanks to Mark Zoback and Jack Dvorkin for your excellent recommendations. I am grateful to Tiziana Vanorio for showing me how real laboratory experiments are done: they helped me better understand my simulations. I would also like to thank Mike Payne, Chris Finn and Ezequiel Gonzalez for the wonderful mentorship during my industry internships, which made me appreciate the *practical* industry problems. A special note of thanks to Ronny Hofmann and Jim Spencer for their incredible suggestions regarding my research. I am grateful to Trilok N. Singh for encouraging me during undergraduate research. Suggestions from Dawn Burgess about editing the thesis were really helpful. I thank Dennis Michael, Bob Clapp and Stanford CEES for access and help with the computational cluster.

There are certain people at Stanford who visibly and invisibly make our stay smoother: SRB and department administrators. I thank Fuad Nijm and Tara Ilich for helping me enormously in terms of administrative hassles. Discussions with both of them have ranged from serious financial and technical problems to banter about habits, cuisines and cultures. Thanks to Susan Phillips-Moskowitz and Lauren Nelson as well.

I am grateful to all my colleagues for sharing time during my stay at Stanford: Ezequiel, Kyle, Kevin, Jeetu, Franklin, Kaushik, Tanima, Richa, Cinzia, Carmen, Hiroki, Piyapa, Ramil, Indrajit, Abhishek, Danica, Stephanie, Adam Tew, Kenichi, Adam Allan, Amrita, Dario, Yu and Xi. I would like to specially acknowledge Youngseuk Keehm and Fabian Krzikalla for our discussions on computational methods. Special thanks to my lunch-n-coffee-mates: Madhur (partner-in-crime for photoshoots) and Nishank, who have been excellent friends. Thanks to Anu and Mita for helping me on various occassions. I sincerely thank Tanima for lots of things, especially her sisterly care during my surgery. I won't forget those long—mostly meaningful—discussions with Kaushik on the patio (sometimes at wee hours of night)!

Lest I forget, I should acknowledge my very special friends: Madhav, Amit, Saurabh, Durga, Sandeep, Sreekar, Saurav, Jayank, Indira and Harry. These people provided me enough strength and distractions, so that I could stay put through my grad life. Friendship with Madhav was forged on Day One at Stanford and evolved through uncountable arguments, cooking and sports (someday I will beat you). Amit, Saurabh and Durga were like my family for the past 3 years. Thanks, mates!

Lastly, any amount of acknowledgement would be insufficient for my extended family: especially my grandparents, my parents and my would-be-in-a-month-wife and her mother! My daddy, Naba Kumar, and my ma, Ratna, have continuously provided encouragement for everything I have done until now, and this PhD *is* their dream. While my childhood dream was to be an accountant, my accountant Daddy's dream was to be a scientist—and so we swapped dreams! Ma has always ensured appropriate (boundary) conditions during my real experiments with life since early childhood. My other-Ma, Purnima, has enquired that I eat-and-sleep properly during most strenuous times. My would-be-in-a-month-wife, Patralika, has been my inspiration, ever since our destiny criss-crossed. A lot of ideas regarding my work, results, writings and slides actually originates in her fertile mind, even though the only rocks she has seen were in the Washington museum. Thanks, folks!

I dedicate this dissertation to my ma, daddy and Patralika. For those who feel that this acknowledgement is a little wordy, this is *just* the perfect start to my thesis.

Contents

List of Tables

List of Figures

Chapter 1
Introduction

1.1 Overview

This dissertation shows the influence of pore-scale heterogeneities on macroscopic elastic, electrical and transport properties of porous media using numerical simulations. Accurate prediction of these physical properties requires understanding the micro-scale physics of the constituents of porous media. This is an active field of research in earth and materials science. Macroscopic property estimation of rocks—which are typically porous media—is essential in the earth sciences, especially in rock physics, to interpret geophysical observables. Theoretical, experimental and computational studies on rocks are generally used to link pore-scale properties (regarded as *micro-scale* in rock physics) to macroscopic or bulk properties. We computationally construct unconsolidated and consolidated rock microstructures and conduct pore-

scale numerical experiments to estimate bulk properties. The construction of these microstructures involves various process-based simulations, as discussed later. Further, our numerical experiments show that pore-scale heterogeneities are important for property estimations.

Pore-scale heterogeneities in structure, force, and stress impact the effective elastic properties significantly in unconsolidated or granular packs. These heterogeneities exist both in laboratory experiments (as reported in the literature) and in simulations (for example, our Granular Dynamics (GD) simulation). However, Effective Medium Theories (EMTs) used for elastic property prediction *ignore* such heterogeneities and hence, fail to predict elastic moduli correctly. We categorically show the evolution of these heterogeneities during the compaction process and their subsequent effects on elastic properties for isotropic and anisotropic compactions. Based on GD simulations, we estimate pressure-dependent *correction* factors which can be used to amend EMT predictions. This correction is a rigorous physical way to compensate for the fact that EMT does *not* account for the presence of pore-scale heterogeneity. We also show the effect of grain-size heterogeneity on effective elastic properties. Granular packs with various grain-size distributions were constructed using a simulation that is a hybrid of Event Driven Molecular Dynamics (EDMD) and GD simulation.

For consolidated microstructures, we show the effect of diagenetic processes on pore-scale microstructural heterogeneity. These diagenetic processes are implemented by using three *computational* diagenesis schemes which mimic rim, nucleation and contact cements. We present computational diagenetic trends of macroscopic elastic, transport and electrical properties, which are in good agreement with laboratory experiments on core plugs. These trends are computed using numerical simulations and depend on diagenesis schemes. We further show that two of the most conventional rock physics models, the contact-cement model and friable-sand model (Dvorkin and Nur, 1996) are reasonably robust for describing the responses of bulk moduli to cementation and sorting. The shear moduli, however, are over-predicted because of the same assumption of homogeneity as in EMTs. We show that the use of pressure-

dependent *corrections* rigorously calculated from GD simulations improves the predictions significantly.

Apart from structural heterogeneity in consolidated microstructures, pore-scale fluid heterogeneity due to partial saturations also impacts elastic property calculations. Using two-phase flow simulation, we create partially saturated microstructures at different porosities. The elastic properties of these microstructures show the impact of patchy fluid saturations on bulk moduli.

The main contributions of this research are:

(a) To quantify the effect of heterogeneity in unconsolidated sediments on macroscopic elastic properties using GD simulation;

(b) To show the effect of grain size heterogeneity, or sorting, on macroscopic elastic properties;

(c) To implement Granular Dynamics simulation;

(d) To show the applicability of a computational recipe to construct realistic consolidated rock microstructures and their property trends.

1.2 Motivation

1.2.1 Need for common rock model

The fundamental aim of rock physics is to relate geophysical observations to in-situ rock properties. Conventional rock-physics models are based on either empirical relations from laboratory measurements or theoretical models based on idealized microstructures. These models have given important insights to understand physical properties and solve in-situ problems. However, these models are always over-simplified, with regard to the geometry they represent and, at times, with the physical interactions within the geometry. Moreover, these effective property estimators differ in the way they characterize microstructure, thereby lacking commonality and constraining cross-property analyses in many cases (Kachanov and Sevastianov, 2005).

With the availability of superior computing power, computational rock physics can now simulate different processes in a common but complex pore-geometry to estimate properties. There have been three broad kinds of approaches to obtain common pore-geometry: stochastic methods (3D reconstruction) (Keehm, 2003, Bekri et al, 2000, Yeong and Torquato, 1998), imaging methods (scanned images, SEM images) (Keehm et al, 2003, Coles et al, 1998), and process-based methods (Bryan et al, 1995, García et al., 2004, Guodong et al., 2004). We concentrated on the *process-based* methods to create numerical microstructures *ab initio* by simulating realistic processes like compaction, sorting and diagenesis.

1.2.2 Need for process-based simulation

The microstructures of the solid and the void parts of the rock jointly determine its transport, electric and elastic properties (Guodong et al., 2005). Analysis of rock microstructures suggests that they change variously due to different geological factors, including sedimentology (grain size distribution, mineralogy), stress conditions (isotropic and anisotropic) and diagenesis (quartz overgrowth, cementation mode and cement material). We use process-based GD and EDMD simulations, and computational diagenesis schemes to numerically model these geological factors. Other microstructure construction methods like imaging methods are often costly and restrict the image resolution; the stochastic methods do not provide a realistic background in terms of modeling sedimentation physics, and they often under-predict connectivity.

1.2.3 Need to exploit high-end computing power

Pore-scale process simulations in complex pore geometries require a lot of computational power. Recent developments in computational technology and algorithms have helped us to simulate larger problems more efficiently (Keehm, 2003). Simulating problems like multiphase fluid flow, elasticity and electrical conductivity on realistic microstructure sizes ($>300^3$ voxels) requires intensive computational resources. With increasing availability of large computing clusters with sufficient

computational power to solve such memory- and CPU-intensive tasks, it is now possible to design flow-simulation, elasticity and electrical-conductivity calculation problems requiring powerful resources. We also use algorithms for GD simulations that are optimized for parallel computing.

1.3 Chapter introduction

This dissertation broadly covers three main topics: an overview of computational rock-physics tools, the properties of granular packs, and the properties of consolidated microstructures.

Chapter (2) introduces the Computational Rock Physics (CRP) tools used in this thesis for constructing granular and cemented virtual rock microstructures and estimating their elastic, transport and electrical properties. We present a brief theoretical background of these tools. Granular Dynamics (GD) simulation, Event Driven Molecular Dynamics (EDMD) simulation and different numerical diagenesis schemes are our microstructure *constructors*. As property *estimators*, we use simulations based on GD, finite elements (FE) and the Lattice-Boltzmann Method (LBM).

Chapter (3) discusses the implementation details for creating and compacting virtual random packs of frictional spherical grains, followed by an analysis of the pack fabric. To create monodisperse packs (packs with a unimodal size distribution), we use GD simulation; for polydisperse packs (packs with a multimodal size distribution), we use a hybrid method involving both EDMD and GD simulation. In this chapter, we provide evidence of structural, force and stress heterogeneity in simulated packs and discuss several microstructural details, including contact number distributions, radial density functions and non-contact, near-neighbor distance distributions.

Chapter (4) discusses unrealistic assumptions in EMTs for predicting elastic properties of compacted frictional granular packs. Using GD simulation, we present the effects of heterogeneity on elastic property calculation. Specifically, we show that the homogeneous-strain assumption of EMT in heterogeneous packs leads to non-

physical, unstable packs and requires *relaxation* through infinitesimal grain rearrangements. These rearrangements, however, do not involve grain sliding. We also introduce pressure-dependent *relaxation corrections* to amend EMT predictions. This correction is a rigorous physical, yet empirical, way to compensate for the fact that EMT does *not* account for the presence of pore-scale heterogeneity. We also present the effects of anisotropic loading (uniaxial strain experiment) on stresses (horizontal/vertical) and stiffness constants. This chapter also discusses the effects of sorting on elastic moduli and compaction-induced permeability changes.

Chapter (5) discusses implementation details of computational diagenesis schemes to construct consolidated microstructures. For these microstructures, we show diagenetic trends of elastic, transport and electrical properties. These trends agree with laboratory experiments on core plugs and hence show the feasibility of using our computational recipe to estimate diagenetic property trends. This chapter also discusses the amendment of a theoretical cement model using pressure-dependent relaxation correction. For fully and partially saturated microstructures, we point out the caveats of estimating elastic moduli using FE simulation.

1.4 References

Bekri, S., Xu, K., Yousefian, F., Adler, P. M., Thovert, J. F., Muller, J., Iden, K., Psyllos, A., Stubos, A. K. and Ioannidis, M. A., 2000, Pore geometry and transport properties in North Sea chalk, Journal of Petroleum Science and Engineering, 25, 107-134

García, X., Araujo, M. and Medina, E., 2004, P-wave velocity–porosity relations and homogeneity lengths in a realistic deposition model of sedimentary rock, Waves Random Media, 14,129-142.

Guodong, J., Patzek, T. D. and Silin, D. B., 2004, SPE90084: Direct prediction of flow properties of unconsolidated and consolidated reservoir rocks from image analysis. In SPE Annual Technical Conference and Exhibition,Houston, Texas, USA.

Kachanov, M. and Sevostianov, I., 2005, On quantitative characterization of microstructures and effective properties, Intl J Sol Str, 42, 309-336.

Keehm, Y., Computational Rock Physics: Transport Properties in Porous media and applications, PhD Thesis, Stanford University, California, 2003.

Yeong, C. L. Y. and Torquato, S., 1998, Reconstructing random media. II. Three-dimensional media from two-dimensional cuts, Physical Review E, 58, 224-233.

Chapter 2
Computational rock physics tools: constructors and estimators

2.1 Abstract

We introduce Computational Rock Physics (CRP) tools for constructing granular and cemented virtual rock microstructures and estimating their elastic, transport and electrical properties. Granular Dynamics (GD) simulation, Event Driven Molecular Dynamics (EDMD) simulation and different numerical diagenesis schemes are our microstructure *constructors*. As property *estimators*, we use simulations based on GD, finite elements (FE) and the Lattice-Boltzmann method (LBM). This chapter presents a brief theoretical background of these tools.

We implement GD simulation to create mechanically-stable, frictional sphere packs at different isotropic and uniaxial stress states. These realistic sphere packs are

created by modeling grain-to-grain interactions based on contact micromechanics. We also use an Event Driven Molecular Dynamics (EDMD) simulation to create polydisperse jammed packs, which are then compacted using GD simulation. Both of these simulations are adaptations of classical molecular-dynamics technique. GD simulation is also used to estimate elastic properties of compacted granular packs.

For elastic and electrical property estimates in cemented microstructures, we use a Finite Element (FE) method. We use a Lattice-Boltzmann method (LBM)-based transport-property simulator to conduct single-phase and two-phase unsteady state flow simulation. Fluid flux from single-phase flow simulation is used to estimate permeability and implement low-flux-based computational diagenesis scheme. From two-phase flow simulations, we obtain fluid (oil and water) distributions at different saturation levels.

The main focus of this chapter is the theoretical background of GD and EDMD simulation. The rest of the simulators—LBM, FE elastic and FE electrical—have been extensively used in rock physics literature and are well established property estimators. Hence, we present a brief overview of these simulators.

2.2 Introduction

It is important to understand the interactions among rock microstructure, pore space and fluids to better interpret geophysical measurements (Arns et al., 2001, Keehm, 2003). Geophysical measurements depend on effective rock properties, which are closely linked with microscopic processes. Hence, understanding micro-scale physics for heterogeneous porous media is important. Parallel developments in material science, biology and chemistry have shown the applicability of micro-scale physics in terms of quantum and molecular simulations to understand macro-scale observations (Bulatov et al., 1998, Li et al., 2002, Agarwal, 2006). In rock physics, we generally consider pore-scale to be micro-scale.

To understand and relate the changes in macroscopic elastic, transport and electrical properties to microstructural changes in rocks, we will construct digital

microstructures and simulate these properties. Granular Dynamics (GD) simulation, Event Driven Molecular Dynamics (EDMD) simulation and different numerical diagenesis schemes are our microstructure *constructors*. In this chapter, we focus on GD and EDMD simulation use for constructing spherical granular packs. We will describe the numerical diagenesis schemes in Chapter 5. As property *estimators*, we use simulations based on GD, finite elements (FE) and the Lattice-Boltzmann method (LBM). Elastic properties of compacted granular microstructures (well sorted and poorly sorted) are computed using GD simulation and compared with FE calculations in Chapter 4. For cemented microstructures, we use FE simulation to compute elastic moduli and electrical conductivity. LBM simulation is used for computing transport properties in granular and cemented microstructures.

Computer simulations are often used to study granular packs (Cundall and Strack, 1979, Campbell and Brennen, 1985, Walton and Braun, 1986, Bardet and Proubet, 1991, Luding et al., 1994a, Ristow, 1994, Wolf, 1996, Potapov and Campbell, 1996, Holtzman et al., 2007). One of the popular methods is GD simulation, also known as the Discrete Element Method (DEM) or force/time-based molecular-dynamics simulation. In recent years, this method has been widely used to study internal states of packs (Makse et al., 2004, Agnolin and Roux, 2007, Guodong et al., 2004) and effects of the assembling process (Agnolin et al., 2005, Silbert et al., 2002a, 2002b), to investigate quasistatic, hysteretic stress-strain relations (Thornton and Randall, 1988, Dobry and Ng, 1989, Kuhn and Mitchell, 1989, Thornton, 2000, Herrmann and Luding, 1998) and to estimate pressure-dependent elastic moduli (Makse et al., 2004, García and Medina, 2006). This method was first proposed by Cundall and Strack (1979) for soil mechanics and geotechnical studies. GD simulation is primarily based on simple interaction rules to estimate forces between two deformable or "soft" particles in contact, and consequent integration of the forces to define the particle motions. Various implementations of GD simulation have been proposed using different grain interaction rules (Schafer et al., 1996), different particle shapes (Ng, 1994, Ting et al., 1993, Jensen et al., 1999, Favier et al., 1999) and different integration schemes (Fraige and Langston, 2004). Efficient algorithms have also been

proposed to improve detection of neighboring grains (Munjiza, 2004) and to increase computational efficiency in obtaining quasistatic stable states (Bardet and Proubet, 1991). In following sections, we primarily focus on the implementation details of GD.

EDMD simulation is another variation of the classical molecular-dynamics approach to simulate particulate systems. Unlike GD simulations, this class of simulations models grain collisions, which are termed *events* (Pöschel and Schwager, 2005, Donev, 2005, Luding, 1995). The grains are considered to be "hard" spheres and each grain-collision is modeled as a binary operation obeying conservation laws (for linear and angular momentum). We use an implementation of this method (Donev, 2005) to create stable *jammed* polydisperse packs (Section 2.4).

To predict elastic and electrical properties in consolidated rocks, rock physicists often use theoretical (Eshelby, 1957, Walsh, 1965, Hudson, 1980, Kuster and Toksoz, 1974) and empirical models (Han, 1986, Greenberg and Castagna, 1992, Gardner, 1974). An alternative approach is to use the FE method to computationally solve equations of elasticity and conductivity in three-dimensional rock microstructure images. These image cubes contain phase-based properties at different voxels. We use a well-established implementation of this method (Garboczi, 1998, 2003) to compute properties primarily for computationally cemented microstructures. In Section 2.5, we present an overview of the implementation and discuss possible sources of error.

We use LBM simulation (Keehm, 2003) for simulating single- and two-phase fluid flow. For a complicated binary microstructure containing grain and pore space, LBM computes the fluid flux through local interaction rules. The fluid flux from single-phase flow simulation is used to compute permeability. The flux is also used to implement a low-flux-based computational diagenesis scheme (Chapter 5). Using two-phase flow simulations, we replicate unsteady state flow experiments of water imbibition in oil-saturated microstructures. The resulting microstructure with different saturations and fluid distributions will be used to compute elastic properties.

2.3 Granular Dynamics simulation

In the following sections, we first discuss the basic micromechanical principles and implementation details of GD simulation. We then discuss macroscopic property (stress and elastic moduli) estimations based on microscopic contact forces.

2.3.1 Theory and implementation

The GD simulation scheme is an adaptation of the classical molecular-dynamics technique (Schafer et al., 1996). This method is based on integrating Newton's equations of motion (for translational and rotational degrees of freedom) for a system of "soft" grains starting from a given initial configuration. This requires an explicit expression for the forces that act between grains in contact with each other. In principle, contact micromechanics should provide such expressions, but the problem of two touching bodies under general conditions is very complicated.

We discuss different force schemes to give an overview of the methodologies in use and to substantiate our use of a particular force law. The *normal* impacts are discussed first to introduce the *normal* force vector, $\boldsymbol{F}^n$, and then the *shear* force vector, $\boldsymbol{F}^s$, is introduced through discussions on *oblique* impacts. The contact forces described herein refer to spherical grains principally. Some of the contact forces can be generalized for non-spherical cases. However, all results in this thesis are for granular packs of spherical grains, and hence, we focus on them primarily.

The contact force vectors are calculated separately for each grain pair in a pack. The total force vector, $\boldsymbol{F}_{ij}^{tot}$, and moment vector, $\boldsymbol{M}_{ij}^{tot}$, for contact between grain *i* and grain *j* are estimated as follows:

$$\boldsymbol{F}_{ij}^{tot} = \boldsymbol{F}_{ij}^{n} + \boldsymbol{F}_{ij}^{s}$$

$$\boldsymbol{M}_{ij}^{tot} = \boldsymbol{l}_{ij} \times \boldsymbol{F}_{ij}^{s} \tag{2.1}$$

where $\boldsymbol{l}_{ij}$ is the vector joining the i^{th} grain center to the *contact center* (between grains *i* and *j*), and × is the cross-product. The contact center is defined as grain-to-grain

contact point. The net force and the net moment on a grain are found by the vector summation of the contact forces and moments due to all its contacts. These net force and moment vectors further describe the translational and rotational motions, which are obtained by numerical integration. We use a centered finite-difference algorithm (Section 2.3.1.3) to integrate equations of motion, as implemented in the original version of DEM by Cundall and Strack (1979).

Like all molecular-dynamics simulations, GD simulation requires the implementation of a suitable boundary condition for property estimation and analysis. One of the usual ways to define simulation box boundaries is to consider rigid or fixed boundaries. Although easy to implement, this approach restricts motions of particles near the boundary and can have boundary artifacts like localization. An efficient way to reduce boundary effects in computational simulations is to use periodic boundary conditions (PBC). We discuss the implementation details of PBC in Section 2.3.1.4.

Another important aspect of estimating forces and solving motions in GD simulation is an efficient algorithm for finding neighboring grain pairs (contact detection). As the model size or number of grains in a granular pack increases, this operation becomes both memory and processor intensive. We discuss our contact detection algorithm in Section 2.3.1.5.

2.3.1.1 Normal Impacts

In most cases, two colliding spheres undergo a deformation which is somewhere between the extremes of inelastic and elastic deformation. The loss of energy is possibly through plastic deformation, viscoelasticity or emission of elastic waves due to the impact (Schafer et al., 1996). The elasticity of the impact is described by the coefficient of normal restitution e_n, defined as,

$$e_n = -{v_F^n}\Big/{v_I^n} \;\in\; [0,1] \tag{2.2}$$

where v_I^n and v_F^n are the pre-collisional and post-collisional velocities, respectively, in the normal direction. Modeling a force that leads to inelastic collisions requires at least two terms: a repulsion term and a dissipation term. The simplest example is a damped harmonic oscillator, where the normal force can be derived as follows:

$$\boldsymbol{F}^n = -k_n \xi \hat{\boldsymbol{n}} - \gamma_n \dot{\xi} \hat{\boldsymbol{n}} \tag{2.3}$$

where ξ is the elastic deformation of the spring (grain in this case), $\dot{\xi}$ is the deformation rate of the spring, k_n is related to the stiffness of a spring, γ_n is a damping constant and $\hat{\boldsymbol{n}}$ is the unit normal vector (grain center-to-center unit vector, or contact normal). For simplicity, we have dropped the subscript *ij* from Eqn. 2.1. The first part of Eqn. 2.3 is the elastic contact force and the second is a damping term. For a spherical grain pack, elastic deformation, ξ, can be parameterized as the *virtual overlap* of the two interacting grains *i* and *j* (with radii R_i and R_j) and is expressed as

$$\xi = max\left(0, R_i + R_j - \left|\boldsymbol{r_i} - \boldsymbol{r_j}\right|\right) \tag{2.4}$$

where $\boldsymbol{r_i}$ and $\boldsymbol{r_j}$ are the position vectors of the two grain centers, and hence, $\left|\boldsymbol{r_i} - \boldsymbol{r_j}\right|$ is the distance between them. It should be noted that this overlap is along the *branch vector*, which is the vector joining the grain centers (or numerically, $\boldsymbol{r_i} - \boldsymbol{r_j}$). Further, the overlap is *normal* to a tangent plane through the contact center and hence, is often referred to as the *normal overlap*. The contact center for this infinitesimal contact is a point on the branch vector which is equidistant from the sphere centers. This force model is commonly referred to as a linear spring-dashpot model.

Hertz theory (Hertz, 1882) predicts a more refined force law for elastic interactions between two elastic spheres. The repulsive force (shown as negative sign) for two spheres in contact in terms of normal overlap ξ is

$$\boldsymbol{F^n} = -k_n \xi^{3/2} \, \hat{\boldsymbol{n}} \tag{2.5}$$

where k_n is a non-linear stiffness (usually termed contact normal stiffness) connected to the material properties of spheres through

$$k_n = \frac{4}{3} E_{eff} \sqrt{R_{eff}} \tag{2.6}$$

where R_{eff} is the effective radius, defined as: $R_i R_j / \left(R_i + R_j\right)$. E_{eff}, the effective Young's modulus, is defined for two grains as

$$1/E_{eff} = (1 - \nu_i^2)/E_i + \left(1 - \nu_j^2\right)/E_j \tag{2.7}$$

where E and ν are Young's modulus and Poisson's ratio for the grain materials. For a monomineralic pack, contact normal stiffness can be calculated from the grain shear modulus, μ_g, and Poisson's ratio, ν_g, as:

$$k_n = \frac{4}{3} \frac{\mu_g}{\left(1 - \nu_g\right)} \sqrt{R_{eff}} \tag{2.8}$$

In order to obtain a dissipative Hertz-type force, a viscous damping term was added to the Hertz force in an *ad hoc* fashion in GD simulations (Ristow, 1994, Pöschel, 1993, Lee, 1994):

$$\boldsymbol{F^n} = -k_n \xi^{3/2}\, \hat{\boldsymbol{n}} + \gamma_n \dot{\xi}\, \hat{\boldsymbol{n}} \tag{2.9}$$

This force has been found to give collisions that become more elastic as the impact velocity increases, contrary to experimental evidence. For low impact velocities, where the Hertz results for elastic contacts should be regained, Eqn. 2.9 produces a coefficient of restitution which approaches zero.

Kuwabara and Kono (1987) and Brilliantov et al. (1996) extended the original Hertz theory by assuming viscoelastic material and derived the following normal force equation:

$$\boldsymbol{F^n} = k_n \xi^{3/2}\, \hat{\boldsymbol{n}} - \gamma_n \left(\xi^{3/2} \dot{\xi}\right) \hat{\boldsymbol{n}}$$

(2.10)

where k_n is identical to the contact normal stiffness in Hertz theory and the damping coefficient, γ_n, is connected to the radii of the spheres and the two coefficients of bulk viscosity. This force leads to a coefficient of normal restitution that decreases with increasing initial velocity, in agreement with experimental results. The damping terms in Equations 2.9 and 2.10 are local damping terms introduced for each contact.

In this thesis, we simulate granular packs with glass and quartz material properties to compare macroscopic properties from laboratory experiments and GD simulations. Glass and quartz are primarily elastic in nature and our GD simulations do not involve very high impact velocities throughout the duration of the simulation. Hence, we choose the Hertzian force equation (Eqn. 2.5) to model grain-to-grain normal interaction. The direction of application of this *normal* repulsive force is along the branch vector. It should be noted that damping of grain motions is necessary to prevent continuous oscillation of an elastic system (Makse et al., 2004). The granular packs, as described in Chapter 3 and 4, obtain *jammed* states with nearly perfect static equilibrium. We introduce a very small viscous *global* damping to suppress very small scale oscillations, instead of *local* damping (Eqns. 2.9 and 2.10).

2.3.1.2 Oblique or tangential Impacts

The tangential or shear force vector, $\boldsymbol{F^s}$, is connected to the normal force vector, $\boldsymbol{F^n}$, by Coulomb's laws of friction, namely,

$$\boldsymbol{F^s} \leq \mu_s \boldsymbol{F^n} \quad for\ static\ friction\ (\boldsymbol{v^s} = 0)$$

$$\boldsymbol{F^s} = \mu_d \boldsymbol{F^n} \quad for\ dynamic\ friction\ (\boldsymbol{v^s} \neq 0)$$

(2.11)

where μ_s and μ_d are the coefficients of static and dynamic friction, respectively, and $\boldsymbol{v^s}$ is the shear component of the relative velocity. The shear or tangential velocity is calculated from total relative velocity, $\boldsymbol{v^{tot}}$, as:

$$\boldsymbol{v}^s = \boldsymbol{v}^{tot} - \hat{\boldsymbol{n}}(\hat{\boldsymbol{n}} \cdot \boldsymbol{v}^{\boldsymbol{tot}}); where$$

$$\boldsymbol{v}^{tot} = \boldsymbol{v}_i - \boldsymbol{v}_j + (R_i\hat{\boldsymbol{n}} \times \boldsymbol{w}_i) + (R_j\hat{\boldsymbol{n}} \times \boldsymbol{w}_j)$$

(2.12)

where $\boldsymbol{v}$ and $\boldsymbol{w}$ refer to the linear and angular velocity vectors of grains *i* and *j*. The simplest shear force law just applies the Coulomb law of dynamic friction, thus giving

$$\boldsymbol{F}^s = -\mu|\boldsymbol{F}^n|sgn(\boldsymbol{v}^s)$$

(2.13)

This force can only slow down the tangential velocity to zero, but cannot explain the reversal of tangential velocity. A model based on tangential elasticity was first proposed by Cundall and Strack (1979) which gives the shear force vector in the tangential direction as:

$$\boldsymbol{F}^s = -min\left(\left|k_s\xi^{1/2}\boldsymbol{\zeta}\right|, |\mu\boldsymbol{F}^n|\right) \cdot \hat{\boldsymbol{t}}$$

(2.14)

where k_s is contact shear stiffness, μ is the coefficient of friction between two grains, $\boldsymbol{\zeta}$ is the tangential displacement vector, and $\hat{\boldsymbol{t}}$ is the unit vector in tangential direction (i.e., $\boldsymbol{\zeta}/|\boldsymbol{\zeta}|$). For the sake of simplicity, both static and dynamic coefficients of friction are assumed to be equal. The first part of the expression, $\left|k_s\xi^{1/2}\boldsymbol{\zeta}\right|$, is the Mindlin (1949) no-slip tangential force between two elastic grains and depends on both normal overlap ξ and tangential displacement vector $\boldsymbol{\zeta}$. Contact shear stiffness, k_s, relates these *deformations* (in terms of overlap or displacement) to tangential or shear force. For a monomineralic pack, k_s is computed from the material shear modulus, μ_g and Poisson's ratio, ν_g as

$$k_s = \frac{8\mu_g}{(2-\nu_g)}\sqrt{R_{eff}}$$

(2.15)

In Eqn. 2.14, $\boldsymbol{\zeta}$ denotes the displacement vector in the tangential direction that took place since the time t_0, when the contact was first established, i.e.,

$$\boldsymbol{\zeta}(t) = \int_{t_0}^{t} \boldsymbol{v}^s(t)dt \tag{2.16}$$

Further, $\boldsymbol{\zeta}$ is defined such that the relative shear displacement between the two grain centers is $2\boldsymbol{\zeta}$. The second part of Eqn. 2.14 sets the maximum limit for tangential force through Coulomb's law of friction. The incremental form of shear displacement and a threshold for frictional sliding separately add two sources of path dependency and hysteresis in the contact force model. In this thesis, we used this model for estimating shear forces.

The implementation of Eqn. 2.14 also requires rotation of tangential force at every time step, dt. For existing contacts, the contact normal, and hence the contact plane, is likely to rotate with grain motion (Fig. 2.1). The incremental rotation of contact plane is estimated to adjust the tangential contact force as follows:

$$\boldsymbol{F}^s_{old} \leftarrow \boldsymbol{F}^s_{old} + (\hat{\boldsymbol{n}}_{old} \times \hat{\boldsymbol{n}}_{new} \times \boldsymbol{F}^s_{old}) \tag{2.16}$$

where $\hat{\boldsymbol{n}}_{old}$ and $\hat{\boldsymbol{n}}_{new}$ are the old and new unit normal vectors respectively.

Schafer et al. (1996) gives a detailed description of the applicability of these contact laws for specific situations. As mentioned earlier, we use Eqn. 2.5 and 2.14 in our GD simulations. Ng (2006) provides good insight into the sensitivity of the simulation to the input parameters.

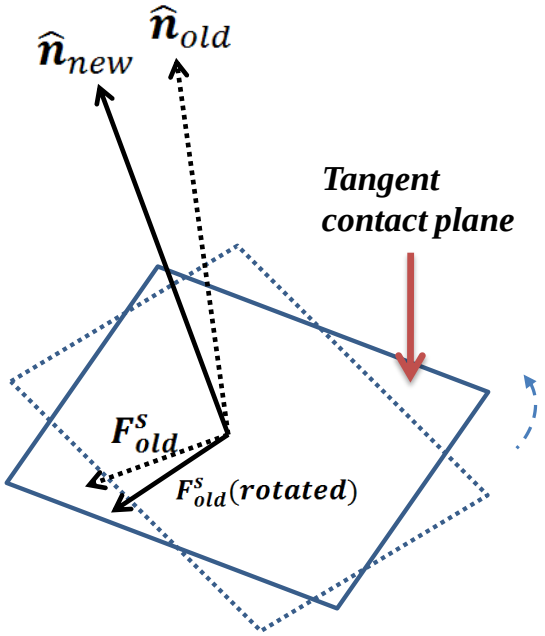

Figure 2.1: Rotation of shear force due to incremental rotation of contact normal.

2.3.1.3 Integration scheme and Time step

We calculate the total contact normal and shear forces due to all neighboring grains for each grain. Based on the total contact force, Newton's equations of translational and rotational motion are solved using a suitable integration scheme. Allen and Tildesley (1987) and Pöschel and Schwager (2005) give a brief overview of different integration schemes in use. Desirable qualities for a successful integration algorithm are (Allen and Tildesley, 1987)

1. It should be fast and should require little memory;
2. It should permit the use of a long time step dt;
3. It should duplicate the classical trajectory as closely as possible;
4. It should satisfy the known conservation laws for energy and momentum;
5. It should be simple in form and easy to program.

We choose the same centered finite-difference procedure used by Cundall and Strack (1979) while proposing the discrete element method. The basic equations of motion for any grain, say the i^{th}, in a zero-gravity system are as follows:

$$\boldsymbol{F}_i^{tot} = \sum_{contacts:\, j} \boldsymbol{F}_{ij}^{tot} = m_i \ddot{\boldsymbol{r}}_\iota + m_i \alpha \dot{\boldsymbol{r}}_\iota$$

$$\boldsymbol{M}_i^{tot} = \sum_{contacts:\, j} \boldsymbol{M}_{ij}^{tot} = mI_i \ddot{\boldsymbol{\theta}}_\iota + mI_i \alpha \dot{\boldsymbol{\theta}}_\iota$$

(2.17)

where $\boldsymbol{F}_i^{tot}$ and $\boldsymbol{M}_i^{tot}$ are the total force and moment vectors of the i^{th} grain with mass m_i and moment of inertia mI_i; $\dot{\boldsymbol{r}}_\iota$and $\dot{\boldsymbol{\theta}}_\iota$ are first derivatives, and $\ddot{\boldsymbol{r}}_\iota$ and $\ddot{\boldsymbol{\theta}}_\iota$ are second derivatives of the linear and angular position vectors, $\boldsymbol{r}$ and $\boldsymbol{\theta}$, with respect to time; and α is the *global* viscous damping, as discussed earlier. The following expressions describe the translational and rotational velocity vectors at time t in terms of values at mid-intervals, $dt/2$:

$$\dot{\boldsymbol{r}}_i^{(t)} = \frac{1}{2}\left[\dot{\boldsymbol{r}}_i^{\left(t-\frac{dt}{2}\right)} - \dot{\boldsymbol{r}}_i^{\left(t+\frac{dt}{2}\right)}\right]$$

$$\dot{\boldsymbol{\theta}}_i^{(t)} = \frac{1}{2}\left[\dot{\boldsymbol{\theta}}_i^{\left(t-\frac{dt}{2}\right)} - \dot{\boldsymbol{\theta}}_i^{\left(t+\frac{dt}{2}\right)}\right]$$

(2.18)

where superscripts refer to the values at respective time-steps and are not exponents. The linear and rotational acceleration vectors at time *t* are estimated as follows:

$$\ddot{\boldsymbol{r}}_i^{(t)} = \frac{1}{dt}\left[\dot{\boldsymbol{r}}_i^{\left(t-\frac{dt}{2}\right)} - \dot{\boldsymbol{r}}_i^{\left(t+\frac{dt}{2}\right)}\right]$$

$$\ddot{\boldsymbol{\theta}}_i^{(t)} = \frac{1}{dt}\left[\dot{\boldsymbol{\theta}}_i^{\left(t-\frac{dt}{2}\right)} - \dot{\boldsymbol{\theta}}_i^{\left(t+\frac{dt}{2}\right)}\right]$$

(2.19)

Using Eqn. 2.19 in Eqn. 2.17, the updates for linear and rotational velocities are obtained in terms of total force and moment vectors at time *t*:

$$\dot{\boldsymbol{r}}_i^{\left(t+\frac{dt}{2}\right)} = \left[A\dot{\boldsymbol{r}}_i^{\left(t-\frac{dt}{2}\right)} + \boldsymbol{F}_i^{tot(t)}\Big/ m_i\right]B$$

$$\dot{\boldsymbol{\theta}}_i^{\left(t+\frac{dt}{2}\right)} = \left[A\dot{\boldsymbol{\theta}}_i^{\left(t-\frac{dt}{2}\right)} + \boldsymbol{M}_i^{tot(t)}\Big/ mI_i\right]B$$

$$where:\ A = 1 - \alpha\frac{dt}{2}; B = 1/(1 + \alpha\frac{dt}{2})$$

(2.20)

Finally, the increments to linear and angular position vectors are computed using the velocity vectors:

$$\Delta\boldsymbol{r}_i = \dot{\boldsymbol{r}}_i^{\left(t+\frac{dt}{2}\right)}dt$$

$$\Delta\boldsymbol{\theta}_i = \dot{\boldsymbol{\theta}}_i^{\left(t+\frac{dt}{2}\right)}dt$$

(2.21)

These increments are used to update the linear and angular positions at each time-step dt. The choice of a suitable time-step is also important to reduce computational cost and enhance integration accuracy. In our simulations, a critical time-step is chosen as a fraction of the time taken for a sound wave or disturbance to propagate in the smallest grain. Further, the quasistatic approximation used to calculate the Hertz force is valid only when the relative velocities of the grains are smaller than the speed of sound in the grains (Makse et al., 2004, Brilliantov et al., 1996). Hence the critical time-step, t^{crit}, is defined as

$$t^{crit} = R_{smallest}\sqrt{\rho_g/\mu_g}$$

(2.22)

where $R_{smallest}$ is the radius of the smallest grain and ρ_g is the density of the grain. The actual time-step, dt, considered in the simulation is a fraction of the critical time-step. For our simulations, we usually choose 0.005 as the fraction.

2.3.1.4 Periodic Boundary Conditions

Specifying boundary conditions is important for computer simulations involving particles, atoms or grains. There are two important aspects of this problem: model size and boundary artifacts. It is important to have a sizeable number of grains within a simulation box in order to represent a realistic material volume. However, the size of the simulation also depends on the availability of memory. Simulations consisting of large numbers of grains can become very intensive in terms of memory and CPU time. Brute force contact detection (as discussed in the next section) involves a time requirement of $\mathcal{O}(N^2)$ where N is the number of particles. Improved techniques can reduce this to $\mathcal{O}(N)$; however, for large systems, this is still a bottle-neck. Hence, it is relatively inexpensive to have a smaller number of particles. However, a model with small or insufficient number of grains is not statistically representative of the material volume, and hence does not allow us to infer effective material properties. Especially with rigid wall boundary conditions, several grains which are in contact with the boundaries behave differently than the inner volume of grains, generating boundary artifacts. For GD simulation, it is impractical to have free boundary conditions, or 'no-boundary' conditions as used in atomistic simulations, due to the repulsive nature of forces. The main goal is to reduce boundary artifacts as much as possible, without increasing the number of grains significantly (Bulatov and Cai, 2006). An efficient way to tackle both these issues is to use Periodic Boundary Conditions (PBC).

By applying PBC, the surface effects are overcome significantly (Born and von Karman, 1912). The general idea of PBC is to replicate the simulation box throughout the space to form an infinite lattice. PBC also maintains the translational invariance of the simulation volume (Bulatov and Cai, 2006) by allowing particles to move freely in the whole space. The implementation is such that there are an infinite number of images of the central simulation box in space. Hence, as any grain moves in the

simulation box, its image also moves in all the neighboring *image* boxes (Fig. 2.2). Moreover, when any particle leaves the central box, one of its images will enter from a neighboring image box. Hence, all grains translate in the same way throughout the space, thereby resulting in translational invariance. PBC can be implemented in one, two or three directions, depending on the requirement of the problem. For GD (and EDMD) simulations in this thesis, we use PBC in all three directions.

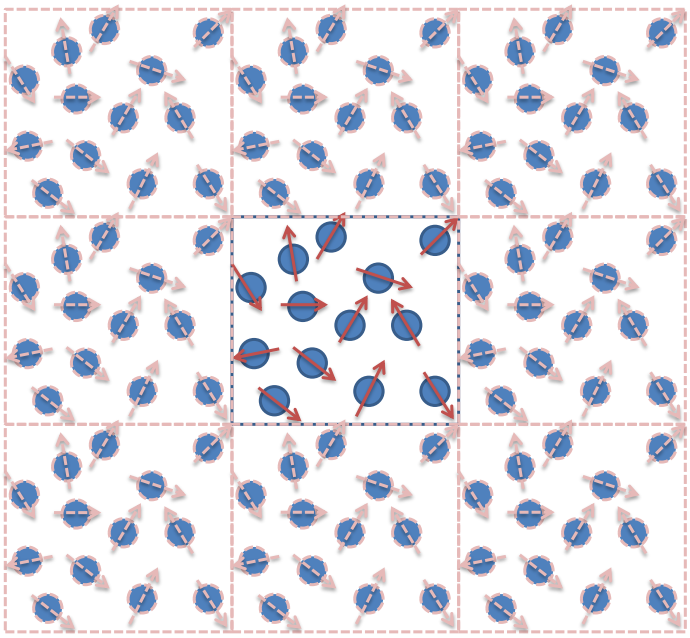

Figure 2.2: Representation of Periodic Boundary Condition in a 2D case. The central cell represents the simulation box. All the neighboring cells have exactly the same images of particles as the central cell. If any particle leaves the central cell, its corresponding image enters through the opposite end.

PBC is implemented by using a *nearest image convention*, which states that the relative distance between any two grains is taken as the shortest of all vectors that connect them. This is easily and efficiently implemented by using *scaled coordinates*. For a grain at position $\boldsymbol{r} = (r_1, r_2, r_3)$ in three dimensions, the scaled coordinates, $\boldsymbol{s} = (s_1, s_2, s_3)$ are defined as:

$$\boldsymbol{s} = \boldsymbol{H}^{-1} \cdot \boldsymbol{r} \tag{2.23}$$

where $\boldsymbol{H}$ is a 3x3 matrix whose column vectors are the repeat vectors of the central simulation box (Bulatov and Cai, 2006). In scaled coordinates, the distance between two grains, *i* and *j*, are calculated as follows:

$$\Delta s_1 = f\left(s_1^i - s_1^j\right)$$

$$\Delta s_2 = f\left(s_2^i - s_2^j\right)$$

$$\Delta s_3 = f\left(s_3^i - s_3^j\right)$$

$$f(S) = S - [S]$$

(2.24)

where [S] returns the nearest integer to S. The main advantage of using scaled coordinates is that the values of *f(S)* always stay within [-0.5,0.5), thereby ensuring that all nearest distances refer to images within the unit cube. Moreover, the operations are vector-based and hence efficient from a computational perspective. The distance vector can be converted to real space for contact detection by using

$$d\boldsymbol{r} = \boldsymbol{H} \cdot \Delta \boldsymbol{s}$$

(2.25)

PBC can hence be used to model virtually an infinite medium but using a small number of grains. However, the use of PBC inhibits the occurrence of long-wavelength fluctuations which are larger than the simulation box (Allen and Tildesley, 1987).

The implementation of PBC also requires three changes in grain and box configurations:

1. The simulation box lengths, hence *H* matrix, are updated after each increment of strain as :

$$L_i \leftarrow L_i + \dot{\varepsilon}_{ij} L_j dt$$

(2.26)

where L_i is the box length in i direction, $\dot{\varepsilon}_{ij}$ is the strain rate and dt is the simulation time-step.

2. For every grain, a displacement increment due to strain rate of the periodic space is added to the velocity increment:

$$\Delta r_i = \dot{r}_i^{\left(t+\frac{dt}{2}\right)} dt + \dot{\varepsilon}_{ij} r_j dt \tag{2.27}$$

where i indicates displacement direction (not grain index).

3. The relative velocity between two neighboring grains is also updated by the component of periodic space increment as follows:

$$v_i^{TOTAL} = v_i^{tot} + \dot{\varepsilon}_{ij} z_j \tag{2.28}$$

where z_j is the vector connecting the centers of two grains (branch vector).

2.3.1.5 Contact Detection algorithm

The force calculation in GD simulation is based on virtual overlap or deformation between two neighboring grains in contact with each other. A system with N grains hence requires about N^2 operations to detect contacts by comparing distances between grain-pairs. This is usually a brute force method of finding contacts, and can be computationally expensive for a simulation with many grains. An improved implementation of contact detection uses cell structures (Allen and Tildesley, 1987). Munjiza (2004) describes several other contact detection algorithms generally used in the discrete element method literature. We implement a cell-structure-based method (Allen and Tildesley, 1987) to increase contact detection efficiency.

This algorithm divides the simulation box into several smaller cells, usually cubes. The dimensions of these cells are chosen such that they can contain the largest grain size. Each grain is mapped to individual cells. Thereafter, cell-lists are prepared for each cell containing the count and information of grains within that cell. The contact

detection algorithm runs by looping over each cell. For any cell, a larger list is prepared by collecting the cell-lists from neighboring cells. By measuring distances in *scaled coordinates* between all grain-pairs in this larger list, we use the overlap rule (Eqn. 2.4) for detecting contacts. In three dimensions, a central cell has 26 neighboring cells around itself. However, we define a *contact mask*, as shown in Figure 2.3, which consists of only 13 neighboring cells to take advantage of spatial symmetry. Since the detection loop runs over all cells, this contact mask can detect all potential contact-pairs. The contacts are stored in a contact-list. For any particular grain in the central cell, we append its contact-list when a contact is detected from the contact mask. We optimize this operation of appending cell-lists simultaneously for both grains in contact. Unlike the brute force detection method, this algorithm requires $13NN_{cell}$ operations, where N_{cell} is the number of cells in a simulation box. The contact lists can be efficiently implemented by using either linked lists or pre-defined arrays.

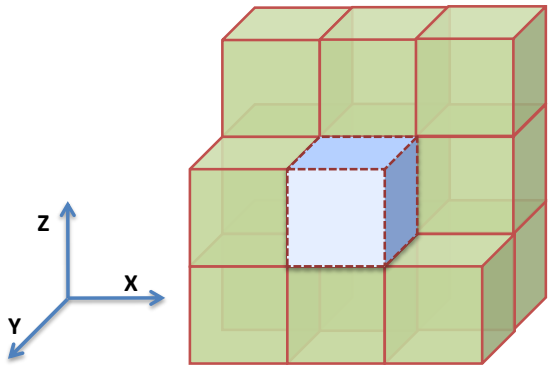

Figure 2.3: Contact mask used for contact detection algorithm. Central cell is colored blue, and neighboring cells are colored green.

2.3.2. Stress and Elastic property estimation

In the preceding sections, we discussed the theoretical background of micromechanical laws and implementation details of different aspects of GD simulation. The microscopic details of a granular pack can be obtained based on these discussions. The main focus, however, is to relate them to macroscopic quantities like effective stress and, most importantly, effective elastic moduli.

Different averaging techniques have been used to obtain the macroscopic average stress tensor based on microscopic forces for a given pack. Based on intensive work in this field (Rothenburg and Selvadurai, 1981a, 1981b, Christoffersen et al., 1981, Weber, 1966, Dantu, 1968), it is now fairly standard to compute average stresses in a granular system. Walton (1987), Digby (1981), Cambou et al. (1995) and Liao et al. (1997), among others, also implemented strategies to calculate effective elastic moduli for granular packs. In the following sections, we describe standard approaches to quantify average stress in a pack and our methodology to calculate elastic moduli.

2.3.2.1 Average stress tensor

An average stress tensor for a granular pack can be defined based on *static equilibrium* of an assembly of randomly shaped particles subjected to a uniform set of boundary tractions $\boldsymbol{T}$ on its surface (Ouadfel, 1998). These tractions are derivable from a continuous boundary stress tensor, σ_{ij}. Based on force equilibration due to static equilibrium, the stresses on the surface must equalize the internal stresses through the following summations:

$$\sum_{\beta \in S} f_i^{\beta} X_j^{\beta} = \sum_{c \in V} f_i^c l_j^c \tag{2.29}$$

where the vector $\boldsymbol{X}^{\beta}$ refers to all locations β on the surface S of pack volume V with forces $\boldsymbol{f}^{\beta}$. Vectors $\boldsymbol{l}^c$ are contact branch vectors (as defined earlier) with contact forces $\boldsymbol{f}^c$ for all contacts c in volume V. The left-hand side represents the average stress tensor, σ_{ij}, as proposed by Rothenburg (1980), based on continuum mechanics. Hence, the average stress tensor, often referred as internal stress tensor, is

$$\sigma_{ij} = \frac{1}{V} \sum_{c \in V} f_i^c l_j^c \tag{2.30}$$

where the summation is carried out over all contacts in a pack volume V. This can also be derived using the principle of virtual work on a grain pack (Kuhl et al., 2000,

Christoffersen et al., 1981), where the sum of all microscopic work (derived through contact forces and displacements) equals the macroscopic work (derived from average stress and strain) due a perturbation on the pack. Kuhl et al. (2000) further proposes to consider the mean of the symmetric and antisymmetric internal stress tensor as the average stress tensor. For numerically computing this term, we follow the approach of Walton (1987) to compute average stress tensor by summing stress contributions from each individual contact for a grain, followed by summing over all grains:

$$\sigma_{ij} = \frac{1}{2V} \sum_{N \in V} \sum_{n} (f_i^n l_j^n + f_j^n l_i^n) \tag{2.31}$$

where summation is taken over all contacts *n* of all grains *N* in volume *V*. It should be noted that *n* typically varies for each grain in a random pack. The sum of stress contributions from each contact for a grain can be volume averaged to obtain the stress tensor for the individual grain. In Chapters 3 and 4, we report the mean of the diagonal elements of this stress tensor for each grain as mean stress per grain.

2.3.2.2 Elastic property estimation

As described later in Chapter 3, we create compacted granular packs using GD simulation. These *jammed* packs are at static equilibrium and hence are characterized by a non-fluctuating average stress tensor over simulation time-steps. Because the average stress tensor depends on contact forces and grain locations, an unstable pack will have a fluctuating average stress tensor.

For calculating elastic moduli, we apply infinitesimal perturbations, $\delta\varepsilon_{ij}$, on the grain pack boundaries. As discussed in PBC implementation, these boundary strains are uniformly distributed on all grains as an initial guess. The exact form of the strain tensor $\delta\varepsilon_{ij}$ depends on the elastic moduli of interest. This perturbation disturbs the static equilibrium of the jammed packs, and the pack is then allowed to gain equilibrium based on Newton's laws. The elastic modulus is estimated as the ratio of

stress perturbation (relative to the static equilibrium state) and applied strain perturbation. We discuss the exact expressions for the stress-strain ratio for different moduli in Chapter 4.

2.4 Event Driven Molecular-Dynamics simulation

Pöschel and Schwager (2005) describe the need for event-driven molecular-dynamics simulation, as opposed to force-driven molecular-dynamics (or, GD) simulation for two types of systems:

1. Systems where particle collision times are infinitesimal compared to non-collision propagation times.
2. Systems where it is difficult to define force interactions based on particle positions.

Granular pack assembly processes satisfy both these criteria for different scenarios. For volume fractions lower than random close packs, the interacting grains can be described as being in a suspension state, with very small collision times. Further, grain packs with irregular shapes have interaction forces which are difficult to define.

For GD simulation, "soft" grains are considered, where interaction forces can be estimated from grain deformations, and subsequently stresses can be easily calculated. For EDMD, "hard" grain interactions are singular, and the task of integrating the equations of motion becomes a problem of processing a sequence of binary grain collisions (Donev et al., 2005). Between these collisions, grains propagate with constant velocities. However, the disadvantage of EDMD for our purposes is the absence of direct interpretation of the physical stress tensor.

The main assumption for applying EDMD is that at any instant, there occurs at most one collision of infinitesimal duration (Pöschel and Schwager, 2005). Further, EDMD schedules a series of *events* or grain collisions that are predicted to happen in the future, based on present grain trajectories. The simulation is then advanced to the next event, unlike GD simulation, where the time is processed continuously, both

during collisions and between. Hence, EDMD is efficient in terms of reducing non-collision propagation time. This increase in simulation speed is one of the main motivations for using event-driven algorithms instead of force-driven algorithms. For our purposes, the preparation of jammed packs for polydisperse systems using GD simulation is too time-consuming. Hence, we use EDMD to create polydisperse jammed packs with frictionless grains.

We use Donev's (2005) implementation of EDMD for frictionless sphere packs to create bi-disperse and polydisperse packs with Gaussian size distributions. This implementation can handle non-spherical shapes as well. However, in this thesis, we concentrate only on spheres. The algorithm is based on sphere-packing algorithms by Lubachevsky and Stillinger (1990). As an initial configuration, a random set of points are initialized as grain centers. For bi-disperse packs, the present implementation initializes these points. We input the random starting points for polydisperse packs with pre-defined size distributions. These initial spheres are non-touching and can be assigned with initial velocities. The growth rates of these spheres can be pre-defined or based on radius ratios.

As these spheres grow, collisions (events) are modeled based on interaction potentials. Pöschel and Schwager (2005) describe the post-collisional velocities of similar packs based on coefficients of restitution. EDMD collisions obey the conservation laws of linear and angular velocities. These events are binary collisions, and the main goal of EDMD is to correctly predict a time-ordered list of these collisions. The onset of jamming is defined as static equilibrium of grains, where grains can no longer grow without interpenetrating neighboring grains. Donev (2005) describes a jammed pack as one where the grains are locked in their positions despite thermal agitation (shaking) and boundary deformations (external loading). As described earlier, these jammed packs are taken as inputs to GD simulation (for non-monodisperse packs only) and compacted to different pressures. The implementation detail of this code is well documented and can be obtained in much more detail from Donev (2005) and Donev et al. (2005a, 2005b).

2.5 Finite Element method: Elastic and Electrical property estimator

We use an implementation of the finite-element method (Garboczi, 1998a, Garboczi, 2003) to estimate elastic and electrical properties of cemented grain packs. This implementation is a well-established method of numerically computing elastic and electrical properties in two-dimensional and three-dimensional images (Arns et al., 2002, Roberts and Garboczi, 2002a, 2002b, Garboczi and Berryman, 2001, Meille and Garboczi, 2001, Garboczi, 1998b, Keehm, 2003, Garboczi et al., 1995).

In the present work, we use this implementation in three-dimensional microstructures representing granular and cemented packs. The numerical computations consider each voxel as a tri-linear element, so that the entire digital lattice can be treated as a finite element mesh (Garboczi and Berryman, 2001). Further, periodic boundary conditions are assumed for the microstructures. The elastic displacements are linearly extrapolated across all voxels, and a variational formulation of the linear elastic equations is imposed. The implementation then finds the solution by minimizing the elastic energy using a fast conjugate-gradient method (Arns et al., 2002). The effective moduli are usually defined by a stress average, although they can also be defined by an energy average (Garboczi, 1998a). For electrical properties, a variational formulation of the linear electrical conductivity equations is imposed. The final voltage distribution is such that the total energy dissipated is maximized and the gradient of energy with respect to voltage is zero.

Garboczi and Berryman (2001) and Roberts and Garboczi (2000) discuss the main sources of error in these computations: (a) finite-size effect; (b) digital resolution; and (c) statistical variation. Arns et al. (2001) conduct several computational experiments on scanned sandstone images to find acceptable model sizes that match elastic properties and transport property parameters. Similar experiments have also been conducted by Keehm (2003), Richa (2010) and Krzikalla (personal communication).

The finite-size effect is due to the fact that even with PBC, the sample sizes can be small compared to a random solid and its scale of heterogeneity. Smaller sample sizes can be faster for computation, but may not be able to represent heterogeneities

properly and hence may fail to be statistically representative. This error can be properly characterized by selecting several different model sizes and assessing the property variations. Richa (2010) conducted such numerical experiments for electrical properties of sandstone and sand (with epoxy) images.

The digital resolution error can be significant, especially for elastic properties. The elastic stiffness in microstructures depends on softer elements like cracks (for cemented microstructures) or contacts (for granular packs). Sufficient image resolutions are required to resolve these softer elements. With a coarser voxel size (lower resolution), the cracks or contacts are often poorly resolved. This results in an overestimation of elastic stiffness. In Chapter 4, we estimate elastic moduli for compacted granular packs at different resolutions. We find that FE estimations of elastic moduli are significantly higher than those of GD estimations, due to the effect of coarse contact voxels. In granular packs, the effective electrical conductivity estimates are not affected significantly when the conducting phase is mainly the pore-filling phase. The conductivity process being mostly dependent on larger pore-spaces, the un-resolved smaller cracks or contacts do not impact effective conductivity considerably.

The source for statistical variation error is simply the randomness of the microstructures. For a finite size, there can be several random arrangements of pores and grains. Each arrangement can have different elastic and electrical properties. Hence, in a large microstructure, different statistically representative parts can have different properties based on microstructural arrangements.

2.6 Lattice-Boltzmann method

For last few decades, there have been several studies to estimate permeability from digital images of rocks. Permeability depends on pore geometry as well as pore size. The work in this field can be generally divided into two groups. In the first group, the computational estimation of permeability involves estimating different parameters, including surface area and grain size distribution, which in turn are used in semi-

empirical models like the Kozeny-Carman relation. These relations are empirical due to the scale factors that are used to fit the data. Walsh and Brace (1984) used a model of pore structure based on cylindrical tubes to derive a formula relating permeability to porosity, formation factor and specific surface area. Based on the work of Berryman relating specific surface area with spatial correlation functions of thin section images (Berryman, 1984), Blair et al. (1993) measured the statistical properties of porous material using image-analysis techniques and used them as inputs to Walsh and Brace's semi-empirical formula. Arns et al. (2002) compute several important microstructural parameters affecting flow, including surface to volume ratio and integral mean curvature from scanned three-dimensional sandstone images.

The second major approach for computing transport properties solves the Navier-Stokes equation for low-Reynolds-number fluid flow in the pore space using various numerical algorithms. Finite-difference, finite-elements, lattice-gas automata and Lattice-Boltzmann methods have been variously used to simulate pore-scale flow through porous media. Keehm (2003) describes these methods in detail. The LBM is a powerful technique for computational modeling of a variety of complex fluid flow problems, including single and mulit-phase flow in complex geometries (Martys et al., 1999). The main advantage of using LBM in computational rock physics is its usability for very complex pore-geometries of rocks (Cancelliere et al., 1990, Ladd, 1994, Martys and Chen, 1996, Keehm, 2003). This method does not idealize the pore-space and hence provides a rigorous estimate of flow properties. Further, LBM can give an accurate solution for flow properties equivalent to finite-element simulation with extensive meshing (Kandhai et al., 1998, 1999). This method is based on cellular automata theory and describes the fluid volume in a complex pore-geometry in terms of the interactions of a massive number of particles following simple local rules (Keehm, 2003, Doolen, 1990, Chopard and Droz, 1998). The rules in this method recover the Navier-Stokes equation at the macroscopic level (Rothman and Zaleski, 1997, Ladd, 1994). In this thesis, we use an implementation of LBM (Keehm, 2003) to simulate single-phase and two-phase fluid flow. We use this simulator for computing permeability from single-phase flow simulation and obtaining fluid-distributions

during an unsteady-state drainage experiment using two-phase flow simulation. The theoretical background and implementation detail of this simulator can be obtained in much more detail from Keehm (2003).

2.7 Acknowledgements

We thank Prof. Aleksander Donev, New York University, for sharing EDMD code. We thank Dr. Edward Garboczi, National Institute of Standards and Technology, for sharing FE code for elastic and electrical properties. We thank Prof. Younseuk Keehm, Kongju National University, for sharing LBM code.

2.8 References

Agarwal, P. K., 2006, Enzymes: An Integrated view of structure, dynamics and function, Microbial Cell Factories, 5:2

Agnolin, I. and Roux, J.-N., 2007, Internal states of model isotropic granular packings. I. Assembling process, geometry, and contact networks, Phys. Rev. E 76, 061302.

Agnolin, I., Roux, J.-N., Massaad, P., Jia, X. and Mills, P., 2005, Sound wave velocities in dry and lubricated granular packings: numerical simulations and experiments, Powders and Grains, Stuttgart, Allemagne.

Allen, M. P. and Tildesley, D. J., 1987, Computer Simulations of Liquids. Oxford Science Publications.

Arns, C. H., Knackstedt, M. A., Pinczewski, W. V. and Garboczi, E. J., 2002, Computation of linear elastic properties from microtomographic images: Methodology and agreement between theory and experiment, Geophys., 67, 5, P1395-1405.

Bardet, J.P. and Proubet, J., 1991, A numerical investigation of the structure of persistent shear bands in granular media. Geotechnique, 41(4):599–613.

Berryman, J.G. and Blair, S.C., 1986, Use of digital image analysis to estimate fluid permeability of porous materials- Application of two point correlation functions, Journal of Applied Physics, 60(6), 1930-1938.

Blair, S. C., Berge, P. A., and Berryman, J. G., 1993, Two-point Correlation Functions to Characterize Microgeometry and Estimate Permeabilities of Synthetic and Natural Sandstones, Lawrence Livermore National Laboratory Report, Livermore.

Born, M. and Von Karman, Th., 1912, Uber Schwingungen in Raumgittern, Physik Z, 13, 297-309.

Brilliantov, N. V., Spahn, F, Hertzsch, J-M and Pöschel, T, 1996, Model for collisions in granular gases, Physical Review, 53(5) , 5382-5392.

Bulatov, V. V. and Cai, W., 2006, Computer Simulations of Dislocations, Oxford University Press.

Bulatov, V., Abraham, F. F., Kubin, L., Devincre, B. and Yip, S., 1998, Connecting atomistic and mesoscale simulations of crystal plasticity, Nature, 391, 669.

Cambou, B., Dubujet, P., Emeriault, F. and Sidoroff, F., 1995, Homogenization for granular materials. Eur. J. Mech. A, Solids 14 2, 225–276.

Campbell, C.S. and Brennen, C.E., 1985, Computer simulation of granular shear flows. J. Fluid. Mech., 151:167.

Cancelliere, A., Chang, C., Foti, E., Rothman, D. H. and Succi, S., The permeability of a random medium: comparison of simulation with theory, *Phys. Fluids A*, **2**, 2085-2088.

Chopard, B. and Droz, M, 1998, Cellular Automata Modeling of Physical Systems, Cambridge Univeristy Press, Cambridge, 341pp.

Christoffersen, K., Mehrabad, M.M. and Nemat-Nasser, S., 1981, A micromechanical desicription of granular material behavior, J Appl Mech, ASME, 48, 339-344.

Cundall, P. A. and Strack, O. D. L., 1979, A discrete numerical model for granular assemblies: Geotechnique, 29(1):47–65.

Digby, P. J., 1981, The effective elastic moduli of porous granular rocks: Journal of Applied Mechanics, 48, 803–808.

Dobry, R. and Ng, T.T., 1989, Discrete modelling of stress-strain behaviour of granular media at small and large strains. In Proc. 1st U.S. Conf. on Discrete Element Meth., Nat. Sci. Found., Washington DC

Donev, A., Torquato, S. and Stillinger, F.H., 2005a, Neighbor list collision-driven molecular dynamics simulation for nonspherical hard particles. I. Algorithmic details, J Comp Phys, 202 2 737-764

Donev, A., Torquato, S. and Stillinger, F.H., 2005b, Neighbor list collision-driven molecular dynamics simulation for nonspherical hard particles. II. Applications to ellipses and ellipsoids, J Comp Phys, 202 2 765-793

Donev, A., 2006, Jammed packings of hard particles, Ph.D. thesis, Princeton University, NJ.

Doolen, G. D. (Editor), 1990, Lattice Gas Methods for Partial Differential Equations, Addison-Wesley, Redwood City, 554pp

Eshelby, J. D., 1957, The determination of the elastic field of an ellipsoidal inclusion, and related problems: Proceedings of the Royal Society of London, Series A: Mathematical and Physical Sciences, 241, no. 1226, 376–396, doi: 10.1098/rspa.1957.0133.

Favier, J. F., Abbaspour-Fard, M. H., Kremmer, M. and Raji, A. O., 1999, Shape representation of axi-symmetrical, non-spherical particles in discrete element simulation using mult-element model particles, Engineering Computations, 16, 4, 467-480.

Fraige, F. Y. and Langston, P.A., 2004, Integration schemes and damping algorithms in distinct element methods, Advanced Powder Technol., 15, 2, 227-245.

García, X. and Medina, E., 2006, Hysteresis effects studied by numerical simulations: cyclic loading-unloading of a realistic sand model, Geophys., 71 2, F13-F20.

Garboczi, E.J., Bentz, D.P. and Schwartz, L.M., 1995, Modelling the influence of the interfacial zone on the D.C. electrical conductivity of mortar, Advanced Cement-Based Materials **2**, 169-181

Garboczi, E. J., 1998a, Finite element and finite difference programs for computing the linear electric and linear elastic properties of digital images of random materials: National Institute of Standards and Technology Internal Report 6269.

Garboczi, E.J., 1998b, The use of computer simulations to interpret and understand electrical measurements, in *Electrically Based Microstructural Characterization II*, edited by R.A. Gerhardt, M.A. Alim, and S.R. Taylor (Materials Research Society, Pittsburgh, 1998), 291-302.

Garboczi, E. J., 2003, User manual for Finite Element and Finite Difference programs: A parallel version of NISTIR-6269, National Institute of Standards and Technology Internal Report 6997.

Garboczi, E.J. and Berryman, J.G., 2001, Elastic moduli of a material containing composite inclusions: Effective medium theory and finite element computations, Mechanics of Materials, 33, No. 8, 455-470

Gardner, G. H. F., L.W.Gardner, and A. R. Gregory, 1974, Formation velocity and density—The diagnostic basics for stratigraphic traps: Geophysics, 39, 770–780,

Greenberg, M. L., and J. P. Castagna, 1992, Shear-wave velocity estimation in porous rocks: Theoretical formulation, preliminary verification and applications: Geophysical Prospecting, 40, no. 2, 195–209.

Guodong, J., Patzek, T. D. and Silin, D. B., 2004, SPE90084: Direct prediction of flow properties of unconsolidated and consolidated reservoir rocks from image analysis. In SPE Annual Technical Conference and Exhibition,Houston, Texas, USA.

Han, D. H., 1986, Effect of porosity and clay content on acoustic properties of sandstones and unconsolidated sediment, Ph.D. thesis, Stanford University, Stanford, CA.

Herrmann, H.J. and Luding, S., 1998, Modeling granular media on the computer, Continuum Mech. Thermodyn., 10, 189-231.

Hertz, H., 1882, On the contact of elastic solids, H Reine Angew Math.

Holtzman, R., Silin, D. B. and Patzel, T.W., 2007, Frictional granular mechanics: A variational approach, Int. J. Numer. Meth. Eng., 00:1-6.

Hudson, J. A., 1980, Overall properties of a cracked solid: Mathematical Proceedings of the Cambridge Philosophical Society, 88, no. 2, 371–384..

Jensen, R. P., Bosscher, P. J., Plesha, M. E. and Edil, T. B., 1999, DEM simulation of granular media – structure interface: effects of surface roughness and particle shape, Int. J. Numer. Anal. Meth. Geomech., 23, 531-547.

Kandhai, D., Vidal, D. J.-E., Hoekstra, A. G.,Hoefsloot, H., Iedema, P. and Sloot, P. M. A., 1998, A comparison between lattice-Boltzmann and finite-element simulations of fluid flow in static mixer reactors, *Int. J. Modern Phys.*, **9**, 1123-1128.

Kandhai, D., Vidal, D. J.-E., Hoekstra, A. G.,Hoefsloot, H., Iedema, P. and Sloot, P. M. A., 1999, Lattice-Boltzmann and finite-element simulations of fluid flow in a SMRX static mixer reactor, *Int. J. Numer. Meth. Fluids*, **31**, 1019-1033.

Keehm, Y., 2003, Computational rock physics: Transport properties in porous media and applications, Ph.D. thesis, Stanford University, Stanford.

Khul, E., D'Addetta, G. A., Herrmann, H. J. and Ramm, E., 2000, A comparison of discrete granular material models with continuous microplane formulations, Granular Matter, 2, 113-121.

Kuhn, M. R. and Mitchell, J.R., 1989, Modelling of soil creep with the discrete element method. In Proc. 1st U.S. Conf. on Discrete Element Meth., Nat. Sci. Found., Washington DC.

Kuster, G. T., and M. N. Toksöz, 1974, Velocity and attenuation of seismic waves in two-phase media, Part I: Theoretical formulations: Geophysics, 39, 587–606.

Kuwabara, G. and Kono, K., 1987, Restitution Coefficient in a collision between Two Spheres, Jap. J Appl Phys, 26, 1230-1233.

Ladd, A. J. C., 1994a, Numerical simulations of particulate suspensions via a discretized Boltzmann equation: Part 1. Theoretical foundation, J. Fluid. Mech., 271, 285–309.

Lee, J., 1994, Heap formation in two-dimensional granular media, J Phys A, 27, L257.

Li, J., VanVilet, K. J., Zhu, T., Yip, S., Suresh, S., 2002, Atomistic mechanism governing elastic limit and incipient plasticity in crystals, Nature, 418, 307

Liao C,-L, Chang, T,-P, Young, D,-H. and Chang, S, C., 1997, Stress-strain relationship for granular materials based on the hypothesis of best fit, Int J Sol Str, 34, 31-32, 4087-4100.

Lubachevsky, B. D., and Stillinger, F. H., 1990, Geometric Properties of Random Disk Packings. J. Stat. Phys., 60:561–583.

Luding, S., Cl´ement, E., Blumen, A., Rajchenbach, J. and Duran J., 1994a, Studies of columns of beads under external vibrations. Phys. Rev. E, 49(2):1634

Luding, S., 1995, Granular materials under vibration: Simulations of rotating spheres. Phys. Rev. E, 52(4):4442

Makse, H. A., Gland, N., Johnson, D.L. and Schwartz, L., 2004, Granular packings: Nonlinear elasticity, sound propagation and collective relaxation dynamics, Phys Rev E 70, 061302.

Martys, N. S. and Chen, H., 1996, Simulation of multicomponent fluids in complex threedimensional geometries by the lattice Boltzmann method, *Phys. Rev. E*, **53**, 743-750.

Martys, N., Hagedorn, J., Goujon, D., and Devaney, J., 1999, Large Scale Simulations of Single and Multi-Component Flow in Porous Media, Proc of SPIE: The International Symposium on Optical Science, Engineering, and Instrumentation, Denver, Colorado, 1999.

Meille, S. and Garboczi, E.J., 2001, Linear elastic properties of 2-D and 3-D models of porous materials made from elongated objects, Mod. Sim. Mater. Sci. and Eng. **9** (5), 371-390

Mindlin, R. D., 1949, Compliance of bodies in contact: Journal of Applied Mechanics, 16, 259–268.

Munjiza, A., 2004, A Combined Finite-Discrete Element Method, John Wiley & Sons., London

Ng. T. T., 1994, Numerical simulations of granular soil using elliptical particles, Comp Geotechnics, 16, 153-169.

Ng. T. T., 2006, Input parameters of Discrete Element Methods, J Engg Mech.

Ouadfel, H., 1998, Numerical simulations of granular assemblies with three-dimensional ellipsoid-shaped particles, PhD. Thesis, University of Waterloo, ON, Canada.

Pöschel, T., 1993, Granular material flowing down an inclined chute: a molecular dynamics simulation, J Phys II Fr, 3, 1, 27-40.

Pöschel, T. and Schwager, T., 2005, Computational Granular Dynamics.

Potapov, A. V. and Campbell, C. S., 1996, Propagation of elastic waves in deep vertically shaken particle beds, Phys. Rev. Lett. 77, 4760

Roberts, A. P., and Garboczi, E. J., 2000, Elastic properties of model porous ceramics: J. Amer. Ceramic Soc., 83, 3041–3048.

Roberts, A.P. and Garboczi, E.J., 2002a, Elastic properties of model random three-dimensional open-cell solids, J. Mech. Phys. of Solids, 50 (1), 33-55.

Roberts, A.P. and Garboczi, E.J., 2002b, Computation of the linear elastic properties of random porous materials with a wide variety of microstructure, Proc. Royal Soc. of London, 458 (2021), 1033-1054.

Rothenburg, L., 1980, Micromechanics of Idealized Granular Systems, Ph.D. Thesis, Carleton University, Ottawa, ON, Canada.

Richa, 2010, Preservation of transport properties trends: computational rock physics approach, Ph.D. thesis, Stanford University, Stanford, CA.

Ristow, G.H., 1994, Granular dynamics: A review about recent molecular dynamics simulations of granular materials. In Stauffer D, editor, Annual Reviews of Computational Physics I, Singapore. World Scientific

Rothenburg, L., and Selvadurai, A. P. S., 1981a, A Micromechanical Definition of the Cauchy Stress Tensor for Particulate Media, Proc. Int. Symposium on the Mechanical Behavior of Structured Media, A.P.S. Selvadurai, ed., Ottawa, Ontario, Canada.

Rothenburg, L., and Selvadurai, A. P. S., 1981b, Micromechanical Aspects of Random Assemblies of Spheres with Linear Contact Interactions, Eighth Canandian Congress of Applied Mechanics, University of Moncton, Moncton, 217-218.

Rothman, D. H., and Zaleski, S., 1997, Lattice-Gas Cellular Aautomata: Simple Models for Complex Hydrodynamics, Cambridge University Press, Cambridge, 297pp.

Schafer, J, Dippel, S and Wolf, D.E., 1996, Force Schemes in Simulations of Granular Materials, J Phs I France, 6, 5-20.

Silbert, L. E., Ertaş, D., Grest, G. S., Halsey, T. C. and Levine, D., 2002a, Geometry of frictionless and frictional sphere packings, Phys. Rev. E 65, 031304

Silbert, L. E., Grest, G. S. and Landry, J.W., 2002b, Statistics of the contact network in frictional and frictionless granular packings, Phys. Rev. E 66, 061303

Thornton, C., 2000, Numerical simulations of deviatoric shear deformation of granular media, Geotechnique, 50 (1), 43-53.

Thornton, C. and Randall, C.W., 1988, Applications of theoretical contact mechanics to solid particle system simulation. In Micromechanics of granular media, Amsterdam. Elsevier

Ting, J.M., Khwaja, M., Meachum, L. R. and Rowell, J. D., 1993, An ellipse-based discrete element model for granular materials, Int J Num and Analy M Geomech., 17, 603-623.

Wolf, D.E., 1996, Modeling and computer simulation of granular media. In Hoffmann KH, Schreiber M, editors, Computational Physics. Springer, Heidelberg

Walsh, J. B., 1965, The effect of cracks on the compressibility of rock: Journal of Geophysical Research, 70, 381–389.

Walsh, J. B., and Brace, W. F., 1984, The effect of pressure on porosity and transport properties of rock, J. Geophy. Res., 89, 9425–9431.

Walton, K., 1987, The effective moduli of a random packing of spheres: Journal of the Mechanics and Physics of Solids, 33, 213–226.

Walton, O. R. and Braun, R, 1986, Viscosity, granular-temperature, and stress calculations for shearing assemblies of inelastic, frictional disks. J of Rheology, 30(5):949–980

Weber, J., 1966, Recherches Concernant les Contraintes Integranulaires dans les Milieux Pulve'rulents, Bull, de Liais. Ponts et Chaussees, No. 20.

Chapter 3
Granular packs: preparation and fabric analysis

3.1 Abstract

In this chapter, we discuss the implementation details for creating and compacting virtual random packs of frictional spherical grains, followed by an analysis of the pack fabric. We create monodisperse (unimodal size distribution) and polydisperse (multimodal size distribution) packs. To create monodisperse packs, we use Granular Dynamics (GD) simulation; for polydisperse packs, we use a hybrid method involving both Event Driven Molecular Dynamics (EDMD) simulation and GD simulation.

For monodisperse virtual packs, we compact using two different boundary conditions (BCs), a fixed-strain boundary condition and a *servo-control* (variable-strain, constant-stress) boundary condition. For the former BC, a user-defined strain is

applied on the pack boundaries; in servo-control, variable strains are applied on the pack boundaries to maintain a constant internal stress. These BCs are used for two different sets of simulated compactions: isotropic and uniaxial. For multi-modal size distributions, we create different packs (for different distributions) at the same isotropic pressures using the servo-control boundary condition.

We investigate the pack fabric primarily in terms of the number of contacts around a grain, elastic deformation of these contacts and the mean stress on each grain. The distributions of all these properties show considerable heterogeneity. Specifically, the contact deformations and mean grain stress have distributions with long tails, thereby showing existence of grains bearing higher than average loads. We find that the average number of contacts in the whole pack (coordination number, or CN) evolves during compaction. This evolution is due not only to formation of new contacts between grains already in the contact network, but also to 'floaters' or 'rattlers' (grains with zero contacts) joining the contact network. Hence, we present the distribution of distances to nearest non-contact neighbors for all grains and study the evolution of this distribution with compaction. We also note that the relations between CN, porosity and stress are non-unique and depend on grain-to-grain friction and loading rate. For uniaxial compaction, we study the directional arrangements of grains using the fabric tensor of the pack. The fabric tensor is a second-rank tensor characterizing the microstructural arrangement of components, in this case, the grains. Under uniaxial compaction, we find that evolution of the fabric tensor elements shows different stress dependence, viz., more contacts form in the axial direction than in the radial direction. Among other microstructural details, we study the radial distribution function and participation number of the pack. The radial distribution function shows long-range correlations between grains. The participation number, being a measure of spatial localization, shows that the mean stress on each grain becomes less heterogeneous with increasing compaction, unlike contact deformations or contact forces.

For polydisperse packs, we present results first for bidisperse packs (bimodal size distribution) and then for Gaussian size distributions with different standard deviations. For bidisperse packs, we present porosity and coordination-number evolution for

different radius ratios and different volume fractions of large grains. We also investigate the effect of grain mineralogy for these packs and find that the porosity and CN depend on grain mineralogy. Like in monodisperse packs, we find strong heterogeneity in terms of coordination number, contact deformations and mean grain stress. In addition, we also find 'floaters'. Larger grains form contact networks which bear the maximum load for these packs. For the more general polydisperse packs with Gaussian size distributions, we study the evolution of porosity and CN with Sorting Index (SI, the ratio of standard deviation to mean grain size) and compaction. The Porosity–SI trend for our simulated packs is reasonably close to experimental trends.

3.2 Introduction

In the field of earth sciences in general, and in the oil and gas industry in particular, understanding loose, unconsolidated sediments is important for predicting borehole stability, sand production and shallow geo-hazards and for monitoring reservoir properties like fluid content, production-induced compaction and storage capacities. Loose, unconsolidated sediments resemble granular packs and can make excellent CO_2 repositories (House et al., 2006, Koide et al., 2004), oil and gas reservoirs, and aquifers (Mathers and Zalasiewicz, 1994, Konrad et al.., 2005). In material science and condensed-matter physics, the study of granular packs and their properties is also an active field of research (Agnolin and Roux, 2007, Herrmann et al., 1998, Hinrichsen and Wolf, 2004, Rojo et al., 2005).

Like most other problems in science, studies of granular packs have been based on theories, experiments and simulations. Theoretical studies (Cumberland and Crawford, 1987, Bideau and Dodds, 1991, Onoda and Liniger, 1990, Berryman, 1983) of sphere packs have referred to random close packs (RCPs) and random loose packs (RLPs) with the idea that sphere packs without any crystalline order have porosity no lower than about 36%. Torquato et al. (2000), however, have questioned the concept of RCP as being ill-defined, since the volume fraction of stable random close packs depends on the assemblage process. Experimental studies have reported mechanical, elastic and transport properties of granular packs (Domenico, 1977, Hardin and Richart, 1963,

Murphy, 1982, Plona, 1980, Agnolin et al., 2005, Kuwano and Jardine, 2002, Han, 1986, Zimmer, 2004, Slater and Lesmes, 2002). These studies mostly report and characterize packs by porosity. Other than porosity, the internal structure of these packs has mostly been uncharacterized, partly because of the difficulty of looking inside the pack. Pioneering works by Bernal et al. (1962), Finney (1970) and Gotoh and Finney (1974) provided important insights into the structure of random close packs by counting grain contacts in tedious laboratory experiments. More recent imaging techniques like X-ray micro-tomography (Richard et al.., 2003, Aste et al., 2004, 2005) and confocal microscopy (Brujić et al., 2003) are beginning to reveal more about the internal pack microstructure. However, the evolution of three-dimensional granular packs with changes in external conditions, like loading, is still practically unknown from experiments.

The arrangement of grains and distribution of internal forces and stresses crucially affect the bulk properties of granular pack (Mueth et al., 1998) like its load bearing capacity (Travers et al., 1987, Guyon et al., 1990), sound transmission (Liu and Nagel, 1992, Leibig, 1994, Agnolin et al., 2005) and shock propagation (Popatov and Campbell, 1996, Sinkovits and Sen, 1995). A rather unrealistic assumption of *homogeneity* is used in theoretical studies involving prediction of bulk properties for granular packs. This assumption of homogeneity in structure, forces, and stresses is valid for regular crystal structures. However, in real granular materials, due to the randomness in grain arrangement and/or their sizes, the distribution of forces and stresses is hardly homogeneous (Mueth et al., 1998). Moreover, these microscopic properties are often unequally distributed over only a few grains in the whole pack. Hence, understanding grain-scale microstructure and its evolution during deformation is critical to understand the behavior of macroscopic mechanical and transport properties. In order to do that, we start by giving an intensive microstructural analysis of granular packs in this chapter and proceed to the effective (or macroscopic) properties in the next chapter.

We create and compact frictional granular sphere packs using Granular Dynamics (GD) simulation. GD simulation, also known as the Discrete Element Method

(Cundall and Strack, 1979), has been used variously and successfully to model packing structures for gravity-sedimented or compacted systems (Makse et al., 2004, 2005, Silbert et al., 2002a, 2002b, Luding, 2004, 2005, Herrmann and Luding, 1998), to reproduce the stress-strain response of packs (Thornton, 2000, Guodong et al., 2003, Holt et al., 2005, Garcia and Medina, 2006), and to predict the pressure dependence of elastic moduli (Makse et al., 2004, Garcia et al., 2004, Holt et al., 2005). This approach acts as an efficient tool not only to reproduce and predict macroscopic properties, but also to study internal structures and properties like the coordination number (CN) and the fabric tensor, a second rank tensor characterizing the microstructural arrangement of components, in this case, the grains. We should also point out that various other computational methods have been presented in the literature to create granular packs (Donev et al., 2005a, 2005b, Agnolin and Roux, 2007, Nolan and Kavanagh, 1992, Holtzman et al., 2007, Bezrukov, et al.., 2002, Clarke and Wiley, 1987, Bryant et al., 2009). Donev (2006) lists a comprehensive collection of several of these methods. We present Donev's classification of packing algorithms (Donev, 2006) in the next section and present our justification for using a *force-based* Granular Dynamics simulation in this study.

In this chapter, we analyze microstructures for two types of sphere packs: monodisperse (unimodal size distribution) and polydisperse (multimodal size distribution) packs. For monodisperse packs, we use GD simulation. Two types of boundary conditions (BC) are used: a strain BC and a 'servo-control' (constant stress) BC. We also present two different loading conditions: isotropic compaction and uniaxial compaction. For polydisperse packs, we use a hybrid method combining Event Driven Molecular Dynamics (EDMD) with GD simulation. EDMD is used to create jammed packs, which are then compacted to different pressures using GD simulation. We discuss the reason for such a hybrid method in Section 3.3.

The primary result of our microstructural analyses in this chapter is the discovery of heterogeneity in internal structure, contact forces and grain stresses in granular packs. This finding is analogous to published experimental and simulation results (e.g., Liu et al., 1995, Mueth et al., 1997, Makse et al., 2004). Our microstructural analyses

in this chapter serve as a prerequisite for analysis of mechanical and elastic properties—microscopic and macroscopic—and to evaluate the validity of the assumptions in theoretical models used to predict effective elastic properties of granular packs.

3.3 Packing algorithms

Most computational algorithms used to model granular packs attempt to model the *jammed* state. Donev et al. (2004, 2005) and Kansal et al. (2002) define *strictly jammed* states as configurations in which grains (or hard spheres in their case) cannot move without interpenetrating each other or increasing the pack volume. A nice description of jamming can also be found in O'Hern et al. (2003), Liu and Nagel (1998) and Agnolin and Roux (2007). A *jammed* packing refers to a pack which is at stable equilibrium. This can also be viewed as an energy minimization problem, wherein the best configuration, in terms of stability, yields the least elastic energy. Before discussing how this impacts our choice of packing algorithm, we present a review from Donev (2005) about the various packing algorithms in use:

- *Serial deposition/sedimentation method:* These algorithms (Nolan and Kavanagh, 1992, Bennett, 1972, Buchalter and Bradley, 1994, Coelho et al., 1997) mostly add grains to an existing disordered array or structure of grains. They typically create RLPs and inhomogeneous anisotropic packs.
- *Overlap elimination method:* These algorithms (Bezrukov et al., 2002, Clarke and Wiley, 1987, Bargiel and Moscinski, 1991, Williams and Philipse, 2003), involving random or force-based grain displacements, eliminate geometric overlaps between particles by displacing the grains one by one until overlaps can no longer be removed or added.
- *Energy minimization method:* These algorithms (Holtzman et al., 2007, Stillinger and Weber, 1985, Kottwitz, 1991, O'Hern et al., 2002) minimize elastic energy, which is computed based on contact deformations of deformable (soft spheres) particles.

- *Molecular/Granular dynamics method:* Methods of this type model grain-to-grain interactions and solve dynamic/kinetic equations (Makse et al., 2004, Zhang and Makse, 2005, Agnolin and Roux, 2007, Donev, 2005, Holt et al., 2005). The interactions can be based on soft (deformable), when dynamic equations are solved, or hard (rigid) spheres, when kinetic equations are solved.
- *Contact network based method:* In this class of methods (Zinchenko, 1994), a contact network is maintained throughout the packing process.

The main focus of our study is to relate the macroscopic mechanical, elastic and transport properties to their microstructural origins. Therefore, we need to choose a method that is as physically realistic as possible. Later, we compare our simulated results with laboratory experiments on glass beads and sand. These laboratory samples are created at certain confining pressures. Hence the choice of our method is also dictated by the possibility of defining a *physical* stress tensor characterizing the simulated packs. Moreover, real materials most likely have non-zero friction between grains during the assembling process, and hence, our computational method should be able to handle friction and its effects. With all these constraints, the Granular Dynamics (GD) simulation involving soft (deformable) frictional spheres is the best choice for our packing algorithm. In terms of the definition of jamming, the interpenetration or deformation of these soft spheres is relatively very small and hence the resultant packs still qualify as jammed states as per Torquato et al. (2000).

As illustrated in Chapter 2, GD is computationally rigorous and intensive. For monodisperse packs and nearly monodisperse packs (i.e., reasonably well-sorted sediments), this method reaches jammed states in a reasonable amount of computing time. However, for creating polydisperse packs using GD simulation, the computation times are lengthy since the near-jammed states have significant temporal fluctuations in average kinetic energy and internal stress. For polydisperse packs (i.e., poorly-sorted sediments), we use the event- (or collision-) driven hard-sphere molecular dynamics simulation, known as EDMD. When creating jammed packs with EDMD,

however, there is no direct notion of stress in these packs, since the algorithm is purely kinematic. To make these simulations relevant to loose sediments, as encountered in rock-physics analysis, we must compact the jammed packs to different pressures. Hence, the outputs from EDMD, viz. the jammed packs, are then compacted to different isotropic pressures using GD simulation. We also set the value of the friction coefficient to a non-zero value while compressing these packs.

3.4 Monodisperse packs

Monodisperse packs refer to packs with particles of uniform size. Geological sediments rarely, if ever, have perfect sorting. However, as a starting point for simulating random packs and also for theoretical effective medium modeling, a monodisperse pack or unimodal size distribution is a good choice. Furthermore, many laboratory experiments (Domenico, 1977, Agnolin et al., 2005, Zimmer, 2004, Murphy, 1982) on artificial materials, like glass beads, use uniform particles. Certain beach sediments have also been reported to be fairly well-sorted. We discuss the effect of sorting in Section 3.5.

For monodisperse packs, we start with a random gas of grains and assign them specific material properties. We choose two specific materials for most of our packs: glass beads (shear modulus: 29 GPa, Poisson's ratio: 0.2) and quartz (shear modulus: 45 GPa, Poisson's ratio: 0.08). We assign a coefficient of friction value of 0.3 in most simulations, unless otherwise stated. As described in Chapter 2, these properties are used for calculating realistic contact stiffness values. Starting with this gas of grains having porosity close to 90%, we compact the packing cube using two different BCs, as discussed in the next section, 3.4.1. We also use two different compaction scenarios: isotropic and uniaxial compaction, which we discuss in Section 3.4.2. In all the simulations, we have periodic boundaries in all three directions. This ensures that grains near any boundary can *see* the grains on the opposite end, thereby avoiding any rigid boundary biases.

3.4.1 Preparation protocols: boundary conditions

The main goal of compressing the suspension is to create configurations that are *jammed*. Each jammed configuration is characterized by a stress tensor and is in stable mechanical equilibrium. Each of these jammed states will henceforth be called a *reference state*. Under both BCs, the stress tensor is calculated by volume averaging the sum of all contact stresses (as explained in Chapter 2) and is henceforth referred to as the internal stress.

Strain BCs are implemented by compacting the simulation box (i.e., reducing the box lengths) isotropically at a specific *strain rate* until a pre-defined porosity is achieved. Zhang and Makse (2005) conduct similar numerical experiments for frictional packs using a constant *compression rate*, instead of strain rate. They show that the jammed state porosity depends on this initial compression rate. Zhang and Makse (2005) also show that the porosity, CN, and pressure follow different non-unique paths based on this compression rate. In formulating the numerical experiment in our case, we invoke the concept of critical porosity introduced by Nur et al. (1998). The critical porosity is described as the porosity where a suspension makes a transition to load-bearing regime and the grains configure themselves to bear external loads. Typically, the critical porosity is reported close to 36-40% porosity for spherical and near-spherical grains (Nur et al., 1998). In the realm of granular physics, this corresponds to an initial jammed state with very low confining stress. For our case, we set a particular strain rate to reach an initial porosity close to the available experimental data on glass beads and sand (Domenico, 1977, Murphy, 1982, Zimmer, 2004, Agnolin et al., 2005). This initial pack is then allowed to relax and reach a static mechanical equilibrium state.

We characterize static mechanical equilibrium by a kinetic energy threshold and a stable finite non-zero stress tensor. It should be noted that like Zhang and Makse (2005), we also observe that for a fixed initial strain rate, the pack jams at a particular porosity. Any porosity larger than this value would lead to complete disintegration of the pack, i.e., the pack relaxes to zero CN and zero internal stress. It should also be noted that the strain rate and the porosity are the only parameters specified in strain

BC. The pack comes to stability through force balance and the internal stress is just a result of this stable configuration. After achieving this initial reference state, we further isotropically or uniaxially compress this pack to obtain several other reference states. We discuss the microstructural properties of these reference states in following sections.

We also use a *servo-control* (variable strain, constant stress) BC. We apply variable strains on boundaries of the simulation box to maintain a constant pre-defined internal (effective) stress, or target stress - P_t. Numerically, this is achieved by setting the strain rate, $\dot{\varepsilon}$, as follows:

$$\dot{\varepsilon} = g(P - P_t) \tag{3.1}$$

where P is the pressure or internal stress of the pack, as described in Chapter 2. The term g is called the *gain factor* and is usually tuned using a trial-and-error method to achieve equilibrium in an optimal way (Makse et al., 2004). For any target stress, a higher gain would delay the convergence to the minimum energy state, since the elastic contact energy would change too fast, hence requiring more steps. A lower than optimum gain would unnecessarily delay the search for the minimum-energy jammed state due to smaller strain steps. The initial configuration is the same random gas of grains with high porosity, and then we start the compaction of the pack based on Eqn. 3.1. The porosity of the pack continually changes (generally decreasing) until the pack is very close to jamming. As the pack gets closer to the jammed state, the stress fluctuations around the target stress become very small. At this point, we turn off the servo-control and let the granular pack relax and converge to minimum energy state. We report two sets of isotropic experiments for monodisperse packs: one where we set the initial coefficient of friction to zero, and a second where we specify a finite non-zero value for the initial stages of compaction. As the pack gets close to jamming, we set the friction to a final value of 0.3. The two methods are merely two ways of creating granular packs, and are similar to other reported simulations in the literature (Magnanimo et al., 2008, Makse et al., 2004). When using the initial frictionless pack during compaction, the final porosities for low target pressures are close to 36%, the random close pack porosity. Setting a finite friction value (0.1) during initial

compaction stages allows the pack to stabilize to ~ 38-39% porosity for low target pressures. These later porosities are close to published laboratory experiments on glass beads and sand. The experimental porosity values are higher than the reported value of random close pack porosity, possibly because of the assembling process. While we have little information about the assembling process in most experiments, our numerical simulation tool helps us analyze these packing scenarios through the effective macroscopic property of volume fraction or porosity.

3.4.2 Compaction protocols: isotropic and uniaxial

We create reference states using both isotropic and anisotropic (uniaxial with zero lateral strain) compaction of granular packs. While isotropic compaction lets us study the evolution of granular pack microstructure and its physical properties, for many earth science problems uniaxial compaction with zero lateral strain is more realistic.

For isotropic compaction using a strain BC, the boundaries of the simulation cube are isotropically reduced (compressed) to create several reference states. We allow the grain pack to relax at every reference state. Since we start from a random configuration of suspension and isotropically compress the simulation cubes, the granular pack is most likely to attain equilibrium with nearly isotropic stresses. However, this is not guaranteed. The servo-control mechanism allows us to guarantee that the stresses are identical (within a reasonable tolerance, say 2 KPa). Using this BC, the random gas of grains is compressed to maintain the same target pressure in each principal direction.

For uniaxial compaction using the strain BC, we create an initial isotropic jammed state close to critical porosity with a very small internal stress in each direction. For further compaction, we uniaxially strain the Z-direction, with zero lateral strain in X- and Y- directions. As in the isotropic case, we allow the pack to relax at each of these uniaxially strained states. With the servo-control BC, we create several isotropic reference states and then create uniaxial reference states by iteratively straining the Z-direction to match a target stress in that direction. The X- and Y- strains are again zero.

For each of these reference states, we determine the directional variation of number of contacts by analyzing the fabric tensor.

3.4.3 Microstructural analyses: Porosity and Coordination Number

In this section, we present the evolution of porosity and coordination number under isotropic and uniaxial compression. For isotropic compression, we present results for both the BCs; however, for uniaxial compression, we present results for only the servo- control BC.

3.4.3.1. Isotropic compaction

For isotropic compaction, we simulate grain packs with glass and sand material properties. We present microstructural analyses for glass beads only. Using the strain BC, we compact a random gas of grains (with coefficient of friction: 0.3) from an initial porosity of ~90% using three different strain rates, viz. 0.00018 s^{-1}, 0.0018 s^{-1} and 0.018 s^{-1}. Zhang and Makse (2005) present results for similar computational experiments with constant compression rates: 2x10 m/s, $2x10^3$ m/s and $2x10^4$ m/s. While our strain rates are mostly different from Zhang and Makse (2005), our porosity–CN relations are asymptotically similar to those from Zhang and Makse at lower porosities (Fig. 3.1). For increasing initial strain rates, we observe lower critical porosities and different porosity–CN relations. The stress-induced changes in porosities show non-unique relations, too, and depend on initial strain rate as well (Fig. 3.2). Porosity–CN–stress relations are mostly used in effective-medium modeling of elastic properties of granular packs. The compressive strain rate is analogous to the pouring height while gravitationally assembling experimental granular packs. For a greater pouring height, the velocities are greater and hence the jamming porosity is lower, whereas for smaller compression rate or smaller pouring height, the jamming porosity is higher. Figure 3.1 shows that the porosity–CN–strain rate relations are non-unique and depend on strain rate used for assemblage. Zhang and Makse (2005) also report the stresses for their specific compression rates and demonstrate that porosity–stress relations are non-unique in their simulations and depend on these compression

rates. However, from our simulated packs with different strain rates, we do not find such relationship between porosity–stress–strain-rate, as shown in Figure 3.4.

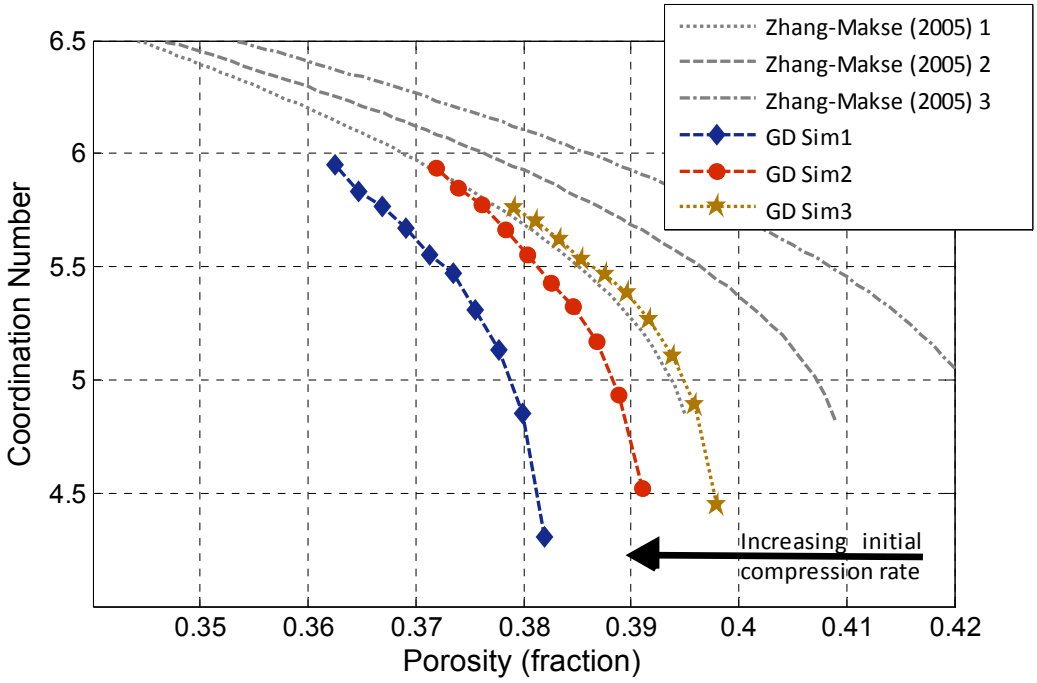

Figure 3.1: Porosity–CN relation for simulated packs using the strain bounday condition. The relations are non-unique and depend on initial strain rate while preparing the sample. Given that our strain rates are different from those reported by Zhang and Makse (2005), our porosity–CN relations are in good agreement with their results asymptotically (for lower porosities). Strain rates - GD Sim 1: **0.018 s^{-1}**; GD Sim 2: **0.0018 s^{-1}**; GD Sim 3: **0.00018 s^{-1}**. Compression rates - Zhang-Makse(2005) 1: **$2x10^{4}$m/s**; Zhang-Makse(2005) 2: **$2x10^{3}$m/s**; Zhang-Makse(2005) 3: **2x10m/s**.

To study the effect of inter-grain friction, we use the strain BC with three different coefficients of friction—0.15, 0.3 and 0.8—for a fixed strain rate of 0.018 s^{-1} (blue diamonds in Fig 3.1). The dependence of the porosity–CN relation on different coefficients of friction for a fixed initial strain rate is not significant (Fig. 3.3). However, the pressure–CN relations show some variation for different coefficients of friction (Fig. 3.4). We observe that a lower coefficient of friction yields a higher CN at a given mean stress. For the finite friction values used in this experiment, we get a CN close to 4.0 for low stresses, as predicted by the theory of isostaticity.

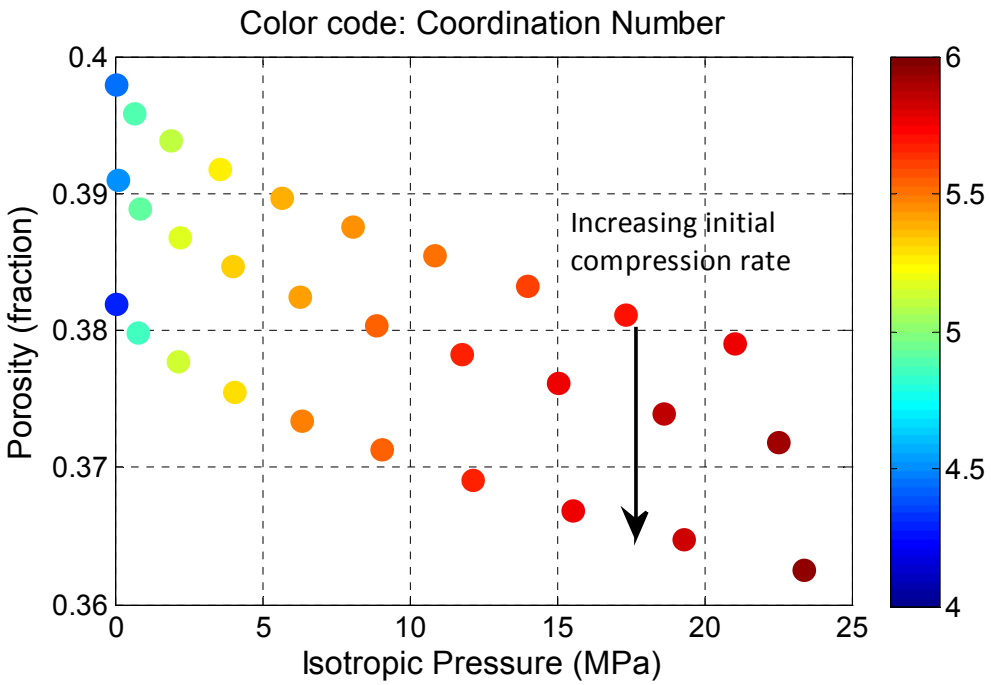

Figure 3.2: Compaction-induced changes in porosity. Packs can have the same porosity at different compaction stages, if the initial porosity is different. Strain rates - GD Sim 1: **0.018 s^{-1}**; GD Sim 2: **0.0018 s^{-1}**; GD Sim 3: **0.00018 s^{-1}**.

An *isostatic packing* is defined as one devoid of force and velocity indeterminacy (Agnolin and Roux, 2007). This means that for any particular load, there is a unique set of equilibrium forces. Further, for any vector of contact displacements, there is a unique displacement vector or field. Based on this theory, a pack of frictionless grains should have a unique CN of 6 and that of frictional grains should have a CN of 4. However, this is based on the assumption that the frictional grains have an infinite coefficient of friction. For an intermediate friction value, as used in our experiments, we have CN values between 4 and 6. It should also be pointed out that isostaticity is a property of the *backbone* or the main force-bearing grains. As with other simulation results in the literature, our simulated granular packs also contain 'floaters' or 'rattlers' (grains with no contacts). This is one of the by-products of zero-gravity simulations. For a system with gravity, the floaters are more likely to equilibrate with their nearest neighbors. As pointed out in Chapter 2, due to our use of periodic BC, we cannot account for gravity. However, Bryant et al. (2009) and Thane (2006) argue that

floaters exist in laboratory granular packs too. Since the isostatic property is based on only the grains taking part in the force network, we should *ideally* report CN without the floaters. However, CN reported in most of our results include floaters, unless otherwise stated. For our monodisperse packs, CN fractionally increases when floaters are excluded. Based on the same arguments as Zhang and Makse (2005), we conclude that since our simulated packs do not have infinite friction between the grains, conditions of *strict* isostaticity are not applicable for our packs. Zhang and Makse (2005) report packs with infinite friction compression rate of $2x10^2$m/s. For these packs, they report CN of 3.98, which is close to the theoretical limit of 4.

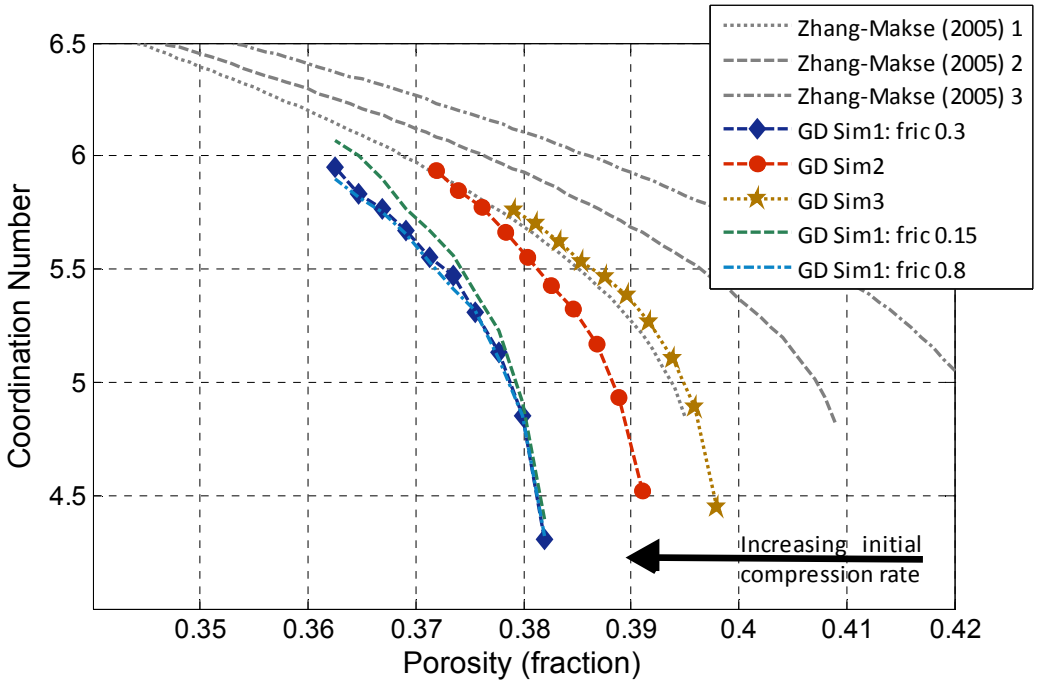

Figure 3.3: Porosity–CN relation for simulated packs using the strain boundary condition. Along with the curves in Fig. 3.1, the effects of different coefficients of friction are plotted for the fastest strain rate (**0.018 s^{-1}**). Porosity–CN relation is reasonably consistent as long as the initial strain rate is same. Strain rates - GD Sim 1: **0.018 s^{-1}**; GD Sim 2: **0.0018 s^{-1}**; GD Sim 3: **0.00018 s^{-1}**. Compression rates -Zhang-Makse(2005) 1: **$2x10^4$m/s**; Zhang-Makse(2005) 2: **$2x10^3$m/s**; Zhang-Makse(2005) 3: **2x10m/s**.

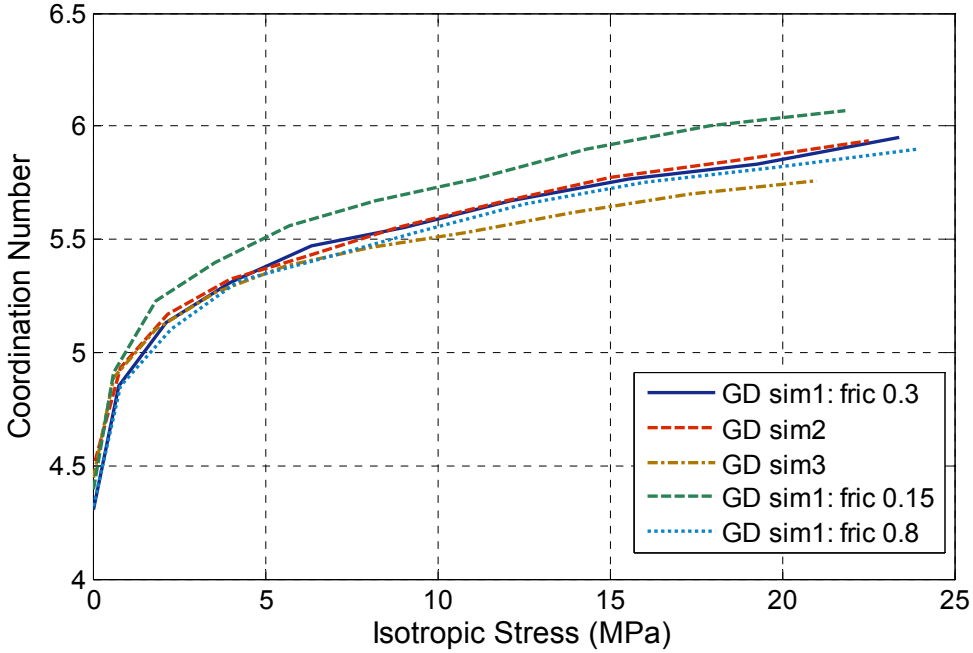

Figure 3.4: Stress–CN relation for simulated packs using the strain bounday condition. Strain rates - GD Sim 1: **0.018 s^{-1}**; GD Sim 2: **0.0018 s^{-1}**; GD Sim 3: **0.00018 s^{-1}**.

For the servo-control BC, we simulate packs with both glass and quartz material properties. We report the results for glass beads here. We pre-define target stresses and compact our packs to reach mechanical equilibrium at these stresses. We impose three numerical criteria for testing mechanical equilibrium: (1) average kinetic energy of the pack; (2) mean stress of the pack; and (3) number of sliding contacts. For equilibrium, the average kinetic energy of the pack should be lower than a pre-defined threshold and the temporal fluctuations of mean stress of the pack should be minimal (1% of the pre-defined target stress). Further, our stable reference states have zero sliding contacts, unless otherwise stated. This is based on the hypothesis that static or stable granular materials in laboratory have zero sliding contacts, or in other words, laboratory grain packs instantly *jam* during assemblage. The onset of jamming is defined as static equilibrium of grains, where the grains can no longer move without disturbing the local arrangement. In terms of hard-sphere simulations (as discussed in Chapter 2, Section 2.4), Donev (2005) describes a jammed pack as one where the

grains are locked in their positions despite thermal agitation (shaking) and boundary deformations (external loading).

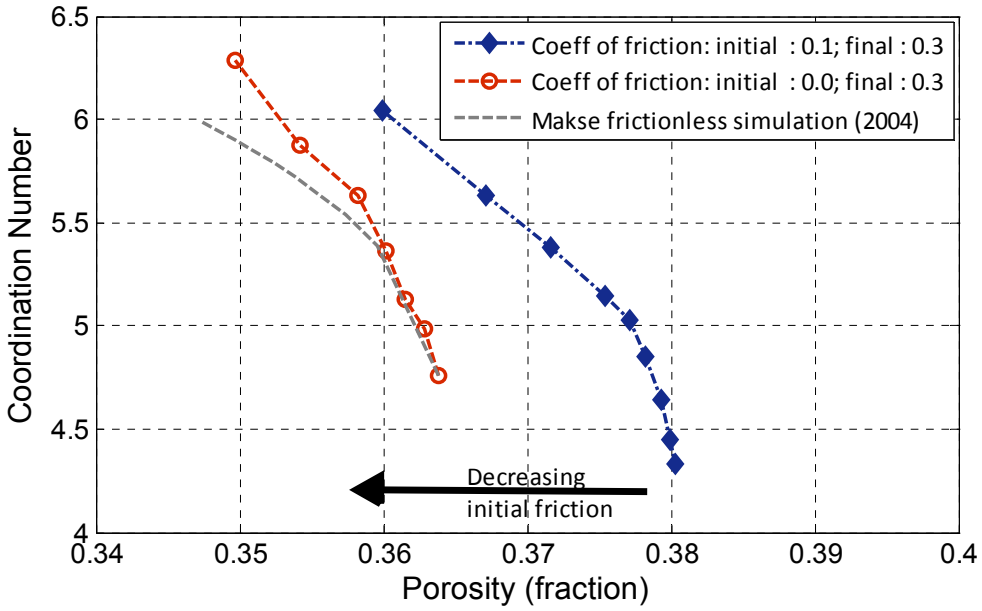

Figure 3.5: Porosity–CN relation for simulated packs using the servo-control or constant-stress BC. The packs are prepared with different initial friction; the final friction is same in both cases. Although the initial porosities are different due to initial lubrication, the relations aysmptotically approach each other.

Using this BC, we test the effect of initial lubrication of the grains. We compress the granular gas of grains close to a pre-defined volume fraction or porosity higher than the RCP limit with a specific coefficient of friction. For the two simulations we report here, we chose initial coefficients of friction of zero and 0.1. We then follow the same approach as Magnanimo et al. (2008) and set the friction to 0.1 in both cases while calculating the servo-control compaction to create the reference packs. When the stress stabilizes, we apply the final friction value of 0.3 and continue the servo-control compression to further stabilize the stress.

The role of the initial coefficient of friction is to create packs with different porosities (Fig. 3.5). This is an important part of the granular-pack problem. Whereas most theoretical work for characterizing RCP and RLP are in terms of volume fraction or porosity, there have been few studies of porosity considering CN and friction

together. We see that friction in the initial assembling process does affect the CN–stress relation (Fig. 3.6). Although both packs have a final coefficient of friction of 0.3, the case with initially frictionless grains shows a lower porosity or higher density. In the next chapter, we discuss the relevance of these experiments in terms of stress–strain curves. For a given stress, CN is larger when initial friction is smaller (Fig. 3.6).

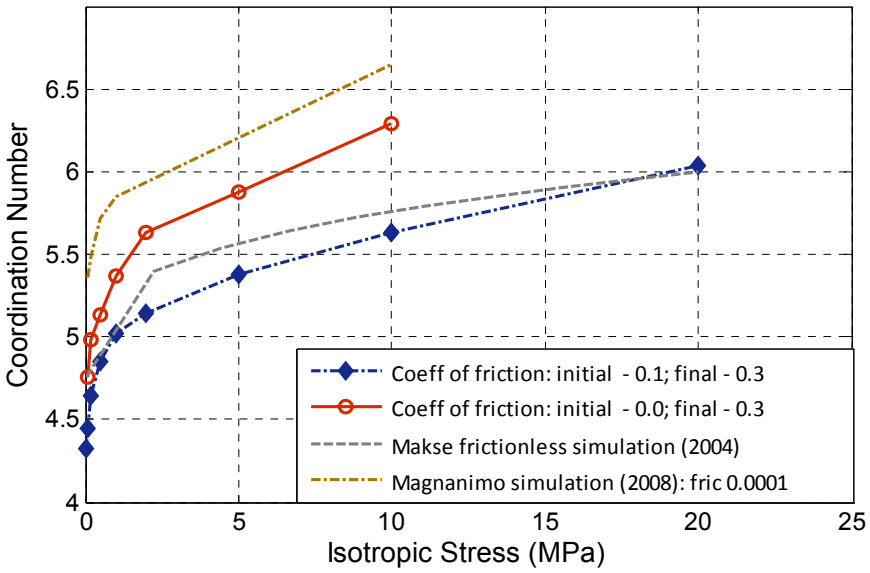

Figure 3.6: Stress–CN relation for the servo-control mechanism showing the effect of initial lubrication. Initial lubrication (lower coefficient of friction) results in higher CN and lower porosity (Fig. 3.4) for the same stress.

At this stage, we should review the two different aspects we have studied using the two different BCs: strain and servo-control. In the strain BC experiments, we concluded that for the same coefficient of friction, the CN–porosity–stress relations depend on the initial compaction rate. In the servo-control experiments, we demonstrate the role of initial coefficient of friction on the porosity, CN, and mean stress. In this case, too, we find that for the same final coefficient of friction, the CN–porosity–stress relations depend on initial friction. Use of frictionless grains during initial compression can be justified by considering that assembling of granular packs in the laboratory often involves air fluviation, which might create an additional lubrication. Further, laboratory granular packs are often tamped during preparation stages. Although this is not the same as setting the friction to lower values, the

physical effect in terms of increased pack density or decreased porosity is similar to that of setting lower initial friction.

3.4.3.2. Uniaxial compaction

For uniaxial compaction, although we create granular packs with glass and quartz material properties, we report fabric analysis for servo-control experiments on glass.

We create several isotropic reference states or jammed granular packs using the same approach as discussed in the earlier section. For each of these packs, we then continue uniaxial compaction in the Z-direction by maintaining the stress in the Z-direction close to a pre-defined target stress (Fig. 3.7). There is zero strain in the X- and Y- directions. However, the stresses in these two directions are not controlled and evolve based on the internal contact geometry. We report the results on macroscopic stresses in the next chapter. To analyze the microstructural details and their directional dependence, we now consider fabric tensors. A fabric tensor is a symmetric, second-rank tensor which characterizes the arrangement of the microstructural components in a multiphase or porous material (Cowin, 1985); in our case, the components are grain locations. Fabric tensors of even orders can be constructed by using the grain locations. The fabric tensor for an individual particle is defined as

$$F_{ij}^{p} = \sum_{C=1}^{C_p} (n^c \otimes n^c) \tag{3.2}$$

where n^c is the unit vector from the center of a grain to the center of the neighboring grain and $\otimes$ denotes the dyadic product. The summation is done for all its neighboring grains (C^p). The average fabric tensor for the whole pack is defined as (Latzel et al., 2000):

$$F_{ij} = \langle n_i n_j \rangle = \frac{1}{N} \sum_{p=1}^{N} \sum_{C=1}^{C_p} (n^c \otimes n^c) \tag{3.3}$$

where N is the total number of grains, and C_p is the number of contacts for particle p. One of the interesting properties of the fabric tensor is that it can be shown that the material symmetries of isotropy, transverse isotropy and orthotropy correspond to the cases of one, two and three distinct eigenvalues of the fabric tensor, respectively. Moreover, the first invariant of the fabric tensor is CN, and in general, the deviatoric fabric tensor quantifies the fabric anisotropy in a granular pack (Luding, 2005). For two different simulated experiments, where uniaxial compression starts at different isotropic pressures, we study the evolution of fabric tensor elements in the three directions (Fig. 3.8). We note that preferential alignment in terms of contacts starts to appear under uniaxial compression. Although we use sphere packs, there is stress-induced preferential alignment in terms of contacts. Most effective-medium models of granular medium do not account for directional dependency of contacts. However, our simulated packs show the need for considering directional CN in effective-medium models for uniaxial compaction.

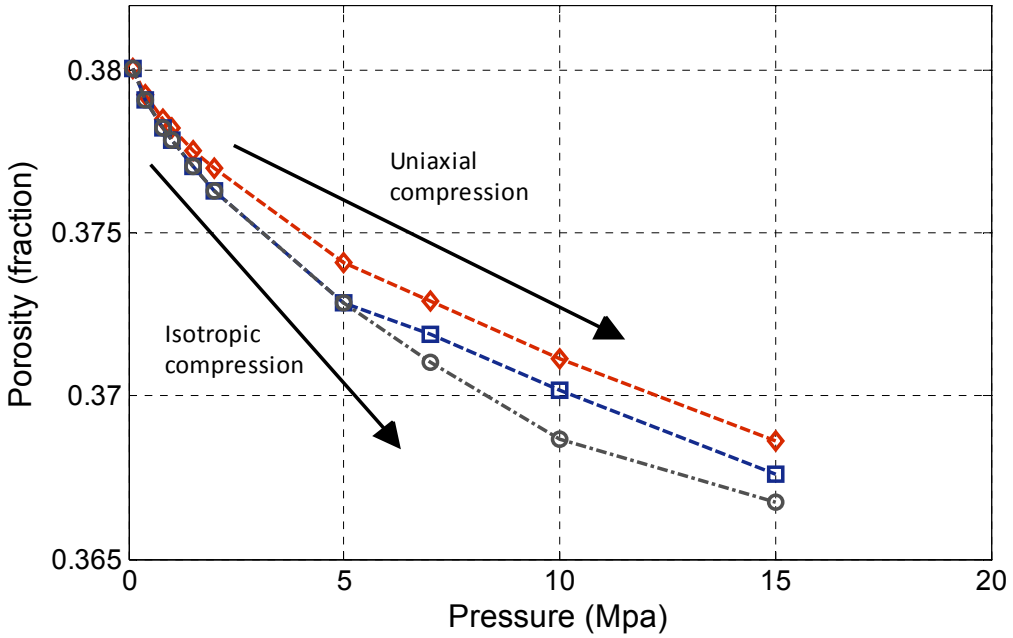

Figure 3.7: Stress–porosity path for different uniaxial experiments. The different lines show different loading paths,with onset of uniaxial compression being different for each of the samples. The isotropic compression and uniaxial compression paths are shown using different arrows, and the departure from isotropic compaction is clearly visible. The X-axis refers to the isotropic mean stress or uniaxial stress values, depending on the compaction stage.

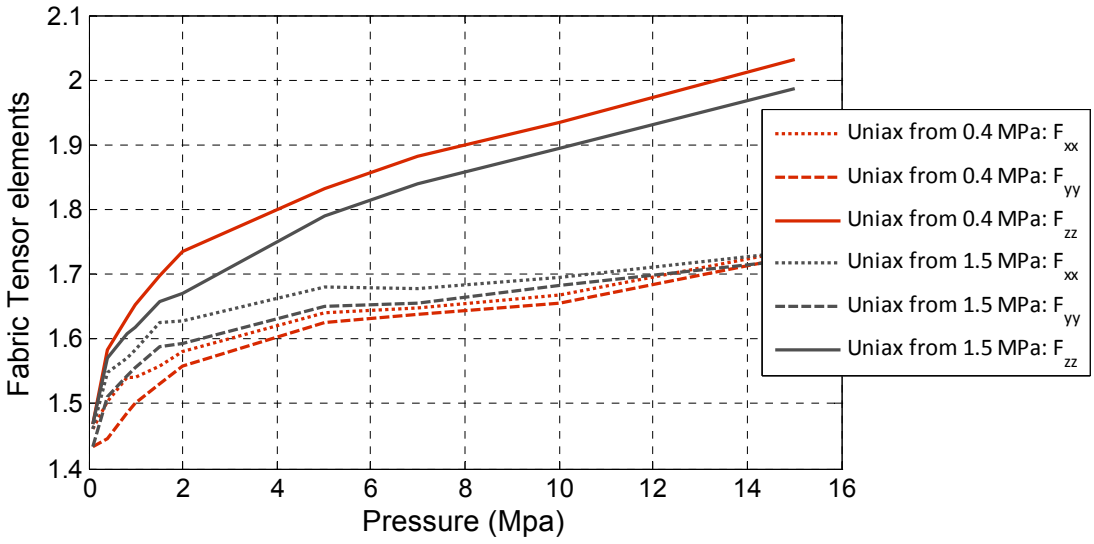

Figure 3.8: Fabric tensor elements, F_{xx}, F_{yy} and F_{zz} in X-, Y- and Z-directions, respectively, for two loading cycles with different starting points for uniaxial compaction, viz. 0.4 and 1.5 MPa. The fabric tensor elements show preferential contact formation under uniaxial compaction, as demonstrated by the difference between F_{zz} and the rest (F_{xx} and F_{yy}).

3.4.4. Microstructural details: presence of heterogeneity

Until now, we have reported CN for several of the simulated granular packs. We have also shown how the elements of the fabric tensor vary under uniaxial compression. While CN is the *average* number of contacts per grain, we have not discussed much about the *variation* in the number of contacts per grain. We mentioned that 'floaters' exist in our simulated packs, as is true in other reported simulations (Zhang and Makse, 2005, Agnolin et al., 2007). At the same time, we have many grains with as many as 10 or 11 neighboring grains (Fig. 3.9). We analyze the distribution of contacts per grain for all grains in the pack and also analyze the shift in the distribution with higher pressure or mean isotropic stress. We notice that there is considerable heterogeneity in the number of neighbors per grain within each pack. This is an interesting feature for *random* packs, since there is hardly any signature of crystalline order. For ordered crystalline systems like cubic or hexagonal packs, there is definite number of contacts for each grain, or in other words, these packs are *homogeneous* in terms of contacts or neighbors. We will discuss briefly the significance of this particular aspect after we present other measures of heterogeneity

in microstructure, and in more detail in the next chapter when we discuss the effect of heterogeneity on elastic property calculations.

To show the heterogeneity in the simulated granular packs, we choose the reference states created using the servo-control mechanism. Henceforth, most of our analyses (including the ones in the next chapter on property estimations) are based on results from the servo-control BC.

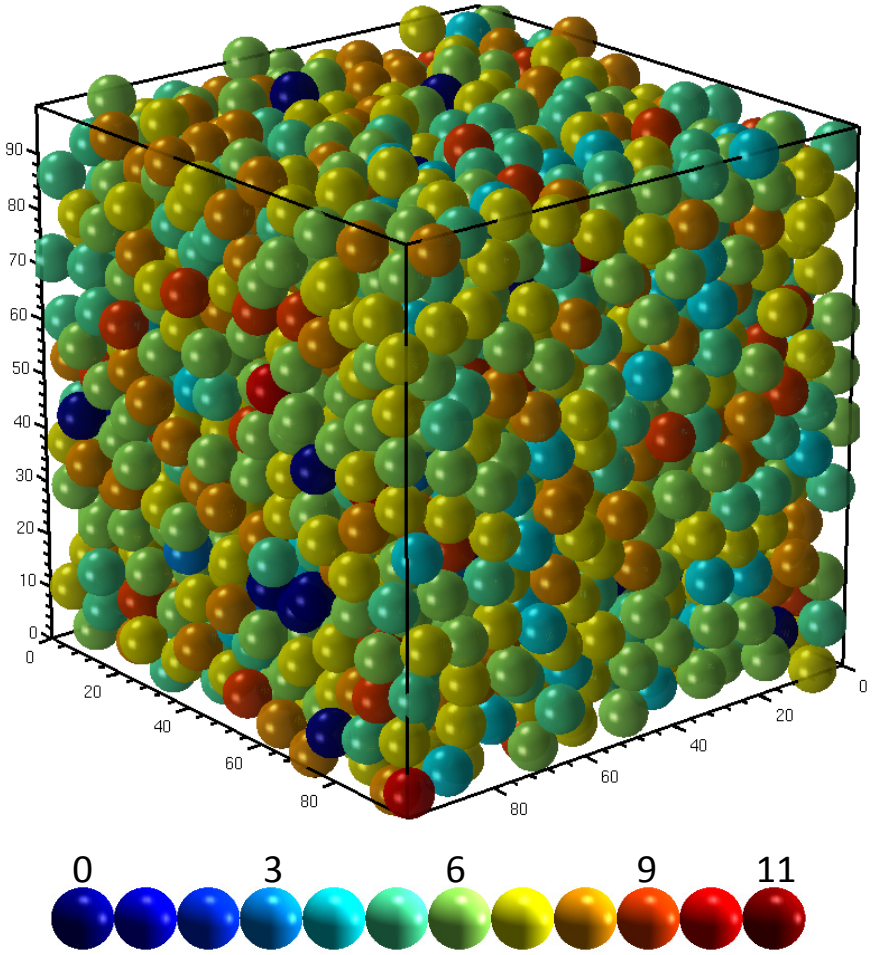

Figure 3.9: Granular pack colorcoded by CN at 10 Mpa pressure.

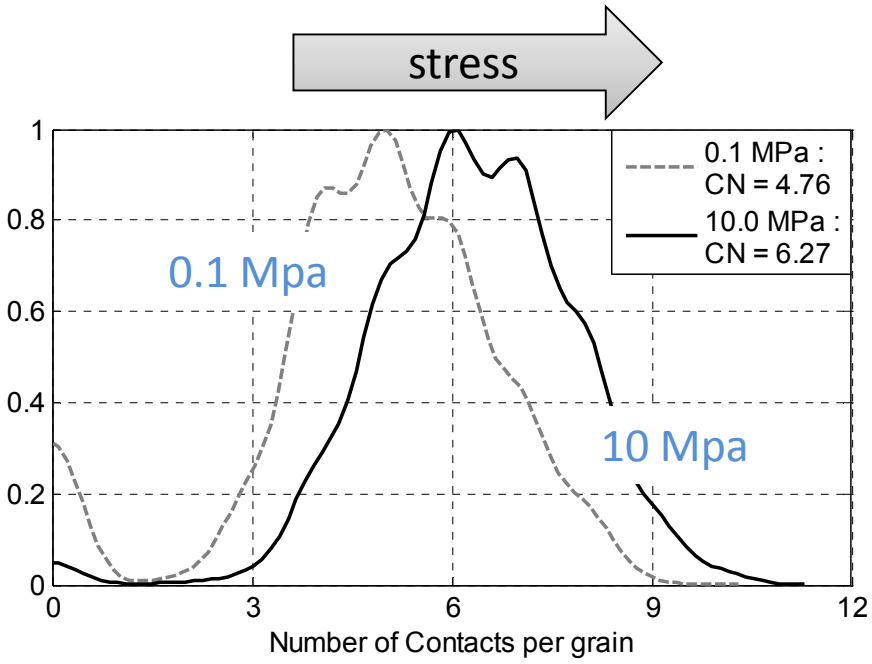

Figure 3.10: Distribution of number of contacts for each grain at two different isotropic pressures. The distribution shows the spread in the number of contacts per grain, i.e., hetereogeneity in terms of contacts. The spread shifts to higher values under increasing stress. (Y-axis: PDF)

Well ordered packs, like hexagonal close packs or simple cubic packs, have a CN of 12 and 6, respectively, which is also the same as the number of contacts each grain has in such packs. However, random close packs have a wide variation in contacts per grain. We choose two reference states at 0.1 MPa and 10.0 MPa. The number of contacts per grain in the pack shows a wide distribution, ranging from zero to ~10 (Fig. 3.9 – 3.10). The existence of grains with zero contacts has been discussed earlier. We also note that the number of floaters decreases with increasing stress, thereby showing that floaters join contact networks or the 'backbone' of the pack. While these floaters can be excluded when comparing theoretical elastic properties, which depend only on the number of grains in the contact network, it is important to include them for geometrical analyses.

The forces in a granular pack are calculated using the contact laws discussed in Chapter 2. The contact laws show that the contact forces are non-linearly proportional to the contact deformations (Chapter 2, Eqn. 2.5 and 2.14). Since the stresses are

related to contact forces and branch vectors (Chapter 2, Eqn. 2.31), the stresses also depend on the contact deformations. While the mean stress in the pack is maintained close to a pre-defined value in the servo-controlled packs, it is worthwhile to study the stresses on each grain. The distribution of contact elastic deformations and mean stress per grain show considerable heterogeneity (Fig. 3.11 – 3.12). These distributions further show the existence of long tails, signifying the existence of contacts with larger than average deformations. We also note that several grains bear higher than average loads, possibly being part of force-chains.

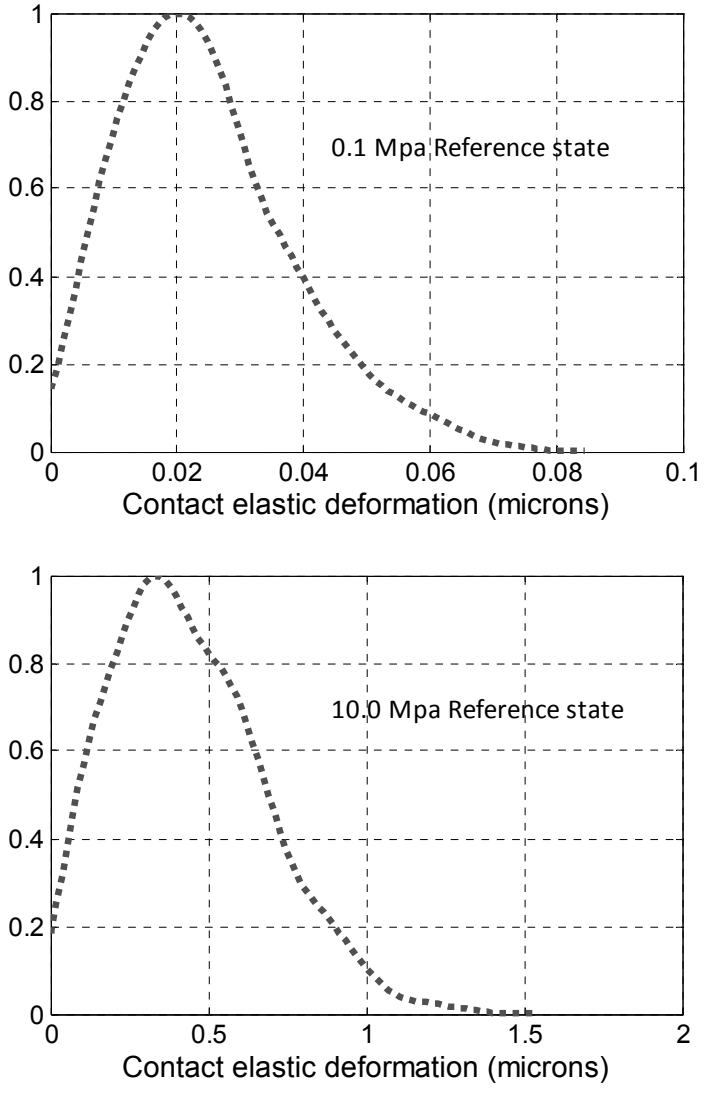

Figure 3.11: Heterogeneity in contact elastic deformations at two different reference states. The change in X-axis scales shows the increase in elastic deformations with increase in average stress of the reference state. (Y-axis: PDF)

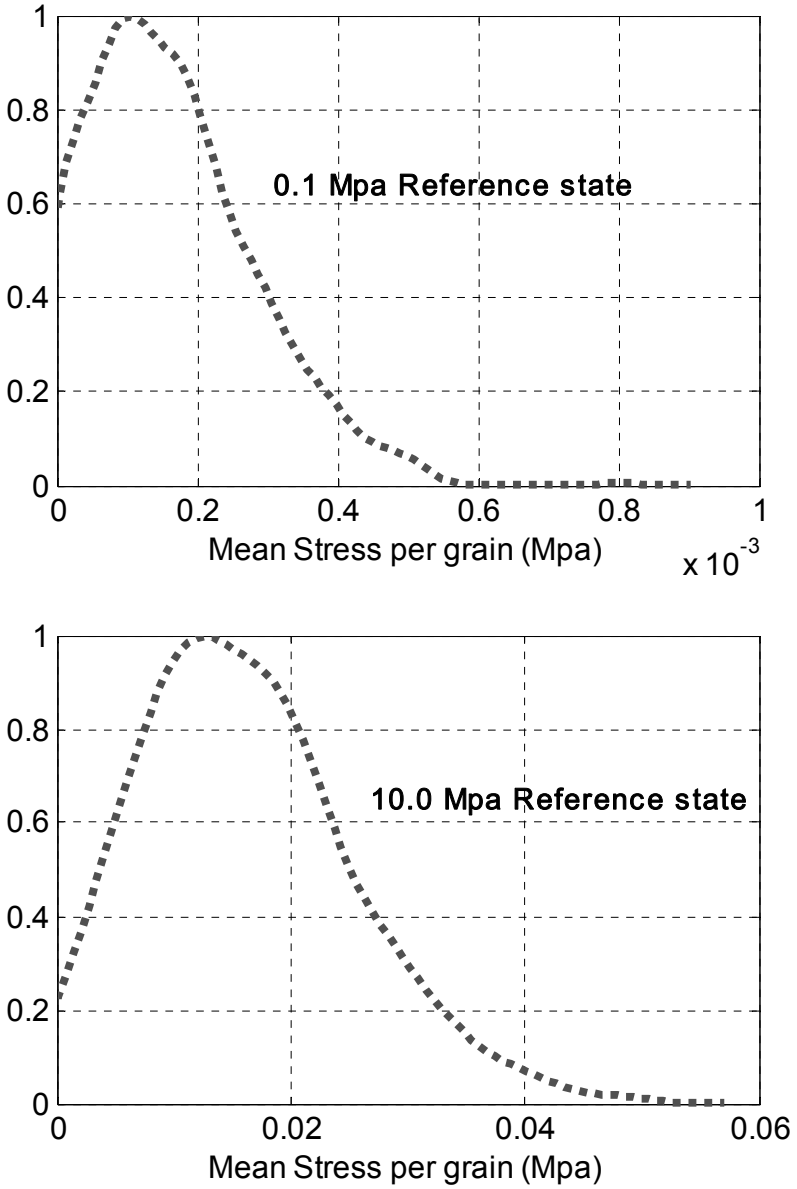

Figure 3.12: Heterogeneity in mean stress on each grain at two different reference states. The change in X-axis scales shows the increase in mean stress on each grain with increase in average stress of the reference state. (Y-axis: PDF)

3.4.4.1. Localization

We showed the existence of considerable heterogeneity in number of contacts for each grain, elastic deformation (hence, forces) for each contact, and mean stress on each grain from our simulated packs. Further, laboratory experiments (Ammi et al.,

1987, Liu et al., 1995, Majmudar and Behringer, 2005) and computer simulations (Radjai et al., 1998, Makse et al., 2004, Makse et al., 2000, Antony, 2000) show that the contact forces are strongly localized along "force chains" (Makse et al., 2005). These chains carry the majority of the load in the granular packs, thus leading to strong localized *heterogeneity* networks. Since the contact forces are non-linear, path-dependent functions of contact deformations, the latter should also show some signatures of localization. Moreover, mean stress on each grain being function of contact forces, they should also show localization. In contrast, if there are relatively long-range crystalline orders in these packs, then the localization would be minimal and there should be spatially homogeneous distribution of deformations or forces or stresses. In this section, we study the degree of localization in: (1) contact deformations; (2) contact forces; and (3) mean stresses per grain using a single *localization index*. We compute a *participation number*, Γ, for each of the three parameters as follows:

$$\Gamma = \left(M \sum_{i=1}^{M} q_i^2 \right)^{-1}$$

where M is total number of contacts or grains in a granular pack, and

$$q_i = d_i \Big/ \sum_{j=1}^{M} d_j$$

where d_j is the deformation at contact j or the total contact force at a contact j or the mean stress on grain j. For the case of spatially homogeneous distribution of these parameters, Γ equals 1, whereas for the limiting case of total spatial heterogeneity or complete localization, Γ approaches *1/M*.

We plot the participation number for both contact deformation and contact forces with pressure and find that it remains constant for the pressure ranges considered in our simulation, viz. 0.05 MPa to 20 MPa (Fig. 3.13). The individual values are lower than 1 and are in the same range as reported by Zhang and Makse (2005). For pressure ranges studied by Zhang and Makse (2005), viz. 0.1MPa to 1 GPa, they observed an

increase in the participation number (for contact forces) with increasing pressure above 10 MPa, indicating that contact forces are gaining spatial homogeneity with increasing stress. However, for our pressure ranges, viz. 0.05 MPa to 20 MPa, the participation numbers for contact deformation and total contact force remain almost constant. However, participation number for mean stress on each grain increases with compaction, unlike those of contact deformation or contact forces. This signifies that with increasing stress, the mean stress on each grain becomes less heterogeneous spatially.

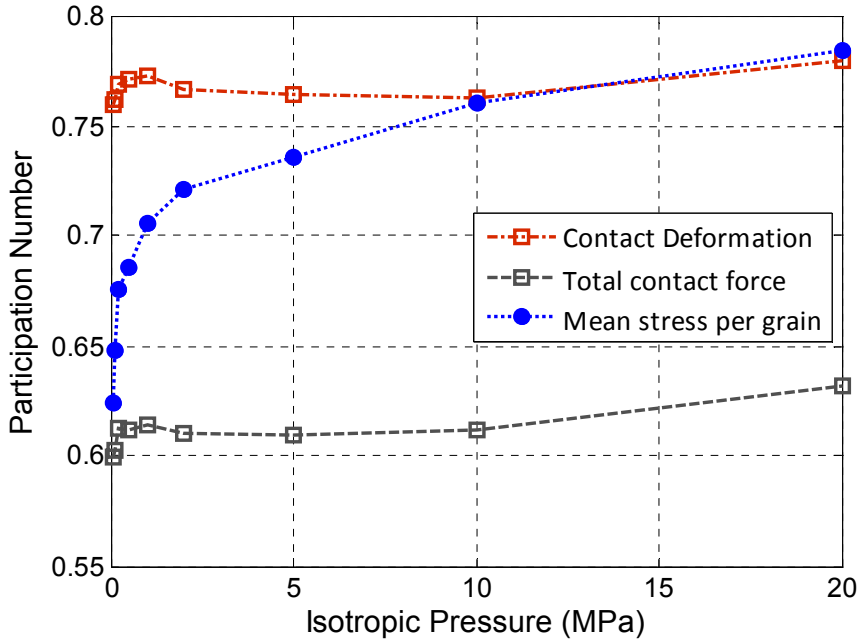

Figure 3.13: Participation number of contact deformation, total contact forces and mean stress per grain. Contact deformations or normal contact overlaps are more *homogeneous* than forces. This can be interpreted by the existence of tangential forces which are path-dependent, resulting in a different heterogeneity for contact forces. Mean stress per grain becomes less heterogeneous spatially with compaction, thereby signifying that all grains start sharing equal loads under more stress.

3.4.4.2. Radial distribution function

The radial distribution function (RDF), also known as the pair correlation function, is a measure to determine the spatial correlation between particles in a system. RDF is typically used in statistical mechanics studies relevant for atomistic and fluid simulations. However, the usage of RDF for random heterogeneous systems, like

granular packs, is essential for studying bulk properties based on microscopic interacting entities, like grains (Torquato, 2001).

RDF gives the probability of finding a pair of grains a distance *r* apart, relative to the probability expected for a *completely* random distribution of grains at the same density (Allen and Tildesley, 1987). The RDF is usually determined by calculating the distance between all grain pairs and binning them into a histogram. The histogram is then normalized with respect to a completely random system (i.e., number density), where grain distances are completely uncorrelated. We compute RDF for two granular packs which are compacted to 10 MPa isotropic pressure using servo-control BC (Fig. 3.14). We note the peaks at r/D = 1, $\sqrt{3}$ and 2 (where r is the radial distance and D is grain diameter), similar to reported simulated packs by Agnolin and Roux (2007), Zhang and Makse (2005) and O'Hern et al. (2003).

The two RDFs in Fig. 3.14 refer to two granular packs with different model sizes or simulation cubes and have different decay lengths with respect to r/D. For a simulation box length of L, it is meaningful to study correlations only up to one-half or one-third of the box length. It should be noted that the dimensions of simulation cube depend on both the number of grains and the individual grain radii. The pack with smaller number of grains (621) has a cube length of 1600 microns and the grain diameters are 200 microns. Hence, correlations beyond r/D of 4 (i.e., 800/200) should typically decay, as shown in Fig. 3.14. For the pack with 2000 grains, the box length is 1000 microns and grain diameter is approximately 85 microns. Hence, we note that r/D shows decay beyond 6 units (i.e., 500/85). For important microstructural properties like CN or the fabric tensor, our results with smaller model sizes are significantly close to published results. At the same time, we reduce computation time and computer memory requirements with the smaller model size.

We also analyze the impact of pressure on RDF for the smaller model size (621 grains), as shown in Figure 3.14. We note that the first and second peaks translate towards lower r/D values with increasing pressure. Further, Truskett et al. (1998) claims that the "shoulder pattern" of the second peak (Fig. 3.15) corresponds to the

formation of a structural order, identifiable as local four-particle hexagonal close pack arrangements which reduces the overall energy of the granular system.

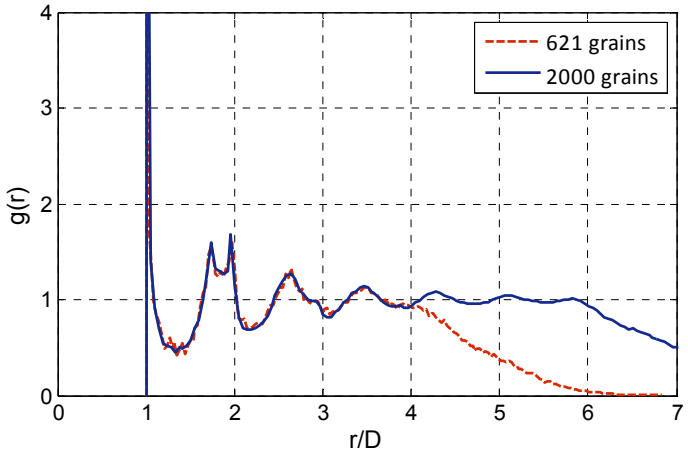

Figure 3.14: RDF for granular packs compacted to 10 Mpa pressure for two different model sizes. Grain radius in pack with 621 grains is approximately double the radius in the pack of 2000 grains. Because of the smaller pack size and larger radius, the RDF decays faster in the pack with 621 grains.

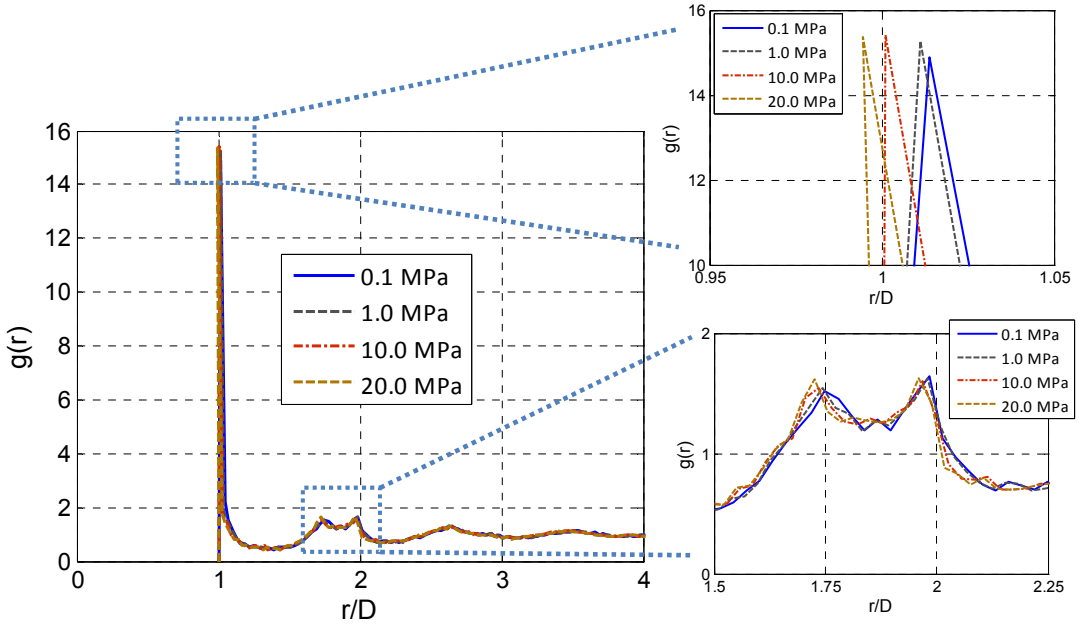

Figure 3.15: RDF of a pack of 621 frictional grains at four different isotropic pressures: 0.1 MPa, 1.0 MPa, 10.0 MPa and 20.0 MPa. The first and second peaks show gradual shift towards lower *r/D* values with increasing pressures.

3.4.4.3 Non-contact nearest-neighbor distance function

Another important microstructural parameter is the non-contact, nearest-neighbor distance function or the "gap distribution function". This is the distribution of distances to nearest neighbors for each grain excluding its contacts. In a way, this corresponds to the second peak of RDF. Pride and Berryman (2009) use a parametric form of this distribution to propose a homogeneous strain-based method to calculate elastic properties. It should be noted that even though their method involves a heterogeneous contact-strain formulation, the method still involves homogeneous *effective* strain and hence can be classified as an Effective Medium Theory (EMT) model. They assume that the gap distribution function is a power-law distribution. From our simulated packs with servo-control mechanism, we choose five different isotropic pressures and compute the distance density function (Fig. 3.16). We note that the distribution shifts to more than one diameter with increasing pressure. For lower pressures, many of the non-contact nearest neighbor grains are close to one grain diameter. However, with higher pressures the non-contact nearest-neighbors are further apart. This behavior of the distance density functions with increasing pressures can be interpreted in terms of the stress—CN relations (Fig. 3.4 and 3.6). The increase in CN with stress is more significant for lower pressures (< 2.0 MPa) compared to higher pressures. This evolution is due not only to formation of new contacts between grains already in the contact network (due to grain rearrangement), but also to 'floaters' or 'rattlers' (grains with zero contacts) joining the contact network. At lower pressures, more grains are closer to each other, as seen from the nearest-neighbor distance functions (peak close to one grain diameter). However, with increasing pressure, grains are spatially farther (peak of nearest-neighbor distance function more than one grain diameter), although there is overall decrease in pack volume.

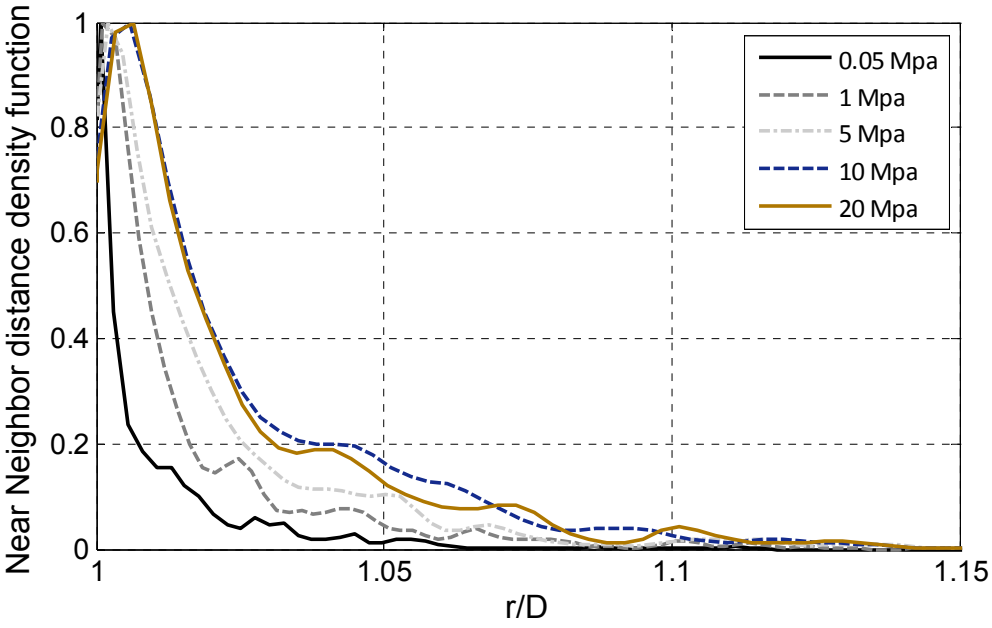

Figure 3.16: Density function for non-contact, nearest-neighbor distances at different pressures. X-axis represents how far the non-contact nearest-neighbors of a grain are located in terms of grain diameter units. Most neighbors (peak in the density function) are located close to one grain diameter at lower stresses. However, these neighbors form contacts with stress, and hence at higher stresses the non-contact nearest-neighbors are farther than the ones at lower stress (shift in peak with stress).

3.5 Polydisperse packs

For real earth sediments, it is more common to have a wider grain-size distribution than a strictly unimodal distribution. In the geology and stratigraphy literature, sediments are often classified as being well-sorted or poorly-sorted based on the grain-size distribution. Furthermore, for reservoir characterization in the oil and gas industry, it is very important to understand the physical properties of these poorly sorted sediments. The macroscopic physical properties of unconsolidated, poorly sorted sediments are affected by lithology (mineralogy and grain-size distribution) and compaction. For studying the effect of mineralogy and sorting, several empirical and heuristic models are used. The existing effective-medium models for well-sorted (strictly speaking, monodisperse) packs are used to predict the effects of compaction by changing different model parameters. In short, a rigorous analysis of the effect of sorting on microstructural and physical properties has been mostly absent.

With the advent of computational rock-physics tools like GD simulation, we can conduct a more rigorous analysis of microstructural details in poorly sorted packs. As a starting point, we restrict ourselves to spherical grains and study the effect of grain size, mineralogy and compaction in detail. We prepare bidisperse packs as our first deviation from monodispersity. We have studied the effect of different radius ratios on porosity and CN. For these packs, we also study the effect of compaction. Then, we present the microstructural properties for truly polydisperse packs. As mentioned earlier, the preparation of stable granular packs or jammed packs with multimodal size distributions is a computationally challenging job. In the next section, we describe our preparation protocol, and then we follow it with our results from simulations. In Chapter 4, we will evaluate the validity of commonly used heuristic models for estimating elastic properties of polydisperse packs.

3.5.1. Preparation protocol: Hybrid EDMD-GD simulation

For monodisperse grain packs, we used two different boundary conditions and two different compaction protocols to create stable jammed packs. These packs were created using GD simulation alone. For the unimodal grain size distribution, GD simulation creates jammed packs within reasonable computation time. However, creating jammed packs for widely different grain sizes is computationally too expensive for GD simulation and the algorithm fails to create stable *strictly jammed* packs. Hence, as discussed earlier (Section 3.3), we use a hybrid model involving both Event Driven Molecular Dynamics and Granular Dynamics. EDMD is an efficient algorithm to create jammed packs for bidisperse and polydisperse packs (Donev, 2006, Poschel and Schwager, 2005). However, these packs consist of frictionless grains and do not allow direct interpretation of physical quantities like stress. Hence, for multimodal grain-size distributions we create jammed packs using EDMD and then use them as an input to GD simulation. We set the coefficient of friction to a finite value of 0.3 and then compact them to different isotropic pressures. This method is similar to one of the servo-control mechanisms we earlier discussed for monodisperse packs, where we use frictionless grains initially and then set the friction to a finite

value. Since we already have a configuration very close to a random close pack using frictionless grains, we cannot implicitly study the effect of friction during the initial compaction process. This would result in dense packs for most cases. Nevertheless, this is an efficient way to study polydisperse packs and the effect of compaction. Moreover, as we mentioned for monodisperse packs, this scenario mimics the realistic case of lubricated grains during assembling process and hence is one of the various ways to study polydisperse packings.

For bidisperse packs, we use four different radius ratios and create jammed packs with different volume fractions for each of these ratios. We then compact them to 10.0 MPa pressure and compare the physical properties of these packs. We also choose one size ratio for which to study compaction in more detail. Since bi-modal mixture models are often used in rock physics to study sand-shale mixtures, we also present some initial results of bidisperse packs using different material properties corresponding to sand and shale. However, it should be noted that shale particles are usually not spherical in shape, so using spherical 'shale' grains is rather unrealistic. A more rigorous treatment may include spherical sand grains and ellipsoidal shale particles. Nevertheless, this exercise explores the effect of mineralogy on packing.

For polydisperse packs, we create four jammed packs with Gaussian size distributions having different standard deviations. As is common in grain-size analysis studies, we define a sorting index based on the standard deviation and mean grain size from these distributions, and then analyze the porosity and CN. We also compact these packs to five different isotropic pressures and analyze the effects of compaction.

3.5.2. Bidisperse pack

We choose four different radius ratios, also known as bi-dispersity ratios: 1:1.2, 1:1.5, 1:2 and 1:3 (Fig. 3.17). The EDMD simulation gives us the initial packs for these size ratios, which we then use as inputs to GD simulation for creating stable compacted packs at 10 MPa pressure (unless otherwise mentioned). The choice of 10 MPa is arbitrary and has been chosen as a measure to compare microstructural properties at some reference value. All the results are presented in terms of volume

fraction of grains. Hereafter, any reference to fraction of grains means specifically the volume fraction.

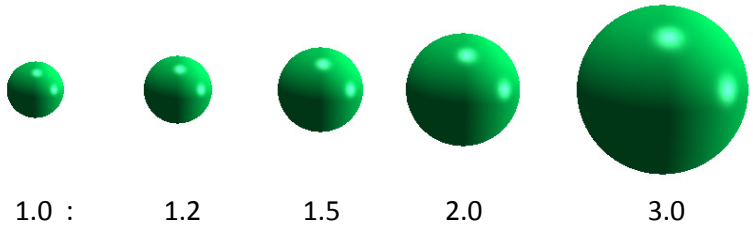

Figure 3.17: Visual representation of size ratios in bidisperse packs

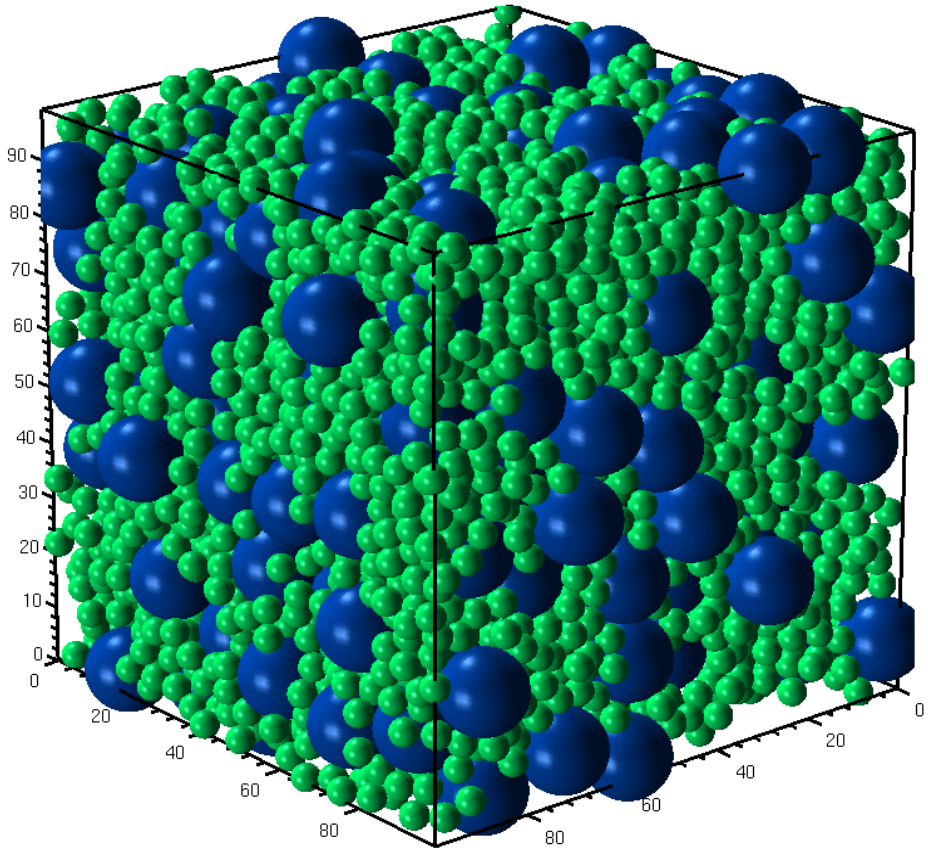

Figure 3.18: Visual representation of bidisperse packs

3.5.2.1. Porosity–Coordination Number–Pressure

To study the effect of radius ratio on porosity, we create stable jammed packs compacted to 10 MPa pressure for different volume fractions. We find that the

porosity varies for different volume fractions and for different size ratios (Fig. 3.19). In fact, for higher size ratios or more bi-dispersity, the change in porosity with various volume fractions is quite distinct. For a radius ratio of 1:3, the porosity of a pack with ~75% large grains is lower than that of 100% large grains by about 7%. We also note that the trough in the porosity–volume fraction plot (Fig. 3.19) deepens with higher size ratios. For realistic analysis involving sand and shale, where the size ratios are about 1:100, the study of porosity is an interesting problem. It should be noted that even though we: (a) do not simulate such high radius ratios and (b) do not consider the impact of initial friction in this analysis, it can still be relevant to hypothesize that the final porosities of realistic sand–shale mixtures depend on many conditions and should not be merely based on volumetric assumptions of filling up the pore-space completely with smaller grains.

Compaction affects physical and elastic properties in a non-linear way. To study the effects of compaction on these various packs, we choose a constant radius ratio of 1:2 and created bidisperse packs at four different pressures: 0.5, 2.0, 5.0 and 10.0 MPa. For this study, we used the material properties of quartz (Fig. 3.21), instead of glass (Fig. 3.19). The general functional form for change of porosity or CN with volume fraction of large grains remains the same at different pressures (Fig. 3.21 and 3.22). However, at any volume fraction, the porosity or CN variation with pressure is non-linear. We also note that as we increase the radius ratios, the trough in the CN–volume fraction plots (Fig. 3.20 and 3.22) have very low values (~2), meaning that there are two contacts per grain on an average. It should be noted that as we increase the size ratios, we have very strong localization in terms of contact forces and contacts. The large grains form very strong contact networks and the smaller grains mostly remain as floaters. Hence the average number of contacts (CN) in the whole pack is as low as two. We also calculated CN using the grains participating in the contact network (i.e., excluding the floaters) and found CN close to the usual values between 4 and 6, as in monodisperse packs.

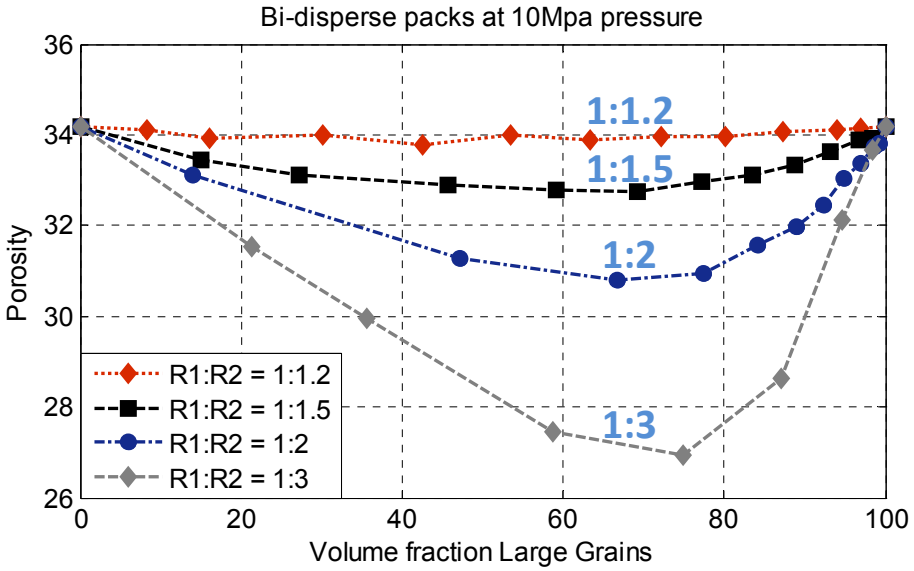

Figure 3.19: Porosity variation with volume fraction of large grains for different size ratios. Same material properties are used for both sizes (glass).

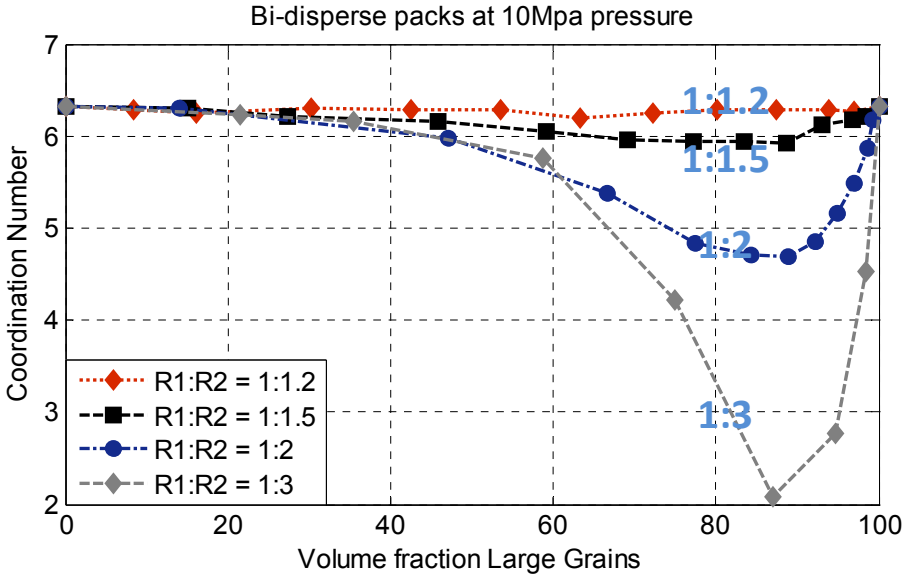

Figure 3.20: CN variation with volume fraction of large grains for different size ratios. Same material property are used for both the sizes (glass). We note that the CN for radius ratio of 1:3 at ~75% volume of large grains is considerably lower. We find that this is because the smaller grains are mostly floaters and the large grains form a strong load bearing network.

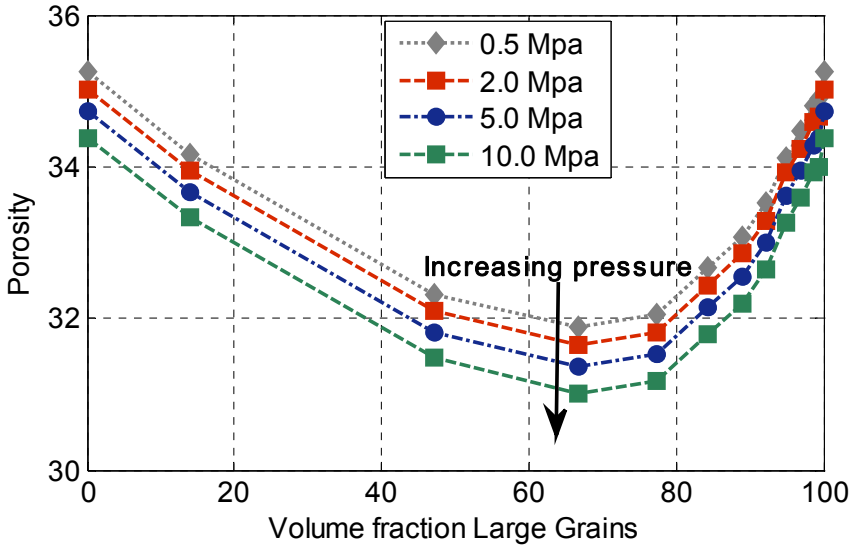

Figure 3.21: Compaction effects on porosity variation with volume fraction of large grains for size ratio of 1:2. The same material properties are used for both sizes (quartz).

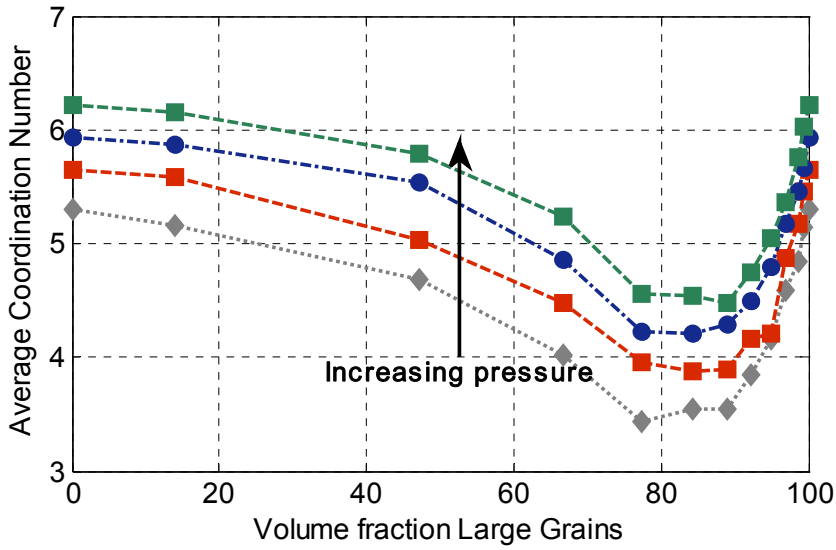

Figure 3.22: Compaction effects on CN variation with volume fraction of large grains for size ratio of 1:2. The same material properties are used for both sizes (quartz).

The above analysis considers the same mineralogy for all the grains. However, in natural sediments and many experimental artificial samples, there is more than one type of mineral. To study the effect of mineralogy, we consider sand–shale mixtures with two radius ratios—1:2 and 1:3—and compare them with mixtures containing the

same materials for both grain sizes (Fig. 3.23 and 3.24). We note that mineralogy also affects a physical property like porosity. The left-most side on Figures 3.23 and 3.24 shows the porosity and CN for a pure clay pack. This is different from the right-most endpoint showing pure sand pack or glass pack. As in the monomineralic case in Figures 3.19 and 3.20, we note the deepening trough shape for higher radius ratios for sand–clay mixtures.

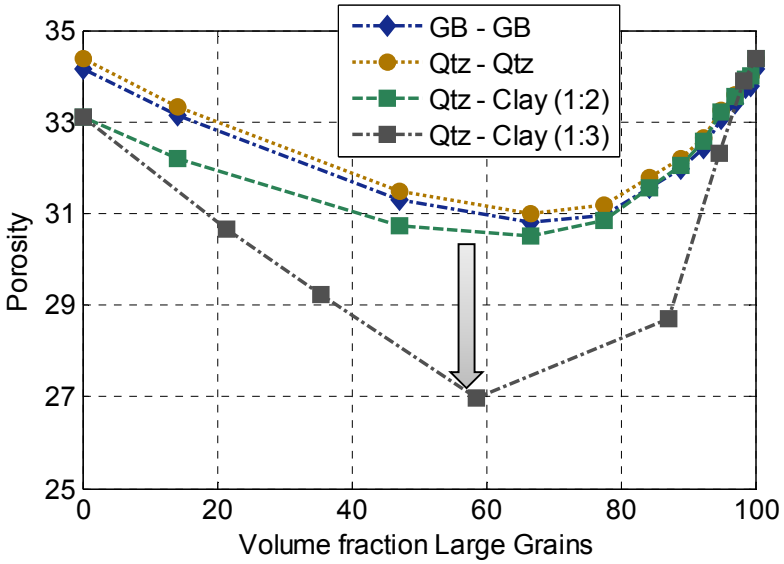

Figure 3.23: Effect of mineralogy on porosity–volume fraction relations.

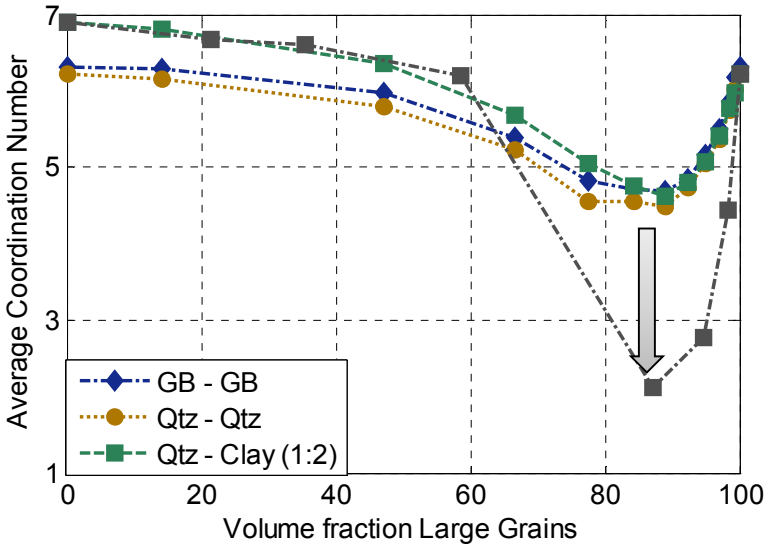

Figure 3.24: Effect of mineralogy on CN–volume fraction relations.

3.5.3. Polydisperse pack with pre-defined distribution

Natural unconsolidated sediments like beach sands or borehole cores mostly show different grain sizes, typically having some characteristic distribution. Stratigraphers often classify sediments as well sorted or poorly sorted, where sorting refers to the spread of the grain-size population. Sorting can be quantified by standard measures of dispersion like standard deviation, interquartile range or absolute deviation. There is no general agreement on which statistical parameters are the most appropriate descriptors of sorting (Flórez-Niño, 2005). Among the various measures of dispersion, some authors have chosen the Coefficient of Variation (CoV) as a descriptor of sorting and have called it the Sorting Index (SI). We adopt the same terminology to describe our polydisperse grain packs with wide size distribution. Poorer sorting are represented by higher SI.

We choose Gaussian size distributions with different SI and create initial jammed packs using EDMD. We then compact them to different pressures and study their physical properties. The analyses are similar to the earlier section on bidisperse packs; however, in this section we have more realistic size distributions. We study the evolution of porosity and CN with pressure for packs with different SI. It should be noted that the choice of a Gaussian distribution is arbitrary, and any pre-defined distribution relevant to a realistic sample can be used for this simulation.

3.4.3.1. Porosity–Coordination Number–Pressure

We create four Gaussian size distributions with different SI: 0.09, 0.18, 0.30 and 0.45. The jammed configurations from EDMD are slightly changed by removing some of the grains with the smallest radii, without changing the SI by a significant amount. Since the smallest grain radius determines the critical time step in GD simulations, elimination of the smallest grains increases the time step and ensures that the integration steps are not too small. On the other hand, this alters the jamming configuration slightly. Since this configuration is still close to the overall energy minima, the GD simulation does not require a particularly large computation time to re-jam the packing. These packs are then compressed to five different pressures. We compare our porosities at lowest simulated pressure (1 MPa) with laboratory samples

(Sohn and Moreland, 1968). We find that the simulated packs have porosities reasonably close to laboratory experiments for different SI (Fig. 3.25). The change in porosities with pressure (or strain–stress relation) is not significantly dependent on porosity; however, poorer sorting can be related to higher loss of porosity in general (Fig. 3.26).

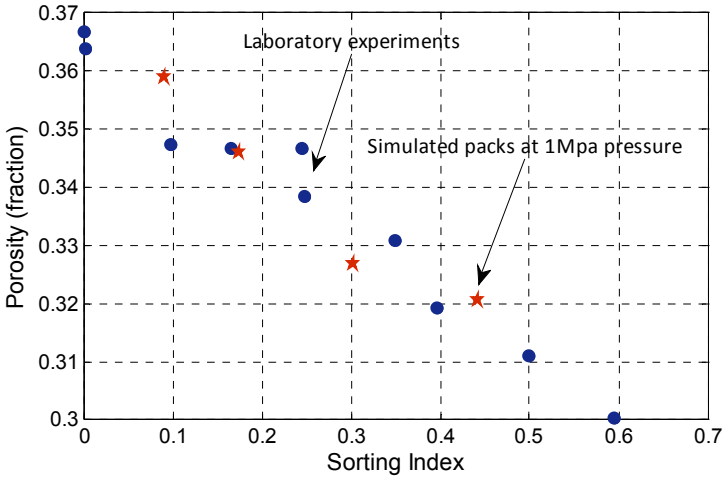

Figure 3.25: Comparison of porosity of simulated packs with laboratory samples (Sohn and Moreland , 1968). Even though our simulated packs are simulated using frictionless grains during initial packing (EDMD) and then compacted with finite friction, we match laboratory porosities reasonably well.

The simulated granular packs help us to analyze the microstructure in much more detail. While our simulated near-critical porosities (low-pressure packs) are close to laboratory experiments (Fig. 3.25), we can also check the internal microstructure, unlike with laboratory samples. We notice that the CN–pressure relations can be related to SI for the distributions we considered (Fig. 3.27-29). The initial CN (at critical porosity or low pressure) is different for different SI. However, we can estimate a functional fit of critical CN (i.e., CN at critical porosity) and SI (Fig. 3.28). The extrapolation of the relation to an SI of 0, which corresponds to a monodisperse pack, yields a CN which is close to the nearly frictionless case considered by Magnanimo et al. (2008) (Fig. 3.6). We propose that this relation can be used for packs with SI in the range considered here. However, this relation should be used cautiously, since it is empirical and is mostly reliable within the data range it is based on (SI: 0.0 ~ 0.5).

We further analyze the pressure dependence of CN for different sorting and present empirical power-law fits to CN–pressure data from simulated packs (Fig. 3.29). We note that the power-law coefficient of the pressure dependence is linearly related to SI (Fig. 3.30). For elastic property estimation using effective medium models, CN–pressure relations are required. Such relations have been reported from both simulations and experiments for monodisperse packs (Makse et al., 2004, 2005, Garcia and Medina, 2005, Murphy, 1982). We have also presented CN–pressure relations from our simulations (Section 3.4.3.1). For polydisperse packs, however, these relations have not been reported in the literature.

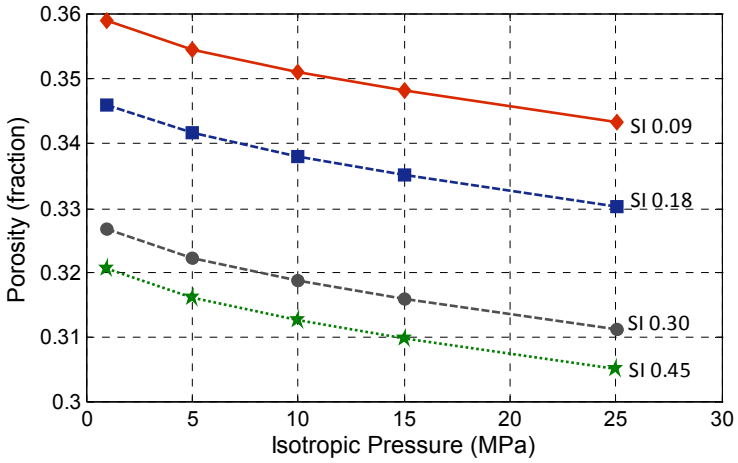

Figure 3.26: Effect of compaction on porosity for packs with different sorting. Poorly sorted packs tend to compact more, significantly as pressure increases.

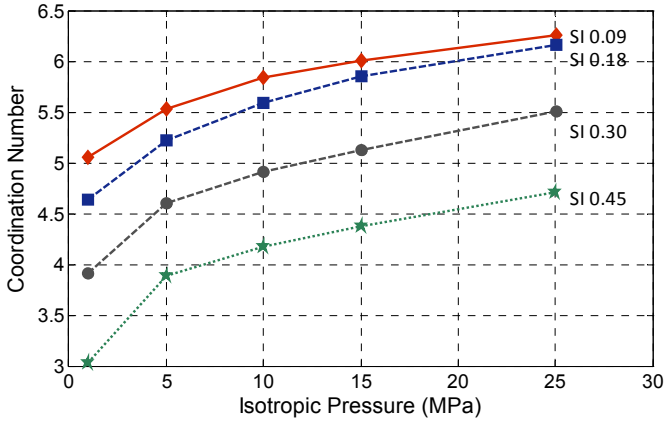

Figure 3.27: Effect of compaction on CN for packs with different sorting.

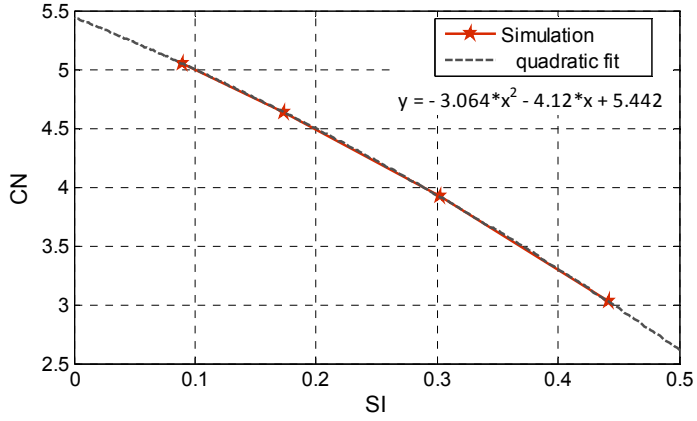

Figure 3.28: Empirical fit to initial CN (at 1Mpa pressure) of packs with different SI.

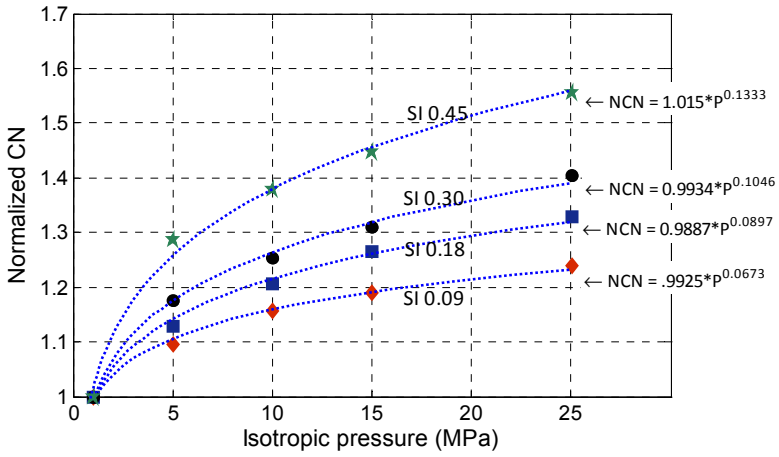

Figure 3.29: Empirical fit to pressure dependence of CN for different sorting. Poorly sorted packs show higher rates of increase of CN with pressure.

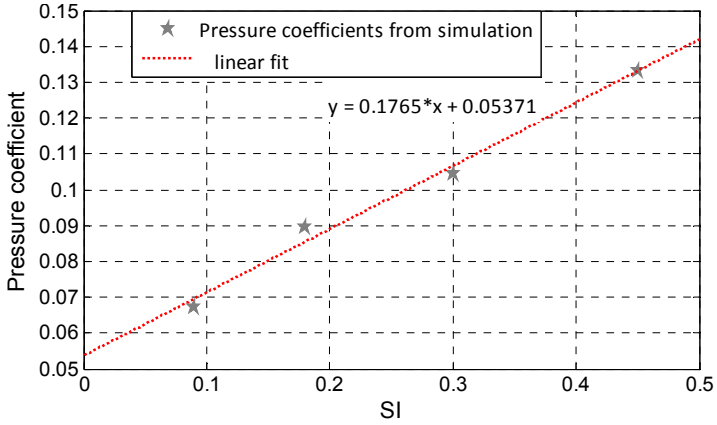

Figure 3.30: Rate of increase of CN (pressure dependence coefficient) shows a linear relationship with SI.

3.6 Summary and conclusions

In this chapter, we have presented an exhaustive microstructural analysis of simulated monodisperse and polydisperse packs. Monodisperse packs are created and compacted using GD simulation. Initial jammed polydisperse packs are created using EDMD simulation and compacted further using GD simulation.

We have shown the non-uniqueness in porosity–coordination-number–stress relations, which are mostly commonly used in theoretical compaction (EMT) modeling. Hence, we point out some of the key factors to account for while using these models. In the next chapter, we discuss more about the pitfalls of the EMT modeling, specifically how the homogeneous strain approximation leads to erroneous predictions due to the heterogeneous nature of granular packs. The presence of heterogeneity in the fabric and its evolution has been shown in this chapter. All these analyses form a pre-requisite for our discussions on elastic property estimations.

For polydisperse packs, we have shown the dependence of fabric properties on mixing proportions, mineralogy and compaction. Our simulated polydisperse packs have porosities reasonably close to those from laboratory experiments. We have presented empirical relations to compute CN at different pressures for packs with SI ranging from 0.05 to 0.5. In the next chapter, we use these microstructural analyses to predict elastic properties based on conventional heuristic models for poorly sorted sediments.

3.6 References

Agnolin, I. and Roux, J.-N., 2007, Internal states of model isotropic granular packings. I. Assembling process, geometry, and contact networks, Phys. Rev. E 76, 061302.

Agnolin, I., Roux, J.-N., Massaad, P., Jia, X. and Mills, P., 2005, Sound wave velocities in dry and lubricated granular packings: numerical simulations and experiments, Powders and Grains, Stuttgart, Allemagne.

Allen, M. P. and Tildesley, D. J., 1987, Computer Simulations of Liquids. Oxford Science Publications.

Ammi, M., Bideau, D. and Troadec, J. P., 1987, Geometrical structure of disordered packings of regular polygon: comparison with disc packings structures, J. Phys. D 20, 424.

Antony, S. J., 2000, Evolution of force distribution in three-dimensional granular media, Phys Rev E 63, 011302.

Aste, T., Saadatfar, M., Sakellariou, A. and Senden, T. J., 2004, Investigating the geometrical structure of disordered sphere packings, Physica A 339, 16

Aste, T., Saadatfar, M., and Senden, T.J., 2005, Geometrical structure of disordered sphere packings, Physical Review E 71 061302.

Bargiel, M. and Moscinski, J., 1991, C-language program for the irregular close packing of hard spheres. Comp. Phys. Comm., 64:183–192.

Bennett, C. H., 1972, Serially Depositied Amorphous Aggregates of Hard Spheres. J. Appl. Phys., 32(6):2727–2734.

Bernal, J.D., Mason, J. and Knight, K.R., 1962, Radial distribution of the random close packing of equal spheres, Nature, 188, 910.

Berryman, J. G., 1983, Random close packing of hard spheres and disks, Phy. Rev. A 27 2, 1053.

Bezrukov, A., Bargiel, M. and Stoyan, D., 2002, Statistical analysis of simulated random packings of spheres. Part. Part. Syst. Charact., 19:111–118.

Bideau, D., and Dodds, J., 1991, Physics of granular media, Nova Science, Commack, New York.

Brujić, J., Song, C., Wang, P., Briscoe, C., Marty, G. and Makse, H., A., 2007, Measuring the coordination number and entropy of a 3D jammed emulsion packing by confocal microscopy, Phys Rev Lett, 98, 248001.

Bryant, S. L., Lerch, C. and Glinsky, M. E., 2009, Critical grain-size parameters for predicting framkework and "floating" grains in sediments, J Sed Res, 79, 817-830.

Buchalter, B. J. and Bradley, R. M., 1992, Orientational order in random packings of ellipses. Phys. Rev. A, 46(6):3046–3056.

Clarke, A. S. and Wiley, J. D., 1987, Numerical simulation of the dense random packing of a binary mixture of hard spheres: Amorphous metals, Phys Rev B 35, 7350-7356.

Coelho, D, Thovert, . J.-F. and Adler, P. M., 1997, Geometrical and transport properties of random packings of spheres and aspherical particles. Phys. Rev. E, 55(2):1959–1978.

Cowin, S. C., 1985, The relationship between the elasticity tensor and the fabric tensor, Mech of Matls, 4, 137-147.

Cumberland, D.J. and Crawford, R.J., 1987, The packing of particles, Handbook of Powder Technology, Vol. 6, New York, Elsevier.

Cundall, P. A. and Strack, O. D. L., 1979, A discrete numerical model for granular assemblies: Geotechnique, 29(1):47–65.

Domenico, S. N., 1977, Elastic properties of unconsolidated porous sand reservoirs, Geophys., 42(7), 1339-1368.

Donev, A., Torquato, S. and Stillinger, F.H., 2005a, Neighbor list collision-driven molecular dynamics simulation for nonspherical hard particles. I. Algorithmic details, J Comp Phys, 202 2 737-764

Donev, A., Torquato, S. and Stillinger, F.H., 2005b, Neighbor list collision-driven molecular dynamics simulation for nonspherical hard particles. II. Applications to ellipses and ellipsoids, J Comp Phys, 202 2 765-793

Donev, A., 2006, Jammed packings of hard particles, Ph.D. thesis, Princeton University, NJ.

Finney, J. L., 1970, Random packings and the structure of simple liquids. I. The geometry of Random Close Packing, Proc. R Soc Lon, Ser A, Mathematical and Physical Sciences, 319, 1539, 479-493.

Flórez-Niño, J. –M., 2005, Integrating geology, rock physics, and seismology for reservoir quality prediction, Ph.D. thesis, Stanford University, Stanford, CA.

Garc´ıa, X. and Medina, E., 2006, Hysteresis effects studied by numerical simulations: cyclic loading-unloading of a realistic sand model, Geophys., 71 2, F13-F20.

Garc´ıa, X., Araujo, M. and Medina, E., 2004, P-wave velocity–porosity relations and homogeneity lengths in a realistic deposition model of sedimentary rock, Waves Random Media, 14,129-142.

Gotoh, K. and Finney, J. L., 1974, Statistical geometrical approach to random packing density of equal spheres, Nature, 252, 202.

Guodong, J., Patzek, T. D. and Silin, D. B., 2004, SPE90084: Direct prediction of flow properties of unconsolidated and consolidated reservoir rocks from image analysis. In SPE Annual Technical Conference and Exhibition,Houston, Texas, USA.

Guyon, E., Roux, S., Hansen, A., Bideau, D., Troadec, J. –P. and Crapo, H., 1990, Non-local and non-linear problems in the mechanics of disordered systems: application to granular media and rigidity problems, Rep. Prog. Phys. 53, 373

Han, D. H., 1986, Effect of porosity and clay content on acoustic properties of sandstones and unconsolidated sediment, Ph.D. thesis, Stanford University, Stanford, CA.

Hardin, B.O. and Richart, F.E., 1963, Elastic wave velocities in granular soils, J. Soil Mech. Found. Div., ASCE, 89, 33-65.

Herrmann, H.J. and Luding, S., 1998, Modeling granular media on the computer, Continuum Mech. Thermodyn., 10, 189-231

Herrmann, H. J. and Wolf, D. E., 2998, Physics of dry granular media, Balkema, Dordrecht.

Hinrichsen, H. and Wold, D. E., 2004, The physics of granular media, 2004, WileyVCh, Berlin.

Holt, R.M., Kjolaas, J., Larsen, I., Li, L., Pillitteri, A. G. and Sonstebo, E.F., 2005, Comparison between controlled laboratory experiments and discrete particle simulations of the mechanical behavior of rock, Int J Roc Mech Min Sc, 42, 985-995.

Holtzman, R., Silin, D. B. and Patzel, T.W., 2007, Frictional granular mechanics: A variational approach, Int. J. Numer. Meth. Eng., 00:1-6.

House, K. Z., Schrag, D. P., Harvey, C. F. and Lackner, K. S., 2006, Permanent carbon dioxide in deep-sea sediments, Proc. Natl. Acad. Sci. U.S.A. 103, 12291.

Kansal, A. R., Torquato, S. and Stillinger, F. H., 2002, Diversity of Order and Densities in Jammed Hard-Particle Packings. Phys. Rev. E, 66:041109.

Koide, H., Shindo, Y., Tazaki, Y., Ijima, M., Ito, K., Kimura, N. and Omata, K., 1997, Deep sub-seabed disposal of CO2: The most protective storage, Energy Convers Mgmt., Vol. 38, Suppl., S253 – S258.

Konrad, C. S., Drost, B. W. and Wagner, R. J., 2005, Hydrogeology of the unconsolidated sediments, water quality, and ground-water/surface-water exchanges in the Methow river basin, Okanogen County, Washington, U.S.G.S. Water-Resources Investigations report, 03-4244.

Kottwitz, D. A., 1991, The densest packing of equal circles on a sphere. Acta Cryst., 47:158–165.

Kuwano, R., Jardine, R., 2002, On the applicability of cross-anisotropic elasticity to granular materials at very small strain, Geotechnique 52, 727–749.

Latzel, M, Luding, S, Herrmann, 2000, Macroscopic material properties from quasi-static, microscopic simulations of a two dimensional shear cell, Granular Matter, 2, 123-135.

Leibig, M., 1994, Model for the propagation of sound in granular materials, Phys Rev E, 49, 1647-1656.

Liu, C. and Nagel, S. R., 1992, Sound in sand, Phys. Rev. Lett. 68, 2301

Liu, C. and Nagel, S. R., 1998, Jamming is not just cool any more, Nature, 396, 21-22

Liu, C., Nagel, S. R., Schecter, D. A., Coppersmith, S. N., Majumdar, S., Narayan, O. and Witten, T. A., 1995, Force fluctuations in bead packs, Science 269, 513.

Luding, S, 2004, Micro-macro transition for anisotropic, frictional granular packings, Int J Sol Str, 41, 21, 5821-5836.

Luding, S, 2005, Anisotropy in cohesive, frictional granular media, J Phys Condes Matter, 17, S2623 – S2640.

Makse, H. A., Johnson, D. L. and Schwartz, L., 2000, Packing of compressible granular materials, Phys Rev Lett 84, 4160-4163.

Makse, H. A., Gland, N., Johnson, D.L. and Schwartz, L., 2004, Granular packings: Nonlinear elasticity, sound propagation and collective relaxation dynamics, Phys Rev E 70, 061302

Magnanimo, V., Ragione, L. La, Jenkins, J. T., Wang, P. and Makse, H. A., , 2008, Characterizing the shear and bulk moduli of an idealized granular material, Euro Phy Lett, 81, 3.

Mathers, S., and Zalaziewicz, J., 1993, A guide to the sedimentology of unconsolidated sedimentary aquifers, British Geological Survery Technical Report, WC/93/32, 117.

Mueth, D. M., Jaeger, H. M. and Nagel, S. R., 1998, Force distribution in a granular medium, Phys Rev E 57 3.

Murphy, W. M., 1982, Effects of microstructure and pore fluids on the acoustic properties of granular sedimentary materials, PhD. Thesis, Stanford University, Stanford, CA.

Nolan, G. T. and Kavanagh, P. E., 1992, Computer simulation of random packing of hard spheres, Powder Tech., 72:149–155.

Nur, A., Mavko, G., Dvorkin, J. and Galmudi, D., 1998, Critical porosity: A key to relating physical properties to porosity in rocks, The Leading Edge, 17, 357

O'Hern, C. S., Langer, S. A., Liu, A. J. and Nagel, S. R., 2002, Random Packings of Frictionless Particles., Phys. Rev. Lett., 88(7):075507–1

Onoda, G. Y. and Liniger, E. G., 1990, Random loose packing of uniform spheres and the dilatancy onset, Phys. Rev. Lett. E 72, 011301.

Plona, T. J., 1980, Observation of a second bulk compressional wave in a porous medium at ultrasonic frequencies, Appl. Phys. Lett.36, 259-261.

Poschel, T. and Schwager, T., 2005, Computational Granular Dynamics.

Potapov, A. V. and Campbell, C. S., 1996, Propagation of elastic waves in deep vertically shaken particle beds, Phys. Rev. Lett. **77**, 4760

Pride, S. R. and Berryman, J. G., 2009, Goddard rattler-jamming mechanism for quanifying pressure dependence of elastic moduli of grain packs, Acta Mech., 185-196.

Radjai, F., Wolf, D. E., Jean, M. and Moreau, J, -J., 1998, Bimodal character of stress transmission in granular packings, Phys Rev Lett, 80 1.

Roji, R. G., Herrmann, H. J. and McNamara, S., 2005, Powders and Grains, Balkema, Leiden.

Silbert, L. E., Ertaş, D., Grest, G. S., Halsey, T. C. and Levine, D., 2002a, Geometry of frictionless and frictional sphere packings, Phys. Rev. E 65, 031304

Silbert, L. E., Grest, G. S. and Landry, J.W., 2002b, Statistics of the contact network in frictional and frictionless granular packings, Phys. Rev. E 66, 061303

Sinkovits, R. S. and Sen, S., 1995, Nonlinear dynamics in granular columns, Phys. Rev. Lett. 74, 2686

Slater, L. and Lesmes, D.P., 2002, Electrical-hydraulic relationships observed for unconsolidated sediments, W. Res. Resr., 38, 1213, 13

Sohn, H. Y. and C. Moreland, 1968, The effect of particle size distribution on packing density, Canadian Journal of Chemical Engineering, 46, 162-167.

Stillinger, F. H. and Weber, T. A., 1985, Inherent structure of liquids in the hard-sphere limit. J. Chem. Phys., 83(9):4767–4775.

Thane, C., 2006, Geometry and topology of model sediments and their influence on sediment properties, M.S. Thesis, University of Texas at Austin, TX

Thornton, C., 2000, Numerical simulations of deviatoric shear deformation of granular media, Geotechnique, 50 (1), 43-53.

Torquato, S., Truskett, T. M. and Debenedetti, P. G., 2000, Is random close packing of spheres well defined?, Phys. Rev. Lett., 84, 2064

Torquato, S., 2001, Random heterogeneous materials: Microstructure and macroscopic properties, Springer-Verlag, New York.

Travers, T., Ammi, M., Bideau, D., Gervois, A., Messager, J. -C., Troadec, J. -P., 1987, Uniaxial compression of 2D packings of cylinders: Effects of weak disorder, Europhys. Lett. 4, 329

Truskett, T. M., Torquato, S., Sastry, S., Debenedetti, P. G. and Stillinger, F. H., 1998, Structural precursor to freezing in the hard-disk and hard-sphere systems, Phys Rev E, 58, 3, 3083.

Williams, S. R. and Philipse, A. P., 2003, Random Packings of Spheres and Spherocylinders Simulated by Mechanical Contraction. Phys. Rev. E, 67:051301.

Zimmer, M., 2003, Controls on the seismic velocities of unconsolidated sands: Measurements of pressure, porosity and compaction effects, Ph.D. thesis, Stanford University, Stanford, CA

Zinchenko, A., 1994, Algorithm for Random Close Packing of Spheres with Periodic Boundary Conditions, J. Comp. Phys., 114:298–307.

Zhang, H. P. and Makse, H. A., 2005, Jamming transition in emulsions and granular materials, Phys Rev E 72, 011301.

Chapter 4
Granular packs: elastic and transport properties

4.1 Abstract

We estimate elastic and transport properties for compacted frictional random granular packs using computational rock-physics tools. Packs created using Granular Dynamics (GD) simulation show considerable heterogeneity in terms of number of contacts, contact elastic deformations and mean grain stresses. For elastic property predictions in these packs, affine strain-based Effective-Medium Theories (EMTs) are commonly used. An affine or homogeneous strain approximation in these heterogeneous packs, based on EMT, leads to violation of Newton's laws of motion, and the resulting packs are unstable. Hence, elastic properties calculated for these unstable packs are non-physical. GD simulation determines local contact-scale

displacements or *relaxations* required to stabilize such an unstable pack. The relaxation displacements are also heterogeneous and depend on complex multi-body force interactions. Further, we find that elastic property calculations based on stable relaxed packs are much closer to laboratory experiments than are EMT predictions.

An appropriate theoretical model to predict stress-dependent elastic properties in a granular pack should account for the existence and evolution of heterogeneity. Our analyses of key microstructural entities like contact numbers, contact stresses and contact relaxations are a prerequisite for a refined theory accounting for the correct physics. We also show that relaxation affects each elastic modulus or stiffness constant differently and that these constants are stress-dependent. In the absence of a rigorous theory giving closed-form expressions for elastic moduli, we present precise *relaxation correction factors* from GD simulations and their empirical fits with pressure. These correction factors can be applied for stiffness constants calculated using EMT for isotropic and uniaxial compaction. These correction factors are based on first principles and, hence improve the rigor of the estimates.

We also compare stress-strain curves from GD simulation to laboratory measurements. Due to the assumption of isotropy in EMT, the estimated stresses at larger strains are higher than both laboratory measurements and GD simulation. For uniaxial experiments, the ratio of stresses in the horizontal and vertical directions is not well predicted by theories of linear elasticity. However, GD simulation agrees reasonably well with laboratory experiments.

We further present elastic and transport property estimations for polydisperse packs discussed in Chapter 3. Conventional semi-heuristic rock physics models for calculating elastic properties in poorly sorted packs are reasonably correct; however, they require proper estimates for well-sorted pack moduli, especially shear modulus. For compaction-induced changes in permeability, different *geometric factors* in Kozeny-Carman relations are required to match simulated datasets.

4.2 Introduction

The non-linear behavior of the elastic and transport properties of granular materials is an active field of research (Makse et al., 2004, Agnolin and Roux, 2007, Mueth et al., 1997, Tkachenko and Witten, 1998, Chan, 2004). In the realm of geosciences, unconsolidated sediments resemble random granular packs. Geoscientists must understand the properties of unconsolidated sediments if they wish to interpret subsurface geophysical properties, predict shallow geo-hazards and borehole stability, or monitor reservoir and aquifer properties. The physical properties of random granular packs are strongly related to their microstructure. For analytical simplicity, most theoretical studies and numerical simulations use granular *sphere* packs to correlate physical properties with microstructural details (Cumberland and Crawford, 1987, Onoda and Liniger, 1990, Berryman, 1983, Walton, 1987, Keehm et al., 2001, Makse et al., 2004, Schwartz and Banavar, 1989, Guodong et al., 2004).

Elastic properties of random granular packs show highly non-linear behavior under an external confining stress (Behringer and Jenkins, 1997, Goddard, 1990, Makse et al., 2004, Pride and Berryman, 2009). The elastic response of a stressed granular pack can be obtained from *dynamic* experiments like wave propagation (Zimmer, 2004, Domenico, 1977, Murphy, 1982, Agnolin et al, 2005), from resonance modes (Johnson and Jia, 2005, Chen et al., 1988), or from controlled small strain *static* experiments (Kuwano and Jardine, 2002, Shibuya et al., 1992, Geoffrey et al., 2003). Kuwano and Jardine (2002) and Shibuya et al. (1992) mention that elastic behavior of granular packs is applicable in static experiments only for very small strain amplitudes ($<10^{-5}$). If laboratory equipment for static experiments can precisely control such infinitesimal strains, these *static* moduli are comparable to *dynamic* elastic moduli (Agnolin and Roux, 2007). For larger strain amplitudes ($>10^{-4}$), granular packs show a stress-dependent non-linearity, known as geometrical or kinetic non-linearity, associated with mechanical compaction (Makse et al., 2004, Mavko et al., 2009, Johnson and Rasolofosaon, 1996). This behavior relates to large-scale grain rearrangements, and is often associated with grain sliding. The moduli calculated from

stress-strain measurements in these experiments are large-strain static moduli and are usually smaller than dynamic moduli or infinitesimal-strain static moduli.

Walton (1987) describes a theoretical model to predict elastic response of a stressed random sphere pack. The spheres are homogeneous, elastically isotropic and either frictionless or infinitely frictional. The normal and tangential forces between two spheres in contact are calculated using normal and tangential contact stiffness, and corresponding displacements. Finally, this model computes the stress perturbation due to infinitesimal strain perturbation in an initially *strained* granular pack. As with infinitesimal strain experiments, this model yields infinitesimal-strain static moduli estimating the *elastic* response of the grain pack. This theoretical model falls in the general category of Effective Medium Theory (EMT) models (Digby, 1981, Duffy and Mindlin, 1957, Norris and Johnson, 1997, Bachrach and Avseth, 2008, Dutta et al., 2010, Duffaut et al., 2010). EMT unrealistically applies the general framework of continuum elasticity for a disordered granular medium. This implies the applicability of homogeneous mean-field strain at all scales (i.e, for all grains), by assuming homogeneous distribution of contacts around grains. Thereby, the disordered pack is considered an *effective* medium, and the stresses are computed on a single *representative* grain under this mean-field strain (Makse et al., 2004). Using stress-strain relations, elastic moduli are computed, and are usually found to over-predict those from dynamic laboratory experiments (Dutta et al., 2010, Makse et al., 1999). Further, EMT assumes a unique strain energy density function. This means that for *any* applied strain, there is a unique stress. Jenkins et al. (2005) mention that for a frictionless granular pack, calculation of stress using EMT is acceptable. The EMT assumption on unique strain energy and Jenkins et al.'s (2005) claim is valid for non-dissipative systems, like a pack of frictionless or infinitely frictional grains. In these two extreme cases, there is no frictional sliding between grains and hence no dissipative losses. However, realistic granular medium almost always have finite friction. For finite friction case, the stress calculation using EMT is valid only if each grain has homogeneous contact distribution which does not change with strain. The general assumption of *homogeneity* in EMT for granular packs is unrealistic.

The main focus of this chapter is to investigate the validity of EMT assumptions and enhance our understanding of stressed granular materials using simulated grain packs. We use Granular Dynamics (GD) simulation to create stressed granular sphere packs using Hertz-Mindlin contact forces (Hertz, 1982, Mindlin, 1949) between grain pairs. The spheres are homogeneous, elastically isotropic and have finite friction. Our stressed packs are characterized by force equilibrium and qualify as random *jammed* packs. The preparation of compacted packs is associated with grain rearrangements involving realistic frictional sliding between grains and changes in number of contacts for each grain. Frictional sliding is irreversible, and inelastic. Further, this is a consequence of Coulomb's law and finite grain friction (as discussed using Eqn. 2.14 in Chapter 2). Henceforth, grain rearrangements involving sliding are referred as *large-scale* grain rearrangements. For computing elastic moduli in GD simulation, we apply an infinitesimal strain perturbation and monitor the stress perturbation and force equilibrium. We ensure that the response to this strain perturbation is strictly elastic by increasing friction before applying this perturbation and, thereby inhibiting any frictional sliding. This approach is similar to numerical methods reported in the literature (Makse et al., 2004, Magnanimo et al., 2008). We observe that the infinitesimal strain perturbation induces force imbalance and unrelaxed stresses, thereby causing *infinitesimal* grain rearrangements. These rearrangements however do not involve any grain sliding nor changes the number of contacts for any grain, and are henceforth referred as *grain relaxation*. The final elastic moduli are the stress-strain ratio when the pack re-gains force equilibrium and the stresses are relaxed. Our infinitesimal-strain *relaxed* elastic moduli at different isotropic and uniaxial pressures are comparable with dynamic laboratory measurements on glass beads and sand (Domenico, 1977, Zimmer, 2004, Agnolin et al, 2005, Murphy, 1982). Moreover, our infinitesimal-strain *relaxed* elastic moduli are lower than infinitesimal-strain EMT elastic moduli, especially for shear moduli (under isotropic compression).

The primary difference between EMT and GD moduli estimation is the allowance for heterogeneous grain relaxation based on first principles. As an initial guess for applying infinitesimal perturbations to all grains in GD simulation, we homogeneously

distribute strains, similar to EMT. The elastic moduli for this homogeneous strain configuration are referred to as *unrelaxed* moduli, and are approximately same as EMT prediction. Due to the considerable heterogeneity in contact numbers, forces and stresses for each grain in GD simulation (as reported in Chapter 3), this homogeneous strain causes significant force imbalance on grains, hence violating mechanical equilibrium. EMT, in contrast, assumes statistically homogeneous packs and ignores all heterogeneities—contact numbers, contact forces and grain stresses—thereby precluding any force imbalance and estimation of consequent *relaxation*. The assumption of force balance under a homogeneous mean strain is physically realizable only in an ordered packing. The concept of relaxation as a reason for failure of EMT has been reported earlier by Makse et al. (1999, 2004) and Jenkins et al. (2005). In the present work, we investigate the exact causes of such relaxation in great detail and study the first principle reasons why EMT fails. We show that EMT calculations fail to match experimental elastic properties since they *ignore the effects of heterogeneity* and unrealistically assume the validity of mean strain in disordered packs.

We further show that the ratio of relaxed to unrelaxed (or EMT) moduli or the *relaxation correction* is related to the measure of heterogeneity in the stressed pack. As shown in Chapter 3, heterogeneity is stress-dependent. The relaxation correction, similarly, depends on stress. We provide functional forms of relaxation correction with stress for different elastic moduli under different compaction scenarios. We show that EMT calculations with these corrections applied are fairly close to experimental results. These corrections are empirical (exponential fits to rigorous relaxation results from GD) and should *ideally* be used for similar conditions (same mineralogy, similar compaction environment). However, we note that for different material properties (viz. sand and glass), these corrections are reasonably similar.

For uniaxial compaction, we provide relaxation corrections for all independent stiffness elements. We compare simulated stiffness constants with stress-induced anisotropy theory. Mavko et al. (1995) predict elastic properties under non-hydrostatic conditions based on data from hydrostatic conditions. We use our simulated isotropic compaction elastic moduli to predict the full stiffness matrix for uniaxial compaction.

Although this model (Mavko et al., 1995) predicts C_{33} (stiffness constant in the maximum stress direction) reasonably close to simulation, the rest of stiffness constants do not match simulated stiffness constants.

For isotropic compaction, the stress-strain estimations from GD simulations are similar to laboratory experiments. EMT stress predictions are higher than both GD simulation and laboratory experiments. Further, for uniaxial compaction, the ratio of stresses in vertical and horizontal directions from GD simulations matches laboratory experiments on sand. However, this ratio does not match the usual linear-elasticity-based expression involving stiffness constants, as discussed in Section 4.7.2.

An alternative approach for computing elastic properties in computational rock physics is using a well-established Finite Element simulation (Arns et al., 2002, Roberts and Garboczi, 2002a, 2002b). As described in Chapter 2, this simulation solves equations of linear elasticity to compute moduli from stress-strain relations in three-dimensional rock microstructure images. Using GD simulation, we create two compacted packs (at 0.1 and 10.0 MPa isotropic pressures). Based on the centers and radii of the spherical grains, we prepare digital microstructures on three-dimensional grids with different resolutions. We compute elastic moduli using FE simulation on these microstructures. Although the accuracy of this method is well-established (Garboczi and Berryman, 2001, Arns et al., 2002), the precision of its calculations depends on the voxel resolution (Roberts and Garboczi, 2000). We note that the FE moduli estimations are significantly higher (>200%) than GD moduli even at very high resolutions (2 micron), thereby restricting the use of this simulation for compacted granular packs (<10.0 MPa).

For the compacted bidisperse and polydisperse packs presented in Chapter 3, we calculate elastic moduli using GD simulation. We analyze the effect of different sizes on elastic properties. We also estimate elastic properties using conventional rock-physics models for poorly sorted packs (friable sand model, Dvorkin and Nur, 1996). The predictions from this heuristic model are reasonably close to estimated elastic properties from simulation. However, the friable sand model requires proper estimates for properties of compacted well-sorted pack as an end-point property. The commonly

used estimate is the EMT prediction. The shear moduli being high in such predictions, we propose the use of our empirical *correction factors*.

We further estimate the permeability of simulated packs using the Lattice-Boltzmann method. Permeability in simulated well-sorted packs is generally higher than in low-porosity cemented rocks. Kozeny-Carman best-fit relationships are also presented. We observe that the empirical geometric factor in this relation varies with sorting: poorer sorting requires higher values for the geometric factor.

4.3 Effective Medium Theory

EMTs (Walton, 1987, Digby, 1981, Duffy and Mindlin, 1957, Brandt, 1955, Norris and Johnson, 1997, Bachrach and Avseth, 2008, Dutta et al., 2010, Duffaut et al., 2010, Pride and Berryman, 2009) estimate the macroscopic elastic response of a pack based on contact forces between pairs of grains in contact. Most EMTs use Hertz-Mindlin contact laws (Hertz, 1882, Mindlin, 1949). Duffy and Mindlin (1957) and Walton (1975) estimate effective elastic properties for regular packs. Brandt (1955), however, considers *random* grain packs, but estimates only the bulk moduli. Digby (1981) and Walton (1987) estimate effective elastic properties using a force-based calculation for adhesive, frictional and frictionless grains in a random granular pack. Norris and Johnson (1997) re-derive the same final forms for the stiffness matrix as Walton (1987) and Digby (1981) by using strain-energy-density functions. Before discussing the assumptions and implementation of EMT, we would like to discuss the significance of *loading path* in the spirit of discussions by Norris and Johnson (1997). Norris and Johnson (1997) consider a thought experiment of an *elastic* medium with two spheres touching at a point. They further consider two force scenarios on this grain-pair resulting in exactly the same total displacement: (1) imparting a normal force followed by a tangential force; and (2) imparting a tangential force followed by a normal force. These two scenarios are two different *loading paths*. If contact force models are such that tangential *contact* force depends on normal *contact* force, these two scenarios will result in different microscopic strain energy. Hence, even if the macroscopic strain on these two grains is same, the strain energy would depend on

loading path. However, if the tangential contact force does not depend on the normal contact force, the strain energy is unique for any loading path. Such an effective medium is typically referred as *hyperelastic* medium (Truesdell and Noll, 1965).

The basic assumptions for almost all EMT models are: (a) random granular packs are statistically homogeneous; (b) all grain displacements are affine to the macroscopic strain of the pack boundary; and (c) there exists a unique strain-energy-density function which can be calculated based on the macroscopic strain and loading path. Assumption (a) implies that there is a homogeneous arrangement of contacts or neighbors around any grain, and each grain has approximately the same number of contacts. Hence, the total stress or strain energy calculation can be done using a single representative grain. Assumption (b) implies that the displacement field of each grain is consistent with the macroscopic deformation. This displacement field does not create any force imbalance, if all grains have homogeneous distribution of contacts (and hence forces). Assumption (c) is a natural consequence of assumptions (a) and (b). Assumption (a) results in force balance for all strains, and assumption (b) gives the same average strain for all grains. Hence, the total strain-energy-density function is unique for a given strain and loading path. This function is used to obtain elastic stiffness tensor and stress. It should be noted that if there was force imbalance at any given strain, i.e., due to violation of assumption (a), the microscopic (grain-scale) local strains would likely be different from the affine strain. This would lead to non-unique strain-energy density (calculated from microscopic grain-scale strains) at that macroscopic strain. Further, assumption (c) is valid for two extreme cases which precludes dissipative frictional losses: infinite friction and frictionless. Since most EMT models are based on these two extreme cases, assumption (c) is safely used to calculate elastic stiffness tensor and stress. For a realistic case with finite inter-grain friction, frictional sliding can occur and hence this assumption is no longer valid.

Walton (1987) derives the effective elastic moduli and stress of a random pack of homogeneous isotropic spheres due to affine deformations. Two sets of elastic properties are calculated: (a) an infinite friction (rough sphere) model, where both normal and tangential contact forces are considered; and (b) a frictionless (smooth

sphere) model, where only normal contact forces are considered. The random pack is subjected to an *initial* macroscopic strain, ε_{ij}, to create a *reference* state. Under the affine or homogeneous strain assumption, grain displacements, u_i, are calculated as:

$$u_i = \varepsilon_{ij} x_j \tag{4.1}$$

where x_j are grain positions. The subscripts refer to the three principal directions. For this macroscopic strain ε_{ij}, the macroscopic average stress of a pack of rough spheres with porosity ϕ is

$$\langle \sigma_{ij} \rangle = -\frac{(1-\phi)n}{\pi^2 B(2B+C)} \begin{Bmatrix} B\,\langle \left(-\varepsilon_{pq} I_p I_q\right)^{\frac{1}{2}} \left[\varepsilon_{ik} I_k I_j + \varepsilon_{jk} I_k I_i\right] \rangle \\ -C\,\langle \left(-\varepsilon_{pq} I_p I_q\right)^{3/2} I_i I_j \rangle \end{Bmatrix} \tag{4.2}$$

where n is the average number of contacts per grain (coordination number), B and C are material elastic properties, and I_n are direction cosines. The quantities within $\langle \cdot \rangle$ are averages over all direction cosines. B and C are combinations of the grain shear modulus, μ, and Lamé's constant, λ:

$$B = \frac{1}{4\pi}\left\{\frac{1}{\mu} + \frac{1}{\lambda+\mu}\right\}; C = \frac{1}{4\pi}\left\{\frac{1}{\mu} - \frac{1}{\lambda+\mu}\right\} \tag{4.3}$$

For smooth spheres, the macroscopic stress of a pack with porosity ϕ and average number of contacts n for an arbitrary strain ε_{ij} is

$$\langle \sigma_{ij} \rangle = -\frac{(1-\phi)n}{\pi^2 B}\left\{-\langle \left(-\varepsilon_{pq} I_p I_q\right)^{3/2} I_i I_j \rangle\right\}. \tag{4.4}$$

For isotropic compression, both models give the same stress (from Eqns. 4.2 and 4.4):

$$\langle \sigma_{ij} \rangle = -p\delta_{ij}, where\ p = \frac{\phi n(-e)^{3/2}}{3\pi^2 B} \tag{4.5}$$

A *further* infinitesimal strain is imposed on the stressed *reference* state to calculate the infinitesimal-strain effective elastic stiffness tensor of the random pack. The complete elastic stiffness tensor, C_{ijkl}^{R}, for a rough sphere pack under arbitrary strain ε_{ij} with porosity ϕ and average number of contacts n is

$$C_{ijkl}^{R} = \frac{3(1-\phi)n}{4\pi^2 B(2B+C)}\Big\{B\,\langle\big(-\varepsilon_{pq}I_pI_q\big)^{\frac{1}{2}}I_jI_k\rangle\,\delta\varepsilon_{il} + B\,\langle\big(-\varepsilon_{pq}I_pI_q\big)^{\frac{1}{2}}I_iI_k\rangle\,\delta\varepsilon_{jl} + B\,\langle\big(-\varepsilon_{pq}I_pI_q\big)^{1/2}I_jI_l\rangle\,\delta\varepsilon_{ik} + B\,\langle\big(-\varepsilon_{pq}I_pI_q\big)^{1/2}I_iI_l\rangle\,\delta\varepsilon_{jk} + 2C\,\langle\big(-\varepsilon_{pq}I_pI_q\big)^{1/2}I_iI_jI_kI_l\rangle\Big\} \tag{4.6}$$

where $\delta\varepsilon_{ij}$ is the infinitesimal strain tensor. For smooth spheres, the equivalent expression is

$$C_{ijkl}^{S} = \frac{3(1-\phi)n}{2\pi^2 B}\Big\{C\,\langle\big(-\varepsilon_{pq}I_pI_q\big)^{1/2}I_iI_jI_kI_l\rangle\Big\}. \tag{4.7}$$

Under isotropic compression, the elastic stiffness tensor C_{ijkl}^{R} can be simplified for rough spheres as follows:

$$C_{ijkl}^{R} = \lambda^R\delta_{ij}\delta_{kl} + \mu^R\big(\delta_{ik}\delta_{jl} + \delta_{il}\delta_{jk}\big) \tag{4.8}$$

where δ_{ij} is Kronecker's delta, and λ^R and μ^R are effective Lamé's constants of the random granular pack (rough spheres) and are given as follows:

$$\lambda^R = \frac{C}{10(2B+C)}\left(\frac{3(1-\phi)^2n^2p}{\pi^4B^2}\right)^{\frac{1}{3}},$$

$$\mu^R = \frac{(5B+C)}{10(2B+C)}\left(\frac{3(1-\phi)^2n^2p}{\pi^4B^2}\right)^{\frac{1}{3}} \tag{4.9}$$

For smooth spheres, C_{ijkl}^{S} can be simplified to

$$C_{ijkl}^{S} = \lambda^{S}\delta_{ij}\delta_{kl} + \mu^{S}\left(\delta_{ik}\delta_{jl} + \delta_{il}\delta_{jk}\right) \tag{4.10}$$

where λ^S and μ^S are effective Lamé's constants of the random granular pack (smooth spheres) and are given by

$$\lambda^{R} = \mu^{R} = \frac{1}{10}\left(\frac{3(1-\phi)^2 n^2 p}{\pi^4 B^2}\right)^{\frac{1}{3}} \tag{4.11}$$

From Eqns. 4.1 through 4.11, there are a few key caveats, which also apply to most other EMTs:

(1) There is no functional variation of coordination number, *n*, and porosity, ϕ, under initial finite strain, ε_{ij}. This formulation assumes that *n* and ϕ do not evolve under strain. However, for compaction of most real granular materials in the range of 0 – 20 MPa, the change in porosity is ~2-3% and that of *n* (from numerical simulation) is ~2-3. In conventional usage of EMT to predict elastic property at a pressure, we most often use compacted porosity and estimated *n* at that particular pressure.

(2) Under isotropic compression, the average stress and effective bulk moduli of both rough and smooth sphere packs are same.

(3) The effective stiffness tensor for rough sphere at any pressure depends on both the finite strain, ε_{ij}, and infinitesimal strain, $\delta\varepsilon_{ij}$ (Eqn. 4.6).

We compare bulk and shear moduli from Walton's frictionless and infinite friction models with laboratory measurements for a random pack of glass beads under hydrostatic compression (Domenico, 1977). We find that bulk modulus predictions are better than shear modulus predictions (Fig. 4.1). Shear moduli predictions from the infinite friction model are higher than experimental data, while those from the frictionless model are lower than the data.

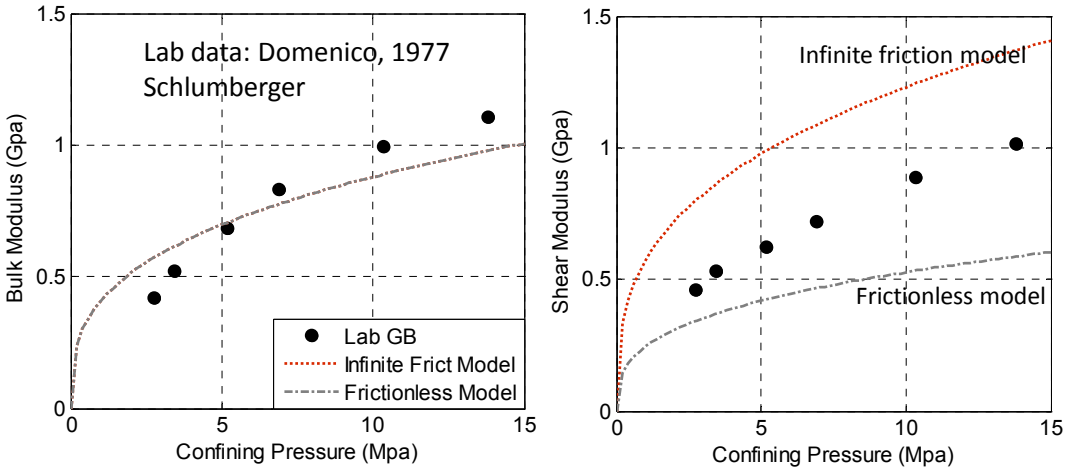

Figure 4.1: Comparison of elastic moduli from Walton's infinite friction and frictionless models (1987) with laboratory dry glass bead data (Domenico, 1977).

Bachrach and Avseth (2008) argue that the assumption of perfectly smooth and infinitely rough spheres in a random pack may be invalid. They present an ad-hoc model to describe contact heterogeneities by considering a binary mixture of frictionless and infinite-friction spheres. Dutta et al. (2010) follow a similar approach of mixing frictionless and infinite-friction spheres. They, however, invert CN from dynamic measurements. Duffaut et al. (2010) argue that the fundamental contact law should consider partial slip at grain contacts, and derive effective properties based on Mindlin's partial slip model (1949). While the binary mixing approaches by Bachrach and Avseth (2008) and Dutta et al. (2010) are heuristic, Duffaut et al.'s (2010) considers occurrence of slip for infinitesimal wave amplitudes. Mavko (1979), Winkler et al. (1979) and Winkler (1983) reject frictional sliding effects at grain or crack contacts in dynamic measurements with wave strain amplitudes of the order of 10^{-6} or smaller. In a more recent publication (Pride and Berryman, 2009), a heterogeneous contact strain based model is proposed. This model considers heterogeneous contact strain accumulation by considering floaters. The granular contact network evolves with pressure or macroscopic strain as floaters join these networks based on a heuristic *gap distribution function*, which we term non-contact, near-neighbor distance distribution function. In Chapter 3, we present simulation results for these distributions at different isotropic pressures. These functions

correspond to gap distribution functions. Although such formalism (Pride and Berryman, 2009) leads to heterogeneous local contact strains or deformations, it does not clarify the macroscopic stability of this locally heterogeneous system. Considering all these aspects, we present our arguments for the failure of EMT based on simulated grain packs in the following section.

4.4 Why does EMT fail?

Failure of EMT in predicting elastic properties of granular packs can be due to either the breakdown of its assumptions or its basic micromechanical contact laws. Coste and Gilles (1999) experimentally confirm the validity of Hertzian laws at the contacts. Makse et al. (1999, 2004) use discrete particle simulations using elastofrictional grains with Hertz-Mindlin contact laws to predict elastic properties of simulated sphere packs. If the micromechanical laws are correct, the failure of EMT *should* involve the breakdown of the theory's assumptions. To understand this problem in detail, we use GD simulation.

We simulate stable jammed packs at different pressures using different boundary conditions and compaction environments, as elaborated in Chapter 3. These jammed packs, termed *reference states,* are characterized by force equilibrium and negligible macroscopic stress fluctuations (<0.0001 MPa). These packs show considerable heterogeneity in terms of contact numbers, contact elastic deformations and mean stress for each grain (Fig. 4.2). These heterogeneities evolve with pressure as well.

In GD simulation, we estimate elastic moduli using a similar methodology as EMT. We apply infinitesimal strains on the pack boundaries. As a first guess for applying these infinitesimal strain perturbations in GD simulation, we homogeneously distribute them on all grains similar to EMT. Under the affine or homogeneous strain assumption, infinitesimal grain displacements, δu_i, are calculated as:

$$\delta u_i = \delta \varepsilon_{ij} x_j \tag{4.12}$$

where x_j are grain positions and $\delta\varepsilon_{ij}$ is the infinitesimal strain perturbation. Unlike EMT, we do not assume force equilibrium in GD simulation, but rather allow the simulation to re-calculate contact forces due to this affine strain. For having macroscopic force equilibrium (stable pack), the sum of all contact forces or the net force on each grain should identically be zero. We show the distribution of net force magnitudes of each grain before and after applying the infinitesimal strain (Fig. 4.3) in a compacted pack. The distribution before applying the infinitesimal strain, i.e., at the reference state, is a delta function at zero, signifying that each grain has zero net force. However, the net force distribution after applying the affine strain perturbation (referred as EMT step) has positive net forces, signifying force imbalance and an unstable pack. GD simulation finds the correct grain displacements to compensate for this force imbalance and regain force equilibrium. These grain displacements are infinitesimal, as discussed in next section, and do not involve grain sliding or change in number of contacts. We refer to these local displacements as grain *relaxations* and the final equilibrium state as the *relaxed* state. The net force distribution at this final *relaxed* state is very close to that of the initial reference state (Fig. 4.3). Hence, affine strain distribution in heterogeneous packs requires subsequent *relaxation* to obey first principles.

In contrast, EMT assumes homogeneous contact distribution, and does not allow any local grain relaxation for any arbitrary strain. This might be a valid approximation in ordered packings, but for random granular packs, the jammed states are highly disordered. Any affine strain on these packs results in force imbalance. EMT thus violates first principles. By ignoring heterogeneity, the assumptions of EMT result in unequilibrated non-physical packs; which is why EMT fails. In the next section, we give further evidence of grain relaxation and its impact on elastic moduli.

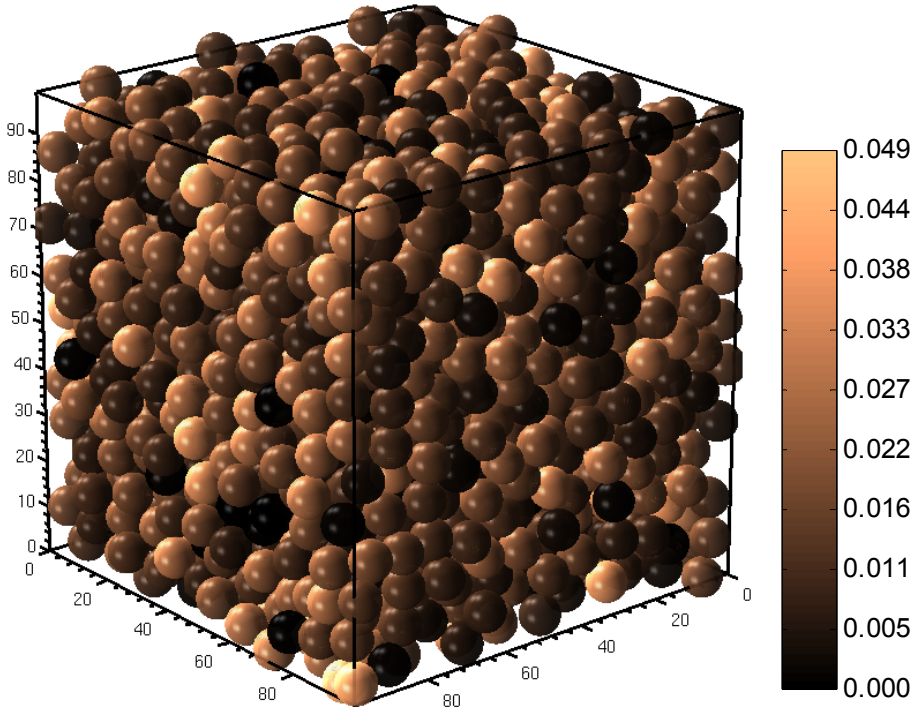

Figure 4.2: Evidence of heterogeneity in mean stress for each grain in a stable granular pack. Color-scale shows stress magnitudes in MPa. The volume average stress of the whole pack is 10.0 MPa.

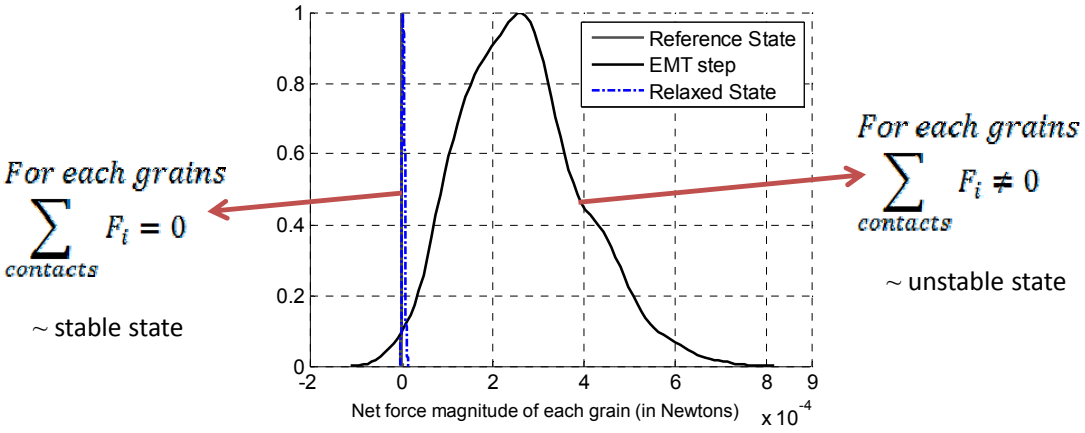

Figure 4.3: Distribution of net force magnitude of each grain at 3 steps: reference state, EMT step (with isotropic affine strains), and final relaxed state. Reference and relaxed states are at force equilibrium, unlike the EMT step. The reference state is at an isotropic pressure of 10.0 MPa and was created using a 'servo-control' boundary condition, as discussed in Chapter 3.

4.5 Relaxation of granular packs

The force imbalance due to infinitesimal affine strain, $\delta\varepsilon_{ij}$, leads to subsequent local grain displacements or *relaxations*. These relaxations are, however, very small and not the same as grain sliding and motion under large strains (>10^{-3}). To compare a suitable measure of these relaxations at different isotropic pressures, we compute the normalized relative displacements between grains in contact as the pack relaxes. The reason for choosing relative displacements between grain-pairs is that contact forces depend on inter-grain distances (Eqns. 2.5 and 2.14). So, a measure of relaxation using relative displacements can be associated with fluctuations in contact forces, and hence local strain energy and effective moduli. We compute relative displacement vectors for grains in contact using relative velocities ($\boldsymbol{v^{tot}}$ in Eqn. 2.12) between the grains as follows:

$$\delta \boldsymbol{u}^c = \int_t^{t'} \boldsymbol{v^{tot}} dt \tag{4.13}$$

where the integral is taken between two states t and t', and dt is the simulation time-step. We consider two cases: (1) state t: reference state and t': EMT step (with affine strain); and (2) state t: reference state and t': final relaxed state. Case (1) refers to all relative displacements related to homogeneous affine strain. For affine strains, $\|\delta \boldsymbol{u}_1^c\|$ is identical for all grain-pairs. Case (2) refers to all relative displacements until the relaxed state with respect to reference state, and hence includes the *homogeneous* affine displacements from case (1) as well. We further define the following mathematically quantity:

$$\Delta = \frac{\|\delta \boldsymbol{u}_2^c\|}{\|\delta \boldsymbol{u}_1^c\|} \tag{4.14}$$

where the subscripts correspond to the two cases (1) and (2). As mentioned, $\|\delta \boldsymbol{u}_1^c\|$ is identical for all grain-pairs. This ratio, Δ, represents the normalized relaxation displacements (since the denominator is same for all pairs). We plot the distribution of

Δ for all grain-pairs at three isotropic reference states at 0.1, 2.0 and 10.0 MPa, for an isotropic infinitesimal strain in Figure 4.4. The relative displacements until the relaxed state are of nearly the same order as the displacement due to infinitesimal affine strain (10^{-5}). This supports our prior claim that grain relaxations are of infinitesimal order. For packs under higher stresses, the spread of the relative displacements distribution gets smaller (Fig. 4.4). Further, we observed that the average number of contacts is the same for reference state, EMT step and relaxed state.

During elastic property calculation using infinitesimal strain, the magnitude of this strain must be reasonably small to ensure that the granular pack responses are in the linear elastic regime. In the linear elastic regime, the elastic moduli are independent of the strain magnitude. Our infinitesimal strains are typically smaller than 10^{-5}. Further, we set infinite friction values during moduli estimation to inhibit any inelastic losses. It should be noted that even with finite friction, inelastic losses (frictional sliding) are not present if a small enough strain ($<10^{-5}$) is applied. Although our infinitesimal strains are of the same order, our choice of infinite friction further ensures no sliding. We calculate elastic moduli by monitoring changes in stress with time, as the internal forces equilibrate. We use stress-strain equations for calculating elastic moduli. In an isotropic compaction, we compute bulk and shear moduli only. For bulk modulus, we apply an infinitesimal isotropic strain ($\delta\varepsilon_{11}= \delta\varepsilon_{22}= \delta\varepsilon_{33}$), and monitor the mean stress of the pack. The bulk modulus is computed as follows:

$$K = \frac{1}{3}\frac{\delta\sigma_{\alpha\alpha}}{\delta\varepsilon_{\alpha\alpha}} \tag{4.12}$$

To obtain shear modulus in an isotropic compaction, we do a pure shear test (viz., $\delta\varepsilon_{11} = -\delta\varepsilon_{22}$, $\delta\varepsilon_{33} = 0$). The shear modulus is calculated as

$$\mu = \frac{1}{2}\frac{(\delta\sigma_{22} - \delta\sigma_{11})}{(\delta\varepsilon_{22} - \delta\varepsilon_{11})}. \tag{4.13}$$

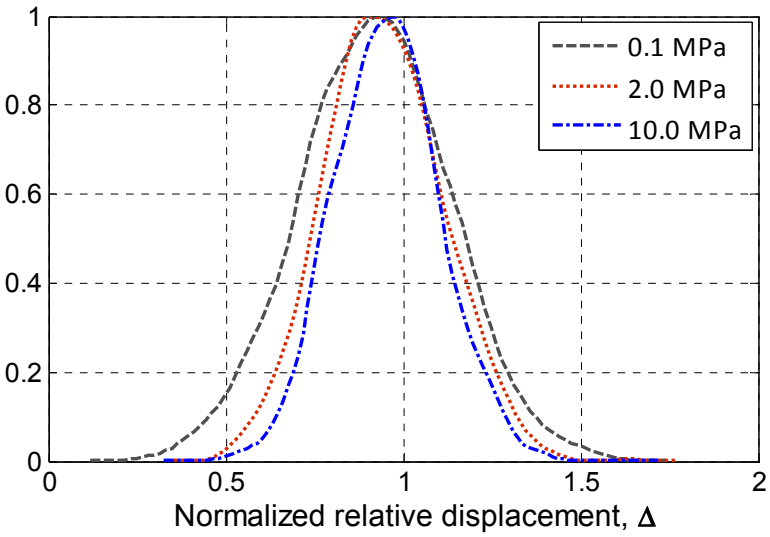

Figure 4.4: PDF of normalized relative displacements between grains in contact during force equilibration. The relative displacements are nearly the same order as the normalization factor, i.e., displacements due to affine strain. For more compacted packs, relative displacements are smaller as the spread of the distribution gets smaller.

We compute the changes in stress in both cases (bulk and shear) relative to the reference state. During force equilibration, we observe that estimated moduli at each simulation step decrease relative to the affine configuration and gradually stabilize (Fig. 4.5). To compare different stress states and both bulk and shear moduli, we normalize the calculated moduli at each step by the EMT moduli. EMT or unrelaxed moduli are the instantaneous moduli when affine strains are applied. They are numerically close to those predicted by Walton's infinite friction model at corresponding pressures. At all pressures, the normalized shear modulus reduction is much greater than the normalized bulk modulus reduction (Fig. 4.5). The magnitude of modulus relaxation (fraction of EMT moduli when the stresses equilibrate) also depends on stress (Fig. 4.5).

In Chapter 3, we showed that heterogeneity evolves with compaction. The amount of relaxation in the moduli is also found to be stress-dependent. We call the ratios of the final elastic moduli to the instantaneous elastic moduli (when affine strains are applied) the *relaxation corrections*. These are the average fractions (Y-axis) as moduli stabilize in Fig. 4.5.

These relaxation corrections are linearly related to heterogeneity (Fig. 4.6). As a measure of heterogeneity, we compute the coefficient of variation of mean stress per grain. In Chapter 3, we showed that heterogeneity in a granular pack also depends on the preparation protocol and compaction environment. The results presented so far in this chapter refer to the initial zero-friction servo-controlled glass bead packs. The final friction in these packs was non-zero (0.3). In Chapter 3, we also reported another servo-controlled experiment with low initial friction, followed by the same non-zero friction (0.3). Using an infinitesimal perturbation method, we estimate elastic moduli and corresponding relaxation corrections for these packs, too. We further compute functional forms (empirical fits) for dependence of relaxation corrections on pressure for both types of packs (Fig. 4.7). In the next section, these functional forms are used with EMT predictions (Walton's infinite friction model) to estimate elastic moduli. In Section 4.6.2, we provide relaxation correction factors for uniaxial compaction.

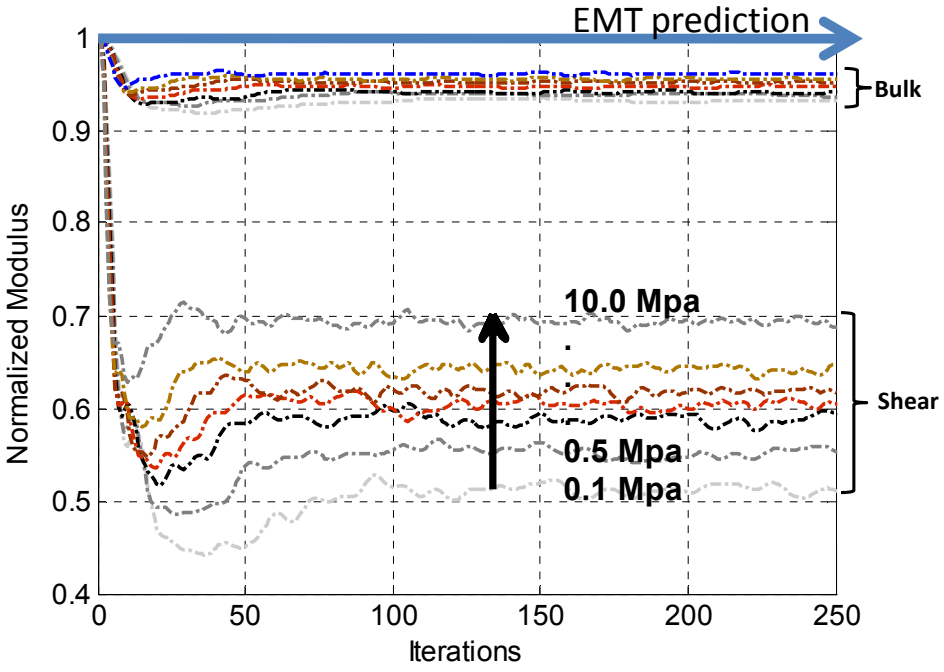

Figure 4.5: Normalized bulk and shear moduli relax with simulation timesteps. After application of an infinitesimal affine strain on an isotropic pack, forces equilibrate with grain relaxations. The effective bulk and shear moduli relax, too. Shear modulus relaxes significantly more than bulk modulus. The amount of relaxation also depends on pressure of the initial pack. *Relaxation corrections* are computed as the average of Y-axis values for the last 100 timesteps.

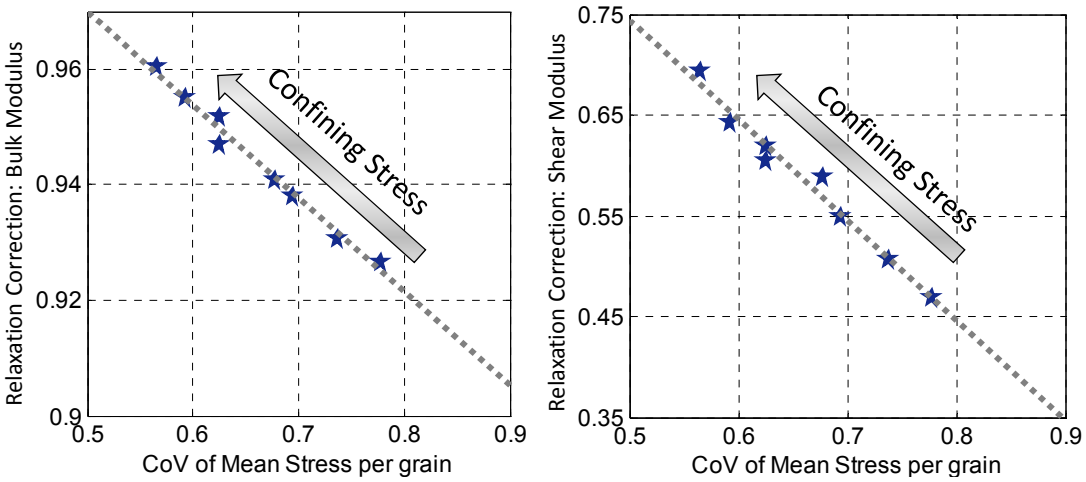

Figure 4.6: Relaxation corrections for both bulk and shear moduli (blue diamonds) are linearly related to measure of stress heterogeneity in simulated packs.

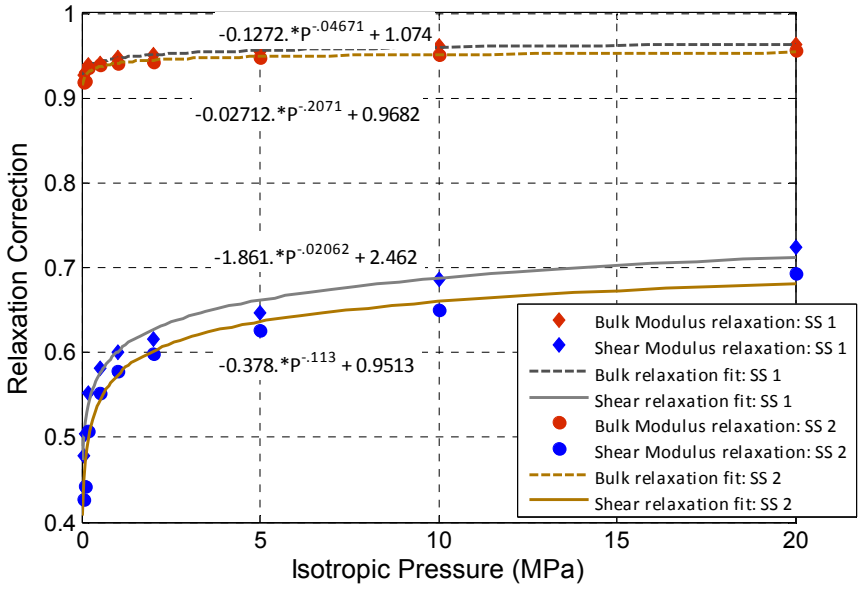

Figure 4.7: Empirical fits to relaxation correction with pressure for bulk and shear moduli. Servo control expts SS1(initial zero-friction) and SS2 (initial finite friction) show reasonably close pressure dependence for relaxation corrections

4.6 Isotropic and anisotropic elastic properties

In this section, we compare elastic properties from GD simulation and EMT with acoustic experiments on granular packs at different pressures. We study both isotropic and uniaxial compactions for glass beads and sand. We also show the applicability of *relaxation corrections* computed from GD simulation to EMT predictions.

4.6.1 Isotropic compaction

First, we consider granular packs under isotropic compaction (Domenico, 1977, Zimmer, 2004). Using GD simulation, we compute bulk and shear moduli of compacted monodisperse sphere packs with glass and quartz material properties (Table 4.1). The glass bead packs were prepared using a servo-control BC with different values of initial friction but the same final friction, as discussed in Chapter 3. We find that our simulated elastic moduli are similar to laboratory experiments (Domenico, 1977) (Fig. 4.8). Zimmer (2004) also reports acoustic measurements on glass beads packs. However, the loading path in Zimmer's glass bead samples has multiple small cycles (increasing and decreasing pressures). As a starting point to understand the breakdown of EMT, we simulate single loading cycles in GD.

We also compute elastic moduli for compacted sphere packs with quartz mineralogy and compare them with experimental dynamic measurements on dry Ottawa sand (Domenico, 1977) and dry Galveston sand (Zimmer, 2004). Unlike glass bead samples, Zimmer's Galveston sand samples had fewer loading cycles. Also, Galveston sand has higher quartz content (~92%) than the other sand samples (Zimmer, 2004). The simulated sphere packs were prepared using two different BCs: a strain BC and a servo-control BC. Although we consider monodisperse sphere packs in GD simulation, our estimated bulk and shear moduli are reasonably close to laboratory measurements (Fig. 4.9). Ottawa sand samples in Domenico's experiments were mostly angular and about 75% had a nominal diameter between 74-104 microns. Hence, we should *ideally* consider angular grains with some sorting. Nevertheless, our estimated results with spherical grains are encouraging.

Table 4.1: Material properties of grains

Mineral	*Poisson's ratio*	*Shear modulus (GPa)*	*Density (kg/cc)*
Glass	0.08	45.0	2650
Quartz	0.2	29.0	2460
Shale	0.3	9	2600

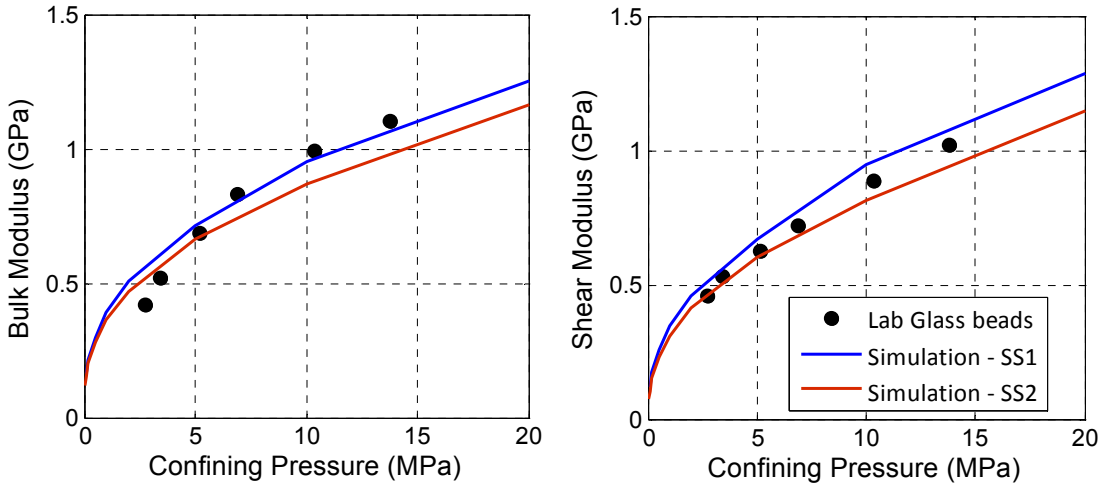

Figure 4.8: Bulk and shear moduli vs. pressure for laboratory experiments (Domenico, 1977). Elastic moduli from GD simulation using two types of initial packs (SS1 and SS2) are reasonably close to laboratory experiments. Servo control packs SS1 (initial zero-friction) and SS2 (initial finite friction) are used. Both the packs, as described in Chapter 3, have a final friction coefficient of 0.3. As shown in Fig. 4.1, EMT predictions for shear moduli are significantly different.

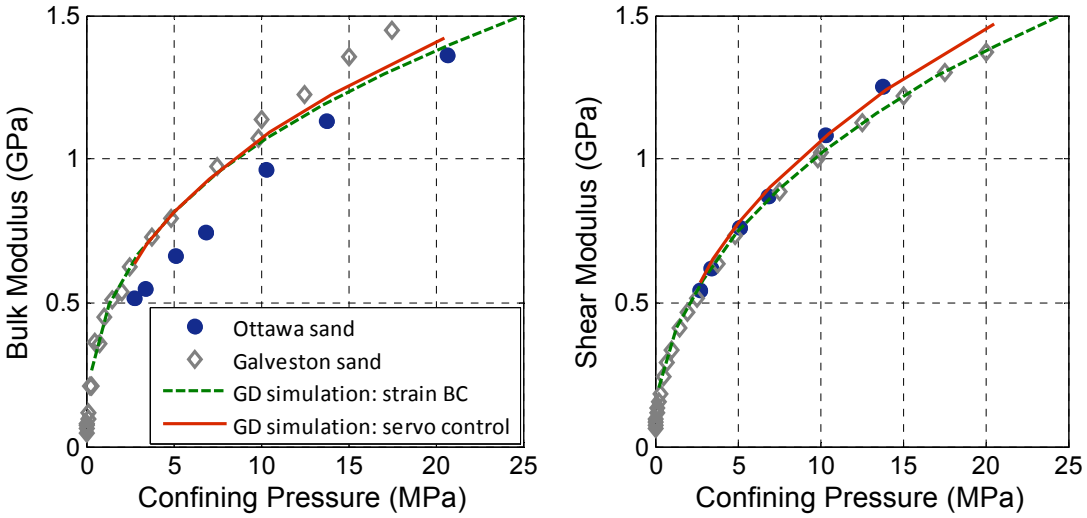

Figure 4.9: Comparison of simulated elastic moduli of quartz packs with laboratory acoustic measurements on sand under confining pressures (Domenico, 1977, Zimmer, 2004). Two types of sands are considered: Ottawa sand (Domenico, 1977) and Galveston sand (Zimmer, 2004). Although real sand packs are hardly well-sorted and spherical, elastic moduli from monodisperse sphere packs with quartz properties are reasonably close to laboratory experiments.

We use Walton's infinite friction model to compare results from GD simulations and laboratory experiments. As shown in Figure 4.1, this model over-predicts shear moduli at all pressures. The use of this model for comparison is justified from earlier theoretical studies and GD simulation conditions. Based on Mavko (1979), Winkler et

al. (1979) and Winkler (1983), we believe that for strain amplitudes corresponding to seismic waves and laboratory experiment waves, there should be no grain sliding. In GD simulations, the strain amplitude that induces slipping gets smaller with lower confining stresses (Makse et al., 2004). Typical wave amplitudes are still lower than this value. Moreover, while computing EMT elastic moduli at any pressure, we use the porosity and coordination number from GD simulation. At any reference state, the friction is set to a very high value while applying infinitesimal perturbation, thereby mimicking infinite friction model. Hence, it is logical to consider infinite-friction EMT while comparing with laboratory experiments and GD simulations.

In Chapter 3, we showed that different BCs give different porosity–CN–stress relations. We use these relations to predict elastic moduli of glass beads from EMT (Fig. 4.10). The estimated elastic moduli from GD simulation do not depend significantly on the type of BCs (Fig. 4.8 and 4.9). For EMT elastic moduli, we apply the functional forms of *relaxation corrections* with pressure (from Fig. 4.7) as:

$$C^{rc}(P) = \chi(P) C^{EMT}(P) \tag{4.14}$$

where $C^{EMT}(P)$ is EMT modulus and $\chi(P)$ is the relaxation correction at pressure P. Unlike the original EMT predictions, the corrected moduli match well with laboratory experiments (Fig. 4.11). The use of empirical fits obtained from rigorous relaxation corrections should ideally be restricted to similar loading environments and mineralogy. However, we use the same relaxation corrections from glass beads simulations for correcting the EMT predictions for quartz sand (Fig. 4.12) and observe reasonable agreement. We propose that these functional forms for relaxation corrections (in Fig. 4.7) can be universally applied for hydrostatic compaction, irrespective of material properties. These corrections are a rigorous physical way to compensate for the fact that EMT does *not* account heterogeneity. It should, however, be noted that these corrections depend on *degree* of heterogeneity. The heterogeneity in a real granular material (unconsolidated sediments) can depend on the level of compaction, compaction history (loading paths) and stress type (hydrostatic or

uniaxial – discussed in the next section). Although we show the applicability of these relaxation corrections for glass beads and sand, these pressure-dependent corrections should still be used with caution for amending EMT predictions depending on the aforementioned factors.

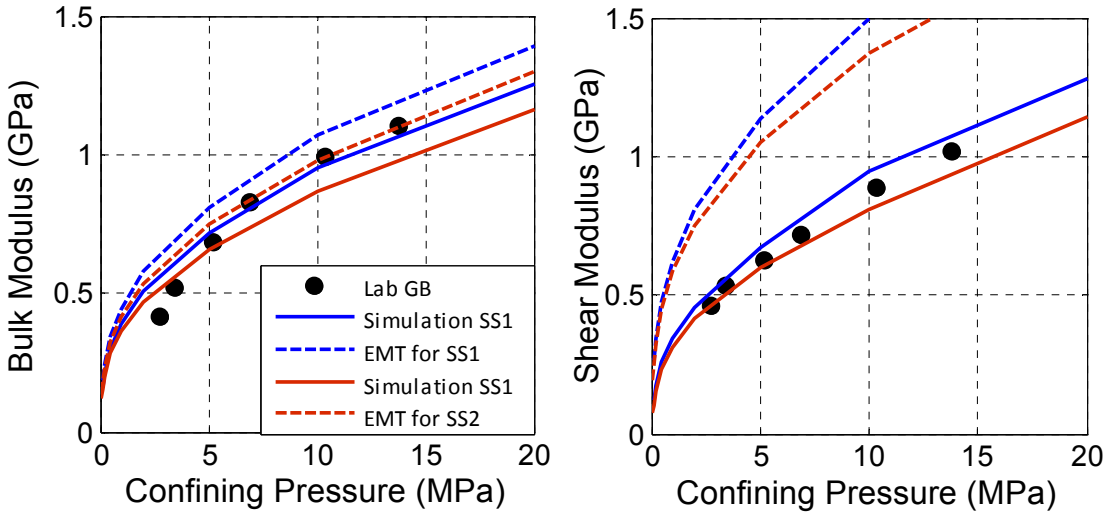

Figure 4.10: EMT (Walton Infinite Friction model) predicts higher shear modulus than GD simulation and laboratory results for glass beads. We use porosity-CN-pressure relations from GD to estimate EMT moduli. SS1 and SS2 are explained in Fig. 4.8 footnote.

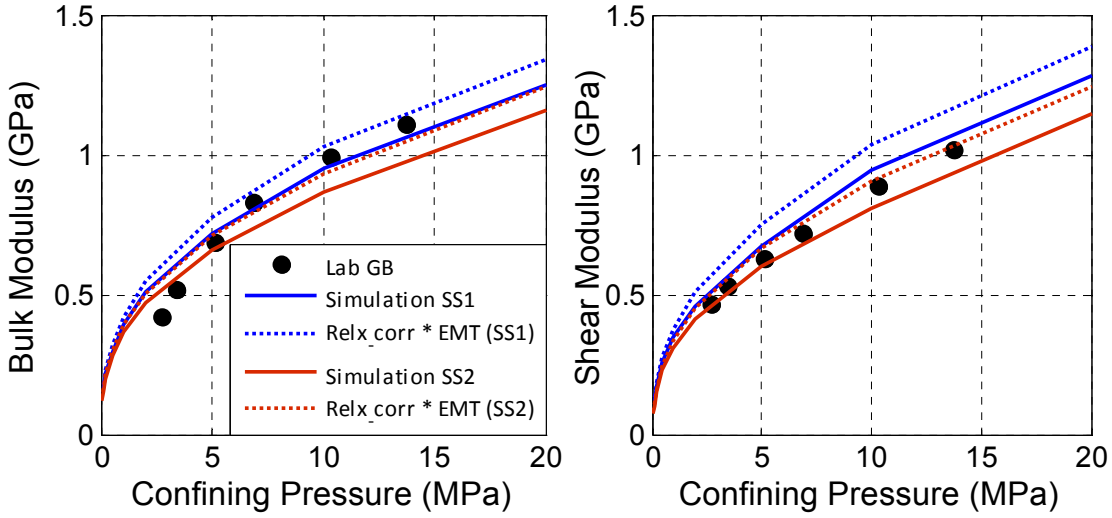

Figure 4.11: EMT moduli (Walton Infinite Friction model) are amended by applying the pressure-dependent relaxation correction. We apply different relaxation corrections, depending on the BC. The corrected moduli match lab data better, especially for shear modulus. SS1 and SS2 are explained in Fig. 4.8 footnote.

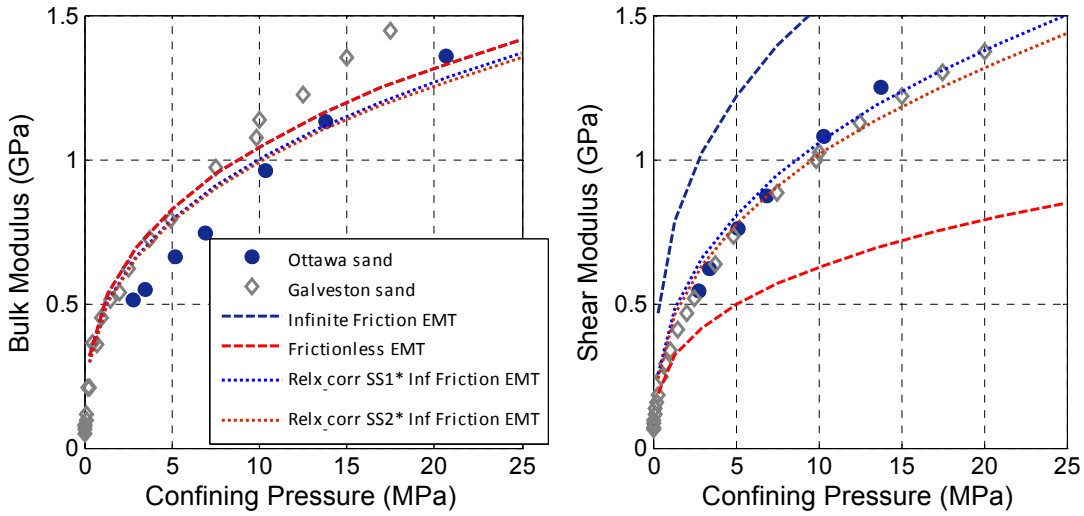

Figure 4.12: EMT moduli (Walton Infinite Friction model) for sand are amended by applying the pressure-dependent relaxation correction for glass beads (SS1 and SS2). SS1 and SS2 are explained in Fig. 4.8 footnote.

4.6.1.1. Comparison of FE and GD elastic properties

An alternative approach for computing elastic properties in computational rock physics is using a well-established Finite Element simulation (Garboczi, 1998a, 2003). This method has been used for calculating elastic properties from high-resolution CT scan images of rocks and synthetic models of rocks and concretes (Arns et al., 2002, 2007, Knackstedt et al., 2008, 2009, Roberts and Garboczi, 2002a, 2002b). As discussed in Chapter 2, this simulation requires discrete mesh geometry of microstructures in a regular three-dimensional grid as an input. Elastic moduli (referred as phase properties) are assigned to all the voxels in this grid. These voxels are then treated as tri-linear mesh to solve linear elasticity equations. The accuracy of this approach depends strongly on the resolution of these voxels. This aspect is specifically important for unconsolidated granular sediments, since grain contact areas are typically small. For coarse grids (low resolution microstructure images), grain contacts can be modeled as too large compared to actual contact areas. This would lead to erroneous elastic property prediction. Using our synthetic packs, we try to find resolutions that can give reasonable elastic property estimations using FE simulation.

We consider spherical packs at two different pressures – 0.1 and 10.0 MPa. GD simulation does not depend on any resolution issue, since the grain packs are not represented by voxels. Based on the centers and radii of spherical grains, we prepare digital binary (grain and pore) microstructures of these packs on three-dimensional grid. We choose four different resolutions – 2, 3, 4 and 6 microns for gridding both the compacted packs. We assign glass properties (Table 4.1) to grain voxels. Bulk and shear moduli from FE simulation using these microstructures are compared with those from GD simulation, which we regard as our *actual* moduli (Fig. 4.13). We observe that the FE elastic properties decrease with higher resolutions (smaller voxel size). However, we cannot infinitely increase the resolution, since it increases the computational size as well. The FE simulation requires 230 bytes per voxel (Garboczi, 1998). The total memory requirement is hence $230N^3$ bytes, where N is the cube length of the microstructure. A realistic cube length in terms of grain radius, r units, is $10r$ (Knackstedt et al., 2003). For our packs with grain radius 100 microns, we choose a cube length of 1200 microns. Our memory requirement ranged from 1.71 Gbytes to 46.27 Gbytes for low resolution (6 microns) to high resolution (2 microns) microstructures. Hence, increasing resolution has significant computational expenses in terms of memory. Roberts and Garboczi (2000) and Arns et al. (2002) use an extrapolation scheme to compute elastic properties at infinitely high resolution using a linear fit on property estimates at lower resolutions (coarser grids). For our simulated microstructures, the intercept of the linear fit through lower resolutions (dashed line in Fig. 4.13) is significantly higher (>200%) than *actual* moduli from GD simulation. Hence the use of the FE method to calculate elastic properties of granular sediments at low pressures (<10MPa) can lead to significant errors, given the over-prediction of contact areas.

In addition, we used an ad-hoc approximation of assigning contact voxels lower elastic moduli than the original grain moduli of glass (Fig. 4.14). We use the contact information from GD simulation to locate voxels near contacts, and assign lower elastic moduli to these voxels. As an estimate, we used the Reuss average of glass and air elastic moduli. We use FE simulation to compute effective elastic properties of

these microstructures. The elastic properties of these microstructures with an ad-hoc material are lower than the original microstructures. A linear-fit through for the computed moduli at different resolutions are still significantly higher than our *actual* GD simulation moduli (Fig. 4.15). However, using such an ad-hoc substitution would require precise information about contacts, which is difficult to obtain in a real CT-scan image.

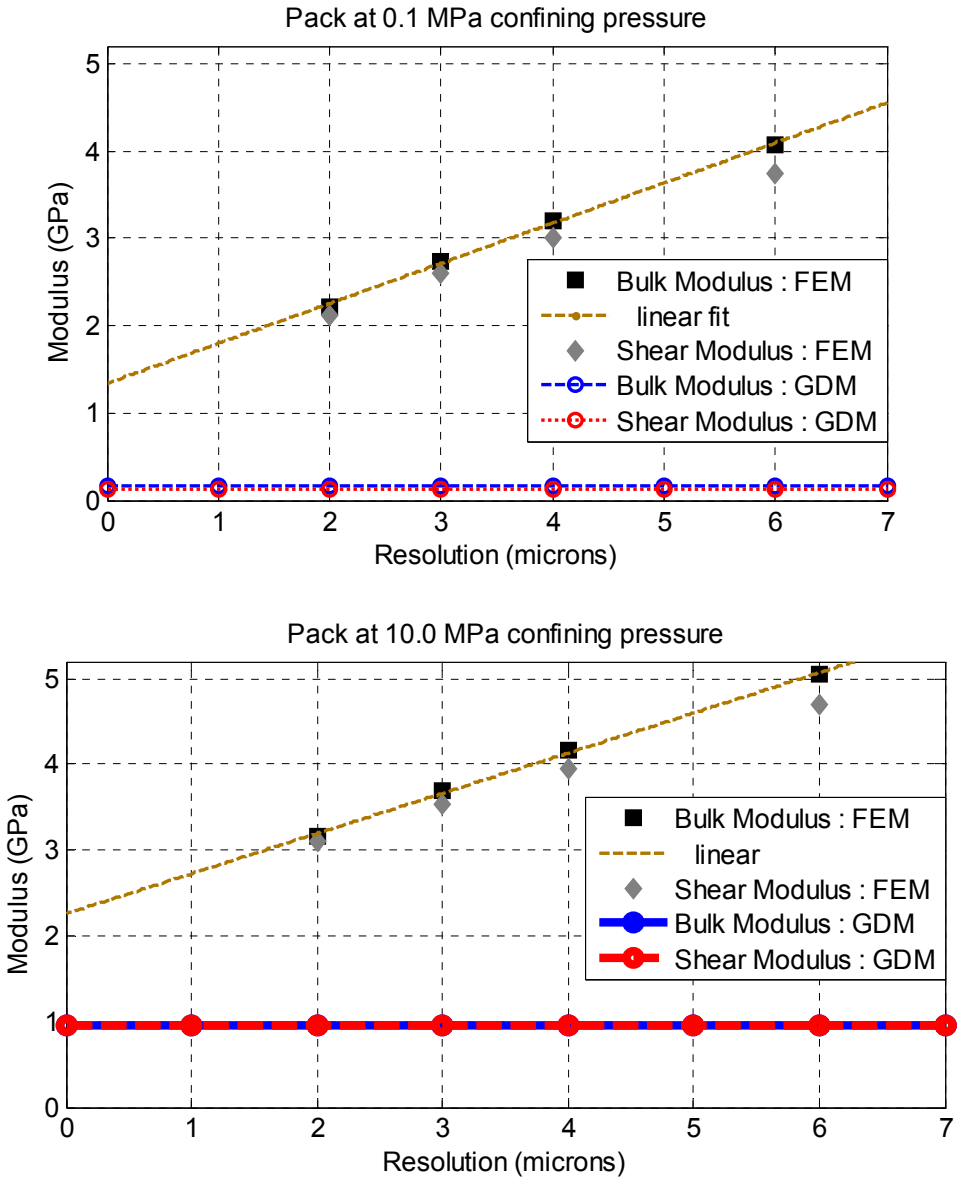

Fig. 4.13: Simulated elastic properties from FEM compared to GD simulation.

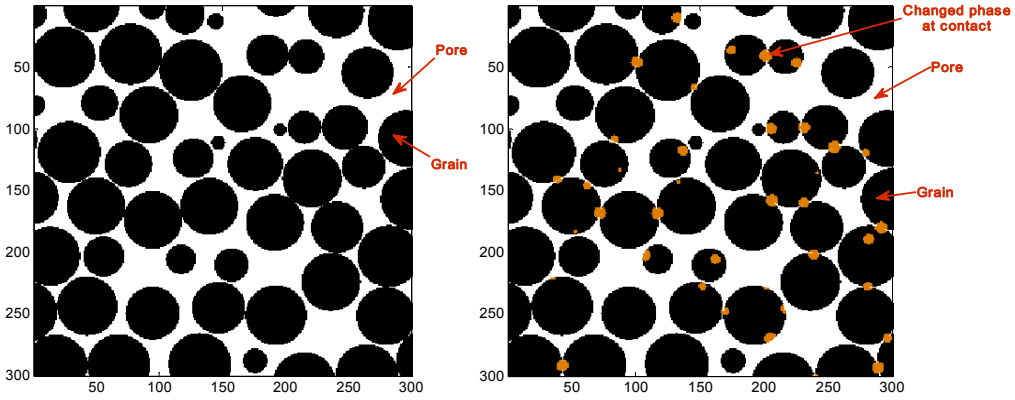

Fig. 4.14: 2-D slice from the gridded cube at 4 micron resolution. The left figure shows 2 phases: grain and pore; the right one shows an additional *patch* phase with lower elastic moduli than the grain moduli (glass).

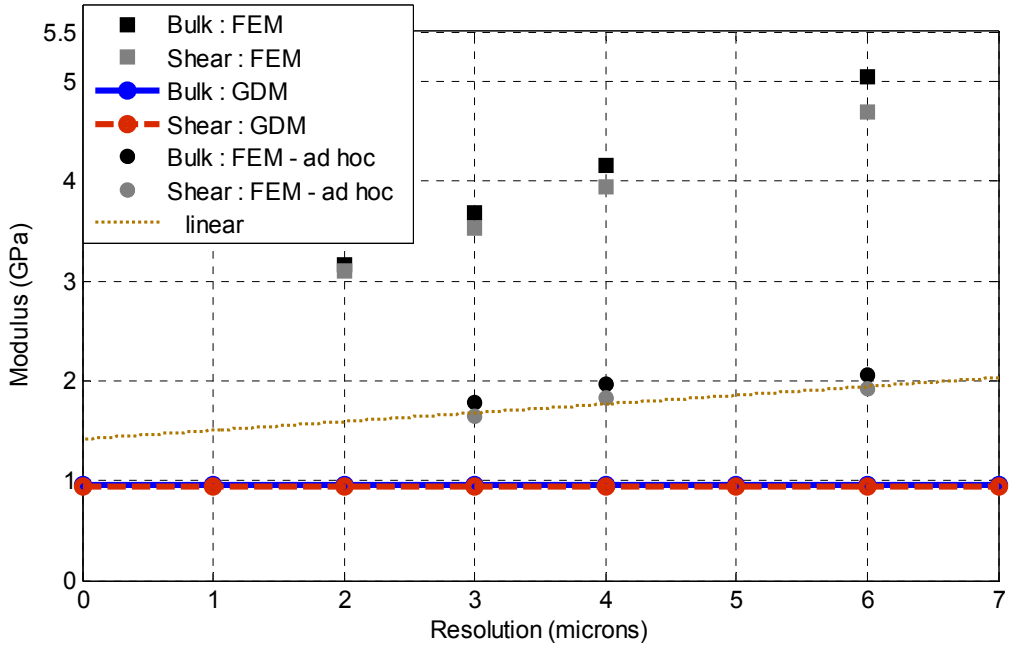

Figure 4.15: Comparison of bulk and shear moduli from FE and GD calculations with ad-hoc properties at contact voxels. The bulk and shear moduli of microstructures with artificial materials at contacts (*patch*) are lower than those with single grain moduli. Compared to GD simulation, the extrapolation of the linear fit for infinite resolution (~zero microns) is still higher (>50%). However, such an approach is difficult in real scanned images and involves precise contact identification.

4.6.2 Uniaxial compaction

In this section, we compare estimated acoustic velocities from GD simulation and EMT with acoustic experiments on granular packs under uniaxial compaction (Agnolin et al, 2005, Murphy, 1982, Myers and Hathon, 2006). As discussed in Chapter 3, we create several uniaxially compacted packs at different axial pressures. These packs are uniaxially compacted in the vertical direction with zero strain in the lateral direction. Most laboratory experiments report vertically propagating P- and S-wave velocities (Vp and Vs) for uniaxial compaction. Vertically propagating Vp and Vs correspond to C_{33} and C_{44} in the stiffness tensor, when the uniaxial compression is in the 3- (vertical) direction.

Agnolin et al (2005) report vertically propagating Vp and Vs at low pressures (lesser than 1MPa) for glass beads. They consider two different packs—dry glass beads and lubricated glass beads—to compare the effect of friction. Murphy (1982) reports vertically propagating Vp and Vs for a loading and unloading cycle in glass beads. He reports that velocities measured in the uniaxial unloading path are close to the hydrostatic loading path of Domenico's samples (1977). Compared to Agnolin et al (2005), Murphy's velocities at very low pressures (< 0.5 MPa) are higher. Holt (2005) also reports P- and S-wave velocities for uniaxial compaction for glass beads. Compared to Murphy (1982) and Agnolin et al (2005), Holt reports higher velocities for approximately the same pressure range. There is considerable variation in acoustic properties, even though the pack material is glass (Fig. 4.16). While Murphy's Vp measurements are reasonably close to Domenico's hydrostatic Vp, the same is not true for Vs. Possible reasons for this incoherence are exact material moduli and/or laboratory assembling process of the packs. It should be noted that glass is an amorphous material and may have different material properties depending on its manufacturing process. Further, Agnolin and Roux (2007) describes comprehensively the significant variation in effective elastic properties of stressed granular packs due to differences in laboratory assembling processes.

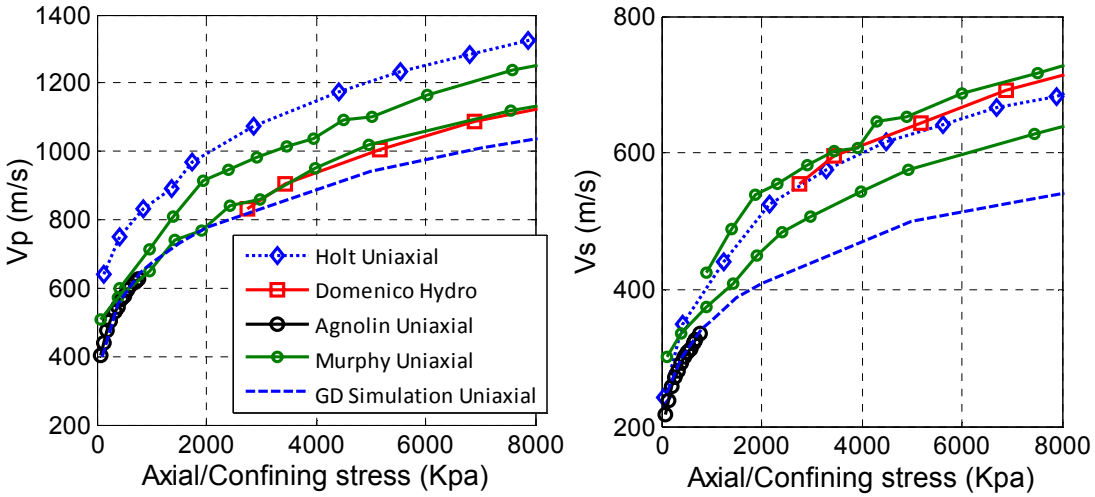

Figure 4.16: Comparison of Vp and Vs for uniaxial compaction of glass beads from various published experimental datasets. Domenico's hydrostatic measurements are also shown as reference. Acoustic velocities computed from GD simulation are reasonably close to Agnolin et al (2005).

As discussed in Chapter 3, we use GD simulation to replicate uniaxial compression experiments by compacting granular glass bead packs in the vertical direction with zero lateral strains. An initial pack is created with isotropic compaction at a very low pressure (0.1 MPa). Subsequent compactions are only in the vertical direction to create stable packs at different uniaxial stresses. For each of these stable packs (reference states), we estimate the full stiffness tensor using infinitesimal strain perturbations. The methodology is similar to bulk and shear moduli estimations for isotropic compressions (Sections 4.5 and 4.6.1). For comparing with laboratory uniaxial experiments, we use C_{33} and C_{44} at different uniaxial pressures to estimate vertically propagating Vp and Vs, respectively. Our simulated estimates of velocities are close to glass bead measurements from Agnolin et al (2005) (Fig. 4.16). For Vp, GD simulation results are close to Murphy's measurements (1982) for the low-pressure regime. However, with increasing uniaxial pressure, his measurements increase faster than the simulation estimates. For Vs, Murphy's velocities are higher than our simulated values and laboratory experiments of Agnolin et al (2005). As stated earlier, a possible explanation for this incoherence is exact material modulus of amorphous glass. Further, the quantitative effect of loading cycle on elastic properties is also

poorly understood. Apart from exact material properties and loading cycle, the elastic properties also depend on the initiation of anisotropic (uniaxial) compression at different stages of isotropic compression (precompaction).

Myers and Hathon (2006) report vertically propagating Vp and Vs in brine-saturated sand samples under uniaxial compaction. These sand samples were initially compacted to an isotropic pressure of ~8.5 MPa. Zimmer (2004) reports significant dispersion in water-saturated sand samples for hydrostatic pressure. We do not compare our simulated dry elastic moduli for uniaxial compaction with Myers and Hathon (2006). In the next section, we compare our stress ratios (horizontal to vertical) to their measurements. However, an interesting aspect of their measurements is the effect of initial isotropic compaction on subsequent uniaxial compactions. To study this aspect of the problem, we create five spherical grain packs with sand properties (Table 4.1) at five isotropic pressures ranging from 2.75 to 10.5 MPa. These packs are subsequently compacted in the vertical direction with zero lateral strain. Using a "servo-control" mechanism (as discussed in Chapter 3), we constrain the vertical stress of the pack after initiating uniaxial compression. Prior to this initiation, servo-control mechanism constrains the isotropic pressure of the pack. We consider six vertical (axial) stresses: 3.5, 5.0, 7.0, 10.5, 14.0 and 20.5 MPa during uniaxial compaction. The loading paths are shown in Figure 4.17 using horizontal and vertical (axial) stresses. It should be noted that "servo-control" constrains only the vertical stress after initiation of uniaxial compression for each of the loading paths. Hence, the horizontal stress during uniaxial compression evolves automatically in the simulation.

At each of these reference states, we conduct infinitesimal perturbation experiments to estimate six stiffness elements: C_{11}, C_{33}, C_{12}, C_{13}, C_{44} and C_{66} (Figs. 4.18 – 4.23). The infinitesimal perturbation experiments are similar to those described for bulk and shear moduli for isotropic compression (Sections 4.5 and 4.6.1). For estimating C_{11} and C_{33}, we conduct two experiments by applying infinitesimal strains $\delta\varepsilon_{11}$ and $\delta\varepsilon_{33}$, respectively. For C_{44}, we apply shear strains $\delta\varepsilon_{12} = \delta\varepsilon_{21}$. This is commonly known as simple shear test. In contrast, for the other shear stiffness element

C_{66}, we do pure shear test, as discussed in Section 4.5. For C_{12} and C_{13}, we conduct two experiments by applying infinitesimal strains $\delta\varepsilon_{11}$and $\delta\varepsilon_{33}$, respectively.

The infinitesimal macroscopic strains are distributed homogeneously as a first guess in each of these experiments. These affine strains cause force imbalance and GD simulation estimates the grain relaxations to equilibrate the unbalanced forces. During relaxation, we monitor the changes in macroscopic stress tensor of the grain pack. The stiffness tensor elements are estimated after the pack stabilizes. We estimate C_{11} and C_{33} using the ratio of change in $\sigma_{11}$and σ_{33} to corresponding strain perturbations, respectively (Eqns. 4.15). For estimating C44, the change in shear stress ($\sigma_{12}$and σ_{21}) is used (Eqn. 4.15). We use perturbations in $\sigma_{22}$and $\sigma_{11}$for calculating C_{12} and C_{13}, respectively (Eqn. 4.15). For a vertical tranverse isotropic (VTI) medium, there are only five independent stiffness elements (Mavko et al., 2009). Hence, using these six elements, we obtain the full stiffness tensor at each reference state in Figure 4.17.

$$\mathrm{C}_{11} = \frac{\delta\sigma_{11}}{\delta\varepsilon_{11}}; \mathrm{C}_{33} = \frac{\delta\sigma_{33}}{\delta\varepsilon_{33}};$$

$$\mathrm{C}_{44} = \frac{1}{4}\frac{(\delta\sigma_{12} + \delta\sigma_{21})}{(\delta\varepsilon_{12} + \delta\varepsilon_{21})}; \mathrm{C}_{12} = \frac{\delta\sigma_{22}}{\delta\varepsilon_{11}}; \mathrm{C}_{13} = \frac{\delta\sigma_{11}}{\delta\varepsilon_{33}} \tag{4.15}$$

The simulated stiffness constants at different pressures show that C_{33} is primarily dependent on axial pressure (Fig. 4.18). The change of compaction from isotropic to uniaxial does not change the pressure trend of vertically propagating P-wave modulus. However, the P-wave modulus in the horizontal direction decreases with change in compaction from hydrostatic to uniaxial (Fig. 4.19). For the shear elements, C_{44} and C_{66} are close to each other and show nearly the same response to the change in compaction (Fig. 4.20-4.21). It should be noted that unlike the vertically propagating P-wave modulus, the shear wave modulus in vertical direction, C_{44}, decreases with change in compaction from hydrostatic to uniaxial. We observed similar relationship in Vs for Murphy's uniaxial experiments (1982) and Domenico's hydrostatic experiments (1977). While Murphy's uniaxial Vp measurements are close to

Domenico's hydrostatic velocities, his Vs values are significantly lower than hydrostatic Vs (Fig. 4.16). We also note that unlike other stiffness elements, C_{13} increases with uniaxial compaction (Fig. 4.23).

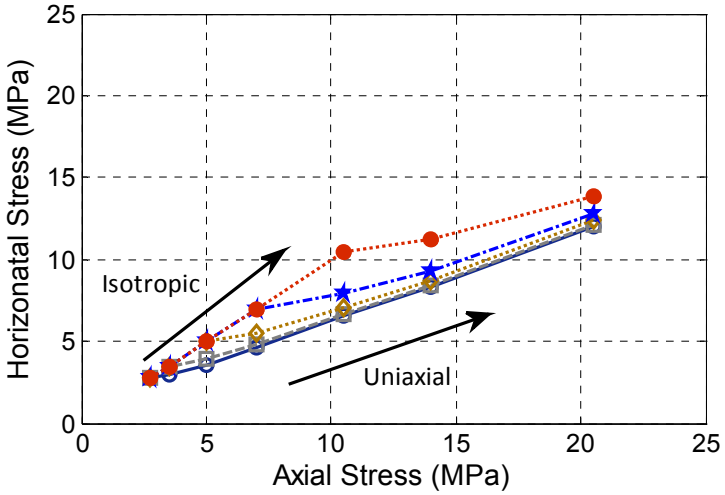

Figure 4.17: Comparison of axial and horizontal stresses for different loading paths. Uniaxial compaction starts at different initial isotropic pressures.

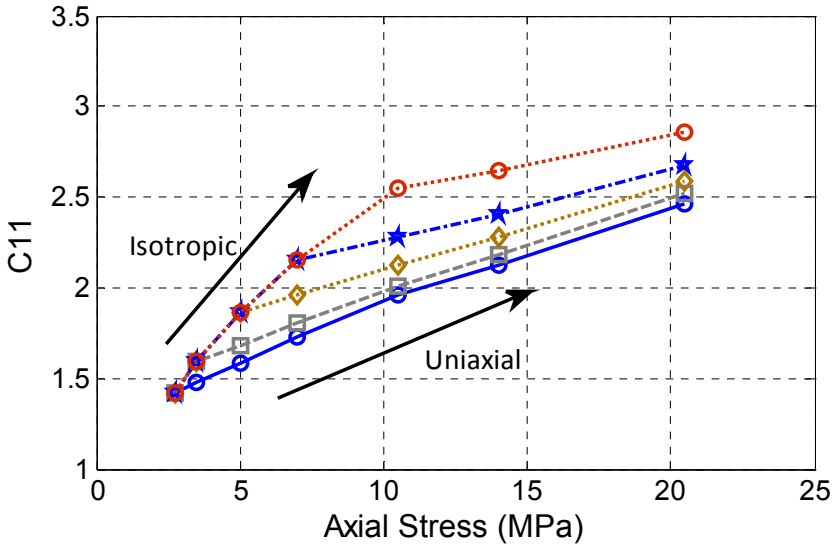

Figure 4.18: Comparison of C_{11} for different loading paths. Uniaxial compaction starts at different initial isotropic pressures.

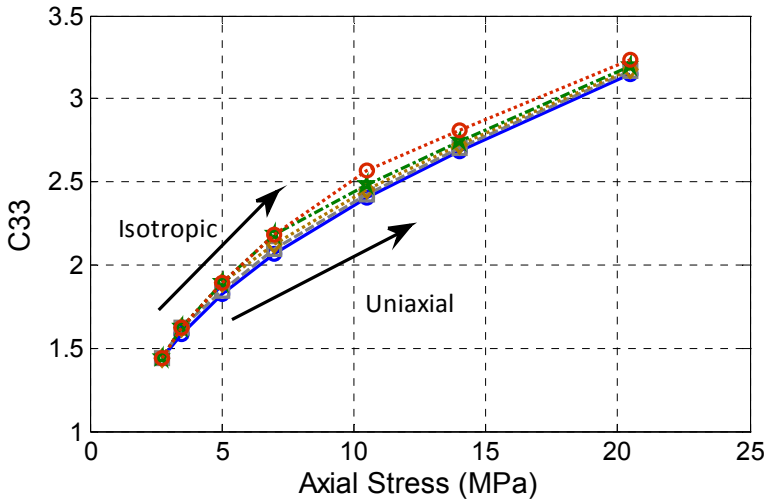

Figure 4.19: Comparison of C_{33} for different loading paths. Uniaxial compaction starts at different initial isotropic pressures.

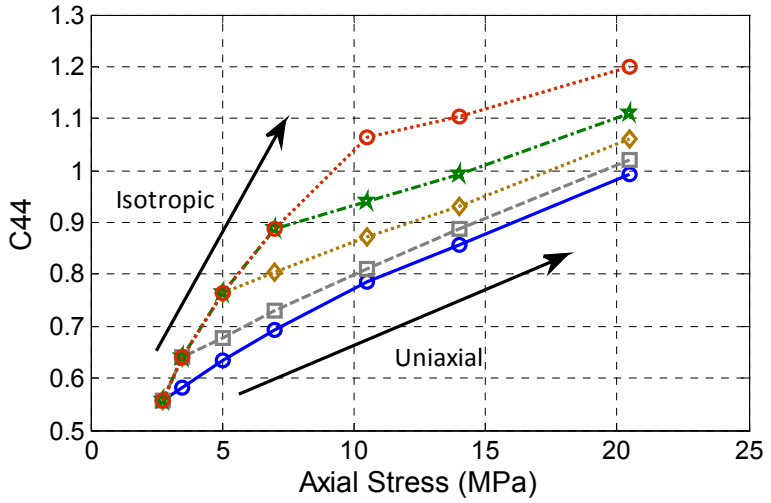

Figure 4.20: Comparison of C_{44} for different loading paths. Uniaxial compaction starts at different initial isotropic pressures.

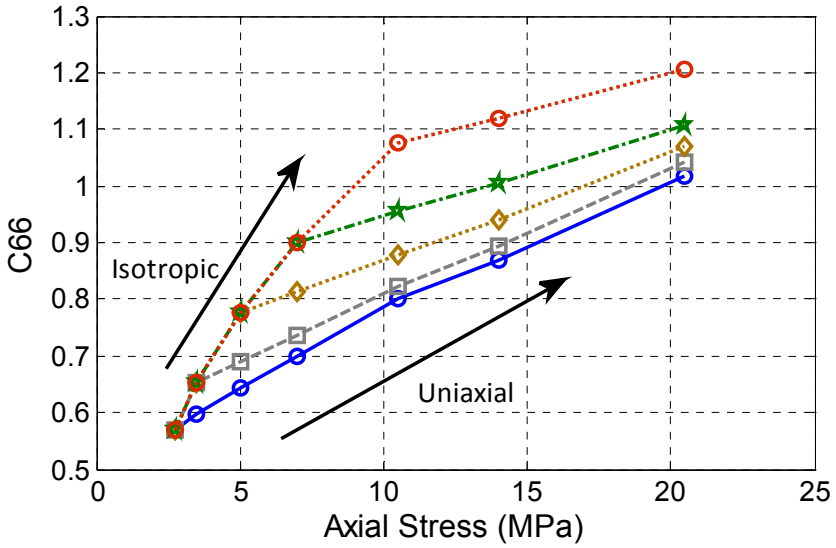

Figure 4.21: Comparison of C_{66} for different loading paths. Uniaxial compaction starts at different initial isotropic pressures.

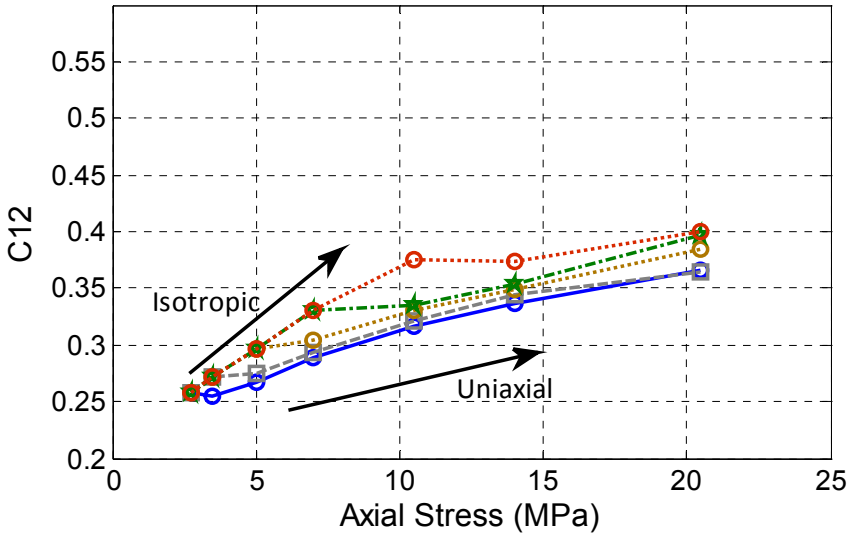

Figure 4.22: Comparison of C_{12} for different loading paths. Uniaxial compaction starts at different initial isotropic pressures.

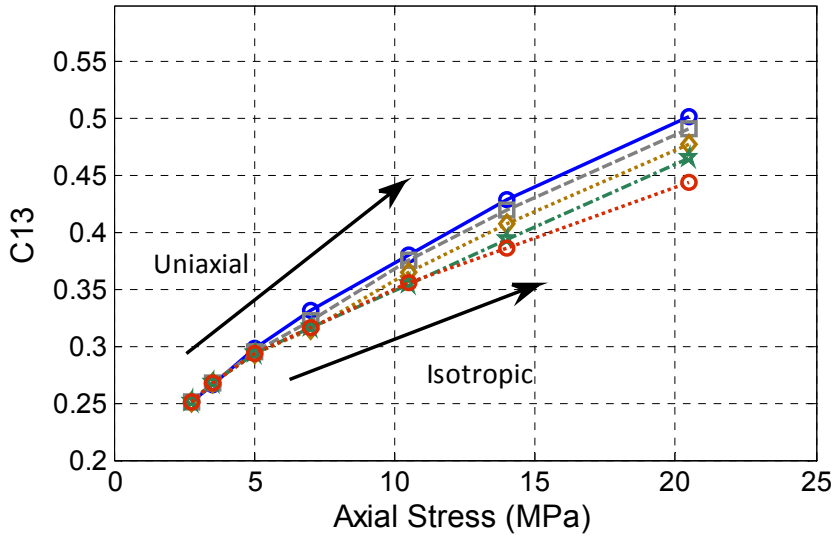

Figure 4.23: Comparison of C_{13} for different loading paths. Uniaxial compaction starts at different initial isotropic pressures.

We use the stress-induced anisotropy theory from Mavko et al. (1995) to model our simulated stiffness constants. This model predicts stress-induced velocity anisotropy using isotropic wave velocities. The generalized pore-space compliances are estimated from these isotropic measurements. The uniqueness of this model is that it does not consider any pre-defined pore-space parameter (e.g., crack shape or aspect ratio). Based on hydrostatic simulations, we derive functional forms of pressure dependence. These functional forms are used to predict the stiffness tensor at anisotropic stresses using Mavko et al.'s model (1995). The model predictions for V_{33} are close to simulated packs; however the simulated V_{11}, V_{44} and V_{66} are smaller than model prediction (Fig. 4.24). A possible explanation of this mismatch is the inelastic frictional losses during compaction in GD simulation, which is typically not accounted for in the theoretical model. This theoretical model assumes that all strains are applied infinitesimally. This inhibits any frictional sliding. However, for higher strains ($>10^{-4}$), an additional source of non-linearity, called geometrical or kinetic non-linearity appears, related to the large-scale grain rearrangements including sliding (Mavko et al., 2009, Johnson and Rasolofosaon, 1996). Our different reference states, as stated earlier, are created by imposing large-strain compactions and hence involve dissipative losses due to grain sliding and rearrangements.

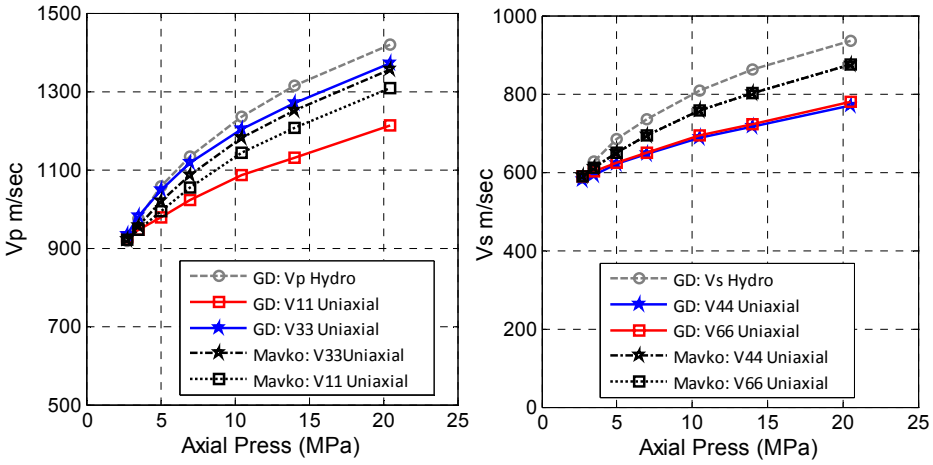

Figure 4.24: Comparison of simulated velocities with stress induced theory (Mavko et al., 1995).

Analogous to hydrostatic compaction case, we estimate *relaxation corrections* from GD simulation for different stiffness tensor elements in uniaxial compaction. For a pack of glass beads under uniaxial compaction, C_{44} has the most significant relaxation (Fig. 4.25). P-wave moduli C_{11} and C_{33} have smaller relaxations. These relaxation corrections can be used tom amend anisotropic EMT predictions (Norris and Johnson, 1999, Walton, 1987). As stated earlier, these relaxation corrections are rigorous physical corrections to compensate for the fact that EMT ignores heterogeneity, and subsequent stress relaxations.

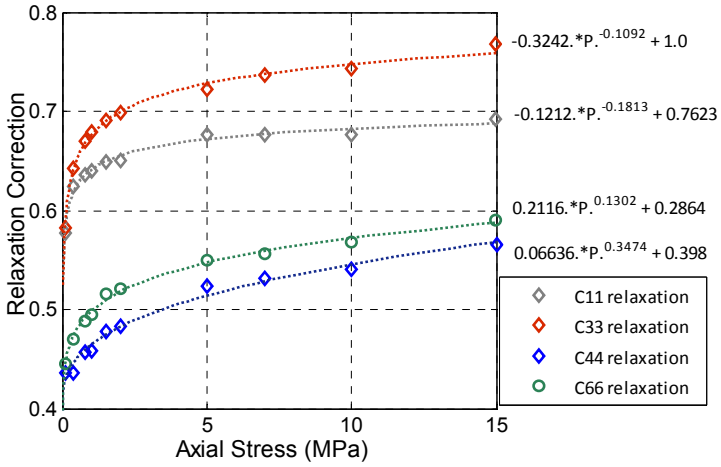

Figure 4.25: Relaxation correction dependence on pressure for C11, C33, C44 and C66 under uniaxial compression.

4.7 Stresses in granular pack

In Chapter 3, we discussed the heterogeneity in terms of mean stress for each grain with a compacted granular pack. We showed the impact of heterogeneity on estimates of elastic moduli for both isotropic and uniaxial compression. In this section, we discuss the macroscopic stresses in granular packs for both of these compaction protocols.

4.7.1 Isotropic compaction

Walton's (1987) EMT predicts macroscopic stresses of granular packs under strain. Jenkins et al. (2005) suggest that the estimation of macroscopic stress using EMT is reasonably valid for isotropic compression. Both frictionless and infinite-friction models predict the same effective stress under bulk compression. The assumption of isotropic distribution of contacts in EMT eliminates tangential forces at any contacts during bulk compression. However, using GD simulation we find that tangential forces exist at grain contacts in a disordered pack even during isotropic compression. During the initial preparation of packs, when large strains of the order of 10^{-3} are applied, the pack rearranges through grain sliding and rotation.

From GD simulation, we compute strains corresponding to different compacted reference states relative to an initial low-pressure jammed pack. Using these strains, we use Walton's infinite friction model to predict stresses. It should be noted that for isotropic compaction, both infinite friction and frictionless models predict the same stresses. We compare these stresses with laboratory experiments (Fig. 4.26). At any volumetric strain, EMT stress predictions are higher than GD simulation and laboratory experiments. This is because EMT precludes any slip by ignoring heterogeneity. As explained before, because of heterogeneity, grains slide at higher stresses (or strains), thereby relaxing the macroscopic stress. For Domenico's glass-bead measurements (1977), we calculate volumetric strains from reported changes in porosity. It should be noted that there are two caveats in these calculations: (1) the compaction-induced changes in porosity are reported for brine-saturated samples; (2) there is ambiguity about the initial porosity in Domenico's glass bead samples. Further,

we also compare these simulated, experimental and theoretical stress-strains with those from Zimmer's glass-bead samples (2004). These samples were however prepared with different loading-unloading cycles. For comparing Zimmer's data with single-cycle GD simulations and laboratory experiments (Domenico, 1977), we consider only the stress-strain values for virgin compaction zones.

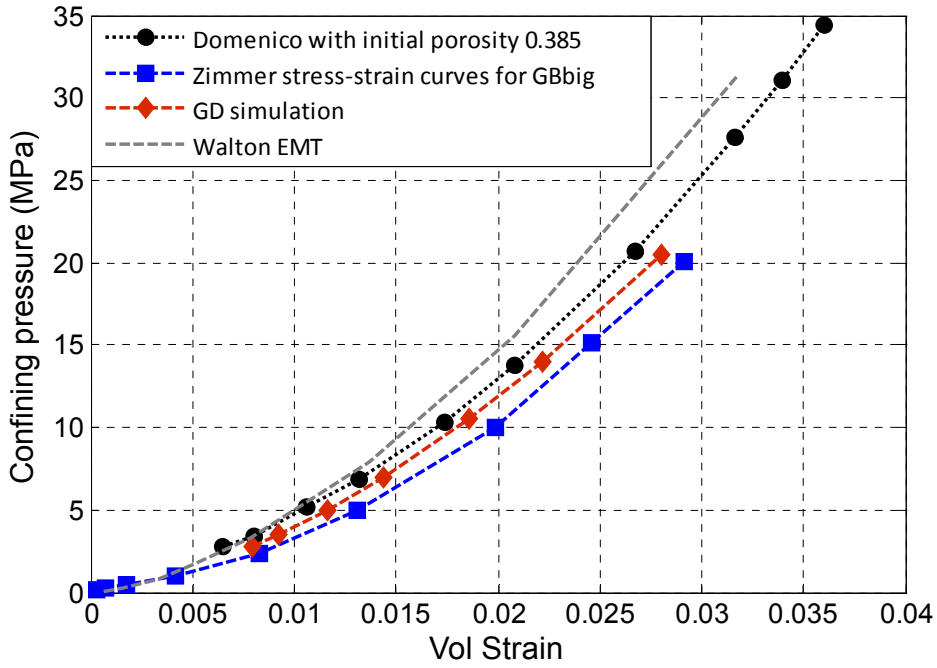

Figure 4.26: Comparison of stress vs. strain from laboratory experiments, EMT and GD simulation. Even for isotropic pressures, EMT predicts higher stresses at higher strains. EMT does not consider grain slipping, which occurs at higher strains, thereby releasing stress. GD simulation stress-strain curves fall between the two different laboratory experiments on glass beads.

4.7.2 Uniaxial compaction

The expression for the horizontal stress to vertical stress ratio, K_0, for a semi-infinite continuum with linear elastic, homogeneous and isotropic properties under uniaxial compaction is

$$K_0 = \frac{S_h}{S_v} = \frac{\nu}{(1-\nu)} \tag{4.16}$$

where ν is Poisson's ratio for the isotropic medium and S_h and S_v are the horizontal and vertical stresses. For an elastic medium with vertical transverse isotropy, the stress ratio can be estimated as follows (Amadei, 1996):

$$\frac{S_h}{S_v} = \frac{E_h}{E_v}\frac{\nu_{vh}}{(1-\nu_{hh})} \tag{4.17}$$

where E_h and E_v are Young's moduli for horizontal and vertical loading respectively, and ν_{vh} and ν_{hh} are the two Poisson's ratios for vertical and horizontal loading. An alternate expression can be derived from stiffness tensor elements C_{13} and C_{33} using linear elasticity for uniaxial compaction as follows:

$$\frac{S_h}{S_v} = \frac{C_{13}}{C_{33}} \tag{4.18}$$

These stress ratios can also be computed for various uniaxial stress states using GD simulation. As reported in Section 4.6.2, we created five isotropically compacted reference states ranging from 2.75 MPa to 10.5 MPa. These isotropic packs were further compacted uniaxially with zero lateral strain. The final reference states are shown in Figure 4.17. For each of these reference states, we calculate K_0, the ratio of average radial stress (in two horizontal directions) to axial stress (S_h/S_v). The experimental K_0 from uniaxial compression on sand with zero lateral strain (Myers and Hathon, 2006) are compared with those from GD simulation (Fig. 4.27). The simulated results show similar behavior as laboratory experimental result: a steep decrease in K_0 for initial uniaxial compaction which subsequently becomes constant. We further notice that the stress ratio reaches an asymptotic value of ~0.58 (Fig. 4.27). Using horizontal and vertical stresses for a uniaxial compaction loading cycle (blue circles in Fig. 4.17), we construct Mohr's circles. Although our simulations are three-dimensional, we have vertical transverse isotropy due to uniaxial compaction. Hence, we construct two dimensional Mohr's circle for stress analysis. Before analyzing these results, we provide a short overview of Mohr's circle and Mohr theory of failure.

Mohr's circle is a graphical method for transforming the stress tensor, and is used for determination of normal and shear tractions acting on a plane of arbitrary orientation relative to the principal stresses (Hudson and Harrison, 1997, Mavko et al., 2009). Further, the Mohr theory of failure, also known as Coulomb-Mohr criterion or the internal friction theory (Jaeger and Cook, 1979) is based on Mohr's circle and is often used for predicting failure of brittle materials. The Mohr-Coulomb criterion, also known as Mohr envelope, expresses the relation between the shear stress and normal stress at failure. By constructing Mohr's circles using pairs of normal- and shear-stresses at failure, the linear Mohr envelope is simply a tangent to these circles. The slope of this line corresponds to angle of internal friction and the intercept is the cohesive strength. Conversely, utilizing the concept of cohesion (i.e., shear strength of rock when normal stress is applied) and the angle of internal friction (equivalent to an inclination angle which causes sliding of a block of similar material), a linear Mohr envelope shows the shear stresses for failure under normal compression (Hudson and Harrison, 1997). Further, using the coefficient of internal friction, μ_i, the ratio of principal stresses can be computed as follows:

$$\frac{S_h}{S_v} = \left[\sqrt{\mu_i^2 + 1} - \mu_i\right]^2 \tag{4.19}$$

From our uniaxial compaction simulations, we use the principal stresses (vertical and horizontal) at different reference states to construct Mohr's circle and fit an envelope for these circles (Fig. 4.28). These reference states are uniaxially compacted stable packs from a single uniaxial loading cycle, represented as black circles in Fig. 4.27. It should be noted that we do not simulate failure in GD simulation, and hence these envelopes (lines with constant slopes in Fig. 4.28) are not strict indicators of failure. In GD simulation, grains rearrange during compaction, often involving grain-sliding due to finite inter-grain friction. We note that a line with slope equal to the inter-grain finite friction used in our simulations ($\mu = 0.3$), does not touch any of the Mohr's circles (Fig. 4.27). We further note that a line with slightly lower slope (0.27) is tangential to the Mohr's circle for the most-compacted reference state (right-most

Mohr's circle in Fig. 4.27). This *apparent* coefficient of internal friction gives a value of 0.5865 from Eqn. 4.19, which is the asymptotic K_0 in Fig. 4.27.

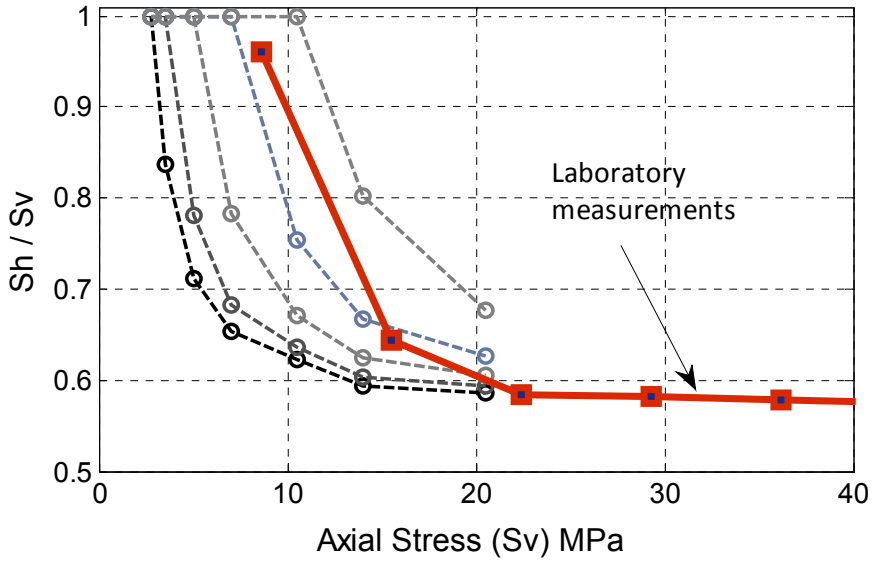

Figure 4.27: Stress ratio K_0 (i.e., S_h/S_v) for uniaxial compaction initiated at different hydrostatic pressures. The ratio asymptotically matches laboratory experiments on sand. Using inter-grain finite friction value (0.3) in Eqn. 4.19 provides the same asymptotic K_0 (0.5865).

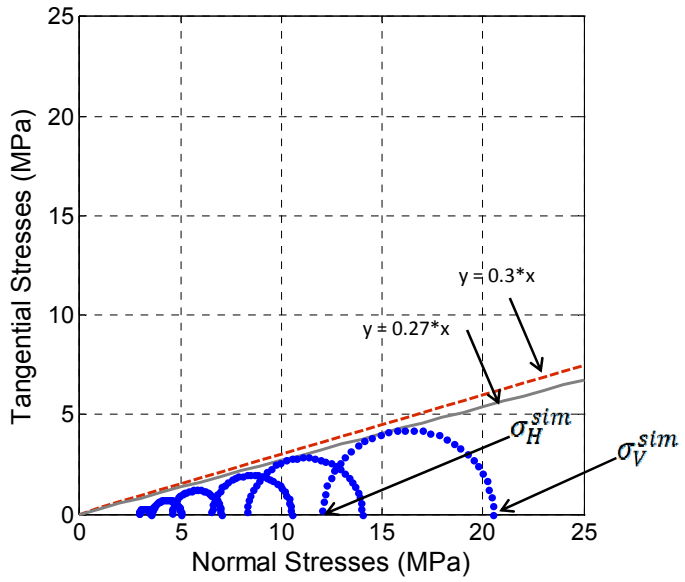

Figure 4.28: Mohr's circle for different uniaxially compacted reference states from a single loading cycle (black circles in Fig. 4.27) using simulated principal stresses. Tangent envelopes are drawn corresponding to finite inter-grain friction (0.3) and an arbitrary value (0.27) which touches the Mohr's circle for highest stress state (right-most Mohr's circle).

We now check the applicability of Eqns. 4.16 and 4.18 to predict simulated stress-ratios. The rationale is to quantify prediction errors, if any, for estimating stress-ratios using elastic constants, which are commonly available from subsurface sonic well-logs and/or rock physics models. These two equations involve three elastic constants: Poisson's ratio, and two stiffness tensor elements, C_{33} and C_{13}. From our simulated elastic properties for uniaxial compaction, we use these three elastic constants to predict K_0. We focus on a single uniaxial loading cycle, as we did for Mohr's circle analysis. For each reference state in this cycle (black circles in Fig. 4.27), we earlier computed the full elastic stiffness tensor (Figs. 4.18 – 4.23).

Eqn. 4.16 predicts stress ratio for a linear elastic and isotropic medium. For using this equation, we consider C_{33} and C_{44} from GD simulation to calculate Poisson's ratio. It should be noted that the reference states used for estimating these stiffness constants have *vertical transverse isotropy* (VTI) instead of isotropy, as Eqn. 4.16 requires. However, C_{33} and C_{44} correspond to vertically propagating Vp and Vs, which are commonly measured in sonic well-logs. Hence, we check the prediction error for stress-ratios using C_{33} and C_{44}. Using these stiffness constants and *assuming* isotropy, we derive stress-ratios as follows:

$$K_0^I = \frac{C_{33} - 2C_{44}}{C_{33}} \tag{4.20}$$

where K_0^I signifies stress-ratio calculation with isotropic assumption. In contrast, we directly use elastic stiffness constants for VTI reference states in Eqn. 4.18 to estimate stress-ratios K_0^{VTI} as well. This approach does not make any assumptions about the isotropic nature of the medium. Although Eqn. 4.18 requires the medium to be linear elastic, our stiffness elements used to estimate K_0^{VTI} are non-linearly related with stress. Comparing both these predictions with simulated stress-ratios, we find simulated stress-ratios are significantly higher (200%) than predicted stress-ratios (Fig. 4.29). Apart from the assumptions in Eqn. 4.16 and 4.18, a possible reason for this mismatch is the strain amplitude difference. The simulated stresses for compacted packs are the

result of *large-scale* grain motions, sliding and rotations. However, the elastic constants used for both these equations are infinitesimal-strain relaxed moduli, which do not consider inelastic losses during large-strain experiments. Hence, the applicability of both the equations is inappropriate, and they do not match realistic stress ratios.

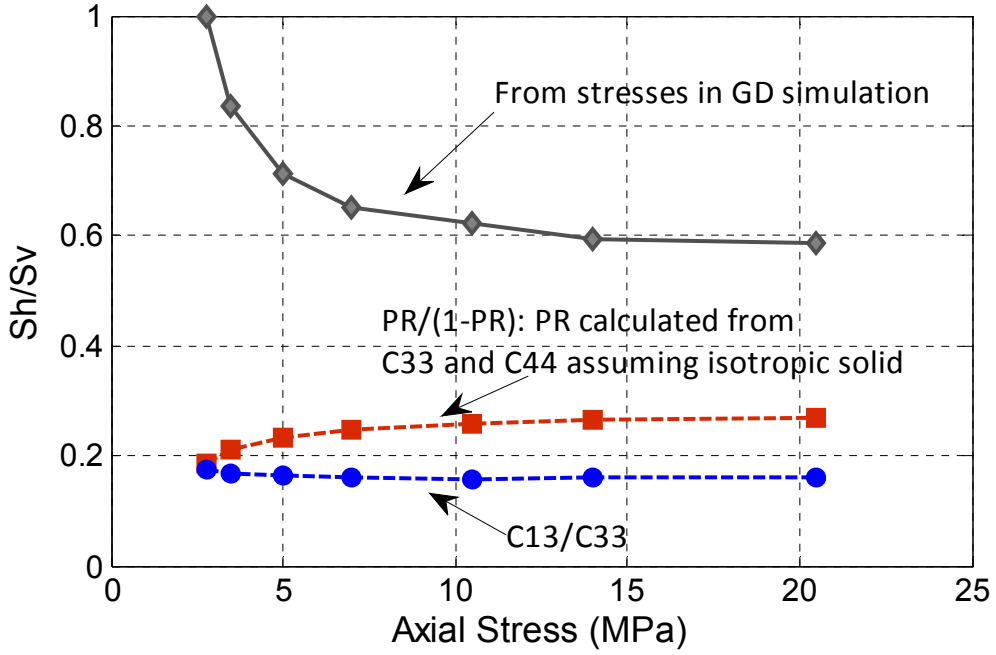

Figure 4.29: Estimates of K_0 (stress-ratio) using Eqns. 4.14 and 4.16 do not match simulated K_0.

4.8 Effect of sorting on elastic properties

The monodisperse packs are a good starting point for understanding granular-pack physics. However, for real earth science problems involving geo-materials, size distributions are hardly ever unimodal. In Chapter 3, we discussed preparation details for bidisperse packs and packs with Gaussian size distributions. In this section, we present elastic property estimates from GD simulation.

4.8.2 Bidisperse packs

Using the bidisperse packs described in Chapter 3, we compute bulk moduli. Glass beads packs with different size ratios (1:1.2, 1:1.5, 1:2 and 1:3) are compacted to 10 MPa. The estimates of bulk moduli for different volume fractions show non-linear behavior (Fig. 4.30). Corresponding to the troughs in porosity and CN plots with varying volume fractions (Chapter 3, Fig. 3.19 and 3.20), the moduli estimates show crests. The height of the crest increases with increasing size ratios (Fig. 4.30). We also note that the bulk moduli do not show changes for higher volume fraction of large grains (>85%). This is due to the fact that the smaller grains are mostly floaters for these volume fractions. For lower volume fractions of large grains, the smaller grains join the contact network (increase in CN in Fig. 3.20) and hence the bulk moduli significantly increase. We also estimated bulk moduli of bidisperse quartz packs at different pressures and different volume fractions (Fig. 4.31 – 33). Figure 4.33 shows compaction and sorting effects on bulk moduli for bidisperse packs with size ratio of 1:2.

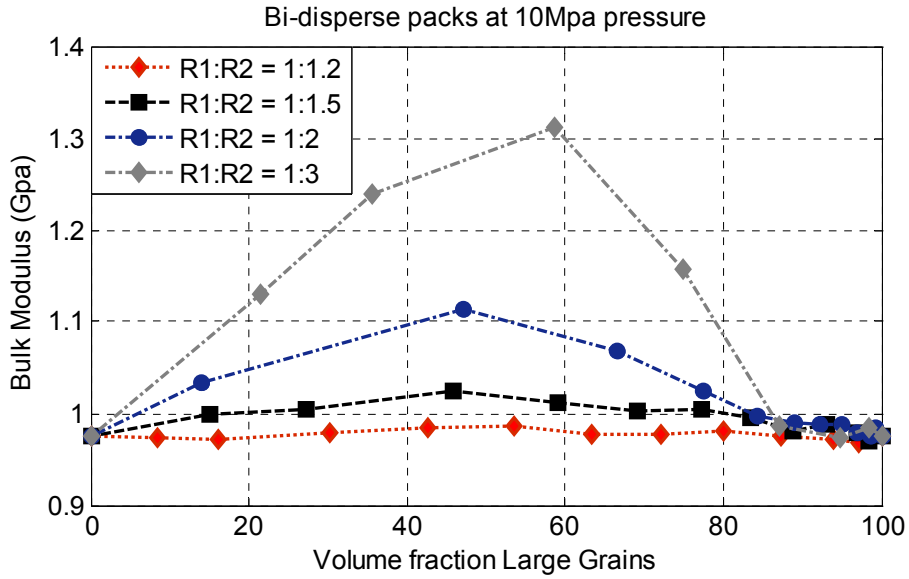

Figure 4.30: Bulk moduli variation with volume fraction of large grains for different size ratios. Same material property are used for both the sizes (glass). We note that the bulk moduli shows crest (inverted V-shape) whose heights increase with increasing radius ratios. We also note that bulk moduli remains constant for different size ratios for high volume fraction (>85%) of large grains. For lower volume fractions of large grains, the smaller grains join the contact network (increase in CN in Fig. 3.20) and hence the bulk moduli significantly increase.

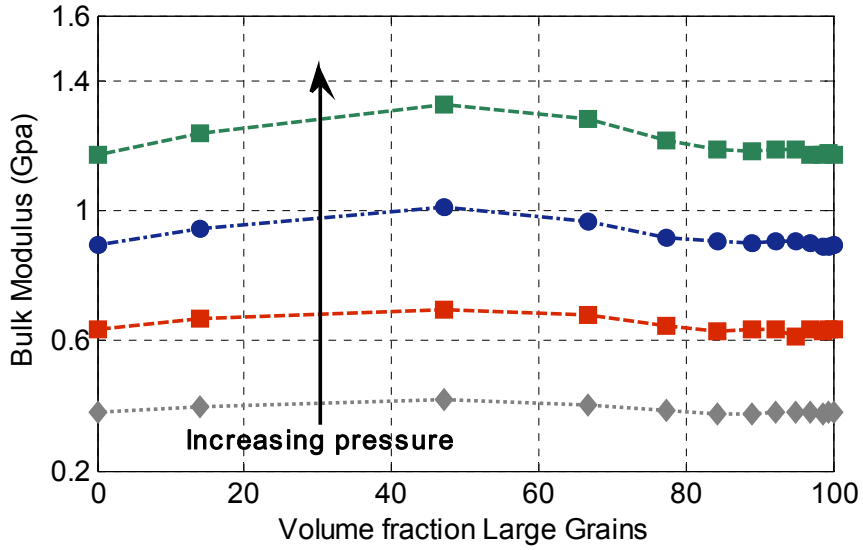

Figure 4.31: Compaction effects on bulk moduli variation with volume fraction of large grains for size ratio of 1:2. The same material properties are used for both sizes (quartz).

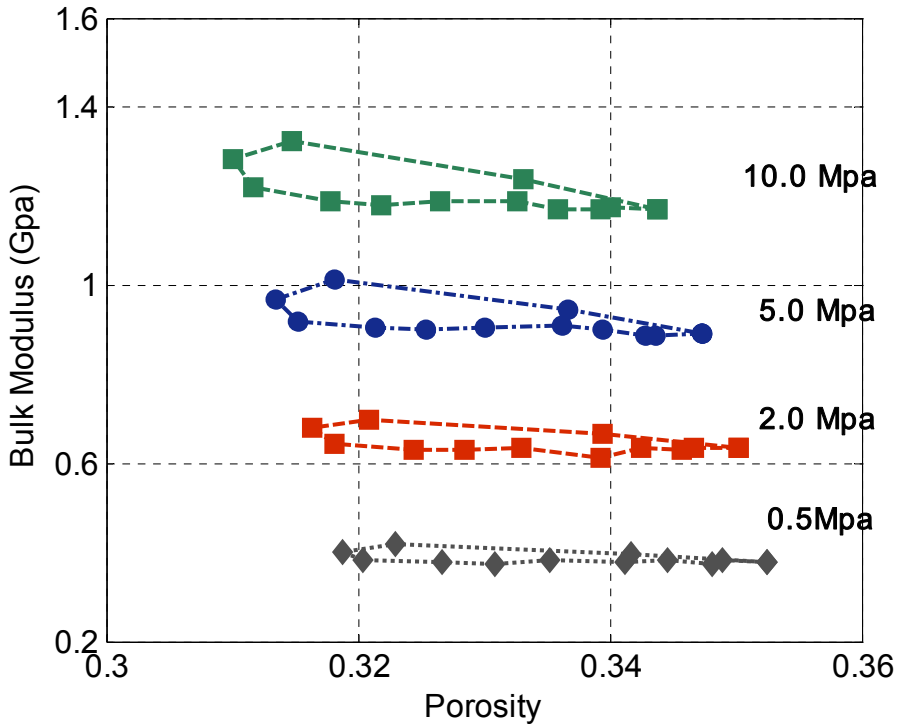

Figure 4.32: Compaction effects in bulk moduli – porosity relations for bidisperse packs with size ratio of 1:2. The same material properties are used for both sizes (quartz).

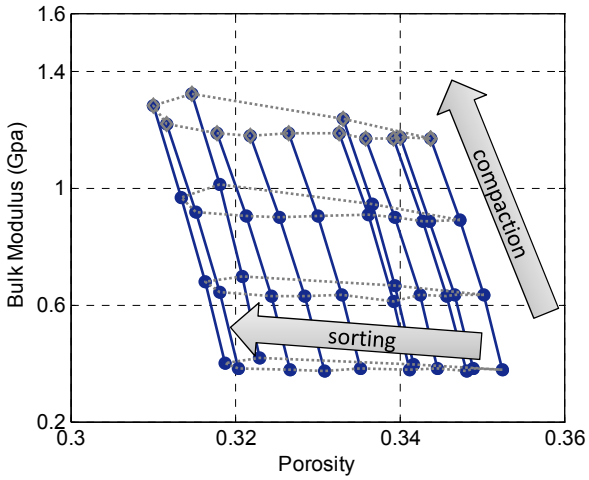

Figure 4.33: Compaction and sorting trends in bulk moduli – porosity relations for bidisperse quartz packs with size ratio of 1:2.

We also estimated bulk moduli for bidisperse packs with different mineralogy. Using the compacted quartz sand-shale (using material properties in Table 4.1) mixtures at 10 MPa reported in Chapter 3, we compute bulk moduli for different size ratios and different volume fractions (Fig. 4.34). It should be noted that we consider spherical shale grains to investigate the *combined* effect of mineralogy and sorting on elastic properties. Bulk moduli show a flat trend with different volume fractions for size ratio of 1:2. However, with increasing size ratio (1:3), the trend shows the usual crest commonly associated with elastic properties of sand-shale mixtures. For realistic size ratios of sand and shale grains (~1:100), we can observe typical crests.

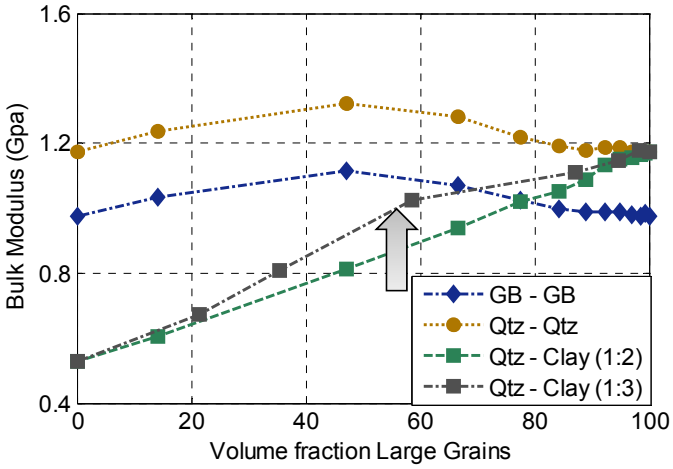

Figure 4.34: Effect of mineralogy and size-ratio on moduli–volume fraction relations.

4.8.2 Polydisperse packs with pre-defined size distributions

We compute bulk and shear moduli using GD simulation for packs with Gaussian size distributions. We consider distributions with four different sorting indices (ratio of standard deviation to mean grain size): 0.09, 0.18, 0.3 and 0.45. We note that the elastic moduli are reasonably close for different isotropic pressures (Fig. 4.35), even though the porosities for different SI range over ~4% at any isotropic pressure (Section 3.4.3.1 and Fig. 3.23).

The prediction of elastic properties using EMTs considers monodisperse packs. Although micromechanical contact force laws for grain-pairs with different radii exist (Timoshenko and Goodier, 1956), analytical solutions for predicting effective elastic properties in poorly sorted packs are non-existent. Flórez-Niño (2005) describes a heuristic solution to predict stress-dependent elastic properties for poorly sorted packs using estimates of *average* contact area and coordination number estimates. The conventional approach to predict elastic properties of poorly sorted packs at higher pressures is to use the modified lower Hashin-Shtrikmann (HS) bounds between two end points: mineral moduli and an estimate of compacted, well-sorted sediment moduli. This approach commonly referred as *friable sand model* (Dvorkin and Nur, 1996) heuristically assumes that points on modified lower HS bounds represent poorer sorting. The most common estimates for elastic moduli of the compacted, well-sorted (monodisperse) end-point are EMT predictions. As extensively discussed in Sections 4.5 and 4.6, EMT predictions, are incorrect, especially for shear moduli. These predictions can, however, be amended by using stress-dependent *relaxation correction* factors, which are based on rigorous GD simulation calculations. As shown in Section 4.6, EMT predictions with relaxation corrections matches GD simulated elastic moduli for well-sorted packs. For the present analysis, we use elastic properties from GD simulation as end-points (Fig. 4.36). Using GD simulation predictions for well-sorted packs at different isotropic pressures, we show friable sand model curves (blue lines) in Figure 4.36. We note that both bulk and shear moduli for poorly sorted packs are close to those predicted using this heuristic model (Fig. 4.36). Further, the compaction

trends of each poorly sorted pack also follow the lower HS bounds for compacted, well sorted packs.

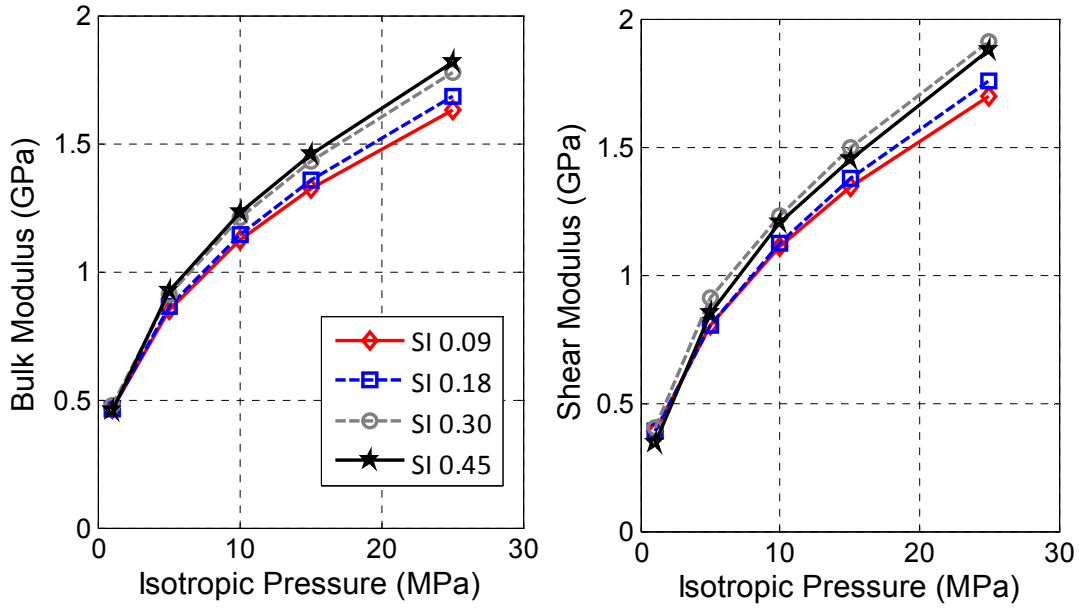

Figure 4.35: Bulk and shear moduli for packs with different sorting indices.

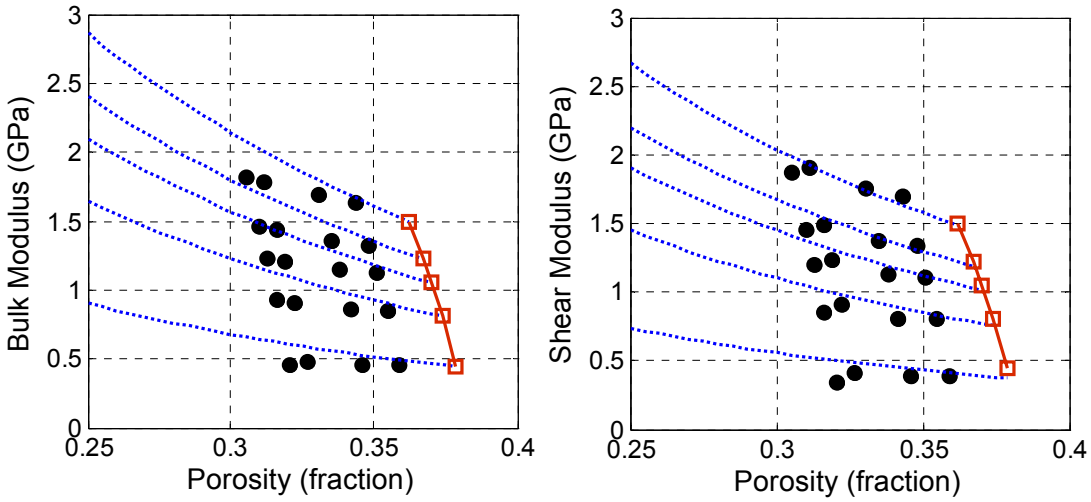

Figure 4.36: Elastic properties for compacted, poorly sorted packs match reasonably well with the friable sand model (Dvorkin and Nur, 1996). The black filled circles are elastic properties of poorly sorted packs. Sorting reduces porosity primarily, compaction increases moduli significantly. The end points of friable sand model curves (blue dotted lines) are GD simulation elastic moduli for monodisperse packs (red squares).

4.9 Compaction-induced changes in permeability

Compaction-induced changes in permeability are important for reservoir production and monitoring. During production, decreasing pore pressure leads to higher effective stresses. The effective stresses non-linearly affect porosity and, hence, permeability. With compacted granular packs from GD simulation, we compute permeability using Lattice-Boltzmann (LB) simulations.

For most practical usage, the Kozeny-Carman relation (Carman, 1961, Mavko et al., 2009) is used to relate porosity with permeability. This is based on flow in an idealized twisted pipe. By applying Darcy's law for laminar flow, this relation expresses permeability, κ, as

$$\kappa = \frac{B\phi^3 d^2}{\tau} \tag{4.17}$$

where ϕ is the porosity, d is the mean grain diameter, τ is tortuosity and B is a geometric factor. While porosity and grain diameters are physically realizable parameters, the other two are mostly used as fitting parameters.

We compare porosity and permeability for monodisperse and polydisperse packs (Fig. 4.37). The best-fit Kozeny-Carman relations are also plotted as a reference. The polydisperse packs have a mean grain diameter of ~80 microns. However, fitting Kozeny-Carman relations for different sorting and grain sizes requires that we change the *geometric factor*, B. For similar mean grain size, poorer sorting (or larger spread of grain size distribution), requires a higher geometric factor to fit permeability.

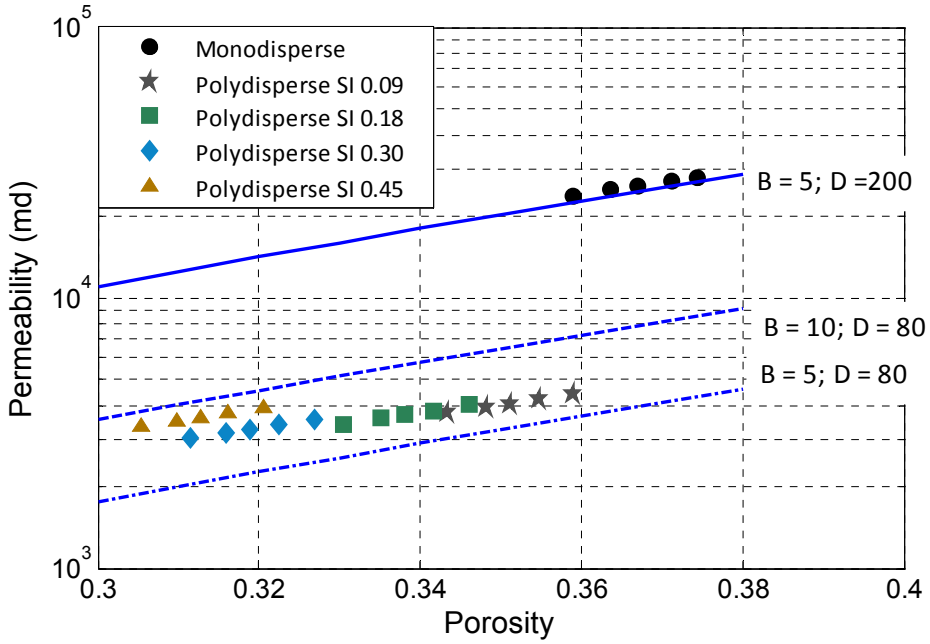

Figure 4.37: Compaction-induced permeability and porosity changes in well-sorted and poorly sorted grain packs. The pressure ranges considered were 0.1 Mpa to 10 Mpa for monodisperse and 1 Mpa to 25 Mpa for polydisperse packs. The best-fit Kozeny-Carman relations are also plotted. For polydisperse packs, even though the mean grain size was same, higher geometric factors were required to fit the data.

4.10 Summary and conclusions

In this chapter, we primarily investigate the validity of EMT assumptions using simulated grain packs. We show that by ignoring heterogeneity and its effects, EMT assumes that mean strain approximation is valid in disordered granular packs. However, our numerical experiments with GD simulations show that affine strain approximation on random initially stable pack violates first principles, thereby resulting in an unstable pack. The elastic moduli of this unstable state thus fail to match laboratory experiments. GD simulation, however, solves Newton's laws to allow for proper rearrangement or relaxation of the granular pack while computing elastic properties. These local rearrangements are heterogeneous and of the same order as the applied infinitesimal affine strain. The relaxed moduli are reasonably close to laboratory experiments on glass beads and sand. Based on the rigorous calculations of relaxation at different pressures using GD simulation, we present pressure-dependent functional forms (empirical fits), which we term *relaxation correction factors*. Further,

we show that EMT predictions with these correction factors applied match experimental results on glass beads and quartz sands. We also present relaxation correction factors for elastic stiffness constants C_{11}, C_{33}, C_{44} and C_{66} for uniaxial compaction. It should be noted that these relaxation correction factors are computed from precise GD simulation results to compensate for inappropriate EMT assumptions. A rigorous theory predicting the amount of relaxation for a heterogeneous system of frictional grain packs as a closed-form expression is absent. These findings, however, are essential pre-requisites to an improved theory which properly accounts for the effects of heterogeneity. Fluctuation-Dissipation theory can be possibly used to characterize the amount of relaxation for granular systems. Based on temporal fluctuation of state observable, like stress, of granular packs, the response under infinitesimal perturbation can be possibly characterized.

We also show the failure of FE in predicting correct elastic properties of granular packs due to voxel resolution. For a set of four realistic image resolutions, the FE elastic moduli are higher than *true* GD moduli. The predictions can be improved by approximating contact voxels; however, this approach is impractical in real scanned images because of the difficulty of contact detection.

For uniaxial compaction, we predict stiffness tensor elements at various uniaxial pressures, starting from different hydrostatic pressures. The hydrostatic data is further used to predict the anisotropic stiffness tensor using the model of Mavko et al. (1995). While the model predicts C_{33} correctly, the rest of the stiffness tensor elements do not match simulated results.

GD simulation reasonably matches stress-strain curves from laboratory experiments. We also show that EMT model predictions of stress deviate from laboratory strains at higher strain values. EMT does not allow any tangential forces during isotropic compression, because it assumes homogeneous contact distribution. This results in no grain sliding, which contradicts our observations of GD simulation at higher strains. Hence, EMT overpredicts the stress.

For bidisperse and polydisperse packs, we present pressure-dependent elastic properties for packs with different sorting. While the conventional rock-physics approach works reasonably well in matching GD simulation data, the prediction of shear moduli for well-sorted end-point packs using EMT should be corrected. We further present permeability predictions using LB simulations for compacted monodisperse and polydisperse packs. For fitting these data with the Kozeny-Carman relationship, we need higher geometric factors for poorly sorted packs with similar mean grain size.

4.11 References

Agnolin, I. and Roux, J.-N., 2007, Internal states of model isotropic granular packings. I. Assembling process, geometry, and contact networks, Phys. Rev. E 76, 061302.

Agnolin, I., Roux, J.-N., Massaad, P., Jia, X. and Mills, P., 2005, Sound wave velocities in dry and lubricated granular packings: numerical simulations and experiments, Powders and Grains, Stuttgart, Allemagne.

Amadei, B., 1996, Importance of anisotropy when estimating and measuring in situ stresses in rock, Int J Rock Mech Min Sci & Geomech Abstr 33, 3, 293-325.

Arns, C. H., Knackstedt, M. A., Pinczewski, W. V. and Garboczi, E. J., 2002, Computation of linear elastic properties from microtomographic images: Methodology and agreement between theory and experiment, Geophys., 67, 5, P1395-1405.

Bachrach, R., and P.Avseth, 2008, Rock physics modeling of unconsolidated sands: Accounting for nonuniform contacts and heterogeneous stress fields in the effective media approximation with applications to hydrocarbon exploration: Geophysics, 73, no. 6, E197–E209

Behringer, R. P. and Jenkins, J. T., 1997, Powders & Grains 97, Balkema, Rotterdam.

Berryman, J. G., 1983, Random close packing of hard spheres and disks, Phy. Rev. A 27 2, 1053.

Brandt, H., 1955, J. appl. Mech. 22 (1955), p. 479.

Carman, P.C., 1961. L'écoulement des Gaz á Travers les Milieux Poreux, Paris: Bibliothéque des Science et Techniques Nucléaires, Press Universitaires de France, 198pp.

Chan, A., 2004, Production-induced reservoir compaction, permeability loss and land surface subsidence, Ph.D. thesis, Stanford University, Stanford, CA.

Chen, Y.-C., Ishibashi, I. and Jenkins, J. T. , 1988, Dynamic shear modulus and fabric. Pt 1: depositional and induced anisotropy, Geotechnique 38, 25-32.

Coste, C., and B. Gilles, 1999, On the validity of Hertz contact law for granular material acoustics: European Physical Journal B, 7, 155–168.

Cumberland, D.J. and Crawford, R.J., 1987, The packing of particles, Handbook of Powder Technology, Vol. 6, New York, Elsevier.

Digby, P. J., 1981, The effective elastic moduli of porous granular rocks: Journal of Applied Mechanics, 48, 803–808.

Domenico, S. N., 1977, Elastic properties of unconsolidated porous sand reservoirs, Geophys., 42(7), 1339-1368.

Duffy, J. & Mindlin, R. D., 1957 Stress-strain relations and vibrations of a granular medium, J. appl. Mech. (ASME) 24, 585-593.

Duffaut, K., Landro, M. and Sollie, R., 2010, Using Mindlin theory to model friction-dependent shear modulus in granular media, Geophysics, 75, 143-152.

Dutta, T., Mavko, G. and Mukerji, T., 2010, Improved granular medium model for unconsolidated sands using coordination number, porosity, and pressure relations, Geophysics, 75, 2, E91-E99.

Dvorkin, J., andA. Nur, 1996, Elasticity of high-porosity sandstones: Theory for two North Sea data sets: Geophysics, 61, 1363–1370.

Flórez-Niño, J. –M., 2005, Integrating geology, rock physics, and seismology for reservoir quality prediction, Ph.D. thesis, Stanford University, Stanford, CA.

Garboczi, E.J. and Berryman, J.G., 2001, Elastic moduli of a material containing composite inclusions: Effective medium theory and finite element computations, Mechanics of Materials, 33, No. 8, 455-470

Geoffroy, H, di Benedetto, H., Duttine, A. and Sauzéat, C. 2003, in Deformation Characteristics of Geomaterials, edited by di Benedetto, H., Doanh, T., Geoffroy, H., and Sauzéat,C., Swets and Zeitlinger, Lisse, pp. 353–363.

Goddard, J.D., 1990, Nonlinear elasticity and pressure-dependent wave speeds in granular media. Proc. R. Soc. Lond. A **430**, 105–131.

Guodong, J., Patzek, T. D. and Silin, D. B., 2004, SPE90084: Direct prediction of flow properties of unconsolidated and consolidated reservoir rocks from image analysis. In SPE Annual Technical Conference and Exhibition,Houston, Texas, USA.

Hertz, H., 1882, On the contact of elastic solids, H Reine Angew Math.

Hudson, J. A. and Harrison, J. A., 1997, Engineering Rock Mechanics: An introduction to the principles, Elsevier Science, Ltd., Oxford.

Jaeger, J. C. and Cook, N. G. W., 1979, Fundamentals of rock mechanics, Chapman and Hall, London.

Jenkins, J., D. Johnson, L. La Ragione, and H.Makse, 2005, Fluctuations and the effective moduli of an isotropic, random aggregate of identical, frictionless spheres: Journal of the Mechanics and Physics of Solids, 53, 197–225.

Johnson, P. A. and Jia, X., 2005, Nonlinear dynamics, granular media and dynamic earthquake triggering, Nature, 2005, 437, 871-874.

Johnson, D. L. and Rasolofosaon, P. N. J., 1996, Nonlinear elasticity and stress-induced anisotropy in rock, J Geophys Res, 100(B2), 3113-3124.

Keehm, Y., Mukerji, T. and Nur, A., 2001, Computational rock physics at the pore scale: Transport properties and diagenesis in realistic pore geometries, TLE, 20, 2, 180-183.

Kuwano, R., Jardine, R., 2002, On the applicability of cross-anisotropic elasticity to granular materials at very small strain, Geotechnique 52, 727–749.

Makse, H. A., Gland, N., Johnson, D. L. and Schwartz, L. M., 1999, Why Effective Medium Theory fails in granular materials, Phys Rev Lett, 83, 5070-5073.

Makse, H. A., Gland, N., Johnson, D.L. and Schwartz, L., 2004, Granular packings: Nonlinear elasticity, sound propagation and collective relaxation dynamics, Phys Rev E 70, 061302

Magnanimo, V., Ragione, L. La, Jenkins, J. T., Wang, P. and Makse, H. A., , 2008, Characterizing the shear and bulk moduli of an idealized granular material, Euro Phy Lett, 81, 3.

Mavko,G., 1979, Frictional attenuation:An inherent amplitude dependence: Journal of Geophysical Research, 84, 4769–4775.

Mavko, G., T.Mukerji, and N. Godfrey, 1995, Predicting stress-induced velocity anisotropy in rocks: Geophysics, 60, 1081–1087

Mavko, G., Mukerji, T. and Dvorkin, J., 2009, The Rock Physics Handbook: tools for seismic analysis of porous media, 2nd edition, Cambridge University Press.

Mindlin, R. D., 1949, Compliance of bodies in contact: Journal of Applied Mechanics, 16, 259–268.

Mueth, D. M., Jaeger, H. M. and Nagel, S. R., 1998, Force distribution in a granular medium, Phys Rev E 57 3.

Murphy, W. M., 1982, Effects of microstructure and pore fluids on the acoustic properties of granular sedimentary materials, PhD. Thesis, Stanford University, Stanford, CA.

Myers, M. T. and Hathon, L. A., 2006, Understanding The Stress Dependence of Velocity in Unconsolidated Sands, AAPG International Abstracts with Program

Norris, A. N. and Johnson, D. L. , Nonlinear elasticity of granular media, J. Appl. Mech. 64, 39 (1997).

Onoda, G. Y. and Liniger, E. G., 1990, Random loose packing of uniform spheres and the dilatancy onset, Phys. Rev. Lett. E 72, 011301.

Pride, S. R. and Berryman, J. G., 2009, Goddard rattler-jamming mechanism for quanifying pressure dependence of elastic moduli of grain packs, Acta Mech., 185-196.

Roberts, A. P., and Garboczi, E. J., 2000, Elastic properties of model porous ceramics: J. Amer. Ceramic Soc., 83, 3041–3048.

Roberts, A.P. and Garboczi, E.J., 2002a, Elastic properties of model random three-dimensional open-cell solids, J. Mech. Phys. of Solids, 50 (1), 33-55.

Roberts, A.P. and Garboczi, E.J., 2002b, Computation of the linear elastic properties of random porous materials with a wide variety of microstructure, Proc. Royal Soc. of London, 458 (2021), 1033-1054.

Schwartz, L. M. and Banavar, J. R., 1989, Transport properties of disordered continuum systems, Phys Rev E, 39, 11965-11970.

Shibuya, S., Tatsuoka, F., Teachavorasinskun, S, Kong, X., -J., Abe, F., Kim, Y., -S., and Park, C.,-S, 1992, Soils Found. 32, 26.

Timoshenko, S. P., and J. N. Goodier, 1956, Theory of Elasticity, 2nd edition, McGraw-Hill, New York, 567 pp.

Tkachenko, A. V. and Witten, T. A., 1999, Stress propagation through frictionless granular material, Phys Rev E, 60, 687-696.

Truesdell, C., and Noll, W., 1965, The nonlinear field theories of mechanics, Handbuch der Physik 1ll/3, S. Flugge, ed., Springer, New York.

Walton, K., 1987, The effective moduli of a random packing of spheres: Journal of the Mechanics and Physics of Solids, 33, 213–226.

Walton, K., 1975, The effective elastic moduli of model sediments, Geophys. J. R. astr. Soc. 43, 293.

Winkler, K. W., 1983, Contact stiffness in granular porous materials: Comparison between theory and experiment: Geophysical Research Letters, 10, 1073–1076.

Winkler, K., Nur, A., and Gladwin, M., 1979, Friction and seismic attenuation in rocks: Nature Publishing Group, 277, 528-531.

Zimmer, M., 2003, Controls on the seismic velocities of unconsolidated sands: Measurements of pressure, porosity and compaction effects, Ph.D. thesis, Stanford University, Stanford, CA

Chapter 5
Consolidated microstructures: elastic, transport and electrical properties

5.1 Abstract

We construct consolidated rock microstructures using computational diagenesis schemes and estimate their elastic, transport and electrical properties. The computational diagenesis schemes progressively add cement to initially compacted sphere packs. The initial sphere packs—well-sorted and poorly sorted—are compacted using granular dynamics simulation.

We use three different computational diagenesis schemes to model the effects of rim, nucleation and contact cements. The rim- and nucleation-cementation (RC and

NC) schemes add cement to free grain surfaces and free pore volumes around grains respectively. The contact-cement (CC) scheme deposits cement in low-fluid-flux zones in the microstructure, which in our case are mostly near grain contacts. The fluid flux is obtained by using Lattice-Boltzmann method (LBM) flow simulation.

We use three computational property simulators to compute diagenetic trends. The elastic (bulk and shear moduli) and electrical (formation factor) properties are estimated using a Finite Element (FE) simulation. We used LBM simulation to compute permeability for single-phase fluid flow and to obtain fluid distributions for a two-phase fluid flow. For a fully-saturated rock matrix, we use the unsteady state two-phase LBM simulation to replicate imbibition of non-wetting fluid (such as oil) by a wetting fluid (e.g., water). At different stages of imbibition corresponding to different water saturations, we estimate bulk and shear moduli of the rock microstructures. Apart from partially saturated microstructures, we also compute elastic moduli for three cases – dry, water -saturated and oil-saturated.

Our estimated elastic, transport and electrical properties for a simulated quartz microstructure are comparable to laboratory measurements on sandstone. Specifically, the NC scheme best matches the dry laboratory elastic, transport and electrical properties of clean sandstone. This shows the feasibility of using computational methods to create realistic rock morphologies. We observe that a theoretical contact-cement model can describe bulk modulus behavior at low cement concentrations (<3%). For shear predictions, theoretical model predictions do not match simulated properties. We propose the use of a *relaxation correction* from GD simulation corresponding to the confining pressure of the initial pack. We also show the effects of sorting (using a compacted, poorly-sorted granular pack) and the cement mineralogy (clay, quartz and feldspar) on different diagenetic trends. The bulk modulus estimations of microstructures with different fluids—dry, fully water-saturated and fully oil-saturated—agree with Gassmann predictions within 2–4% error. The error decreases with lower porosities and is smaller for the oil-saturated case. The source of this relatively small error is unrelaxed stress at pore-voxels with smaller connectivity. We further show the heterogeneity in Skempton's coefficients computed for each fluid

voxel. For partially saturated microstructures, the simulated elastic properties are within bounds described by effective fluid models (Voigt and Reuss fluid mixing).

5.2 Introduction

The focus of this chapter is to construct consolidated microstructures from initially compacted spherical packs and analyze their elastic, transport and electrical properties. Consolidation is described as any process whereby loosely aggregated sediments become compact and coherent rocks, and it commonly reduces the sediment porosity (Fuchtbauer, 1974, Stone and Siever, 1996, Paxton et al., 2002, Flórez-Niño, 2005). Consolidation processes include lithification and diagenesis, and are often associated with burial (pressure), temperature and pore-fluids (concentration of solutes). Lithification commonly consists of compaction of sediments, cementation (precipitation of dissolved minerals in sediment interstices) and authigenesis (chemical reaction of sediments with pore-fluids). The effects of mechanical compaction include grain sliding and rearrangement (at lower pressures) and crushing (at higher pressures). Mechanical compaction is dominant until grain stabilization is reached (Stone and Siever, 1996, Flórez-Niño, 2005). In Chapters 3 and 4, we discussed compaction of loose packs at relatively lower pressures (<25 MPa) without grain crushing.

The main sources of post-compaction porosity reduction are effects of diagenesis (Paxton et al., 2002). Diagenesis broadly describes any chemical, physical or biochemical change in sediment after initial deposition and before metamorphism. Further, the onset of diagenesis inhibits further mechanical compaction (Stephenson et al., 1992, Flórez-Niño, 2005) and is associated with significant changes in elastic, transport and electrical properties (Dvorkin and Nur, 1996, Avseth et al., 2005, Keehm, 2003). Different diagenetic processes (quartz overgrowth, mineral alteration, and cementation) modify the sediment or rock morphology differently. The final geometrical distribution of various components in a composite rock determines its effective properties (Keehm, 2003, Dræge et al., 2006). Hence, to understand the impact of diagenesis on effective properties, it is important to characterize the changes in microstructures. While laboratory analysis is an important tool for characterizing

exact morphology and estimating effective properties, computational simulations in realistic rock microstructures are also used to understand such processes (Keehm, 2003, Guodong et al., 2004, Garcia et al., 2004).

Computational schemes to study diagenetic processes can be reaction-dependent or flow-dependent. Reaction-dependent diagenetic schemes involve solving exact reaction kinetics in realistic microstructures. This approach is motivated by published works suggesting reaction kinetics to be the main controlling factor for diagenesis in sedimentary rocks (Rimstidt and Barnes, 1980, Nagy and Lasaga, 1991). Keehm (2003) argues that realistic diagenetic processes involve both reaction-dependent and flow-dependent processes, especially where flow-rates are higher than reaction-rates. For rock physicists, the goal is to relate the changes in microstructure to changes in porosity and effective physical properties. Hence, the *geometric effects* of diagenetic processes are most relevant for property estimation. In this chapter, we use three different computational diagenetic schemes that attempt to replicate the effects of three cementation scenarios, viz., cements at contacts, cement at grain rims, and quartz nucleation (cements away from contacts). Although nucleation and overgrowth in quartz are usually classified as devitrification of quartz, we would broadly refer to them as diagenesis. Henceforth, *cements* refer to all materials in the microstructure added after compaction. Furthermore, all computational methods to add cements are referred as *computational diagenetic schemes*. The computational diagenetic schemes are referred as RC, NC or CC, depending on the mode of cementation: rim, nucleation or contact. While RC and NC are based on morphology, CC is based on fluid flux. In the following sections, we describe the diagenetic schemes in detail.

We initiate computational diagenesis on well-sorted and poorly sorted spherical quartz packs at three different pressures: 15, 25 and 35 MPa. These packs were compacted using Granular Dynamics (GD) simulation. Based on the centers and radii of the spherical grains, we prepare a digital microstructure on a three-dimensional grid. We refer to these gridded microstructures as *data cubes*. While preparing grids, we choose 3 and 6 microns resolutions for well-sorted and poorly sorted packs, respectively. We then use these data cubes for computational diagenesis and property

estimation to create diagenetic trends. As property estimators, we use Finite Elements (FE) simulations for elastic and electrical properties and Lattice-Boltzmann-Method (LBM) simulation for fluid transport properties. The elastic property of the initial compacted pack with zero cement is estimated using GD simulation along with FE simulation (using data cube). We used LBM simulation to compute single-phase fluid flow permeability and to obtain fluid distributions for a two-phase fluid flow. The unsteady state two-phase LBM simulation is used to replicate imbibition: pumping of wetting fluid (water) into a microstructure fully saturated with non-wetting fluid (oil). At different stages of imbibition corresponding to different water saturation, we estimate bulk and shear moduli of the rock microstructures using FE simulation. In addition to partially saturated microstructures, we also compute elastic moduli for water-saturated and oil-saturated cases.

The diagenetic trends of elastic, transport and electrical properties for simulated quartz microstructures are comparable to laboratory measurements on sandstone. Specifically, the NC scheme best matches the laboratory (dry) elastic, transport and electrical properties of clean sandstone. The results show the feasibility of using computationally constructed microstructures to understand and predict diagenetic trends. We also compare the behavior of these trends with a theoretical cementation model (Dvorkin and Nur, 1996). The bulk moduli predicted by this theoretical model are in excellent agreement with simulated elastic properties for low cement concentrations (<3%). For this theoretical model, we use the porosity and coordination number of the initial compacted pack from the GD simulation.

The theoretical model also predicts the effect of finite gridding on the elastic properties of the zero-cement data cube. For shear moduli, the theoretical model suffers from the same deficiencies as EMT, which arise from ignoring heterogeneity, as discussed in Chapter 4. The shear over-predictions can be amended by using a *relaxation correction* (Fig. 4.7, Chapter 4) corresponding to the pressure of the initial pack. The amended shear moduli are in excellent agreement with simulated results.

For fluid-saturated elastic-property estimations, simulated moduli for water-saturated and oil-saturated microstructures are in reasonable agreement with

Gassmann predictions (within 2–4%). We observe that the source of this error is unrelaxed stress at pore-grain boundaries due to a displacement discontinuity in the FE calculations. This negligible error decreases with stiffness contrast (oil-saturated errors are lower than water-saturated) and with lower porosities (lower specific surface area). We further show the heterogeneity in Skempton's coefficients computed for each fluid voxel, which is also a measure of error in FE calculations for fluid-saturated microstructures. For partially saturated microstructures, the simulated elastic properties are within bounds described by effective fluid models (Voigt and Reuss fluid mixing).

In the following sections, we discuss in details the protocols for preparing consolidated microstructures. We then present property estimations for consolidated microstructures and compare them with laboratory measurements and theoretical models. We then present the effect of compaction of the initial pack. In Section 5.5, we compare fluid-saturated elastic moduli with those predicted by Gassmann's equations for fully and partially saturated cases.

5.3 Preparation protocol

Our numerical recipe for creating consolidated microstructures involves two major steps:

(a) *Preparation of initial data cube with zero-cement:* This involves creating compacted packs at a chosen pressure (isotropic or uniaxial) with user-defined grain size distributions using GD simulation. These packs are further transformed into binary data cubes representing grains and pores in a three-dimensional grid;

(b) *Computational diagenetic scheme:* This involves implementing computational diagenetic schemes (RC, NC and CC) on three-dimensional data cubes to create consolidated microstructures.

In the following sub-sections, we discuss both these steps and our consolidated microstructures in detail.

5.3.1 Preparation of initial data cube

We construct compacted sphere packs with quartz grains (shear modulus: 45 GPa, Poisson's ratio: 0.08) at three different isotropic pressures (15, 25 and 35 MPa) using GD simulation. The choice of the pressure is arbitrary. For a realistic scenario, pressure depends on the depth of burial and tectonic forces at which diagenesis starts. Typically, temperature is the controlling factor for onset of diagenesis (Flórez-Niño, 2005) and hence the choice of pressure or depth depends on the subsurface temperature gradient. The size distribution of the initial pack is also user-defined. We chose two different size distributions for realistic representation of well-sorted and poorly sorted sediments. For well-sorted packs, we create two packs with 621 and 2092 grains at different pressures mentioned earlier to study the effect of initial pack size. We find that the effective bulk and shear moduli of these two packs from GD calculations are reasonably similar (Table 5.1). A smaller pack is computationally cheaper, so we use a pack of 621 grains for well-sorted packs.

Table 5.1: Comparison of effective bulk and shear moduli for varying pack size

#Grains	15 MPa	25 MPa	35 MPa
621	Bulk – 1.27 GPa Shear – 1.32 GPa	Bulk – 1.58 GPa Shear – 1.71 GPa	Bulk – 1.81 GPa Shear – 1.99 GPa
2092	Bulk – 1.25 GPa Shear – 1.24 GPa	Bulk - 1.56 GPa Shear – 1.62 GPa	Bulk - 1.78 GPa Shear – 1.91 GPa

For the poorly sorted pack (referred as polydisperse pack in Chapter 3 and 4), we create a single compacted pack at an isotropic pressure of 25 MPa using a hybrid EDMD–GD simulation. The histograms of grain sizes for the well-sorted and poorly sorted packs are shown in Fig. 5.1. The initial porosity for the poorly sorted pack at 25 MPa is 31.14%, compared to 36.68% for the well-sorted pack.

The initial compacted packs are then transformed to a regular three-dimensional grid based on grain centers and radii. These binary grid microstructures (data cubes) representing grains and pores are used for computational diagenesis modeling and property calculations. The choice of cube size and grid resolution depends on three

main factors: grain size distribution, total number of grains, hence volume of the pack, and computational resources. For well-sorted packs at different pressures, we have the same grid resolution (6 microns) and cube size (200x200x200) (Fig. 5.2). For poorly-sorted packs, we choose a smaller grid size (3 microns) and larger cube size (300x300x300) (Fig. 5.3). Further, due to the finite size resolution of the data cubes, the zero-cement data cube porosities are smaller than initial pack porosities (Table 5.2). The loss in porosity is primarily due to over-prediction of contact zones; i.e., the contact voxels are larger than the actual contact volumes. The excess material at contact voxels due to finite gridding in zero-cement data cubes has an effect similar to cementation. We analyze the effect of this *pseudo*-cement while discussing elastic properties. These data cubes are then cemented using different computational diagenetic schemes, as discussed in the next section.

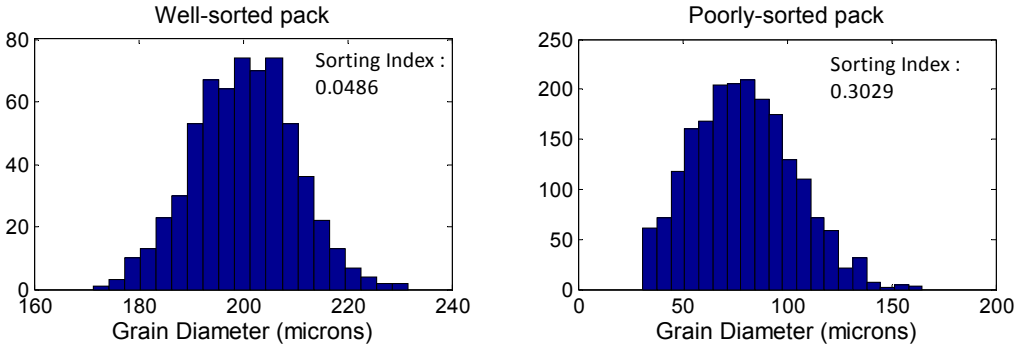

Figure 5.1: Grain size histograms for well-sorted (left) and poorly-sorted pack (right). Sorting index (standard deviation/mean grain size) is a measure of the spread of the grain size distribution, also termed the coefficient of variation.

Table 5.2: Comparison of compacted pack *actual* porosities with data-cube porosities

Sorting	**Compacted pack porosity**	**Data cube porosity**
Well-sorted at 15MPa	37.13%	35.66%
Well-sorted at 25MPa	36.68%	35.22%
Well-sorted at 35MPa	36.31%	34.85%
Poorly sorted at 25 MPa	31.14%	31.09%

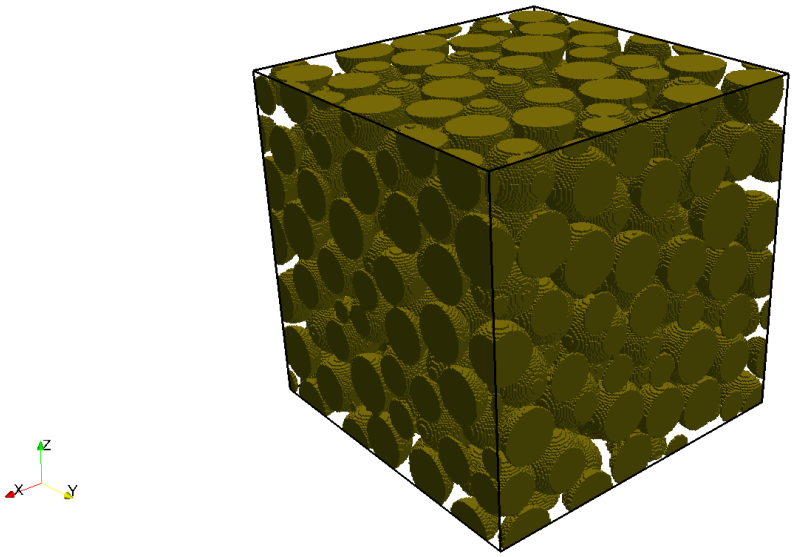

Figure 5.2: 3D data cube (200x200x200 with 6 micron resolution) for a well-sorted pack at 25 MPa pressure.

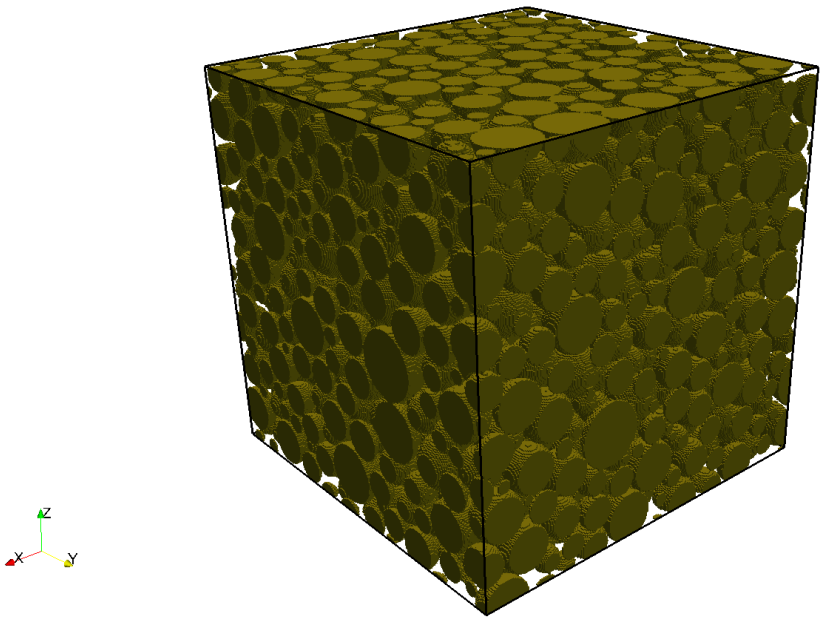

Figure 5.3: 3D data cube (300x300x300 with 3 micron resolution) for a poorly sorted pack at 25 MPa pressure.

5.3.2 Computational diagenetic schemes

We use three different computational diagenetic schemes. These schemes do not simulate actual diagenetic processes: they attempt to emulate the *effects* of diagenesis on the pore-space. These schemes add cement to microstructure interstices differently (Fig. 5.4). Numerically, adding cement implies changing pore voxels to grain voxels. These new microstructures are used for property estimation.

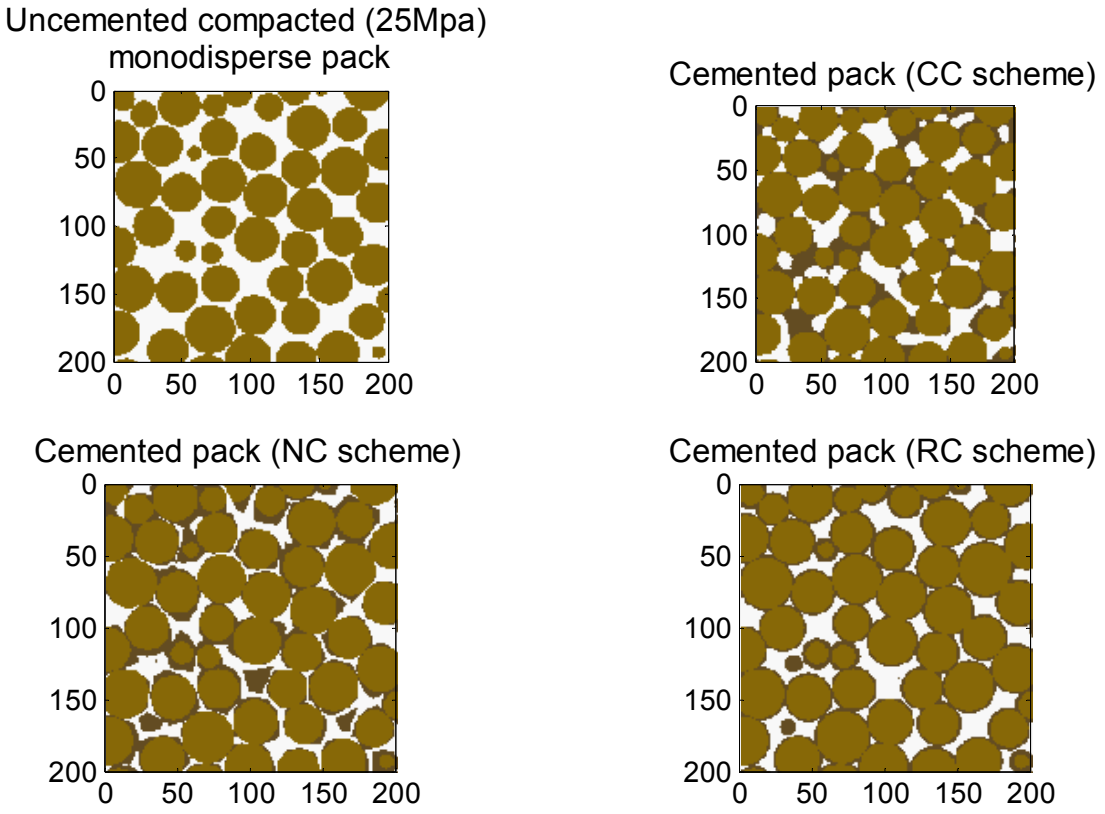

Figure 5.4: 2D slices from consolidated (cemented) packs and an unconsolidated (uncemented and compacted) pack, showing the difference in location of cement with different schemes. White color shows pore-space. Cement is shown as the dark color around the lighter colored grains. The final shapes of the grains are also considerably different than initial spherical grains.

5.3.2.1. Rim-cement (RC) scheme

The RC scheme adds cement at grain-pore boundaries. There are two possible implementations of this scheme. In a binary data cube, the grain-pore boundary voxels can be numerically detected, and adjacent pore voxels can be converted to grain

voxels (Keehm, 2003). This implementation is useful for CT scan images of physical samples, where information about grain centers and radii is difficult to extract. For our regular sphere packs, we have precise information about grain centers and radii. We add rim cements by numerically increasing the radius of each grain (Fig. 5.5) in the initial compacted pack. The increment (δr) is *proportional* to the initial grain radius. These packs are then transformed to regular grids. The difference between the final porosity and initial data cube porosity is the amount of cement added. Fig. 5.6, 5.7 and 5.8 shows an example of the final pore-space, the grain-space and slices of consolidated microstructures with ~15% cement (compared to total sample volume), respectively. The cement material is same as the grain material in these figures.

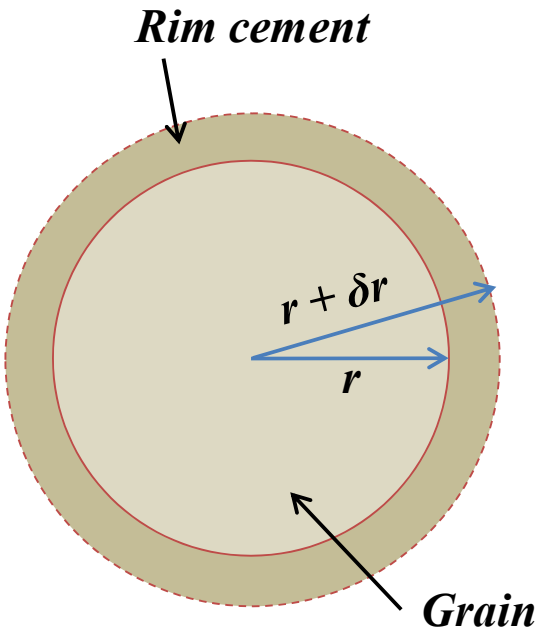

Figure 5.5: Numerical implementation of rim cement. Adding rim cement is the same as increasing the radii of the grains. The increments are proportional to initial grain radii.

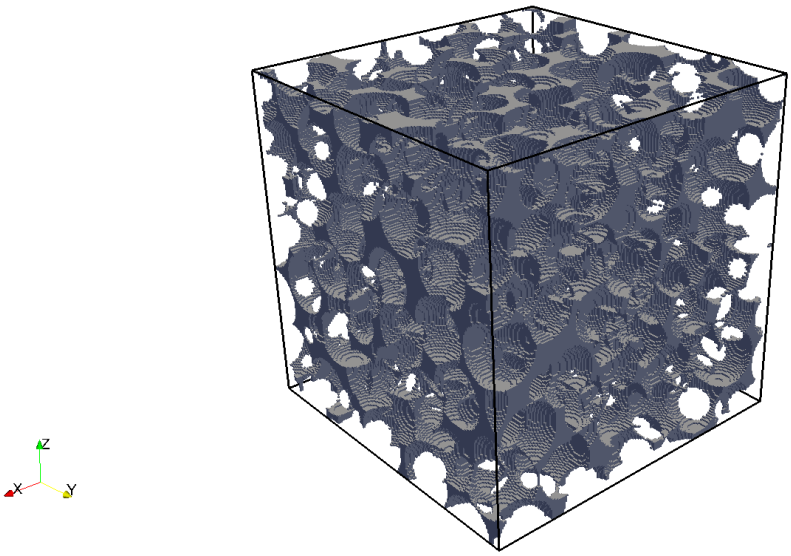

Figure 5.6: Final pore-space after adding ~15% rim cement (compared to total sample volume) to a compacted, well-sorted pack at 25 MPa isotropic pressure.

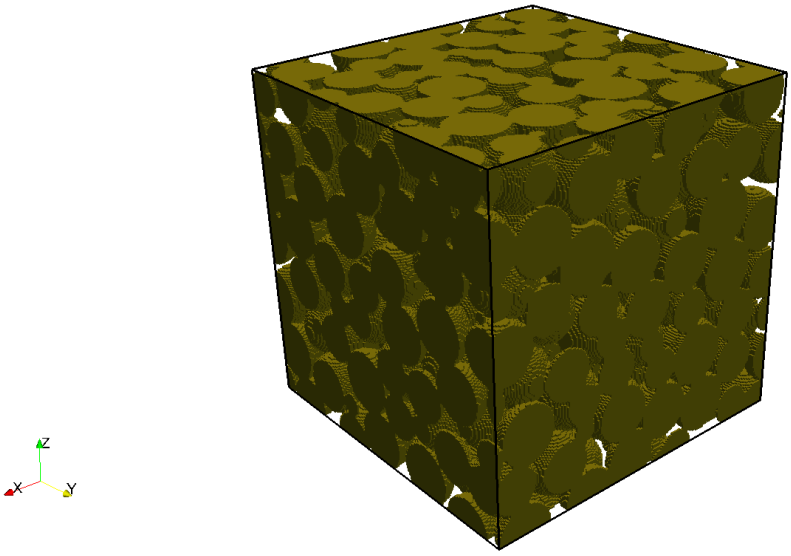

Figure 5.7: Final grain-space after adding ~15% rim cement (compared to total sample volume) to compacted well-sorted pack at 25 MPa isotropic pressure.

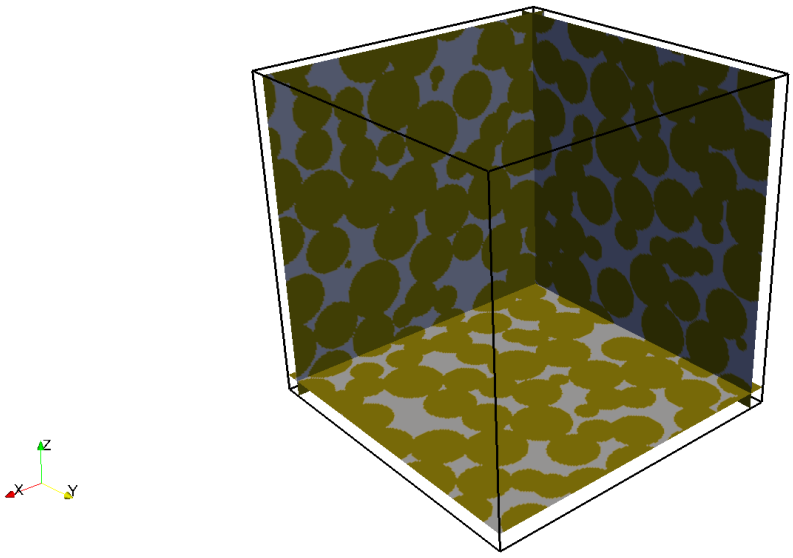

Figure 5.8: Slices in X-, Y- and Z- dimensions from the final consolidated microstructure having 15% rim cement (compared to total sample volume).

5.3.2.2. Nucleation-cement (NC) scheme

The NC scheme is designed to simulate the effects of nucleation and quartz overgrowth. This scheme uses a grain-growth model proposed by Schwartz and Kimminau (1987). Guodong et al. (2004) implemented a similar scheme by including initial grain-size dependence. We use the original Schwartz-Kimminau grain-growth model.

This model adds cement on grain surfaces based on the following relation:

$$\delta r(\hat{\boldsymbol{r}}) = min\left(\alpha l(\hat{\boldsymbol{r}})^{\beta}, l(\hat{\boldsymbol{r}})\right) \tag{5.1}$$

where $\delta r(\hat{\boldsymbol{r}})$ is the cement increment at a direction $\hat{\boldsymbol{r}}$ relative to the grain center, $l(\hat{\boldsymbol{r}})$ is the distance from the original uncemented grain surface to the surface of the grain-circumscribing polyhedron, in the direction $\hat{\boldsymbol{r}}$ (Fig. 5.9). We define the circumscribing polyhedron for a spherical grain as a volume bounded by intersecting planes through its contacts. Coefficient α controls the amount of cement, and exponent β determines

the direction of grain growth (cement). For a positive β, the grain growths protrude into the available pore volume around a grain. This replicates the nucleation type of growth in quartz sediments. For $\beta = 0$, NC scheme has the same effect as RC scheme. A negative β adds cement near the contact of the sphere and the circumscribing polyhedron. This replicates the CC scenario. However, our modeling of the CC scheme, as discussed next, involves flow-based calculations. Although the grain-growth model is capable of simulating to some degree all three schemes we discuss, we use positive values of β to simulate nucleation only. By increasing α, we create several packs with different amounts of cement. Figures 5.10, 5.11 and 5.12 show the pore-space, grain-space and directional slices from a consolidated microstructure with ~15% cement (compared to total sample volume), respectively. The final grain shapes are non-spherical and are visually comparable to realistic sandstone samples.

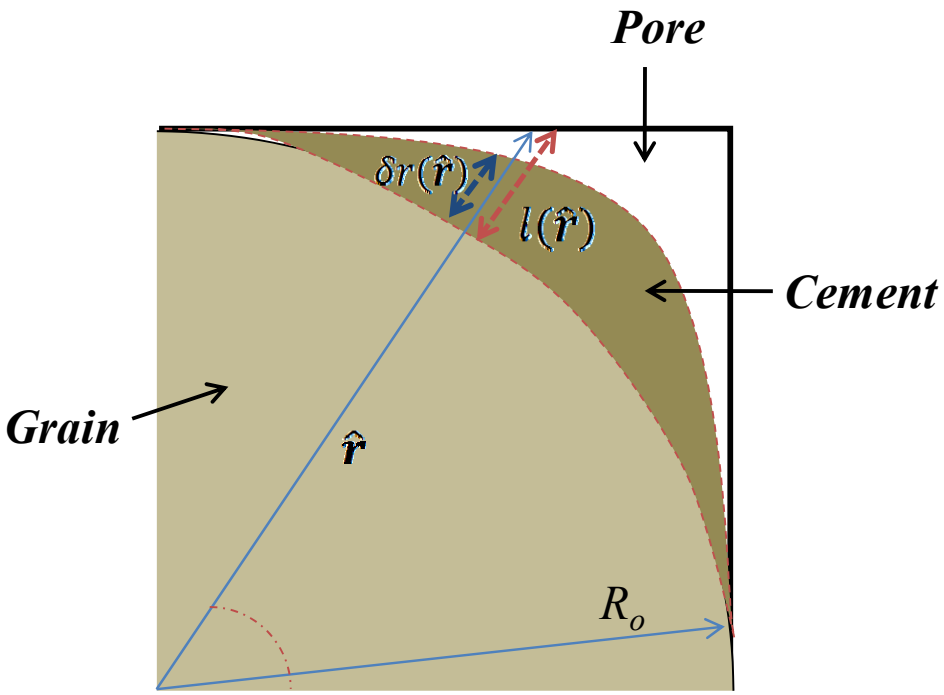

Figure 5.9: 2D demonstration of the NC scheme on a grain with an initial radius R_0; $\delta r(\hat{\mathbf{r}})$ is the grain growth (cement) in direction $\hat{\mathbf{r}}$, and $l(\hat{\mathbf{r}})$ is the distance of the original grain surface from the circumscribing polyhedron surface in direction $\hat{\mathbf{r}}$.

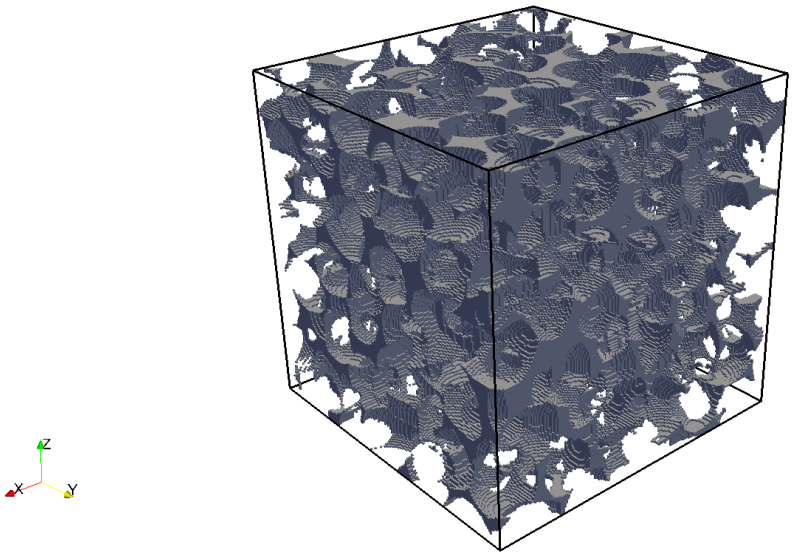

Figure 5.10: Final pore space after adding ~15% nucleation cement (compared to total sample volume) to a compacted, well-sorted pack at 25 MPa isotropic pressure.

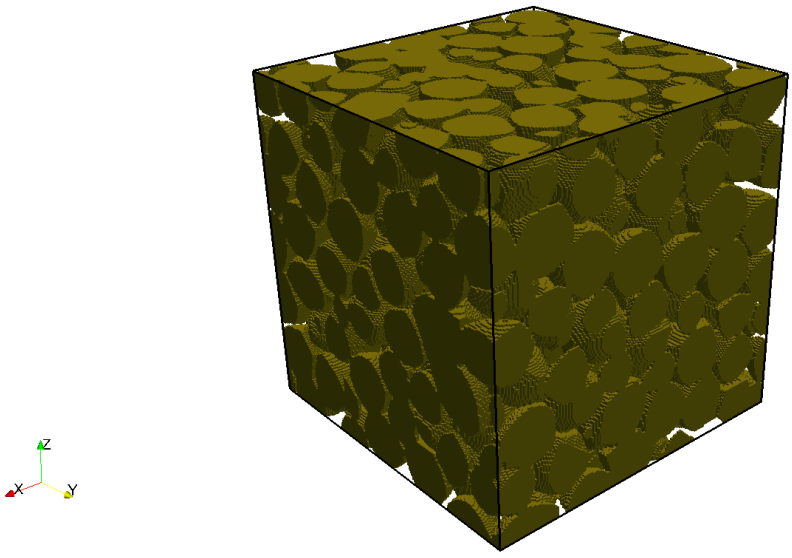

Figure 5.11: Final grain space after adding ~15% nucleation cement (compared to total sample volume) to a compacted, well-sorted pack at 25 MPa isotropic pressure.

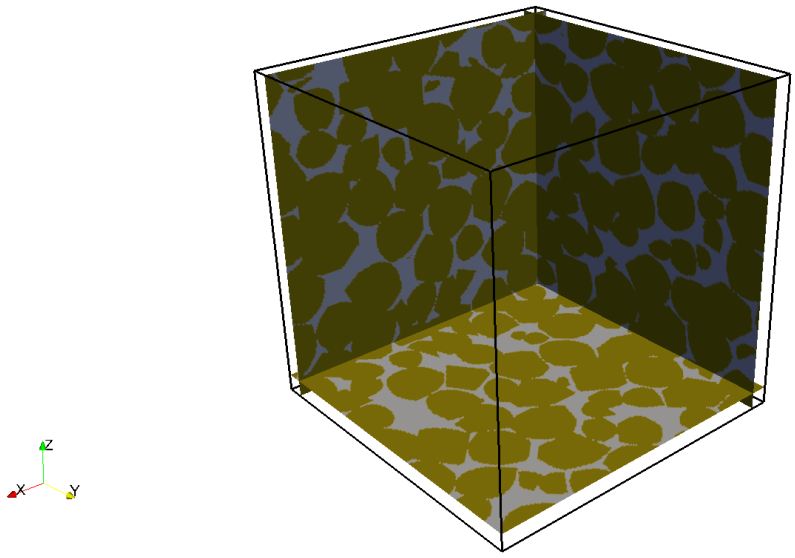

Figure 5.12: Slices in X-, Y- and Z- dimensions from final consolidated microstructure having 15% nucleation cement (compared to total sample volume).

5.3.2.3. Contact-cement (CC) scheme

The CC scheme is implemented by simulating fluid flow and cementation in tandem. Keehm (2003) discusses this implementation for sandstone CT scans. This scheme replicates geologic scenarios where super-saturated pore fluids preferentially deposit cement at low-flux zones. LBM is used for flow simulation, since it can handle very complicated pore geometry and can replicate changes in flow due to small changes in pore microstructure (Chopard and Droz, 1998, Keehm, 2003). For our spherical grain packs, fluid flux is typically lowest near grain contacts (Fig. 5.13). At every iteration of the CC scheme, low-flux pore voxels are selected after the flow simulation. These voxels are then transformed into grain voxels. Further iterations are done until either the porosity of the consolidated microstructure reaches zero or the pore network loses connectivity for flow. Figures 5.14, 5.15 and 5.16 show the pore space, the grain space and directional slices from a consolidated microstructure with ~15% cement (compared to total sample volume) using the CC scheme. The flow simulation is done in the X-direction. The average fluid flux is usually higher in the

flow direction. The pore-geometry (Fig. 5.14) shows considerable structural anisotropy due to preferential deposition of cement in the low-flux directions, Y and Z.

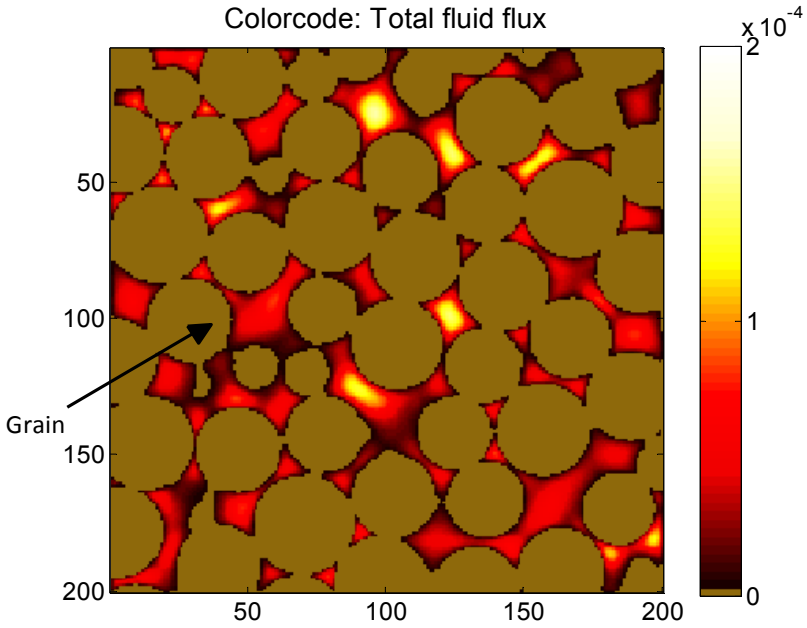

Figure 5.13: 2D slice from a 3D microstructure after flow simulation showing total fluid flux at pore voxels. The low flux zones (darker colors) are preferentially near grain contacts and grain boundaries.

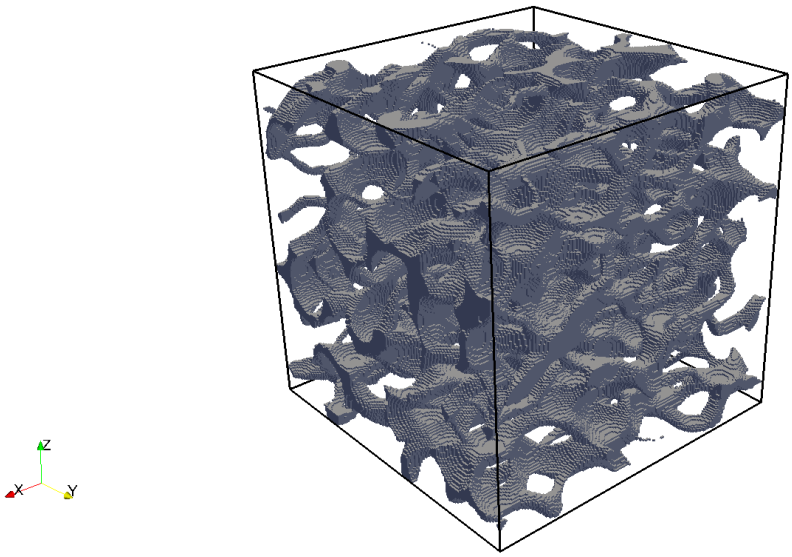

Figure 5.14: Final pore-space after adding ~15% contact cement (compared to total sample volume) to a compacted, well-sorted pack at 25 MPa isotropic pressure. The pore space shows structural anisotropy in the flow simulation direction (X-direction) compared to non-flow directions (Y and Z).

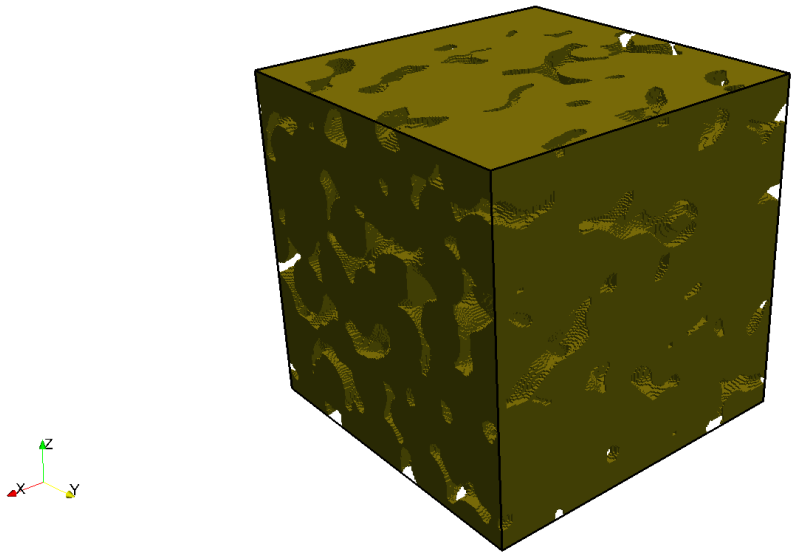

Figure 5.15: Final grain space after adding ~15% contact cement (compared to total sample volume) to a compacted, well-sorted pack at 25 MPa isotropic pressure.

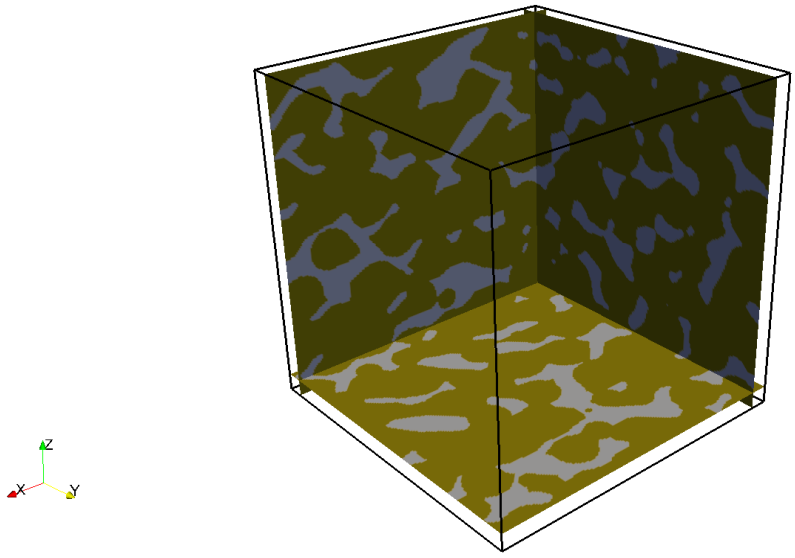

Figure 5.16: Slices in X-, Y- and Z-dimensions from the final consolidated microstructure having 15% contact cement (compared to total sample volume).

5.4 Diagenetic trends

The consolidated microstructures at different porosities (due to different amounts of cement) are used for property estimation. We will discuss the effect of diagenesis on well-sorted and poorly sorted packs created at 25 MPa. We then present the effect of initial compaction on diagenetic trends. As discussed in Chapter 2, FE simulation treats each voxel in data cubes as a tri-linear mesh to solve the linear elastic and electrical conductivity equations. LBM solves local fluid interaction rules to simulate fluid flow. In this section, we discuss permeability from single-phase fluid flow.

5.4.1 Elastic property

For estimating elastic moduli, we assign quartz material properties (Table 5.3) to all grain voxels for the NC scheme. For the RC and CC schemes, the cement voxels are assigned three different material properties corresponding to quartz, clay and calcite cement (Table 5.3). Simulated elastic moduli for quartz cement are compared with laboratory experiments on dry clean sandstones (Han, 1986) and show reasonable agreement (Fig. 5.17). Arns et al. (2002) compared elastic moduli from Fontainebleau sandstone images with the same experimental dataset and observed similar agreement. For our synthetic samples, we note that diagenetic trends for CC scheme are the stiffest compared to those for RC and NC schemes. For the same cement volume, CC scheme has maximum cements at contacts compared to RC and NC scheme. Hence, CC scheme generates the stiffest microstructures. In contrast, NC scheme adds cement away from the contacts, thereby resulting in the most compliant microstructures.

We also compare the elastic moduli of a zero-cement microstructure from GD and FE simulations (Fig. 5.17). Elastic moduli from FE simulation for the zero-cement microstructure are high compared with those from GD simulations. This is because of the finite grid size in the data cube used for FE simulation. The transformation of initial packs to three-dimensional grids based on grain centers and radii over-predicts contact volumes. This has the same effect as adding extra cement on the contacts. The volume of total cement is the difference in porosity of compacted packs and the zero-cement data cube (Table 5.2). Although these differences are small (<1.5%), the effect

on elastic moduli is significant. We investigate this change in moduli using the theoretical cementation model (Dvorkin and Nur, 1996).

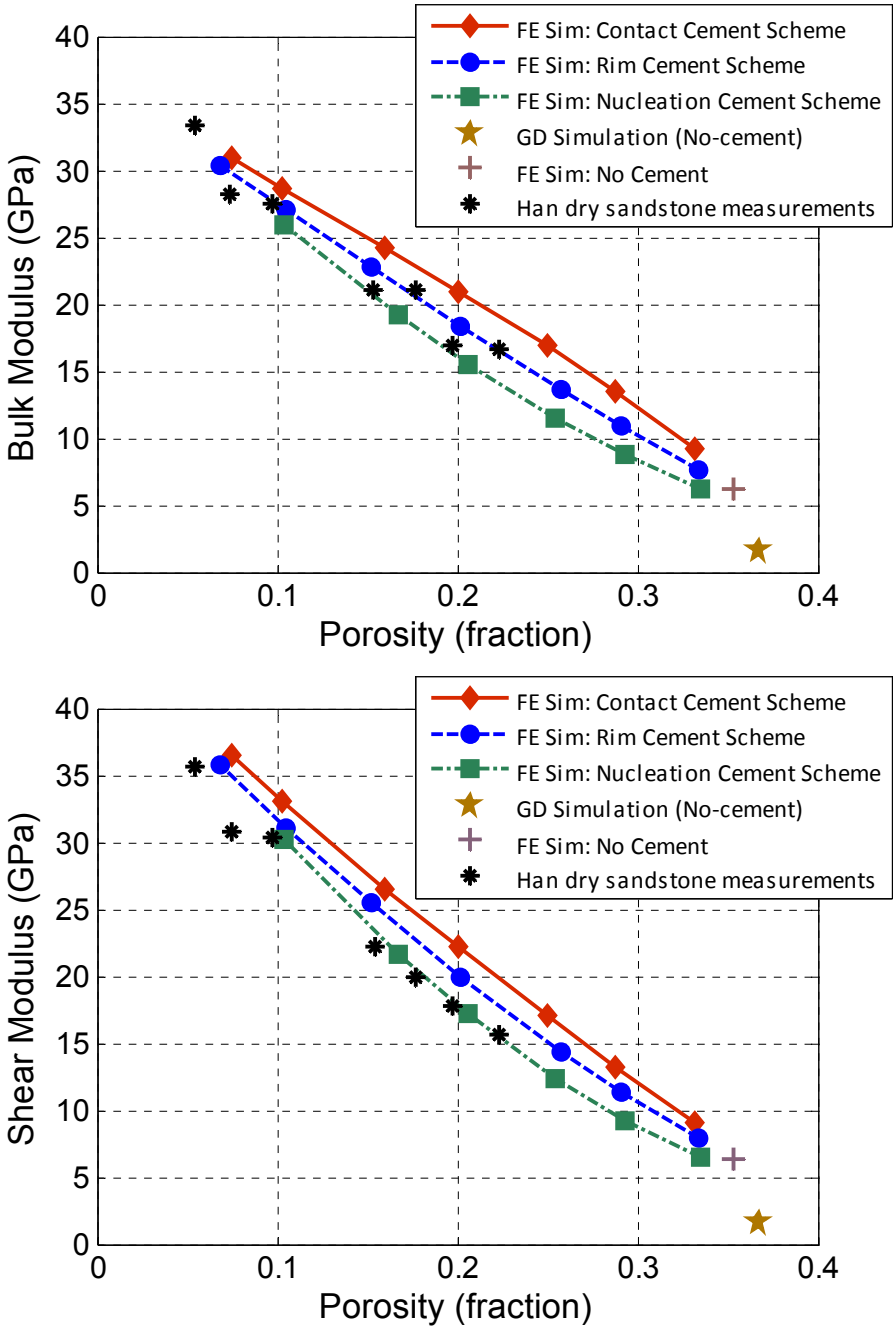

Figure 5.17: Diagenetic trends of bulk (top) and shear (bottom) moduli for different computational diagenetic schemes. The simulated elastic properties of consolidated microstructures are comparable to laboratory measurements on dry, clean sandstone (Han, 1986). The FE estimation of the zero-cement microstructure is higher than the GD simulation estimation due to finite grid size which over-predicts contacts.

The theoretical cementation model (Dvorkin and Nur, 1996), often called the cemented sand model, uses a rigorous contact-problem solution for two grains with contact cement developed by Dvorkin et al. (1994). Based on an effective-medium approximation, this model estimates the effective elastic properties of a pack of grains (Mavko et al., 2009, Avseth et al., 2010). Further, the model considers two different schemes of adding cement. Scheme 1 (called the Dvorkin contact cement model) adds cement *only* at contacts. Scheme 2 (called the Dvorkin surface cement model) deposits cement on the whole grain surface. For the same total cement volume, the concentration of cement at the contacts for Scheme 1 is higher than those for Scheme 2. A detailed explanation of the derivation and usage is given in Dvorkin et al. (1994) and Mavko et al. (2009). Using the porosity (36.68%) and coordination number (6.21) of the initial compacted pack at 25 MPa from the GD simulation, we estimate the elastic properties. The bulk moduli from this theoretical model (Scheme 1: Dvorkin contact cement model) predict rapid initial stiffening of the rock for small concentrations (<3%) of cement (Fig. 5.18). The model also matches the FE estimation for the zero-cement cube, signifying that the effect of finite gridding is similar to adding contact cement. Bulk moduli for Scheme 2 are significantly lower than simulated moduli. A possible explanation is that finite grid size or resolution affects the contact voxels primarily. Thus the zero-cement microstructure behaves as if there were 1.5% contact cement. Further cementation using the RC, NC and CC schemes adds cement differently; however, the effect of initial *pseudo* cementation exists.

The theoretical model predictions for shear moduli are higher than simulated moduli. For estimating effective elastic moduli, this theoretical model uses assumptions of statistical homogeneity of all grain contacts similar to those used by EMT models described in Chapter 4. Like EMT, this model ignores the presence of structural and stress heterogeneity in the initial compacted pack. A possible way to compensate for heterogeneity is to use the *relaxation correction* introduced in Chapter 4 for compacted granular packs. We compute the relaxation correction (from Fig. 4.7) corresponding to the pressure (25 MPa) of the initial compacted pack used for

cementation. The amended shear moduli (relaxation correction multiplied with theoretical model Scheme 1 predictions) are in excellent agreement with the simulated elastic moduli for consolidated microstructures (Fig. 5.18). It should also be noted that for bulk moduli, relaxation corrections are typically small (correction factor >0.92). Hence, the theoretical cementation model predicts bulk moduli reasonably well.

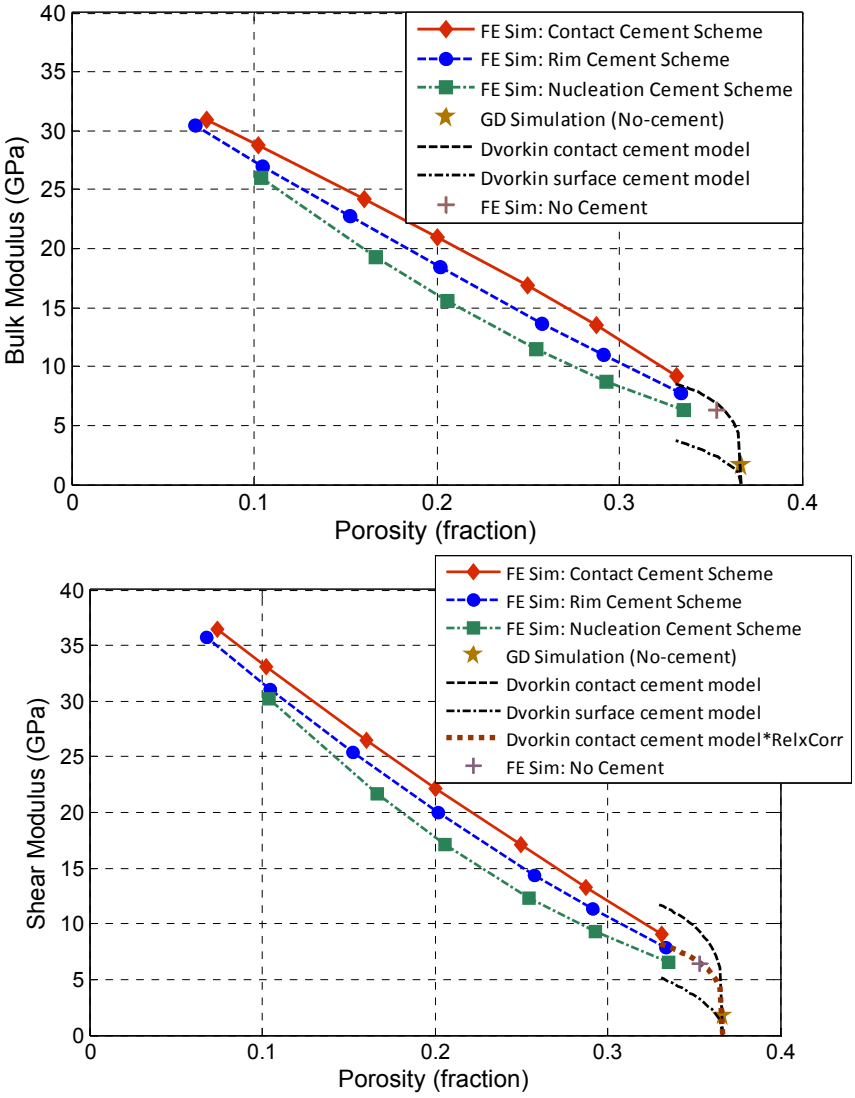

Figure 5.18: Theoretical cementation model (Dvorkin and Nur, 1996) predictions, using porosity (36.68%) and coordination number (6.21) from GD simulation, are compared with simulated moduli. Bulk moduli for contact-cement model (Scheme 1) predict stiffening due to small concentrations of cement. The model ignores heterogeneity in the initial compacted pack and has problems in predicting shear moduli similar to those of EMT. The amended shear moduli using relaxation correction (as discussed in Chapter 4) are in excellent agreement with simulated data.

Table 5.3: Mineral properties of grains and cements (Mavko et al., 2010)

Mineral	Quartz	Clay	Calcite
Bulk modulus (GPa)	36.6	25.0	70.0
Shear modulus (GPa)	45.0	9.0	29.0

5.4.1.1 Effect of initial sorting

Using an initial poorly sorted compacted pack (25 MPa isotropic pressure), we use our three computational diagenetic schemes to create cemented microstructures. These microstructures are further used for elastic property estimation using FE simulation. The diagenetic trends of elastic properties from this initial poorly sorted pack are different from corresponding trends for an initial well-sorted compacted pack (Fig. 5.18). It should be noted that we include the FE elastic moduli of the initial zero-cement microstructure in Figure 5.19, unlike our earlier analyses in Section 5.4.1.

For modeling the effect of sorting, we use the friable sand model (Dvorkin and Nur, 1996). This model follows the modified lower Hashin-Shtrikman bound between two end-points: the mineral moduli and an estimate of the well-sorted unconsolidated sediment's elastic moduli. The elastic moduli of this well-sorted sediment are generally predicted using an Effective Medium Theory (EMT) model. However, EMT predictions for shear moduli are typically wrong. In Chapter 4, we proposed the use of *relaxation corrections* on EMT predictions for estimating the well-sorted unconsolidated sediment shear moduli. In Figure 5.19, we show modified lower Hashin-Shtrikman predictions. However, in the present analysis, we use FE moduli predictions (zero-cement, well-sorted) as our unconsolidated sediment end-point. As discussed earlier, the microstructure corresponding to this end-point contains a small concentration of cement at contacts due to finite grid size. Nevertheless, the simulated elastic moduli of the zero-cement, poorly sorted microstructure follow the friable-sand model predictions (Fig. 5.19).

The elastic moduli for NC cement scheme also follow the friable-sand model for low concentrations of cement (<5%). Quartz overgrowths in the NC scheme mostly occur away from the contacts for lower concentrations of cement. For such scenario,

the NC scheme does not impart significant stiffness to the rock frame. However, with increasing cement concentration, the near-contact zones are likely impacted, thereby stiffening the rock frame. From simulated results, the NC scheme diagenetic trend for higher cement concentrations (>5%) diverges from the friable-sand model.

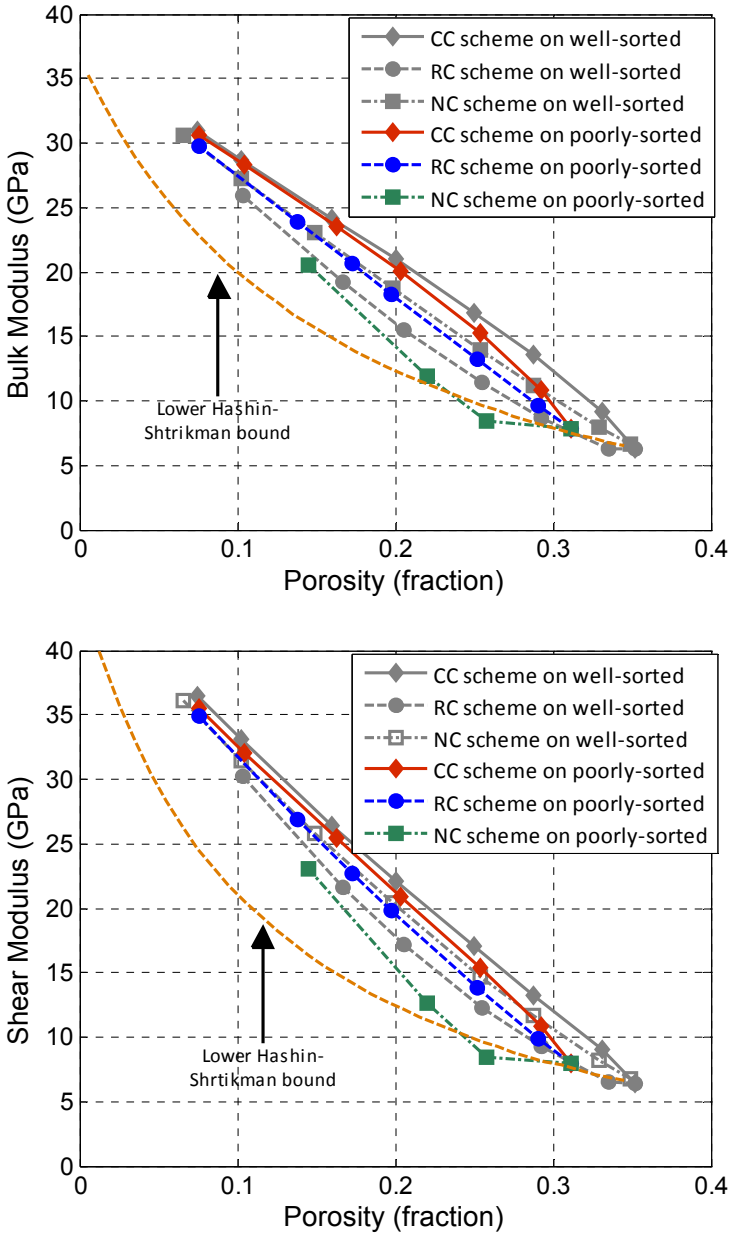

Figure 5.19: Comparison of diagenetic trends of bulk (top) and shear (bottom) moduli for two different initial compacted packs (25 MPa): well-sorted and poorly sorted. The friable-sand model, or modified Lower Hashin-Shrtikman bound between the mineral modulus and the unconsolidated end-point (FE moduli for a well-sorted data cube) shows the effect of sorting. The NC scheme follows this model for low cement concentrations (<5%).

5.4.1.2 Effect of cement material properties

Naturally occurring sandstones almost always contain more than one mineral (quartz). Apart from quartz cements, clay and calcite cements are particularly common. We estimate the effective elastic properties of microstructures for RC and CC schemes using different cement material properties (Table 5.3). Grain nucleations in sandstones are typically associated with quartz cement because of syntaxial growth of existing grains (along crystallographic faces). Hence, it is geologically impractical to model the effects of the NC scheme using different material properties. For RC and CC schemes, clay and calcite cements show distinct diagenetic trends (Fig. 5.20). It should be noted that calcite cements are stiffest for bulk moduli; however, for shear moduli, quartz cemented microstructures are stiffer than calcite or clay cemented microstructures.

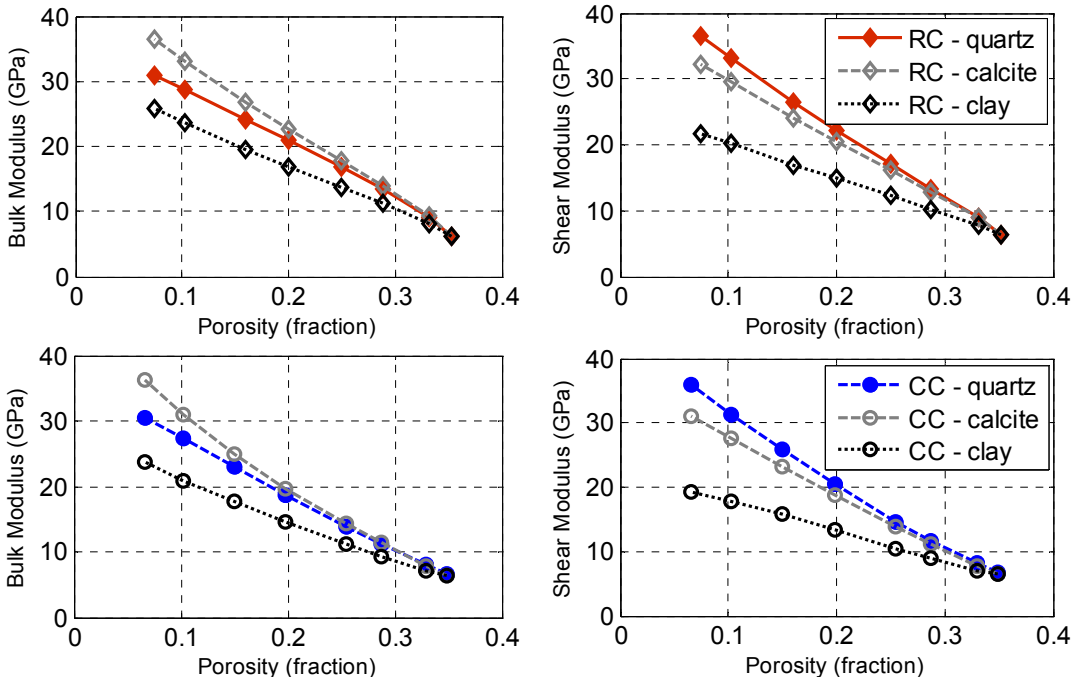

Figure 5.20: Effect of cement material on elastic moduli for CC and RC schemes. Microstructures with clay cements are softest for both schemes. Calcite cements have contrasting effects for bulk and shear moduli.

5.4.1.3 Effect of initial compaction

The onset of diagenesis often depends on depth of burial. For different temperature and pressure gradients, the initial packing structure and its properties vary. Using GD

simulation, we create compacted well-sorted packs at three different pressures: 15, 25 and 35 MPa. We use these packs for further consolidation using computational diagenetic schemes.

Diagenetic trends depend less on initial compaction than on the mode of diagenesis (Fig. 5.21). For realistic scenarios, burial depth (corresponding to pressures ~ < 40 MPa) therefore affects elastic properties less than the type of diagenetic process.

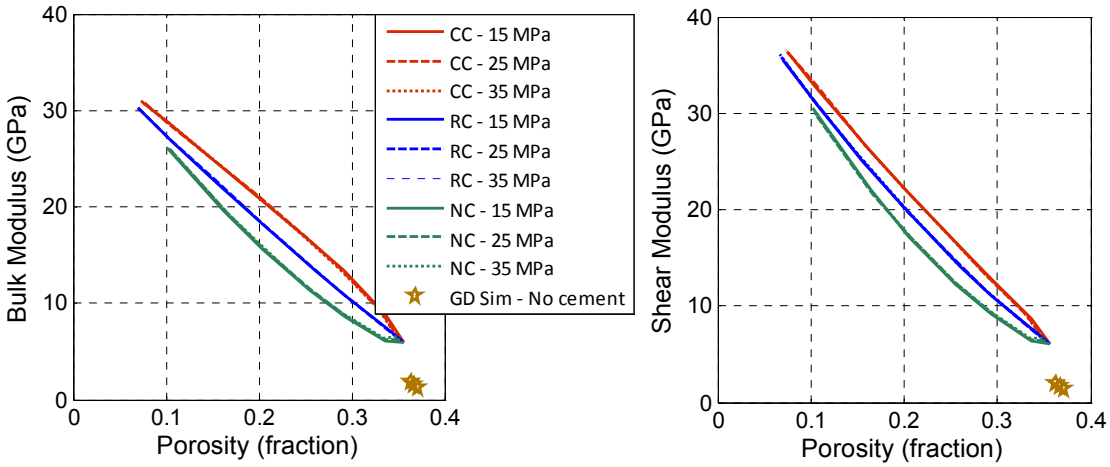

Figure 5.21: Effect of initial compaction on diagenetic trends of elastic properties. Initial compacted states (15, 25 and 35 MPa) do not show considerable effect on elastic properties if compared to the effect of different diagenesis schemes. Elastic moduli from GD simulation for compacted packs are shown for reference.

5.4.2 Transport property

We estimate uni-directional (X) permeability from a single-phase LBM simulation. We use the same microstructures used for the elastic property analysis, but we focus on diagenetic trends obtained for well-sorted and poorly sorted packs at 25 MPa.

The estimated diagenetic trends of permeability for RC, NC and CC schemes (Fig. 5.22) are compared with laboratory measurements on Fontainebleau core-plugs (Gomez, 2009, Bourbie and Zinszner, 1985). The CC scheme (for both types of sorting) preserves high permeability with decreasing porosity, since the low-flux zones are cemented, leaving high-flux zones, which are the major flow paths, open. The RC and NC schemes have similar diagenetic trends. The permeabilities of the initial zero-

cement microstructures depend on sorting and grain size. In general, the laboratory experiments are comparable to simulated RC and NC diagenetic trends.

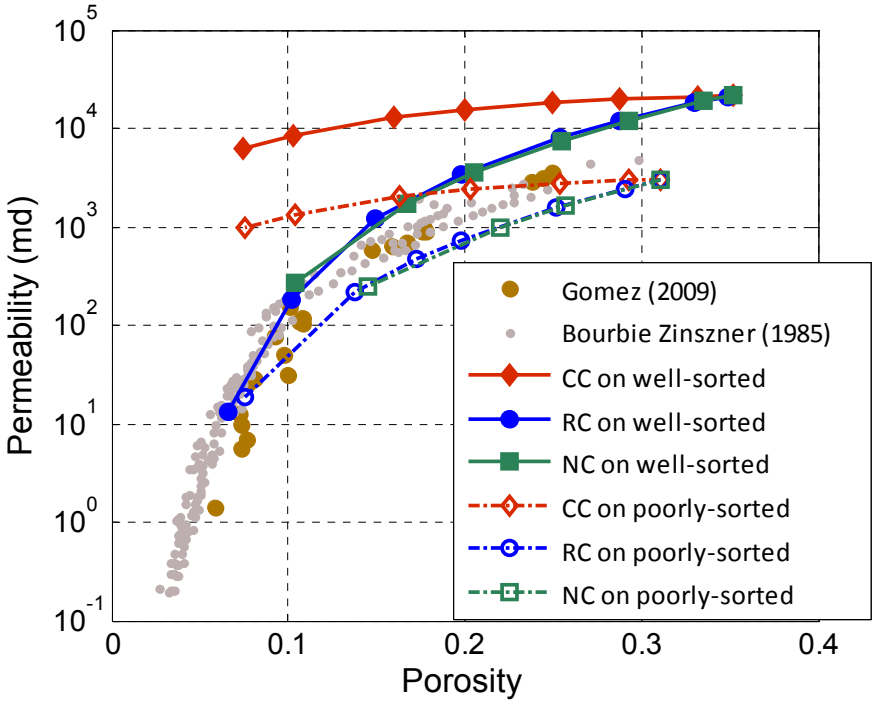

Figure 5.22: Comparison of simulated diagenetic trends for initially well-sorted and poorly sorted packs with laboratory core-plug measurements on Fontainebleau sandstone. The NC and RC schemes show behavior similar to core plugs.

We also compare the permeability estimations with the Kozeny-Carman relation independently for initial well-sorted and poorly sorted packs. The Kozeny-Carman relation (Carman, 1961) estimates the permeability of a porous medium using generalized parameters like porosity, surface area and grain size (Mavko et al., 2009). Although this relation is typically used to analyze permeability results on realistic pore geometries, the derivation is based on flow through a pipe having a circular cross-section. This derivation contains a specific surface area term, which is usually calculated for a pack of identical spheres. The usual final functional form relating permeability (κ) with porosity (ϕ) is as follows:

$$\kappa = B\frac{\phi^3}{(1-\phi)^2}d^2 \tag{5.2}$$

where B is a geometric factor and d is the mean grain size. Mavko and Nur (1997) further modified this relation to include the effect of percolation porosity (ϕ_c), which is described as the porosity below which the pore space is disconnected and flow is inhibited. The typical range of percolation porosity is 1-3%, although it depends on the mechanism of porosity reduction (Mavko et al., 2009). The modified Kozeny-Carman (Mavko and Nur, 1997) is as follows:

$$\kappa = B\frac{(\phi - \phi_c)^3}{(1-(\phi-\phi_c))^2}d^2 \tag{5.3}$$

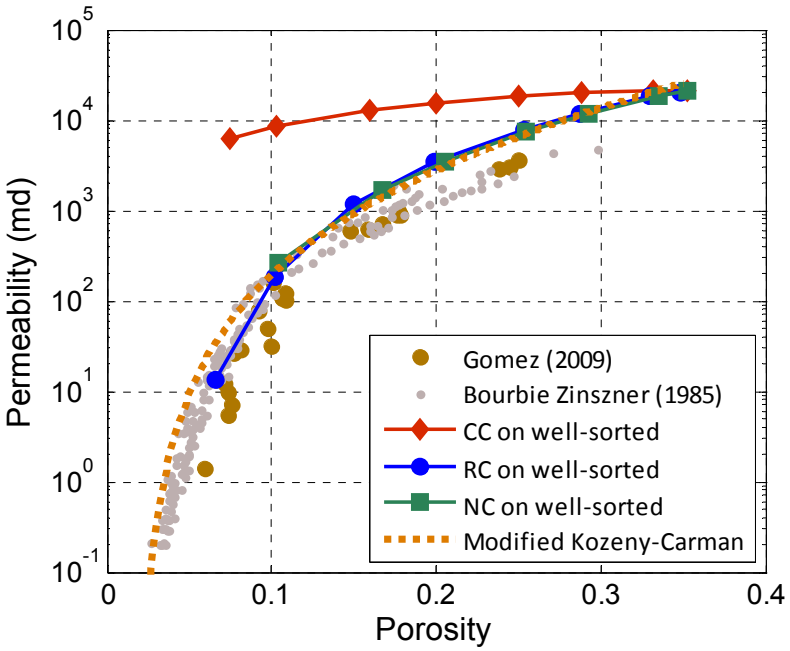

Figure 5.23: RC and NC diagenetic trends for permeability are calibrated with modified Kozeny-Carman relation using mean grain size 200 microns, geometric factor 8 and percolation porosity 2%.

For using Equation 5.3, we use mean grain size of 200 and 80 microns for initially well-sorted and poorly sorted packs respectively (Fig. 5.23 and 5.24). The choice of grain size is heuristic. These values are the mean grain size for uncemented packs. However, the grain sizes evolve with diagenesis, and it is difficult to justify the continued use of the same grain size. However, defining appropriate grain sizes with

cementation is equally difficult. The best-fit parameters for the modified Kozeny-Carman model for simulation microstructures are a percolation porosity of 2% (for both well-sorted and poorly sorted cases) and geometric factors of 8 and 12 for well-sorted and poorly sorted microstructures, respectively. We find that the RC and NC schemes match the Kozeny-Carman relations, but it is difficult to match the CC scheme.

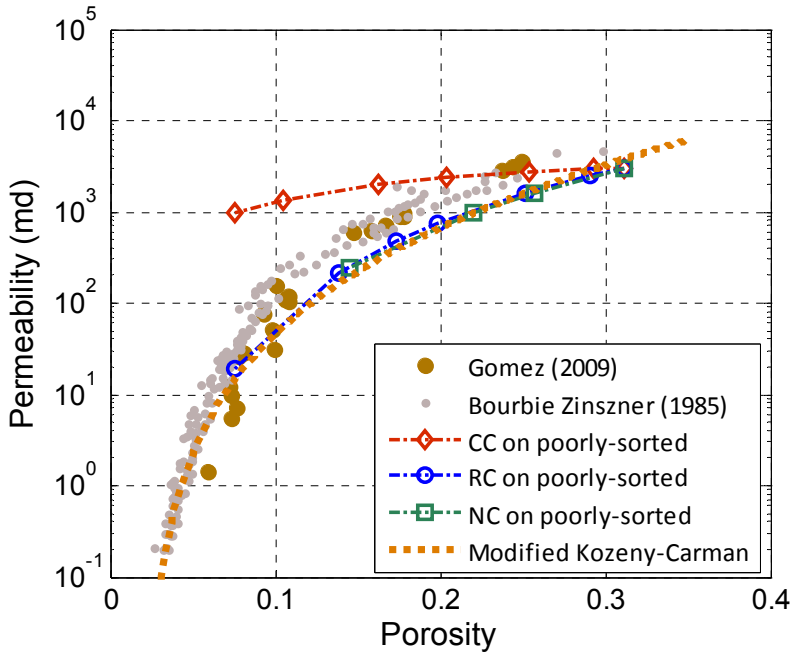

Figure 5.24: RC and NC diagenetic trends for permeability are calibrated with the modified Kozeny-Carman relation using a mean grain size of 80 microns, a geometric factor of 12 and a percolation porosity of 2%.

5.4.3 Electrical property

For electrical conductivity estimations, we use FE simulation. As mentioned earlier, this simulation solves linear electrical conductivity equations in microstructure cubes with a different phase property (conductivity) at each voxel. We assign water conductivity (0.5 S/m) to pore voxels and quartz conductivity to the grain voxels. Quartz conductivity being typically low (10^{-15} S/m), it is reasonable to assume zero conductivity for grain voxels in numerical simulations. For most crustal rocks, minerals are insulators, and electrical conductivity is predominantly ionic conduction in pore-fluids (Mavko et al., 2009). For our simulation, surface conduction is ignored.

However, it is important to note that that surface conduction can be important in a quartz matrix when water conductivity is below 0.01 S/m (Revil and Glover, 1997).

We use simulated X-directional electrical conductivity for calculating the formation factor. The formation factor, *F*, is the ratio of the conductivity of the pore-fluid (σ_w) to the effective conductivity of the saturated microstructure, σ_w (Archie, 1942):

$$F = \frac{\sigma_w}{\sigma} \tag{5.4}$$

The simulated formation factors show different diagenetic trends for CC, RC and NC schemes (Fig. 5.25). The NC and RC schemes in initially well-sorted and poorly sorted packs give diagenetic trends similar to laboratory experiments on clean Fontainebleau sandstones (Gomez, 2009). We also note that formation factors corresponding to CC scheme lie on the lower Hashin-Shtrikman bound. The lower Hashin-Shtrikman bound for formation factor for a rock with porosity ϕ is given as follows (Berryman, 1995):

$$F^{HS-} = 1 + \frac{3}{2}\frac{(1-\phi)}{\phi} \tag{5.5}$$

Archie's law (1942) relates formation factor to porosity in brine-saturated clean sandstones and forms the basis for resistivity log interpretation (Mavko et al., 2009). This law is generally expressed as

$$F = \frac{a}{\phi^m} \; or \; F = \frac{a}{(\phi - \phi_c)^m} \tag{5.6}$$

where *a* and *m* are known as the tortuosity factor and the cementation exponent respectively, and ϕ_c is the percolation porosity. These coefficients are usually determined empirically. The original formulation of Archie's law assumes *a* to be 1. Wyllie and Gregory (1953) introduced this coefficient as a function of porosity and

formation factor of the original unconsolidated pack before cementation (Gomez, 2009). The cementation exponent *m* varies between approximately 1.3 and 2.5 for most sedimentary rocks, and is usually close to 2 for sandstones (Mavko et al., 2009). For our simulated microstructures, the NC and RC scheme trends are best matched by using Archie's law (a=1) with a cementation exponent of 1.3 and a percolation porosity of 6%. We also estimate the directional conductivity to compute formation factors in different directions. Diagenetic trends of formation factor for NC and RC schemes show isotropic behavior; however, the CC scheme shows anisotropic conductivity (Fig. 5.26). The anisotropy is due to the flow-based diagenesis scheme which deposits cement in low-flux zones. For an X-directional pressure gradient in LBM, the low-flux zones are associated with the Y- and Z-directions. Cement is preferentially deposited in the Y and Z directions, which results in conductivity anisotropy.

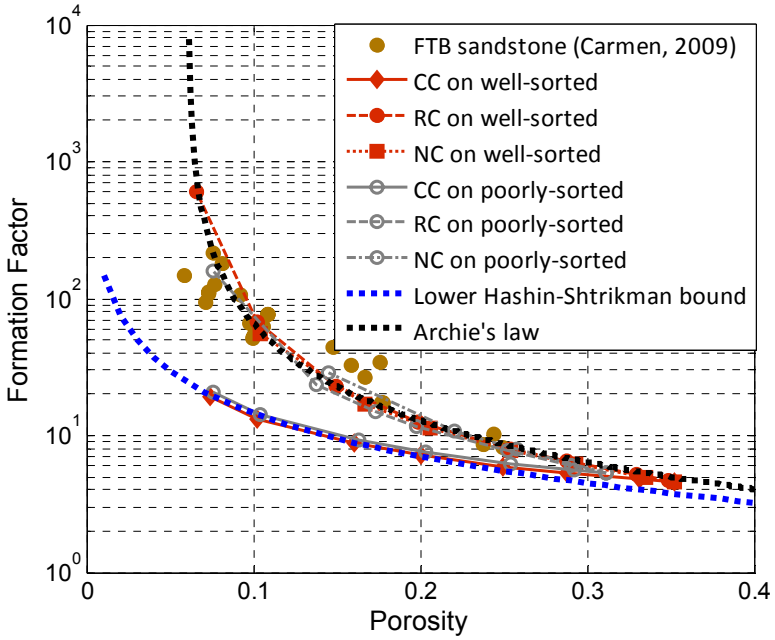

Figure 5.25: Comparison of formation factor for different computational diagenetic schemes. The NC and RC schemes are comparable with laboratory experiments on Fontainebleau sandstone (Gomez, 2009) and are best matched by Archie's law (a=1) with a cementation exponent of 1.3 and percolation porosity of 6%. The CC scheme follows the lower Hashin-Shrtikman bound (Berryman, 1995).

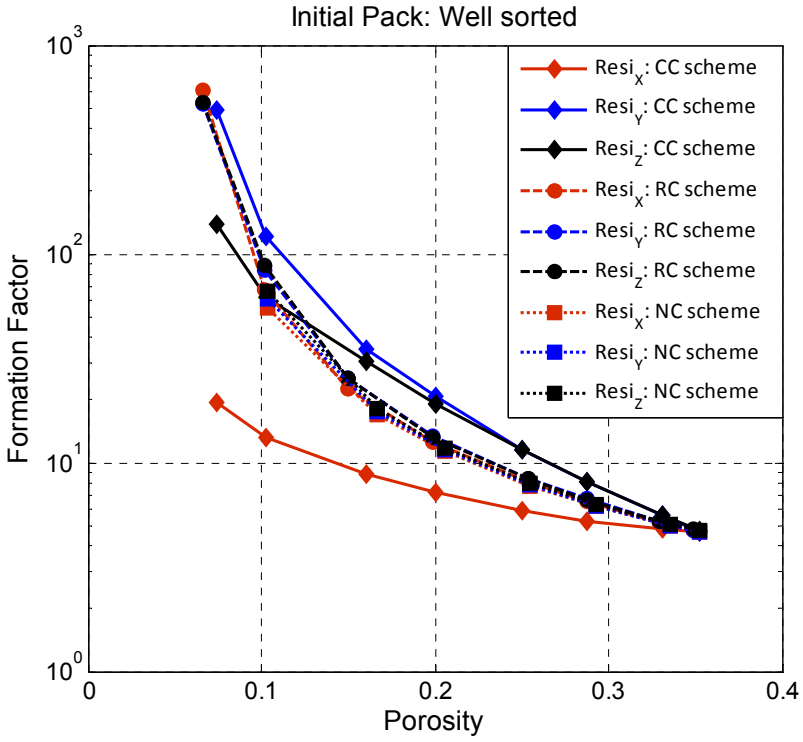

Figure 5.26: Formation factors computed using directional conductivity estimations. The RC and NC schemes show isotropic behavior; however, the CC scheme shows anisotropy. The anisotropy is due to the preferential deposition of cement in the CC scheme. Low-flux zones in an X-directional fluid pressure gradient are mostly along Y- and Z-directions.

5.5 Fully and partially saturated microstructures

The effect of fluid properties on elastic properties of rock is important for reservoir characterization. In the following sections, we analyze estimated elastic properties of consolidated microstructures for different fluid saturations and fluid types (oil and water). These consolidated microstructures are constructed by applying the NC scheme on an initially compacted well-sorted pack at 25 MPa. For computing elastic properties of fully saturated (oil and water) microstructures, we assign corresponding fluid properties (Table 5.4) to pore-voxels. We use FE simulation to estimate bulk and shear moduli. We use two-phase LBM simulation to obtain partially saturated microstructures with different water saturations.

5.5.1 Elastic properties of fully-saturated microstructures

One of the most important problems in rock-physics analysis of logs, cores and seismic data is using seismic velocities in rocks saturated with one fluid to predict those saturated with a second fluid (Mavko et al., 2009). The isotropic Gassmann equations (Gassmann, 1951) are most commonly used to relate bulk and shear moduli of a saturated porous medium to corresponding dry-rock moduli. Mavko et al. (2009) discusses various commonly used forms of this equation. The saturated bulk modulus K_{sat} can be calculated from the dry-rock bulk modulus K_{dry} and the fluid modulus K_{fl} as follows:

$$\frac{K_{sat}}{K_{min} - K_{sat}} = \frac{K_{dry}}{K_{min} - K_{dry}} + \frac{K_{fl}}{\phi(K_{min} - K_{fl})} \tag{5.7}$$

where $K_{min}$and ϕ are the mineral bulk modulus of the rock matrix and the porosity of the rock, respectively. For shear modulus, Gassmann shows that both fluid-saturated moduli (μ_{sat}) and dry-rock moduli (μ_{dry}) are the same. Gassmann's theory assumes a homogeneous mineral modulus and a statistical isotropy of the pore geometry. This theory is valid only at sufficiently low frequencies or quasi-static conditions, which allow the compression-induced pore pressure to equilibrate throughout the pore-space.

Table 5.4: Fluid properties of water and oil (Han, 1986, Castagna et al., 1993, Arns et al., 2002)

Fluid	Bulk modulus (GPa)	Shear modulus (GPa)
Oil	0.5	0.0
Water	2.2	0.0

In FE elastic-property calculation, a small strain is applied to the microstructure which induces strain energy, which is then minimized using a conjugate gradient optimization. The final stress tensor (averaged over the whole microstructure) is used to compute the elastic moduli. For a well-connected pore space, the stresses are usually equilibrated through finite deformation. The deformation of each mesh depends on the corresponding property of the voxel.

Using our numerically constructed microstructures, we assign fluid properties to all pore voxels (Table 5.4). All grain voxels have quartz material properties. We use microstructures at different porosities obtained using the NC computational diagenetic scheme on an initially well-sorted pack (at 25 MPa). The estimated bulk moduli from FE calculations are in excellent agreement with Gassmann's predictions (Fig. 5.27), and the percentage errors are less than 2% and 4% for water-saturated and oil-saturated cases, respectively (Fig. 5.28). The percentage errors decrease with lower porosities. Gassmann's predictions for fluid-saturated conditions were computed using FE estimations for dry microstructure. It is important to note that for numerical purposes, we assign a very small finite bulk modulus (0.0001 GPa) to pore-voxels in FE calculations for the dry microstructure.

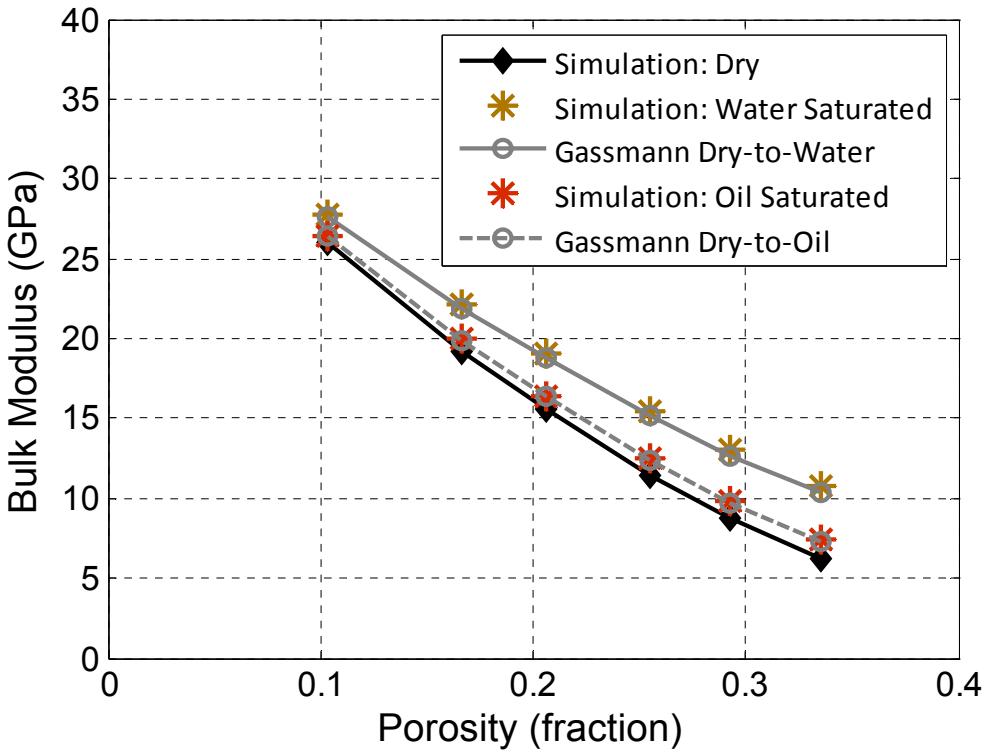

Figure 5.27: Comparison of simulated elastic properties for water-saturated and oil-saturated cases with Gassmann's predictions. We use dry rock moduli from FE simulation for Gassmann's equations.

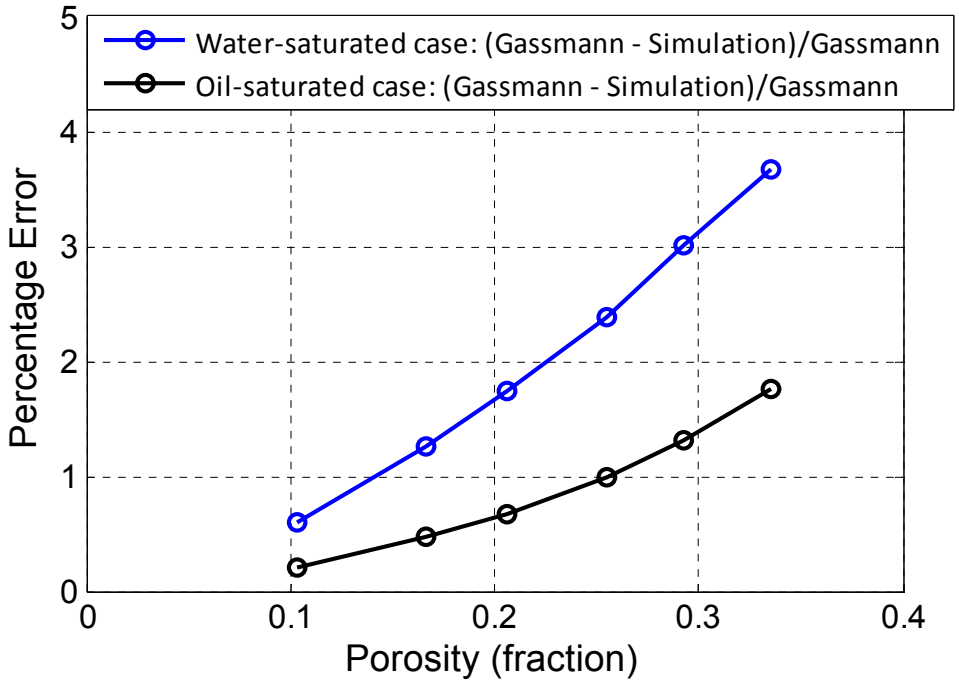

Figure 5.28: Percentage error in simulated moduli with Gassmann's predictions versus porosity. The errors are smaller for more compliant pore fluid (oil).

Although the prediction errors are relatively small, we further investigate the source of error. For FE calculations of dry and saturated states, the difference is the pore-voxel moduli. Hence, we focus on pore-space voxels, and particularly on the pore pressure due to the applied strain. For an arbitrary pore space in a homogeneous linear elastic medium filled with a pore fluid with bulk modulus, K_{fl}, the induced pore pressure, dP, under compressive stress $d\sigma$ (due to a compressive strain) is related using Skempton's coefficient and can be expressed as follows (Mavko et al., 2009):

$$B \equiv \frac{dP}{d\sigma} = \frac{1}{1 + K_\phi\left(1/K_{fl} - 1/K_{min}\right)}$$

$$= \frac{1}{1 + \phi\left(1/K_{fl} - 1/K_{min}\right)\left(1/K_{dry} - 1/K_{min}\right)^{-1}} \tag{5.8}$$

where K_{min} is the bulk modulus of the constitutive material (say, mineral), K_ϕ is the pore-space stiffness, ϕ is the porosity and K_{dry} is the effective bulk modulus of the dry, porous solid. Equation 5.8 will be true only when either (a) there is a single pore, (b) all pores are well-connected, and the frequency of compression as well as the viscosity of the pore-fluid is low enough for any pressure differences to equilibrate; or (c) all pores have same dry-pore stiffness.

Using the pore-voxel stresses and effective global stresses from FE simulation at the final configuration, we estimate the ratio of the average stress per voxel to the average global stress. Average stress is defined as hydrostatic stress, and hence the denominator in the ratio is constant for a given microstructure under a specific strain. Moreover, this ratio for each voxel represents the voxel-based Skempton's coefficients. We also compute a *global* Skempton's coefficient using Equation 5.8 and bulk properties. For a completely relaxed pore-space where all induced pressures have equilibrated, voxel-based Skempton's coefficients should be equal to the global Skempton's coefficient. For two different porosities (10.14% and 33.5%) in fully water-saturated conditions, the voxel-based Skempton coefficients have a wider distribution, approximately centered on the global Skempton coefficient (Fig. 5.29). The distribution for the low-porosity microstructure (10.4%) has smaller tail of high, un-equilibrated pressures than does the distribution for the high-porosity (33.5%) microstructure. This explains the smaller prediction errors with decreasing porosities (Fig. 5.28). The source of this un-equilibrated pressure is the displacement discontinuity in FE calculations at phase-boundaries, and the low connectivity of certain pore-voxels. We observe that relatively higher unrelaxed fluid stresses exist at pore-voxels adjacent to grain contacts, which have lower connectivity (Fig. 5.30). High porosity microstructures have higher specific surface area and relatively higher number of such pore-voxels (adjacent to contacts). Hence, there are more un-equilibrated pore pressures in high porosity samples, and consequently higher error. Moreover, a strain-energy convergence criterion (termed *tolerance*) is used for estimating elastic properties in FE simulation. A lower tolerance would possibly allow further relaxation by minimizing the energy. This would relax the induced pressures

further, and hence the errors would be smaller. The water-saturated conditions have higher errors due to higher pore-space moduli. For practical usability of FE simulation, the *tolerance* should be lowered with increasing pore-fluid stiffness. Nevertheless, the errors are reasonably small.

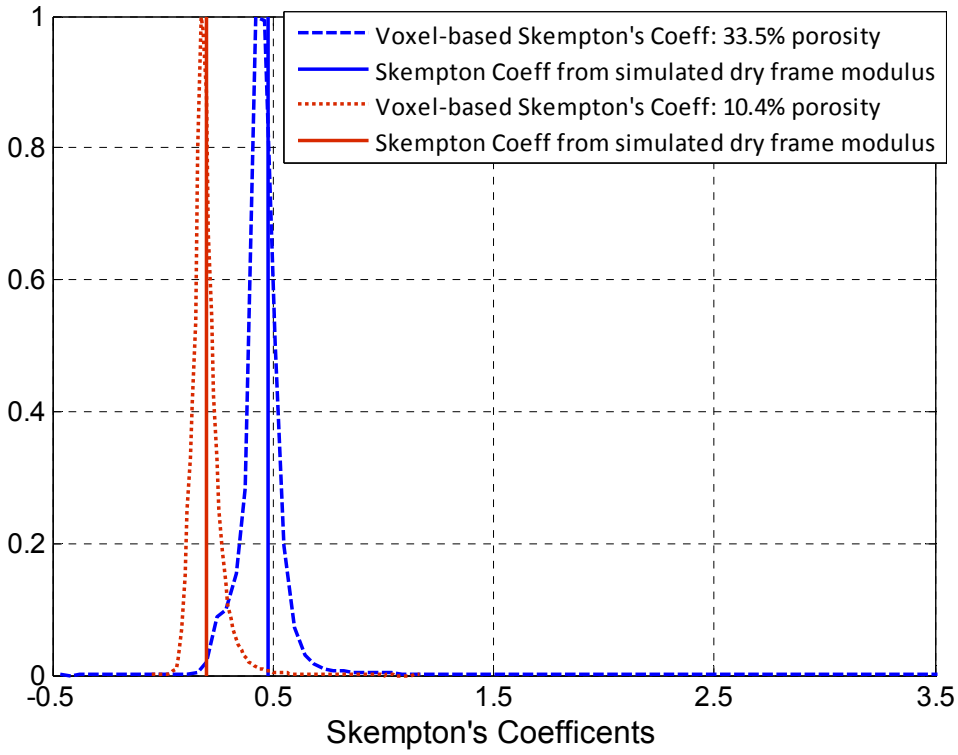

Figure 5.29: Comparison of voxel-based and global Skempton's coefficients. Voxel-based Skempton's coefficients are the ratio of the average stress per fluid voxel to the average global stress.

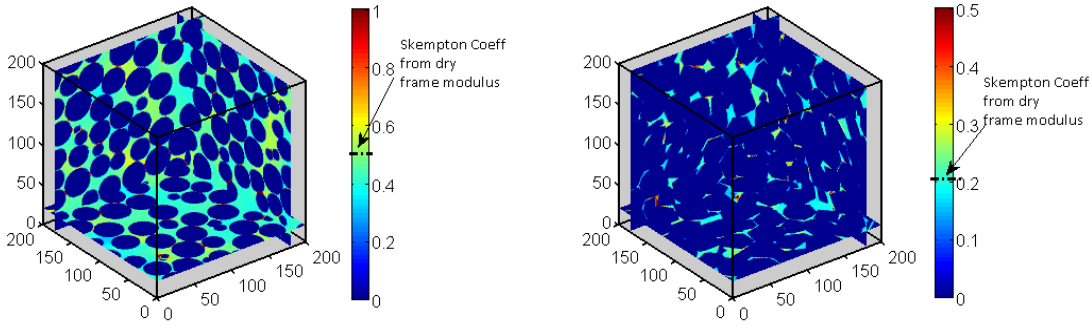

Figure 5.30: Slices from two 3D microstructures with different porosities (left: 33.5%; right: 10.5%) colorcoded by voxel-based Skempton Coefficient (SC). Higher values of SC signify unrelaxed pore pressures. Pore voxels adjacent to contacts have lower connectivity and typically have un-equilibrated pressures compared to well-connected pore voxels.

5.5.2 Elastic properties of partially-saturated microstructures

The most common approach for estimating elastic properties of partially saturated rocks is to use Gassmann's fluid substitution equations with an effective fluid bulk modulus (Mavko et al., 2009). The effective fluid bulk modulus, K_{fl}^{*}, is often calculated as the Reuss average of individual fluid-phase moduli:

$$\frac{1}{K_{fl}^{*}} = \sum_{i} \frac{S^{i}}{K_{fl}^{i}} \tag{5.9}$$

where S^{i} is the concentration of the *i*-th fluid phase with bulk modulus K_{fl}^{i}. The Reuss average signifies an isostress condition. This implicitly assumes that induced pressures in all fluid phases in the pore-space are the same under a compressive stress. This is possible when all fluid-phases are uniformly mixed with each other, so that induced pore pressures can equilibrate to an average value. This average value can be calculated using Equations 5.8 and 5.9. Mavko and Mukerji (1998) explain that for patchy saturations, where fluid phases are not intimately mixed with each other, the low-frequency seismic velocities are always higher than in a uniformly mixed fluid. Elastic properties for rocks with patchy saturation can be approximately modeled by using a Voigt average for effective fluid bulk modulus:

$$K_{fl}^{*} = \sum_{i} S^{i} K_{fl}^{i} \tag{5.10}$$

Using the LBM unsteady-state two-phase flow simulation, we replicate water imbibition in a fully oil-saturated microstructure. We consider different microstructures with a range of porosities (10% - 33%) created using the NC computational diagenetic scheme. At different stages of the two-phase flow simulation, the pore-space has different concentrations and saturations of oil and water (Fig. 5.30-5.31). We estimate the elastic properties of these partially saturated microstructures using FE simulation. The elastic properties of oil and water are mentioned in Table 5.4.

Using the bulk modulus for the oil-saturated microstructure from FE calculations and Equations 5.9 and 5.10 (referred as the lower and upper bounds), we plot Gassmann's predictions in Figure 5.32. The oil-saturated and water-saturated moduli are plotted for reference. Due to unrelaxed pore pressures at grain-pore boundaries, Gassmann's prediction for the water-saturated case does not match the FE simulation estimation. For the sake of comparison, we scale Gassmann's predictions to match the FE simulation bulk modulus. We use the *scaled* upper and lower bounds for comparisons with partially saturated elastic moduli from FE simulation.

The estimated bulk moduli for partially saturated microstructures at higher porosities (>25%) are close to *scaled* lower-bound predictions; for lower porosities (<20%), the predictions are close to *scaled* upper-bound predictions (Fig. 5.34). As discussed before, proximity to the upper bound suggests higher unequilibrated pore pressures in the oil and water phases. Unequilibrated pore pressures in FE simulations mostly occur at pore-voxels with smaller connectivity due to insufficient resolution of the displacement discontinuities. For earlier results on fully-saturated microstructures, we pointed out that with lower porosities, the specific surface area and the number of voxels around the contacts decrease. Hence, the un-equilibrated pore pressures are lower, too. For partially saturated microstructures, higher unrelaxed pore pressures for low-porosity rocks suggest larger inter-phase boundaries between fluid phases, i.e., oil and water. Occurrences of patchy saturations of water and oil phases are a possible explanation of larger fluid-phase boundaries, and hence, higher induced pore pressures.

We also note that even for high porosity rocks (33.5%), the simulated elastic moduli of partially saturated microstructures do not *strictly* follow the lower bound. Partially saturated microstructures follow the lower bound *only* under the assumption of completely equilibrated pore pressure; in other words, the induced pore pressures are same as the Skempton's coefficient. From FE simulation, we estimate voxel-based Skempton's coefficients (as discussed in Section 5.4.1) and compare with global Skempton's coefficients (Eqn. 5.8). For fluid modulus, we use Equations 5.9 and 5.10 (Fig. 5.33). We note that the voxel-based Skempton's coefficients form a bi-modal distribution and are different from the *global* Skempton's coefficient. The peaks of

this distribution correspond to oil and water pore pressures, and are approximately equal to Skempton's coefficient for completely oil- and water-saturated cases.

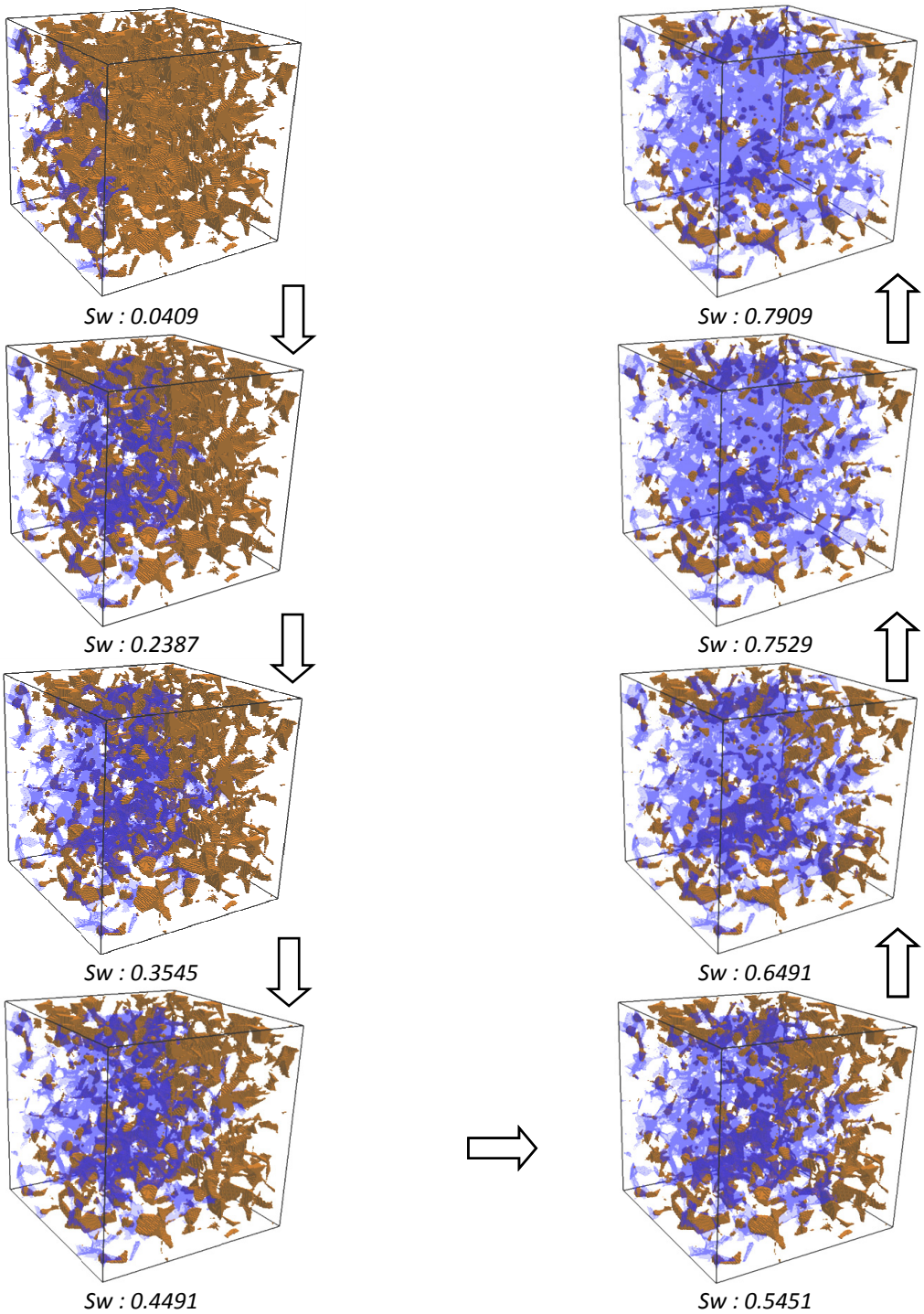

Figure 5.30: Oil (brown) and water (blue) concentrations at different saturations for two-phase imbibition simulation in a microstructure with 10.5% porosity.

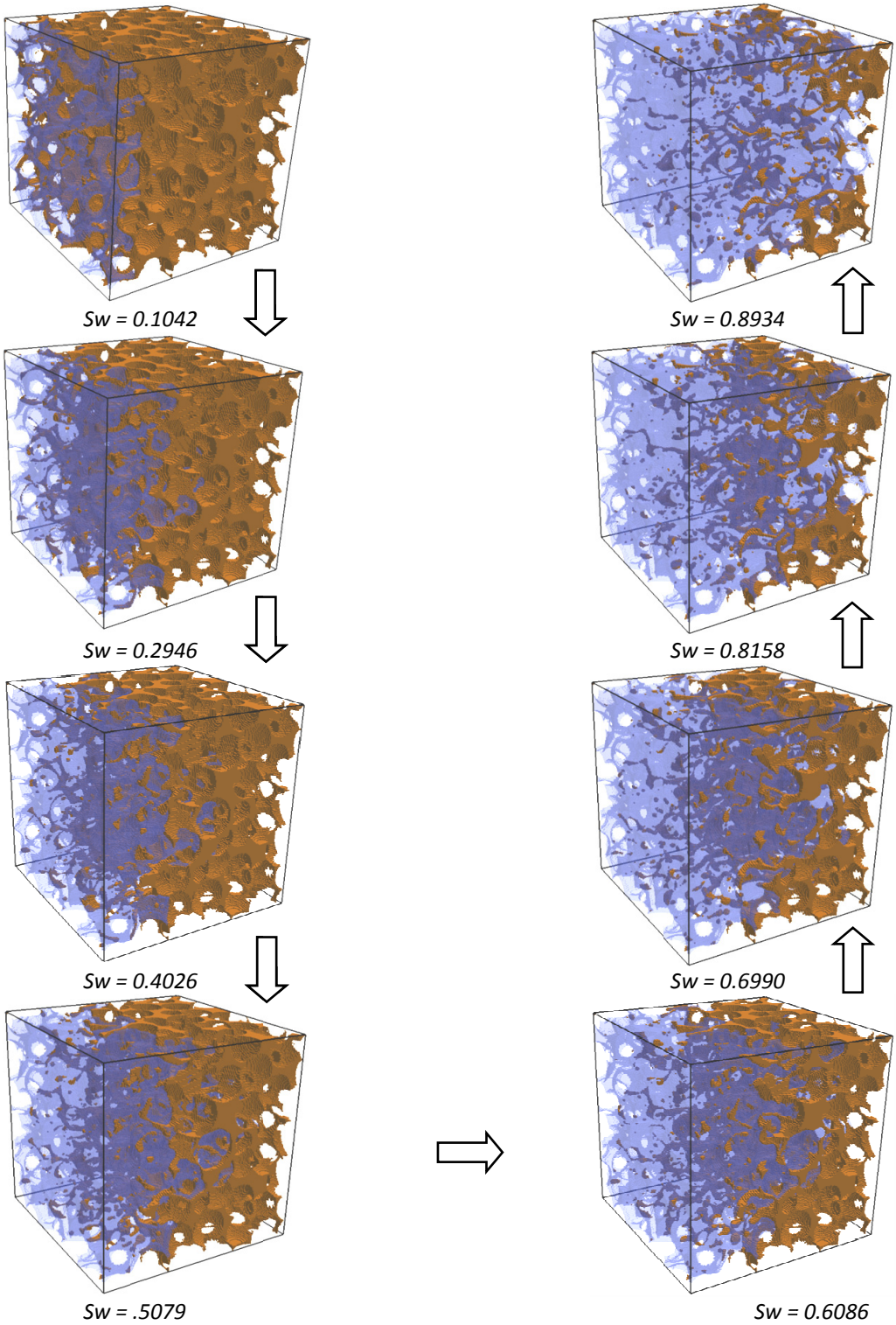

Figure 5.31: Oil (brown) and water (blue) concentrations at different saturations for two-phase imbibition simulation in a microstructure with 29.3% porosity.

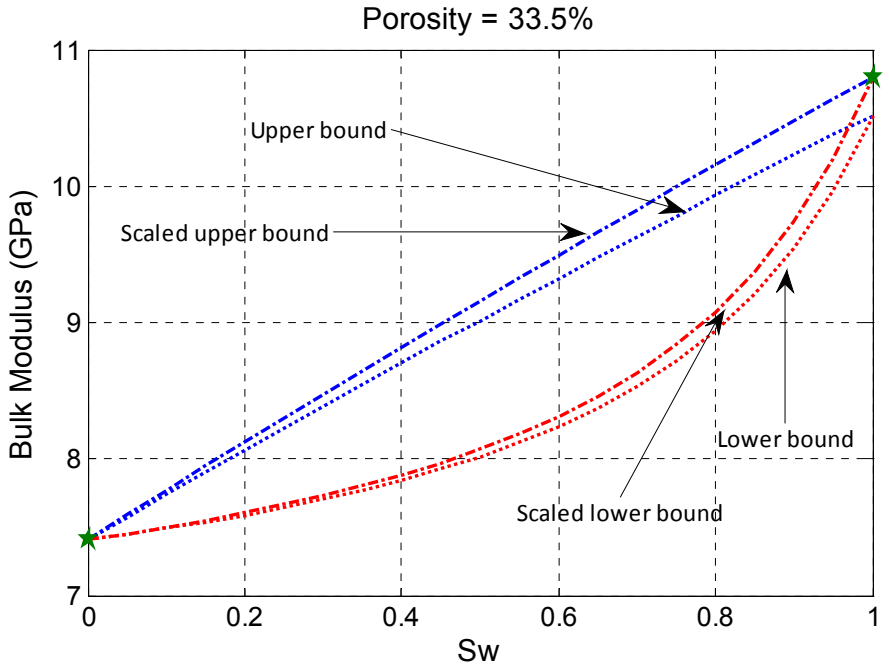

Figure 5.32: Comparison of upper and lower bounds for partially saturated rocks using the effective fluid model for Gassmann's equations. FE modulus estimations for oil-saturated and water-saturated cases are shown for reference. Gassmann's predictions do not match for Sw = 1, due to unrelaxed pore pressures in FE simulation. For further comparisons, we use *scaled* upper and lower bounds to match the oil-saturated and water-saturated end points from FE simulation.

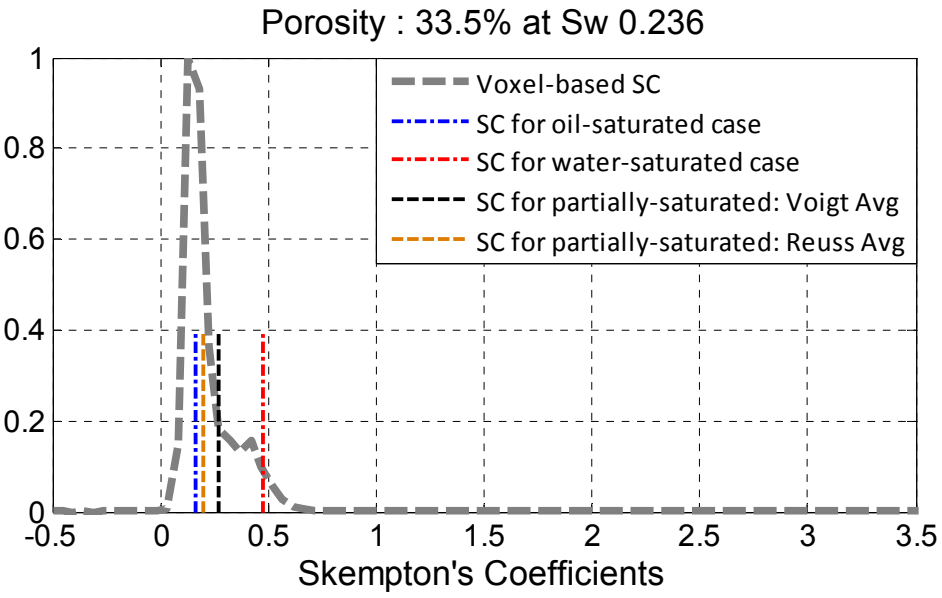

Figure 5.33: Comparison of voxel-based and global Skempton's coefficients for partially saturated case.

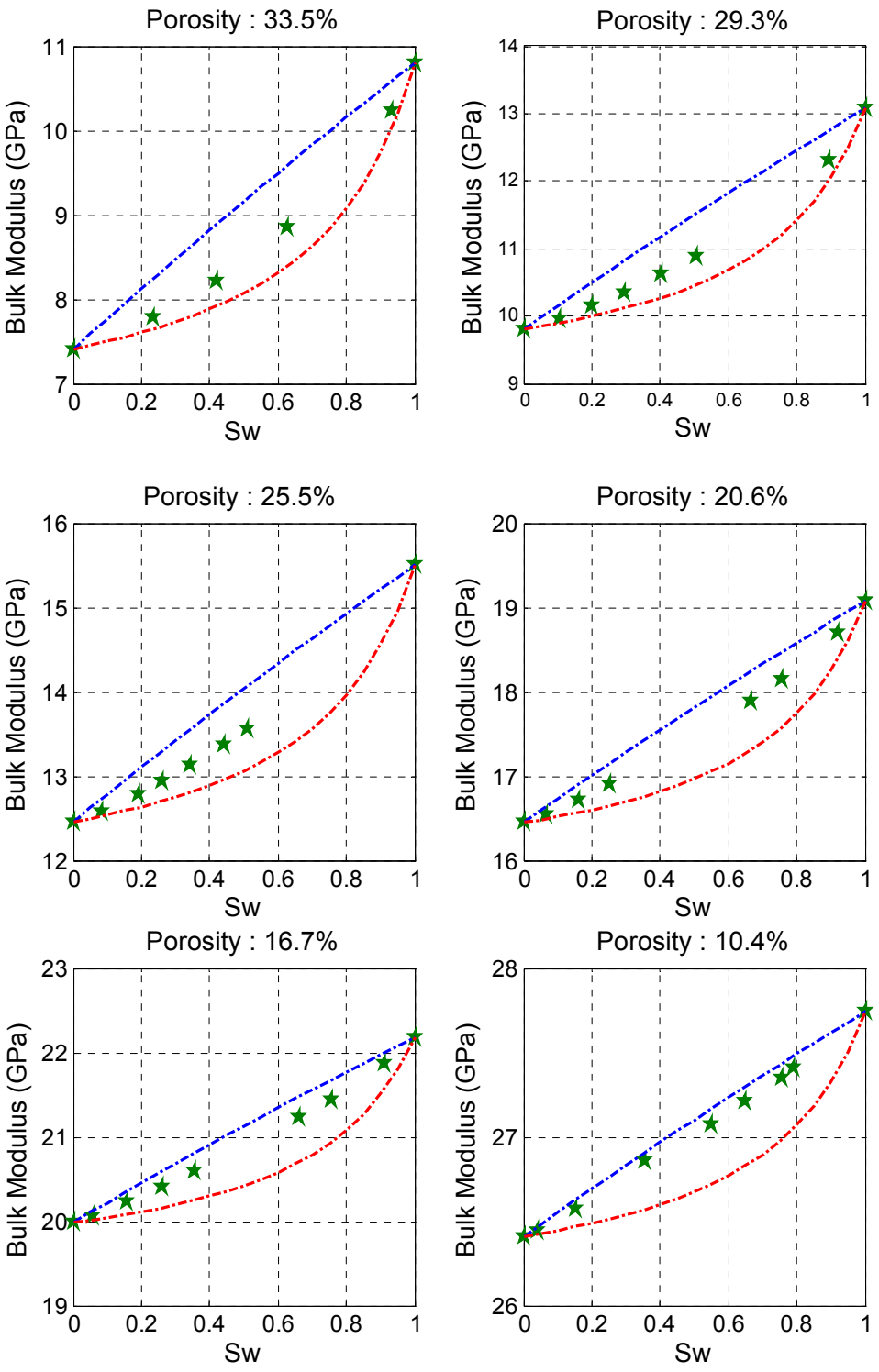

Figure 5.34: Comparison of bulk moduli FE predictions (green stars) for partially saturated microstructures with *scaled* upper (blue) and lower (red) bounds using the effective fluid model in Gassmann's equations. For high porosities (<25%), FE predictions are close to the lower bound; for lower porosities (<20%), they fall nearly on the upper bound.

5.6 Summary and discussions

We constructed consolidated microstructures using three computational diagenetic schemes. These schemes attempt to model the effects of rim, nucleation and contact cements The schemes progressively add cement to well-sorted and poorly sorted packs at different pressures. The estimated diagenetic trends of elastic, transport and electrical properties are in reasonable agreement with laboratory experiments on clean sandstones. This shows the feasibility of a computational scheme to predict different geologic "*what-if*" scenarios, like initial compaction (isotropic/uniaxial) and sorting, and different diagenesis schemes, cement amounts and cement materials. Further, we note that diagenetic trends of elastic properties for CC scheme are stiffer than those for RC and NC scheme. In contrast, NC scheme produces the most compliant microstructures. In CC scheme, the bulk of the cement is deposited near contacts. In contrast, for the same total amount of cement, RC scheme equally distributes the cements around the grain surface; NC scheme adds the cements away from the contacts. Since contacts are the most compliant part of the rock microstructure, CC scheme stiffens the rock geometry most. NC scheme, instead, preserve the compliant contact areas, thereby producing the most compliant rock geometry.

Comparing elastic moduli from GD simulation and FE calculations for uncemented well-sorted packs, we note that the latter method predicts higher moduli. Finite grid size used in transforming compacted packs from GD simulation to three-dimensional grids used for FE calculations adds *pseudo*-cement at contacts. The higher moduli are explained by using a theoretical cementation model (Dvorkin and Nur, 1996). This theoretical model predicts the increase in bulk moduli for low cement concentrations (<3%); however, for shear moduli, the theoretical predictions are higher than FE estimations. Like other EMT models described in Chapter 4, this model assumes homogeneity of all contacts in a granular pack. Hence, using a *relaxation correction* corresponding to the pressure of the un-cemented packs improves the theoretical prediction. The relaxation corrections, as discussed in Chapter 4, are empirical, pressure-dependent corrections based on rigorous GD

simulation calculations. These corrections are a rigorous, yet heuristic, way to include the effects of structural and stress heterogeneity.

Using poorly sorted packs, we present diagenetic trends for various diagenesis schemes. We show that initial uncemented packs follow the heuristic modified lower Hashin-Shtrikman bound (friable-sand model, Dvorkin and Nur, 1996) used to model poorer sorting. Moreover, nucleation cements (the NC scheme) also follow the modified lower Hashin-Shrtikman bound for cement concentrations <5%. This scheme adds cements primarily away from the contacts; therefore, for low cement concentrations it shows the same effect as sorting (modified lower Hashin-Shtrikman bound). For well-sorted packs at different pressures (15, 25 ad 35 MPa), the estimated diagenetic trends of elastic properties are similar to those of our computational diagenetic schemes.

For transport and electrical properties, our simulated diagenetic trends for RC and NC schemes agree with laboratory experiments on clean sandstone plugs. For the CC scheme, the electrical properties follow the lower Hashin-Shtrikman bound (Berryman, 1995). The RC and NC scheme elastic properties are fitted using Archie's law with a cementation exponent of 1.3. It should be noted, however, that simulated diagenetic trends have less scatter than those from laboratory experiments, possibly because of the perfect homogeneity of the microstructure material and the absence of the small cracks typical of realistic samples. However, numerical modeling of crack formation in consolidated microstructures is a separate problem and can be possibly included in future works.

We further studied the fluid-saturation effect on elastic properties using FE simulation. We note that simulated elastic moduli from FE simulation are within 2-4% of Gassmann's predictions. The discrepancy decreases with porosity and is smaller for oil-saturated microstructures than water-saturated ones. This relatively small error is due to un-equilibrated pore pressures, typically for pore-grain boundary voxels and pore-voxels with low connectivity. In FE calculations, due to finite grid size, there is a displacement discontinuity at the phase boundaries, i.e., grain-pore boundaries for single fluid systems. Insufficient resolution leads to higher un-equilibrated pore

pressures. With lower porosities, the specific surface area is smaller, and hence the grain-pore boundaries are also smaller. Also, the number of pore-voxels with lower connectivity decreases. This explains the decreasing percentage error in fluid-saturated cases with decreasing porosity. We further presented the distribution of Skempton's coefficients per pore-voxel to show the un-equilibrated pore pressures under compressive strain. For partially saturated rocks, estimated elastic properties from FE simulations are generally within the upper and lower bounds prescribed by an effective fluid model. With lower porosity, FE calculations are closer to the upper bound, suggesting un-equilibrated pore pressures. The source of these un-equilibrated pore pressures are unrelaxed stresses in pore-voxels and displacement discontinuities at fluid phase boundaries. A possible explanation is the introduction of patchy saturations in low-porosity microstructures during the imbibition process.

5.6 References

Archie, G. E., 1942, The electrical resistivity log as an aid in determining some reservoir characteristics: Trans. Americ. Ints. Mineral. Met., 146, 54-62.

Arns, C. H., Knackstedt, M. A., Pinczewski, W. V. and Garboczi, E. J., 2002, Computation of linear elastic properties from microtomographic images: Methodology and agreement between theory and experiment, Geophys., 67, 5, P1395-1405.

Avseth, P., T. Mukerji, and G. Mavko, 2005, Quantitative seismic interpretation: Applying rock physics tools to reduce interpretation risk: Cambridge University Press.

Avseth, P., T. Mukerji, G. Mavko and Dvorkin, T., 2005, Rock-physics diagnostics of depositional texture, diagenetic alterations, and reservoir heterogeneity in high-porosity siliciclastic sediments and rocks – A review of selected models and siggeted workflows, Geophysics, 75, 5, 75A31-75A47.

Berryman, J., 1995, Mixture of Rock Properties: Rock Physics and Phase Relations: A Handbook of Physical constants: American Geophysical Union Reference Shelf 3, 205.

Bourbie, T., and B. Zinszner, 1985, Hydraulic and acoustic properties as a function of porosity in Fontainebleau sandstone: Journal of Geophysical Research, v. 90, B13, 11524-11532.

Carman, P.C., 1961. L'écoulement des Gaz á Travers les Milieux Poreux, Paris: Bibliothéque des Science et Techniques Nucléaires, Press Universitaires de France, 198pp.

Castagna, J. P., Batzle,M. L., and Kan, T. K., 1993, Rock physics—The link between rock properties and AVO response, in Castagna, J. P., and Backus,M. M., Eds., Offset-dependent reflectivity—Theory and practice of AVO analysis: Soc. Expl. Geophys., 135–171.

Chopard, B. and Droz, M, 1998, Cellular Automata Modeling of Physical Systems, Cambridge Univeristy Press, Cambridge, 341pp.

Dræge, A., Johansen, T. A., Brevik, I. and Dræge, C. T., 2006, A strategy for modeling the diagenetic evolution of seismic properties in sandstones, Petroleum Geoscience, 12, 4, 309-323.

Dvorkin, J., A. Nur, and H.Yin, 1994, Effective properties of cemented granular material: Mechanics of Materials, 18, 351–366

Dvorkin, J., and A. Nur, 1996, Elasticity of high-porosity sandstones: Theory for two North Sea data sets: Geophysics, 61, 1363–1370.

Flórez-Niño, J. –M., 2005, Integrating geology, rock physics, and seismology for reservoir quality prediction, Ph.D. thesis, Stanford University, Stanford, CA.

Fuchtbauer, H., 1974, Sediments and sedimentary rocks 1, in Sedimentary Petrology by W. V. Engelhardt, H. Fuchtbauer and G. Muller, Part II. John Wiley and Sons, New York, 464 pp.

Garc´ıa, X., Araujo, M. and Medina, E., 2004, P-wave velocity–porosity relations and homogeneity lengths in a realistic deposition model of sedimentary rock, Waves Random Media, 14,129-142.

Gassmann, F., 1951,Über die Elastizität poroser Medien:Vierteljahrsschrift der Naturforschenden Gesellschaft in Z urich, 96, 1–23.

Gomez, C., 2009, Reservoir characterization combining elastic velocities and electrical resistivity measurements, Ph. D. Thesis, Stanford University, Stanford, CA.

Guodong, J., Patzek, T. D. and Silin, D. B., 2004, SPE90084: Direct prediction of flow properties of unconsolidated and consolidated reservoir rocks from image

analysis. In SPE Annual Technical Conference and Exhibition,Houston, Texas, USA.

Han, D. H., 1986, Effect of porosity and clay content on acoustic properties of sandstones and unconsolidated sediment, Ph.D. thesis, Stanford University, Stanford, CA.

Keehm, Y., 2003, Computational rock physics: Transport properties in porous media and applications, Ph.D. thesis, Stanford University, Stanford.

Mavko, G., and A. Nur, 1997, The effect of a percolation threshold in the Kozeny-Carman relation: Geophysics, 62, 1480–1482.

Mavko, G. and Mukerji, T., 1998, Bounds on low-frequency seismic velocities in partially saturated rocks, Geophysics, 63, 3, 918-924.

Mavko, G., Mukerji, T. and Dvorkin, J., 2009, The Rock Physics Handbook: tools for seismic analysis of porous media, 2nd edition, Cambridge University Press.

Nagy, K. L. and Lasaga, A. C., 1991, Dissolution and precipitation kinetics of Gibbsite at 80c and pH3, Geochim. Cosmochim. Acta, 56, 3093.

Paxton, S. T., Szabo, J. O., Ajdukiewicz, J. M. and Klimentidis, R. E., 2002, Constructions of an intergranular volume compaction curve for evaluating and prediction compaction and porosity loss in rigid-grain sandstone reservoirs: American Association of Petroleum Geologists Bulletin, 86, 2047-2067.

Revil, A., and P. Glover, 1997, Theory of ionic-surface electrical conduction in porous media: Physical Review B, 55, 3, 1757-1773.

Rimstidt, J. D. and Barnes, H. L., 1980, The kinetics of silica-water reaction, Geochim. Cosmochim. Acta, 44, 1683-1699.

Schwartz, L. M. and Kimminau, S., 1987, Analysis of electrical conduction in the grain consolidation model, Geophysics, 52(10):1,402–1,411, 1987.

Stone, N., and R. Siever, 1996; Quantifying compaction, pressure solution and quartz cementation in moderately- and deeply-buried quartzose sandstones from the Greater Green River Basin, Wyoming, in Siliciclastic Diagenesis and Fluid Flow: Concepts and Applications, Crossey, L, *et al.* (eds.): Society of Sedimentary Geology, Special Publications, **55**, 129-150.

Wyllie, M. and A. Gregory, 1953, Formation factors of unconsolidated porous media: Influence of particle shape and effect of cementation: Transactions of AIME, 198, 103-110.